

**Bimetallic Cyano-Bridged Complexes as a Bi-functional Molecular Device for
Simultaneously Detection and Degradation of Aqueous Environmental Pollutants and
Photophysical Properties of Isocyano Complexes**

by

HO, Pui Yu Ivy

A Thesis Submitted to

The Education University of Hong Kong

in Partial Fulfillment of the Requirement for

the Degree of Doctor of Philosophy

July 2018

ProQuest Number: 10974418

All rights reserved

INFORMATION TO ALL USERS

The quality of this reproduction is dependent on the quality of the copy submitted.

In the unlikely event that the author did not send a complete manuscript and there are missing pages, these will be noted. Also, if material had to be removed, a note will indicate the deletion.



ProQuest 10974418

Published by ProQuest LLC (2019). Copyright of the Dissertation is held by the Author.

All Rights Reserved.

This work is protected against unauthorized copying under Title 17, United States Code
Microform Edition © ProQuest LLC.

ProQuest LLC
789 East Eisenhower Parkway
P.O. Box 1346
Ann Arbor, MI 48106 - 1346

Statement of Originality

I, Ho, Pui Yu Ivy, hereby declare that I am the sole author of the thesis and the material presented in this thesis in my original work except those indicated in the acknowledgement. I further declare that I have followed the Institute's policies and regulations on Academic Honesty, Copy Right and Plagiarism in writing the thesis and no material in this thesis has been published or submitted for a degree in this or other universities.

Ho, Pui Yu Ivy

Abstract

The aim of this research was to investigate the potential multi-functionality of bimetallic complexes through synthesis, characterization, and catalytic studies. Herein we proposed a molecule design strategy called indicator/catalyst displacement assay (ICDA), which are composed of an indicator and receptor for molecular sensing, meanwhile the indicator/receptor serve as catalyst to amplify the sensor signal and degrade the molecules into smaller substances.

In chapter 2, a bimetallic complex $\{[\text{Ru}(\text{}^t\text{Bubpy})(\text{CN})_4]_2-[\text{Fe}(\text{H}_2\text{O})_3\text{Cl}]_2\} \cdot 2\text{H}_2\text{O}$ (**RuFe 1**) ($\text{}^t\text{Bubpy}$ = 4,4'-di-*tert*-butyl-2,2'-dipyridyl) was synthesized and characterized, and proved is capable of functioning as a chemodosimeter for oxalic acid with restoration of $[\text{Ru}^{\text{II}}(\text{}^t\text{Bubpy})(\text{CN})_4]^{2+}$ characteristic emissive properties. Meanwhile, the Fe^{III} form adduct with oxalic acid which catalyze the photooxidation of oxalic acid into carbon dioxide and also catalyze the decolorization of organic dye methyl orange, the sensing properties of this complex can be amplified up to 50 times.

Another example of ICDA, a bimetallic complex $\{[\text{Fe}(\text{}^t\text{Bubpy})(\text{CN})_4]-[\text{Cu}(\text{dien})(\text{ClO}_4)]_2\} \cdot \text{CH}_3\text{C}(\text{O})\text{CH}_3$ (**FeCu 1**) (dien = diethylenetriamine) was reported in chapter 3. This complex was synthesized and characterized, the presence of cyanide induce colorimetric change. The Cu^{II} -cyanide adducts can be oxidized to cyanate with hydrogen peroxide. The addition of coloring agent phenolphthalin can also amplify the signal with detection limit from 500 ppb to 9.5 ppb. A series of Fe(II)-Cu(II) complexes with different number cyanide subunits were synthesized. The complexes $[\text{Fe}^{\text{II}}(\text{CN})_6]-[\text{Cu}^{\text{II}}(\text{dien})(\text{H}_2\text{O})]_2$ (**FeCu 2**), $[\text{Fe}^{\text{II}}(\text{}^t\text{Bubpy})(\text{CN})_4]-$

$[\text{Cu}^{\text{II}}(\text{dien})\text{Cl}]_2$ (**FeCu 3**) and $\{[\text{Fe}^{\text{II}}(\text{Bubpy})_2(\text{CN})_2]_2-[\text{Cu}^{\text{II}}(\text{dien})]\}\text{Cl}_2$ (**FeCu 4**) were also found capable of oxidizing cyanide, but only when the cyanide concentration reach threshold. Further kinetic and thermodynamic measurements were conducted and suggested that the differences in threshold were controlled by both thermodynamic and kinetic properties of the complex.

In chapter 4, a series of ruthenium (II) 2-(2-hydroxyphenyl)benzoxazole (HPBO) complexes **1-3** containing different isocyanide ligands have been synthesized and characterized. The structures of complexes *trans,trans,trans*- $[\text{Ru}(\text{PBO})_2(\text{PhNC})_2]$ (**1b**), *trans,trans,trans*- $[\text{Ru}(\text{PBO})_2(\text{Br}_3\text{PhCN})_2]$ (**1e**), *cis,trans*- $[\text{Ru}(\text{PBO})_2(\text{PPh}_3)(\text{ClPhNC})]$ (**2c**) and *cis,trans,cis*- $[\text{Ru}(\text{PBO})_2(\text{PhNC})_2]$ (**3b**) have been determined by X-ray crystallography. The photophysical properties so as the electrochemical properties of the complexes were also studied.

Acknowledgements

First, I would like to express my deepest gratitude to my principal supervisor, Dr. C. F. Leung, for his enduring guidance, invaluable advice and precious comments throughout my study and on this thesis. Besides, I would like to thank my associate supervisor Dr. Lincoln Fok and Dr. Stephen C. F. Chow for his kind assistance and guidance at the beginning of my study.

I would like to thank Prof. T. C. Lau and Dr. Vincent C. C. Ko and their research group in The City University of Hong Kong for their help to perform the NMR and fluorescence measurement. Without their kind assistance, it would be impossible for me to finish this study. Special thanks go to Dr. C. R. Ng, and Dr. S. S. C. Cheng for their arrangement of instrumental measurement, helpful discussion, and continuous support.

Prof. Michael H. W. Lam in The City University of Hong Kong is also thanked for his assistance in my enrollment of this degree as well as his teaching from my undergraduate. My gratitude also goes to Dr. K. L. Ho, Dr. Y. M. Ho, Dr. C. K. Koo and Mr. C. C. Yeung from Prof. Michael H. W. Lam research group. They have been so generous and patient for kind discussion on both the academic and personal problems.

All the groupmates in Chow's and Leung's group including Mr. Samson C. S. Chan, Dr. Keith Y. F. Ho, Ms. Joyce O. Y. Wong, Dr. Asta L. F. Lai, Dr. Rex C. W. Chan, Mr. Eric C. L. Kwok, Mr. F. Yu, Mr. K. Y. Lee, Mr. Michael P. K. Chan, Ms. Lisa S. Liu, are acknowledged for their kindness and helpfulness.

I would also want to express my sincere thanks to technicians staff in The Education University of Hong Kong, especially Mr. Raymond Y. T. Chui, Ms. Cindy S. Y. Leung, Mr. Kelvin K. T. Po, Ms. Clara S. L. Mok, Mr. C. K. Cho and Dr. Wilson W. L. Wong, for their continuous support and creating such an enthusiastic and happy working environment.

Last but not least, special thanks are giving to my family for their continued gracious support and encouragement during my study. My deepest gratitude goes to my sister, Ms. Carol P. Y. Ho who has been a source of strength and perspective throughout my struggle to achieve this study.

Table of Contents

Chapter 1: Introduction

1.1	An overview of water pollution.....	1
1.2	Basic concept of Schiff base ligands	2
1.2.1	Transitional metal complexes with Schiff base ligand.....	2
1.2.1.1	Ruthenium (II) Complexes	7
1.2.1.2	Iron (II) Complexes	10
1.2.1.3	Heterobimetallic Complexes	10
1.3	Strategies for Molecular Sensing.....	12
1.3.1	Indicator displacement assays (IDAs).....	15
1.4	Strategies for Environmental Remediation.....	22
1.4.1	Fenton Reaction.....	23
1.4.2	Photo-Fenton Reaction.....	23
1.4.3	Fenton-like Reaction	24
1.4.4	Fenton and Fenton-like Reaction with Metallic complex	25
1.4.5	Fenton-like reaction with bimetallic.....	26
1.5	Strategies for Signal Amplification	27
1.6	Strategies for Latent Catalyst.....	32
1.7	Objectives	34

Chapter 2: Ru(II)-Fe(III) Bimetallic Complex as a Multifunctional Device for Detection, Signal Amplification, and Degradation of Oxalate

2.1	Introduction.....	38
-----	-------------------	----

2.2	Experimental.....	45
2.2.1	Materials and Reagents	45
2.2.2	Syntheses	45
2.2.3	Physical Measurements and Instrumentation.....	45
2.2.4	Spectroscopic and Spectrofluorimetric Titration.....	46
2.2.4.1	General Parameters.....	46
2.2.4.2	Binding Constant Determination	47
2.2.4.3	Binding Constant for $[\text{Ru}^{\text{II}}(\text{}^t\text{Bubpy})(\text{CN})_4]_2-[\text{Fe}^{\text{III}}(\text{H}_2\text{O})_3\text{Cl}]_2$ Adducts	47
2.2.4.4	Binding Ratio Determination for $[\text{Ru}^{\text{II}}(\text{}^t\text{Bubpy})(\text{CN})_4]_2-[\text{Fe}^{\text{III}}(\text{H}_2\text{O})_3\text{Cl}]_2$ Adducts by Job's Plot	47
2.2.4.5	Binding Constants for $[\text{FeCl}_3]$ -[substrate] Adducts.....	48
2.2.5	Method Detection Limits of RuFe 1 toward Oxalate	48
2.2.6	Photocatalytic Degradation of Organic Substrates by RuFe 1	49
2.2.7	Catalytic Signal Amplification of RuFe 1 toward Oxalate.....	49
2.2.8	<i>In Vivo</i> Toxicity Assay for RuFe 1	49
2.3	Results and Discussion	51
2.3.1	Synthesis of Tetranuclear Bimetallic Complex RuFe 1	51
2.3.2	Electronic Absorption and Luminescent Properties of RuFe 1	55
2.3.3	Detection of Oxalate Anions	59
2.3.3.1	Chemodosimetric Properties of RuFe 1 toward Oxalate	59
2.3.3.2	Binding Constant and Binding Mechanism of RuFe 1 with Oxalate...	65
2.4	Photocatalytic degradation of Oxalate by RuFe 1	69

2.4.1	Catalytic Signal Amplification of RuFe 1 towards Oxalate	75
2.4.2	Detection, Amplification, and Photo-degradation of Oxalate in Real Water Samples by RuFe 1	79
2.5	Conclusions.....	86

Chapter 3: A Multifunctional Bimetallic Molecular Device for Ultrasensitive Detection, Naked-Eye Recognition and Elimination of Cyanide Ions

3.1	Introduction.....	87
3.2	Experimental.....	96
3.2.1	Materials and Reagents	96
3.2.2	Synthesis.....	96
3.2.3	Physical Measurements and Instrumentation	97
3.2.4	UV-vis Spectroscopic Titration	98
3.2.4.1	General Parameters	98
3.2.4.2	Binding Constant Determination	98
3.2.4.3	Spectroscopic UV-vis Titrations of FeCu 1-4 by Cyanide and Common Anions	98
3.2.5	Spectroscopic UV-vis Titrations of FeCu 1 by Common Anions.....	98
3.2.5.1	Signal Amplification by FeCu 1 in Cyanide Detection.....	99
3.2.5.2	Oxidation of Cyanide to Cyanate with FeCu 1-4 as the Catalyst	99
3.3	Results and Discussion	100
3.3.1	Syntheses and Characterization.....	100
3.3.2	Electronic Absorption Properties.....	107

3.3.3	Chemodosimetric Responses of FeCu 1 toward Cyanide and Different Anions	114
3.3.4	Binding Constant and Binding Mechanism of FeCu 1 with Cyanide	119
3.3.5	Elimination of Cyanide by catalytic oxidation with FeCu 1 as the catalyst	122
3.3.6	Catalytic Signal Amplification by FeCu 1 in Cyanide Detection.....	127
3.3.7	Application of FeCu 1 to Practical Water Samples	132
3.4	Kinetic Investigations of Catalyst Displacement Assay with FeCu 2-4	134
3.4.1	Degradation of Cyanide in Practical Wastewater Samples by the CDA system	141
3.5	Conclusions.....	144

Chapter 4: Synthesis, structure and photophysical properties of isocyano

Ruthenium (II) 2-(2-hydroxyphenyl)benzoxazole complexes

4.1	Introduction.....	145
4.2	Experimental.....	153
4.2.1	Materials and Reagents	153
4.2.2	Syntheses	153
4.2.3	Physical Measurement and Instrumentation.....	158
4.2.3.1	General Parameter	158
4.2.4	Crystallographic Studies.....	158
4.3	Results and Discussion	161
4.3.1	Synthesis and Characterization	161

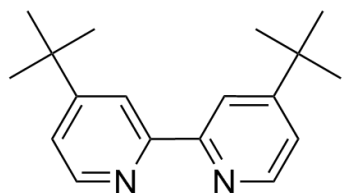
4.3.2	X-ray Crystallography.....	194
4.3.3	Electronic Absorption and Luminescent Properties of 1 , 2 and 3	203
4.3.4	Electrochemical properties.....	212
4.4	Conclusion.....	217
Chapter 5: Conclusion and Future Work		
5.1	Summary of the Thesis.....	218
Reference		220

List of Abbreviations

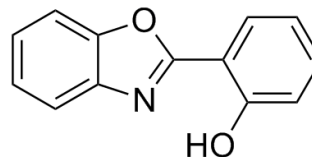
ACN	acetonitrile
bpy	2,2'-bipyridine
^t Bubpy	4,4'-di- <i>tert</i> -butyl-2,2'-dipyridyl
CHCl ₃	chloroform
CHN	carbon, hydrogen, nitrogen analysis
ClO ₄ ⁻	perchlorate
CN	cyanide
CT	charge transfer
Cu	copper
CV	cyclic voltammetry
dien	diethylenetriamine
DMF	dimethylformamide
DMSO	dimethylsulphoxide
EtOH	ethanol
GS	ground state
HOMO	highest occupied molecular orbital
HPBO	2-(2-hydroxyphenyl)benzoxazole
ILCT	Intraligand charge transfer
λ	absorption wavelength
λ_{em}	emission wavelength
L	ligand
LC	ligand centred

LMCT	ligand to metal charge transfer
LUMO	lowest occupied molecular orbital
MC	metal centered
MeOH	methanol
MS	mass spectroscopy
¹ MLCT	singlet metal to ligand charge transfer
³ MLCT	triplet metal to ligand charge transfer
m/z	mass to charge ratio (MS)
NMR	nuclear magnetic spectroscopy
PBO	2-(2-hydroxyphenyl)benzoxazole
RNC	isocyanide
Ru	ruthenium
TLC	thin layer chromatography
tpy	2,2':6',2''-terpyridine
UV/Vis	ultraviolet/visible

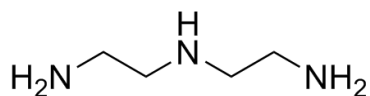
Ligands employed in this thesis



4,4'-di-tert-butyl-2,2'-dipyridyl
(tBupby)



2-(2-hydroxyphenyl)benzoxazole
(HPBO)



diethylenetriamine
(dien)

Chapter 1: Introduction

1.1 An overview of water pollution

Freshwater conservation has become a worldwide challenge. Unlike other natural resources, such as petroleum or earth metals, there are no substitutes for the use of freshwater. Unfortunately, accessible freshwater only constitutes ~1% of the total volume of water on Earth.¹ Large quantities of freshwater are required to support human activities, such as agriculture and industry, and freshwater shortages can result in ecological and agricultural limitations and deterioration.

In addition to the available quantity, the quality of freshwater is also a critical issue. The extensive use and improper disposal of organic and inorganic chemicals from various human activities have led to significant water pollution throughout the world. In the past, several incidents involving significant contamination of water sources resulted in severe financial, political, and health costs.²⁻

⁶ The practical and cost-effective treatment of contaminated water has thus been a long-standing challenge for modern society. After World War II, organic and inorganic chemicals have been widely used for the mass production of consumer products. Today it is known that most of these chemicals have very poor degradability and tend to accumulate in the environment.⁷⁻¹¹

In environmental monitoring, analytical detections are performed using conventional methods to detect target contaminants; however, most require sample preparation procedures or the use of expensive bench-top instruments, which results in difficulties during on-site monitoring. Moreover, there is a time lag between sample analysis and the decision making required to solve the environmental problem, which may result in a delayed resolution and also serious accidents if

people consume polluted food or water in the interim. Therefore, in addition to regulatory and legislative tools for the control of industrial pollution, new potential technology that can quickly determine contaminant levels and subsequently degrade them into harmless materials is highly desirable.

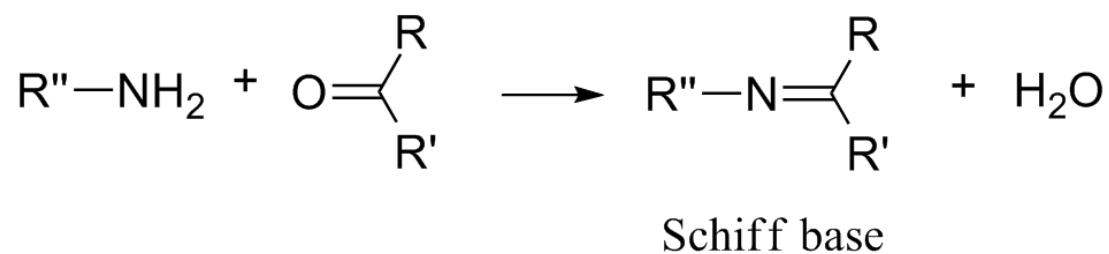
1.2 Basic concept of Schiff base ligands

Schiff base was first reported by Schiff in the last century,¹² which are formed by condensation of amines and carbonyl compounds as shown in Scheme 1.1. The key feature of Schiff bases are their imine functional groups formulated as $\text{RHC}=\text{N-R}'$, where R and R' could be alkyl, aryl, cycloalkyl or heterocyclic groups, and therefore both steric and electronic effect of the ligand can be readily fine-tuned.¹³ Schiff bases are commonly studied ligands as a result of the lone pair electron on the nitrogen atom of the amine group, and most in the presence of others donor atoms such as N, S, O donor group which allow the formation of highly stabilized polydentate metal complex. Schiff base is widely used for industrial purposes,¹⁴ and also utilized as a pharmacophore for their biological properties such as anti-inflammatory activity, antitumor activity and antibiotic activity.¹⁵

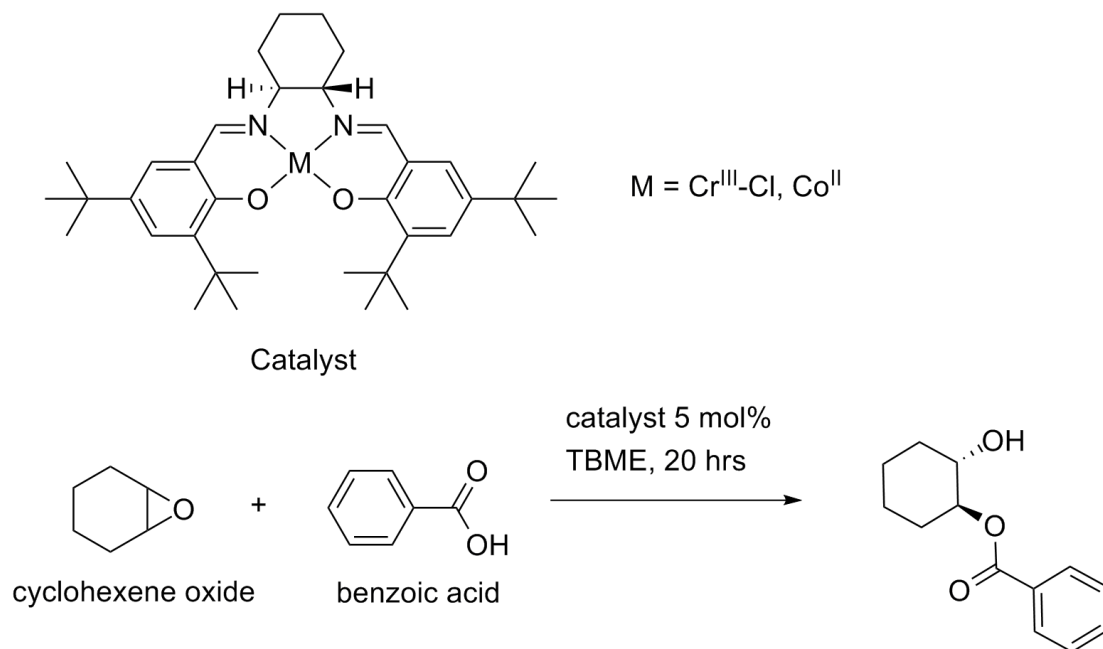
1.2.1 Transitional metal complexes with Schiff base ligand

Schiff bases metals compounds were found to have interesting catalytic and photophysical properties, therefore, provoked wide interest. For instance, Jacobsen et al. have found that a cobalt (II) and chromium (III) complex with a salen ligand can effectively catalyze the ring opening reaction of large epoxides with good enantioselectivity as shown in Scheme 1.2.¹⁶ While with the

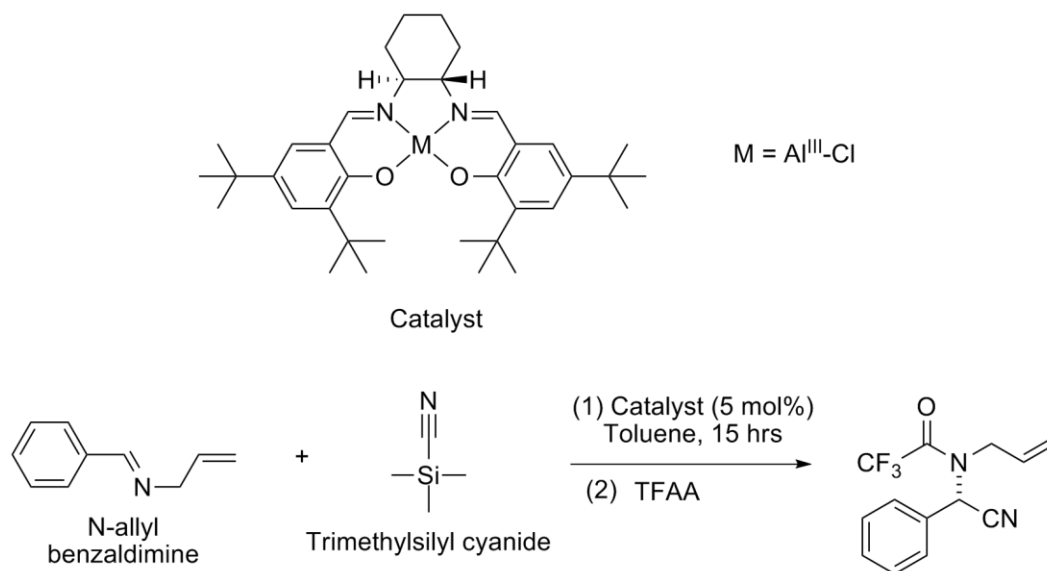
change of metal center to aluminum (III) the complex is capable to catalyze the Strecker reaction, which is an additional reaction of trimethylsilyl cyanide (TMSCN) to *N*-allyl benzaldimine as shown in Scheme 1.3.¹⁷ Such examples reflected the variability of Schiff base complexes in structures and properties.



Scheme 1.1 Synthetic route of Schiff base by the condensation of amines and carbonyl compounds.



Scheme 1.2 Enantioselective ring-opening of cyclohexene oxide with benzoic acid catalyzed by Cr^{III} and Co^{II} salen complexes.¹⁶



Scheme 1.3 Additional reaction of trimethylsilyl cyanide (TMSCN) to *N*-allylbenzaldimine (Strecker reaction) catalyzed by Al^{III} salen complex.

1.2.1.1 Ruthenium (II) Complexes

Luminescent ruthenium (II) metal complexes bearing imine ligands have been investigated extensively not only for their catalytic but also their photophysical properties. One of the extensively studied ruthenium (II) complexes with diimine ligands is $[\text{Ru}(\text{bpy})_3]^{2+}$ which first reported by Adamson et al.,¹⁸ this complex show interesting emitting properties with strong luminescence in the visible light region. This work has drawn the attention of researchers to investigate luminescent ruthenium complexes and their photochemistry. Numerous research found that ruthenium (II) polypyridyl usually exhibit fairly strong luminescence in the visible light region, which can be explained by use of molecular orbital diagram of octahedral ruthenium (II) complex shown in Figure 1.1. As shown, there are four common types of electronic transitions in octahedral metal complexes:

- (i) Metal-centered (MC): Transitions localized on the central metal
- (ii) Ligand-centered (LC): Transitions localized on the ligand
- (iii) Metal-to-ligand charge transfer (MLCT): Electron transition from a metal-based orbital to a ligand-based orbital
- (iv) Ligand-to-metal charge transfer (LMCT): Electron transition from a ligand-based orbital to a metal-based orbital

In the case of $[\text{Ru}(\text{bpy})_3]^{2+}$, where the complex has a diamagnetic t_{2g}^6 electronic configuration when excited by light absorption, one electron will transfer from the metal-centered HOMO to the ligand-centered LUMO. After intersystem crossing, the electron will populate the $^3\text{MLCT}$ state

and deactivated through the emission of light, loss of heat (radiationless deactivation) and populate ^3MC state with ligand dissociation and back to ground state. As the lowest excited state lay on $^3\text{MLCT}$ state, the emission was found to have relatively long solution lifetime.¹⁹

With the change of ligand, the relative energy of the orbitals may be different which subsequently affect their photophysical and electrochemical properties. For instance, the terpyridine ligands in $[\text{Ru}(\text{tpy})_2]^{2+}$ have weaker ligand field strength due to distortion of the octahedron geometry, which results in a smaller d-d splitting and smaller energy different between $^3\text{MLCT}$ and ^3MC excited states compared to $[\text{Ru}(\text{bpy})_3]^{2+}$. Therefore $[\text{Ru}(\text{tpy})_2]^{2+}$ is emissive only at low temperature as the non-radiative deactivation pathway through ^3MC is favored at room temperature.²⁰

Instead of changing the diimine ligand, modification of the ancillary ligands also result in varied photophysical properties of the complexes. The ruthenium (II) complex with mixed ligands $[\text{Ru}^{\text{II}}(\text{bpy})(\text{CN})_4]^{2-}$ was first reported by Bignozzi et al.,²¹ this complex shows strong oxidizing power and solvatochromic behavior with chemical and photochemical stability in aqueous and acidic solutions. The cyanide ligands also provide a site for modifications. Therefore, this mixed ligand ruthenium complexes have been utilized in the development of luminescent chemosensors for various molecules including anion,^{22,23} cations,²⁴⁻²⁶ O_2 ,²⁷ DNA sequences,^{28,29} etc.

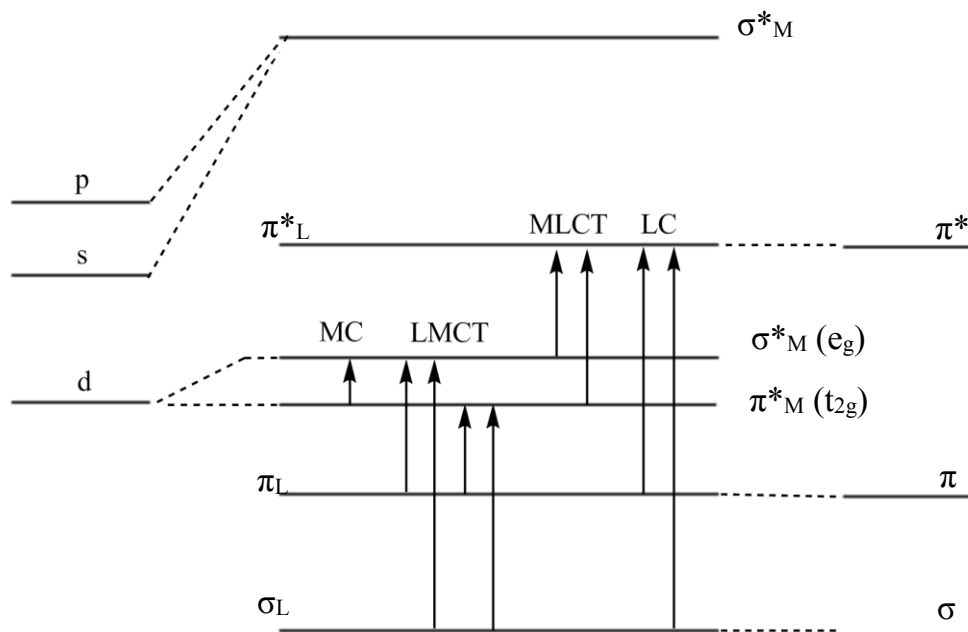


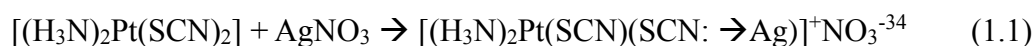
Figure 1.1 Schematic presentation of molecular orbitals and electronic transitions in octahedral Ru(II) metal complex, where L and M refer to ligand and metal respectively.

1.2.1.2 Iron (II) Complexes

Numerous iron complexes with diimine base ligand have been synthesized. Iron (II) complexes share some spectroscopic and electrochemical properties of ruthenium (II) analogues with intense visible absorptions.³⁰ The main different between iron (II) and ruthenium (II) complex is that when iron complexes excited by visible light, a singlet MLCT (¹MLCT) will be promoted which will relax via intersystem crossing to a lower-lying ligand field (LF) state by nonradiative decay with shorter lifetime therefore makes iron (II) complex non-emissive, but more efficient, instead, for the conversion of solar energy into electricity and to be applied in solar cell.^{31,32}

1.2.1.3 Heterobimetallic Complexes

Instead of monometallic complex, scientists also have long been interested in bimetallic complexes which contain two or more different metal centers.³³ To hold two metal atom in close proximity for integrity, bimetallic complexes are usually composed of bridging ligand which links the metal centers. One of the easiest ways to assemble a large bimetallic complex is to use complexes as building blocks and consider complexes as Lewis acid and base pair,³⁴ known also as “complexes as ligands” strategy.^{35,36} Examples of such assembly are:



Where the platinum and iridium complexes as the base in the reactions. The requirement of this bimetallic assembly is that the bridging ligand is a ditopic ligand which is capable of coordination at two separate sites. Common bridging ligands include cyanide,^{38,39} carbonyl,^{40,41} chloride,⁴² nitride^{43,44} and polydentate ligands.^{45,46} Bimetallic complexes can be separated into three classes according to their electrochemical properties also known as Robin-Day classifications.⁴⁷

Class I: Electronic interaction between metal centers are absolutely negligible with extra electron fully localized on one metal atom.

Class II: Electronic interaction occurs between metal centers with the exhibition of intervalence charge-transfer band with low activation energy, where the extra electron is localized on an identifiable metal atom.

Class III: Electronic interaction occur between metal centers and the electron is fully delocalized between metal centers with large electronic coupling.

Both class I and class II bimetallic complexes can be considered as supramolecular species as individual properties of each metal complex are maintained whereas class III species should be considered as a large molecular entity.⁴⁷ For class I and II bimetallic complexes, the combination of metallic centers will not destroy the electrochemical properties of individual metal complexes but will cause the appearance of new photochemical and thermal properties.

Heterobimetallic complexes with diimine ligands are widely studied as potential solar energy converter, multielectron catalyst and chemosensor. Ruthenium (II) bipyridine complexes have been extensively used in the construction of bimetallic complexes as their properties are well studied as mentioned before. Demas and co-workers have studied a series of bimetallic complexes with $[\text{Ru}^{\text{II}}(\text{bpy})_2(\text{CN})_2]$ and $[\text{Ru}^{\text{II}}(\text{phen})_2(\text{CN})_2]$ as building blocks,⁴⁸ and found that the addition of other transitional metal center on the CN linkage has quenched the luminescence of ruthenium (II) complexes. These properties were then utilized in the development of molecular sensors^{49,50}.

1.3 Strategies for Molecular Sensing

The early detection of toxic substances such as cyanide, lead, and mercury is critical to the environmental protection because they are hazardous to humans and other organisms. Compared with traditional instrumental or analytical methods such as molecular sensing using chemosensors and chemodosimeters are favorable as they are more cost-effective, rapid, easy-to-use, and applicable to different areas such as in medicine and in the environment. Chemosensors are defined as abiotic molecules that bind with analyte through non-covalent interactions, typically reversibly, to yield a measurable signal.⁵¹ Chemodosimeters are defined as abiotic molecules that interact with the analyte to generate an irreversible observable signal, which usually involves the breaking and formation of covalent bonds. Both of these are composed of molecular recognition and signaling subunit(s), where the former acts as receptors to provide the sensor selectivity towards the analyte and the latter generates a signal during the binding event, typically through optical signals, such as color change⁵² or fluorescence emission.⁵³

To form a functioning molecular sensor, a mechanism for communication between the recognition and signaling subunits is required. The most common approach is an indicator-spacer-receptor (ISR) approach,⁵⁴ in which the subunits are covalently bound as shown in Figure 1.2. Although this approach is frequently applied in molecular sensing, it has its own limitations, in particular, its difficult syntheses. Scientists have therefore developed an alternative approach, the indicator-displacement assay (IDA), to overcome the constraints in the development of molecular sensors.

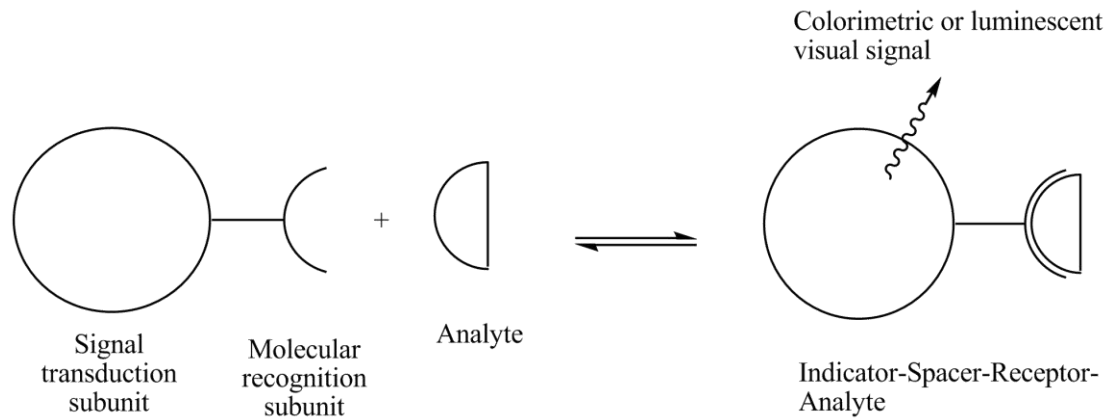


Figure 1.2 A chemosensor/chemodosimeter based on the indicator-spacer-receptor approach.

1.3.1 Indicator displacement assays (IDAs)

In the IDA system depicted in Figure 1.3, the molecular recognition subunit is typically called the receptor, and the signaling subunit is the indicator. The characteristic of an IDA is that the two subunits are usually non-covalently bonded and form an aggregate. When an analyte is introduced into the system, a competitive displacement occurs between the indicator and the analyte for the receptor, which results in the change of the molecular ensemble, and in turn generates an optical signal when luminogenic or chromogenic indicators are used.⁵⁵ Based on this mechanism, the affinity between the indicator and the receptor must be comparable to that between the receptor and the analyte. Compared with a traditional molecular sensor, an IDA has many advantages. Firstly, the two subunits do not need to be covalently bound, and thus the same receptor can be used with different indicators. Secondly, as there is no covalent bonding between the two subunits, there is more flexibility in molecular design and a simpler synthesis can be used. Thirdly, these assays work well in both aqueous and organic media.⁵⁶

Inouye *et al.*⁵⁷ have reported the first chemosensing ensemble for the detection of acetylcholine shown in Scheme 1.4. The fluorescence emission of a pyridinium dye was quenched by tetraphenolate through a photoinduced electron transfer (PET), but emission signal could be readily assumed in the presence of acetylcholine.

IDAs have been used to sense different types of analyte, including but not limited to cations, anions and neutral molecules. Assay reported by Anslyn *et al.*⁵⁸ shown in Scheme 1.5 is an IDA system with the combination of a receptor having three guanidinium group and a commercially available

indicator 5-carboxyfluorescein. The receptor was first bound to the fluorescein indicator by hydrogen bonding. As the receptor was reported to have a higher affinity towards citrate than other carbonate anions, the introduction of citrate displace the fluorescein indicator, as a consequence, free the indicator from the assay, resulting in a decrease of absorbance and fluorescence signal.

Florea has reported an IDA system for sensing of neutral small hydrocarbon molecule by cucurbit[*n*]urils (CB*n*).⁵⁹ As shown in Scheme 1.6, CB6 is first assembled with 5-(4-aminobutylamino)naphthalene-1-sulfonate dye, the addition of hydrocarbon gas with carbon atom less than 6 will displace the dye and show markedly decrease in fluorescence intensity. This system not only differentiate sizes but also have a preference for saturated and less bulky hydrocarbon molecule.

Instead of the organic molecule, metallic complexes were also used in IDA systems. Chow C.F. *et al.* have reported a series of cyano-bridged bimetallic chemosensors, e.g., $M_A-C\equiv N-M_B$, [$M_A = \text{Re(I)}, \text{Fe(II)}, \text{Ru(II)}, \text{and Os(II)}$ and $M_B = \text{Ni(II)}, \text{Cu(II)}, \text{Pt(II)}, \text{and Ln(III)}$]. One of the examples of $\text{Ru}^{\text{II}}-C\equiv N-\text{Pt}^{\text{II}}$ complex shown in Scheme 1.7 has been applied for the detection of sulfhydryl-containing amino acid and peptides.⁶⁰ Such system is also applicable for the determination of cyanide,⁶¹ carboxylic acids,⁶² and biogenic amines.⁶³ Throughout their previous investigations, M_B was selectively coordinated to the analyte to form stable M_B -analyte adducts. The thermodynamics of the formation of these stable adducts eventually resulted in the cleavage of the cyano-bridge of the bimetallic complex. Consequently, the $M_A-C\equiv N$ complex was released and resumed its characteristic spectroscopic properties producing a chemosensing/chemodosimetric response.

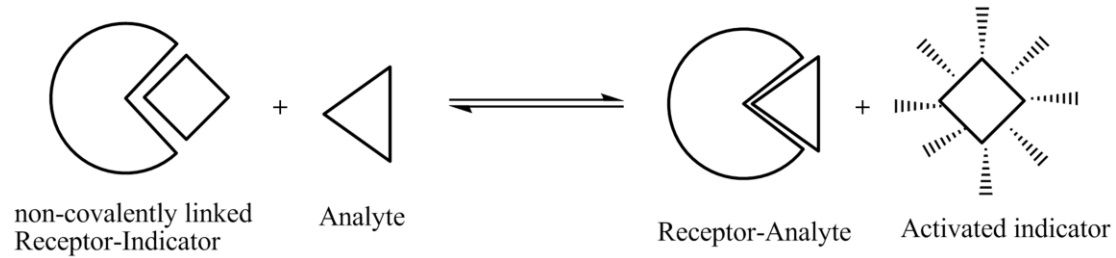
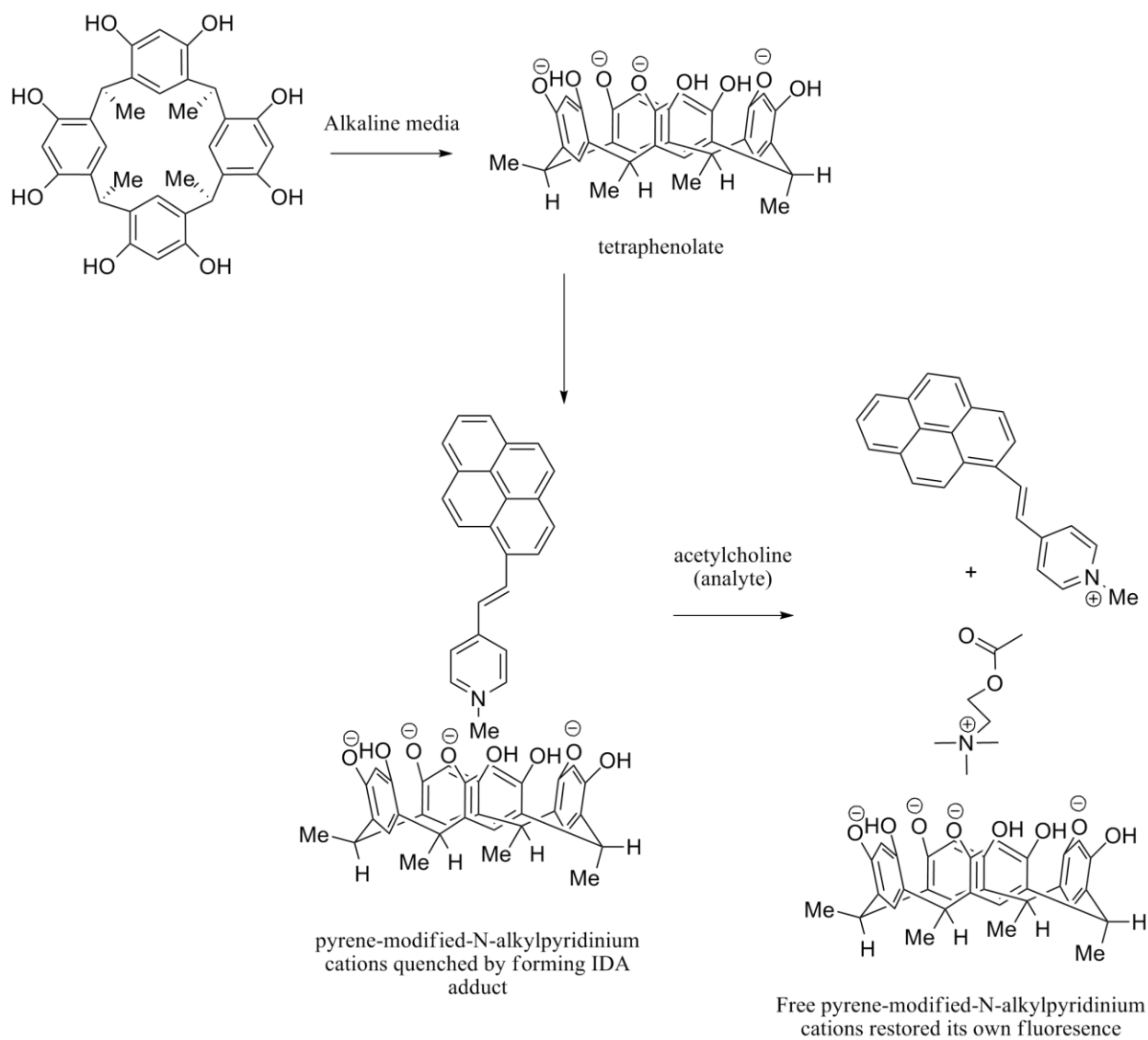
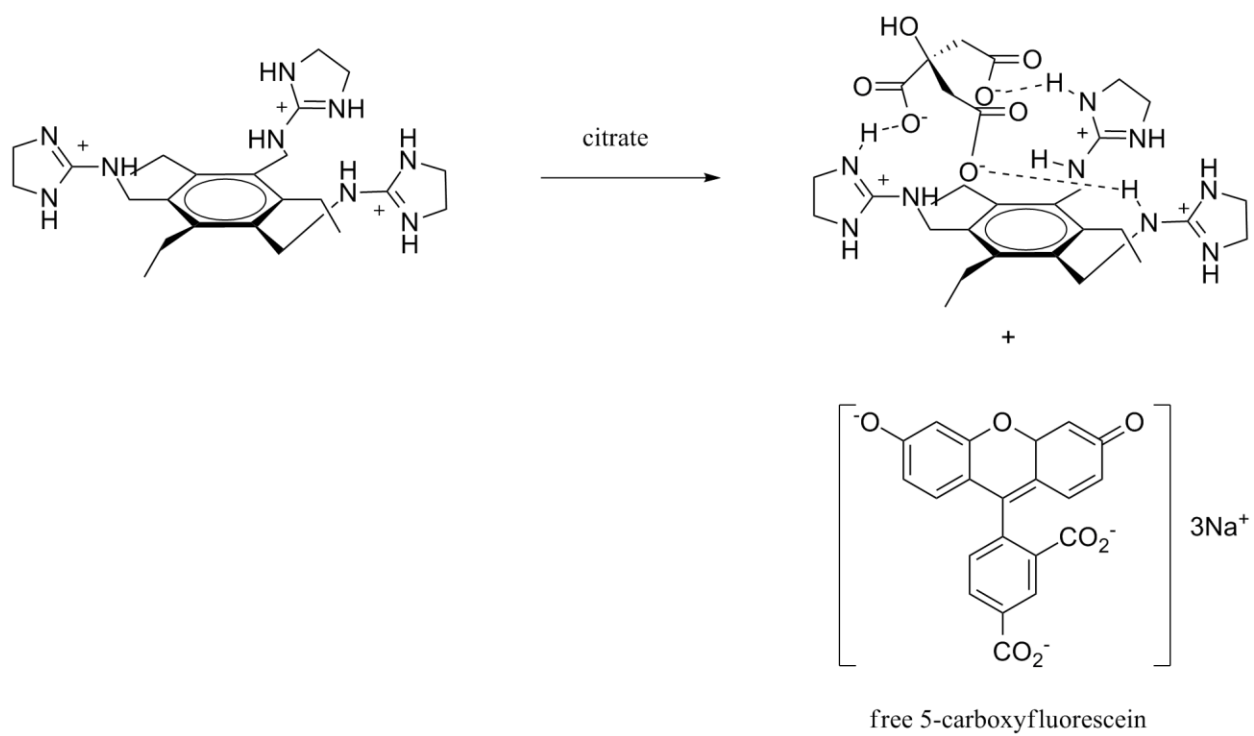


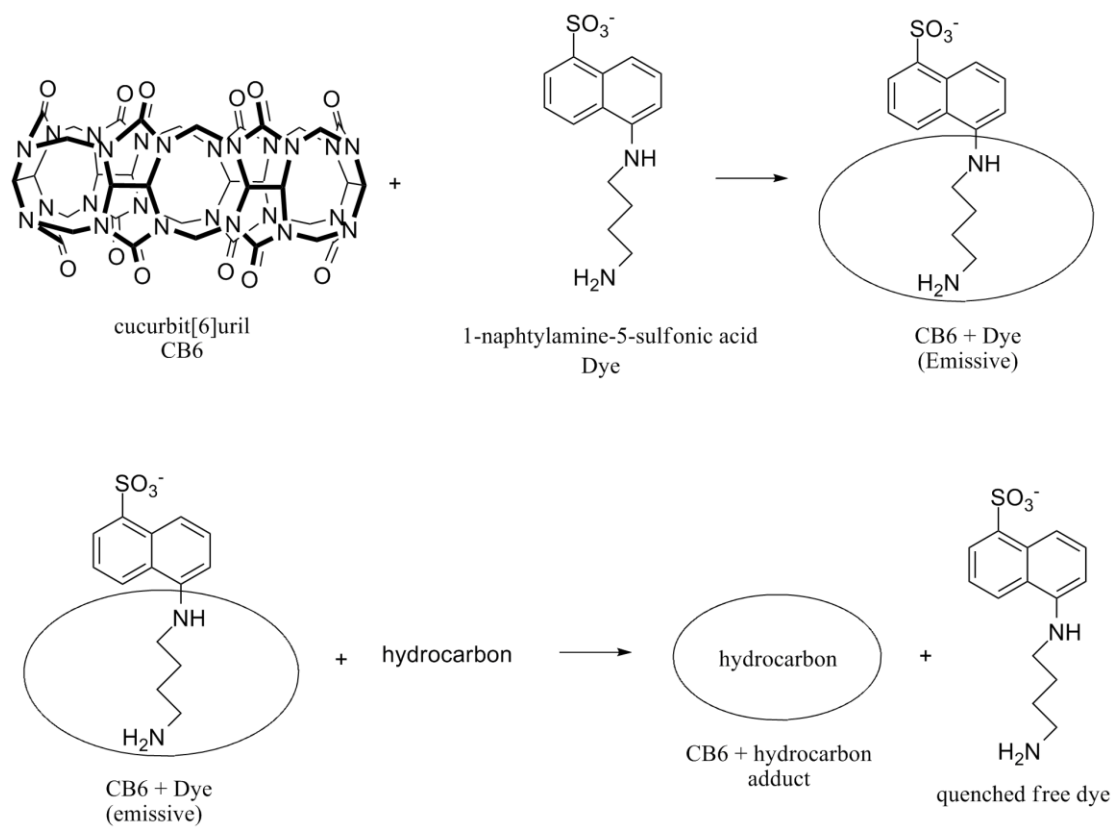
Figure 1.3 Schematic of an indicator-displacement assay (IDA).



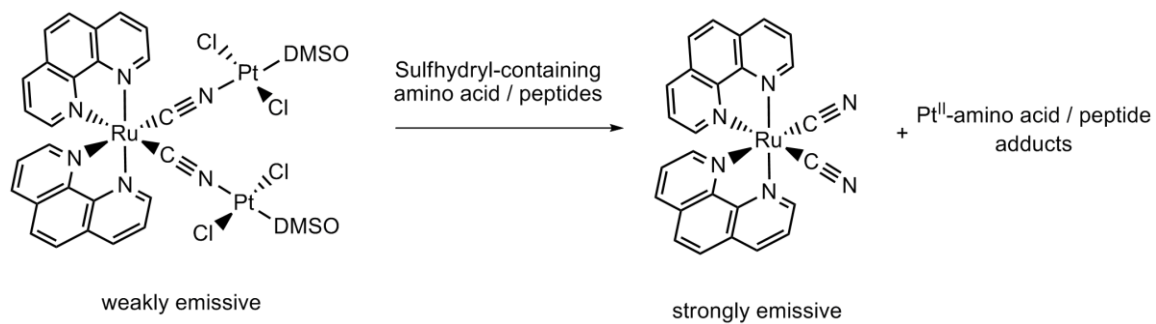
Scheme 1.4 An example of chemosensors using the indicator-displacement assay approach.⁵⁷



Scheme 1.5 Chemosensing of citrate with IDA system consists of a receptor with three guanidinium group and a 5-carboxyfluorescein indicator.⁵⁸



Scheme 1.6 Chemosensing ensemble based on CB6 and 1-naphthylamine-5-sulfonic acid dye for hydrocarbon.⁵⁹



Scheme 1.7 Examples of chemosensors using a bimetallic IDA approach.⁶⁰

1.4 Strategies for Environmental Remediation

The approaches in environmental conservation are not only limited to the development of pollutant detection methods. As environmental contamination is a global concern, efficient devices for pollution remediation are also highly desirable. Different strategies have been reported for environmental remediation. Traditionally, the removal of undesired substances in the environment is accomplished by adsorption methods, such as heterogenous adsorption processes or chemical oxidation using strong oxidants, such as ozone and chlorine. However, these methods have several drawbacks, such as the formation of undesirable toxic substances and the use of expensive and hazardous chemicals.⁶⁴ Biological degradation is now the main route for the removal of contaminants; however, chemicals with low biodegradability or high chemical stability have limited the use of biological treatments.⁶⁵

The use of advanced oxidation processes (AOPs) for the complete oxidative mineralization of pollutants had been extensively studied. This approach aims to completely mineralize pollutants into CO₂ and H₂O or at least to less harmful intermediates. The term AOP was first defined by Glaze *et al.* and refers to any system that generates hydroxyl radicals using different combinations of oxidants, radiation, and catalysts.⁶⁶ Fenton and photo-Fenton reactions are one of the typical AOP examples.

1.4.1 Fenton Reaction

Fenton H. J. H. first reported the Fenton process a century ago and demonstrated that trace amounts of ferrous salts and hydrogen peroxide could oxidize tartaric acid.⁶⁷ Today, the Fenton reagent refers to a mixture of hydrogen peroxide and ferrous ion,⁶⁸ where hydrogen peroxide catalytically decomposes into hydroxyl ($\cdot\text{OH}$) and hydroperoxyl radicals ($\cdot\text{OOH}$)⁶⁹ as shown below:



These radicals have high standard redox potentials of up to 2.8 V⁷⁰ and they are able to oxidize organic substances such as azo dyes,⁷¹ herbicides,⁷² pharmaceutical compounds,⁷³ and phenols⁷⁴ through oxidation. The application of Fenton process is not limited to pollution degradation. In the work of Shelor *et al.*,⁷⁵ Fenton reaction was used for the sample digestion for iodinalysis of milk. The Fenton reagent was also applied for the measurement of amino acids and primary amines with the presence of Fenton reagents and Schiff base derivatives.⁷⁶

1.4.2 Photo-Fenton Reaction

The degradation rate of organic substances by the Fenton reagent is strongly dependent on environmental conditions. When the Fenton reagent is combined with UV-Vis irradiation, photo-

Fenton reaction, the efficiency of the organic degradation is enhanced by the photolysis of ferric ions (Fe^{3+}) to regenerate Fe^{2+} ions (equation 1.5).⁷⁴



The mineralization of organic substances through the photo-Fenton reaction is also improved when compared with the Fenton reaction. As shown in the work of Kiwk *et al.*, the degradation of anthraquinone sulfonate by a photo-Fenton system was eight times faster than in the dark,⁷⁷ and the complete mineralization of anthraquinone sulfonate to carbon dioxide was achieved by the photo-Fenton process within 2 h.

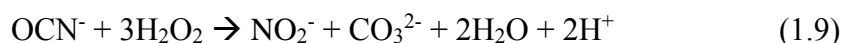
1.4.3 Fenton-like Reaction

The Fenton reaction has been modified and studied intensively, and some similar systems have been developed. The oxidation of organic substances by a mixture of low-valent transition metal complexes and hydrogen peroxide is commonly attributed to a “Fenton-like” mechanism.⁷⁸ Various transition metal ions e.g. Cu^{II} ,⁷⁹⁻⁸¹ Cr^{III} ,^{82,83} Co^{II} ,^{84,85} Mn^{II} ,⁸⁶ Ni^{II} ,⁸⁷⁻⁸⁹ Cd^{II} ⁹⁰ and transition metal mixtures were investigated and used for the degradation of organic substances.

One of the more extensively studied transitional metal is Cu^{II} , which shows a higher efficiency in the production of oxidizing species at neutral pH than ferrous ion.⁸² Proposed mechanisms for the Fenton-like reaction of Cu^{II} is shown below:



The Cu^{II} ion is first reduced by hydrogen peroxide to Cu^{I} , which is subsequently re-oxidized and produce hydroxyl radicals.⁹¹ The application of the Fenton-like reaction of Cu^{II} includes the oxidative destruction of cyanide:⁹²



In this reaction, cyanide is first oxidized to cyanate and eventually turned into carbon dioxide and nitrate in the presence of excess hydrogen peroxide. Another example was the reduction of hazardous high-valent heavy metals, such as hexavalent chromium.⁹³ In the work of Abu-Saba *et al.*, Cr^{VI} ion was reduced by Cu^{I} produced from superoxide redox cycling.

1.4.4 Fenton and Fenton-like Reaction with Metallic complex

Fenton reaction catalyzed by metallic complex was also widely studied. Different kinds of ligands have found can affect Fenton reaction in terms of rate and products. Zuo and Holgné have investigated the mechanistic and kinetic properties of Fe(III)/Fe(II)-oxalate complexes in hydrogen peroxide formation,⁹⁴ found that oxalate radicals were produced during photolysis of the Fe(III)-oxalate complexes result in increased formation of hydrogen peroxide and superoxide, which later proved by Tachiev *et al.* that the formation of peroxide by iron with carboxylic acid

ligands have higher reaction rate than free iron catalyst.⁹⁵ More ferric complexes were also investigated by Pignatello and Baehr, and it was shown that relatively mild chemical oxidation reaction can be performed using ferric nitrilotriacetate (NTA) complex compared with traditional Fenton reagent ($\text{Fe}^{2+} + \text{H}_2\text{O}_2$).⁹⁶

1.4.5 Fenton-like reaction with bimetallic complexes

Instead of the change of ligands, the presence of other metal cations are also studied to facilitate Fenton reaction. Bimetallic system of Fe coupled with different metal i.e. Cu, Ni, Co were also studied for their potential use in Fenton reactions.⁹⁷ Guimaraes *et al.* have proved that the presence of Cu can significantly increase the radical formation in oxidation of quinoline as follows:⁹⁸



Yip *et al.* have investigated the photo-Fenton-like catalytic properties of bimetallic Cu/Fe clay in the degradation of organic dye Acid Black 1 (AB1).⁹⁹ The Cu/Fe clay was prepared by chemical vapor deposition method with a 1:1 mole ratio. Degradation of AB1 by the bimetallic and respective monometallic clay was investigated at different pH. The bimetallic system was found to be more applicable over a broaden pH range and exhibited less metal leaching compared with the monometallic system.

Dong *et al.* further investigated the bimetallic Fenton reaction by introducing different metals i.e. Cu^{2+} , Co^{2+} , Ce^{3+} and La^{3+} into modified amidoximated polyacrylonitrile (PAN) fiber together with Fe and compared their performance in the degradation of Rhodamine B (RhB).¹⁰⁰ It was found that the reductive potential (ΔE) of $\text{Cu}^{2+}/\text{Cu}^+$ was lowered in the bimetallic system, leading to a faster $\text{Cu}^{2+}/\text{Cu}^+$ redox cycle and a higher catalytic performance with a 3-fold increase in the oxidative degradation of RhB in dark compared with the monometallic iron system.

1.5 Strategies for Signal Amplification

Sensing methods with high selectivity and sensitivity are highly desirable. Scientists put efforts to enhance detection sensitivities. Detection using a signal amplification strategy, in which the sensitivity of the sensing process is increased by forming a large number of reporter molecules through the catalytic reaction in the presence of the analyte, has thus gained attention. Enzyme-linked immunosorbent assay (ELISA) is an example of signal amplification, in which the antigen is identified by measuring the catalytic activity of a reporter enzyme that is attached to the antibody as shown in Figure 1.4.¹⁰¹ Typically, chromogenic reporter molecules are catalytically produced as the indicator.¹⁰² Recently, fluorogenic,¹⁰³ electrochemiluminescent,¹⁰⁴ and quantitative PCR reporters¹⁰⁵ have also been used in ELISA systems.

Chemists have also explored the development of molecular sensors with catalytic signal amplification properties similar to that of ELISA.¹⁰⁶ In the work of Anslyn *et al.*,¹⁰⁷ a Cu (I)-catalyzed Huisgen cycloaddition reaction was amplified (Scheme 1.8) in the presence of regulatory elements for the detection of metal ions (Scheme 1.9). In this protocol, Cu (II) first forms an

assembly with exogenous species such as EDTA. When other transition metal ions (Zn^{II} , Pb^{II} , Cd^{II}) were added, a competitive displacement occurs, frees the Cu (II) ions which react with sodium ascorbate, and results in the *in situ* generation of a Cu (I) catalyst. The Cu (I) ions then catalyze the formation of 1,4-substituted triazole from an alkylazide and a terminal alkyne. The subsequent change in fluorescence behavior and thus amplifies the signal for analyte detection.

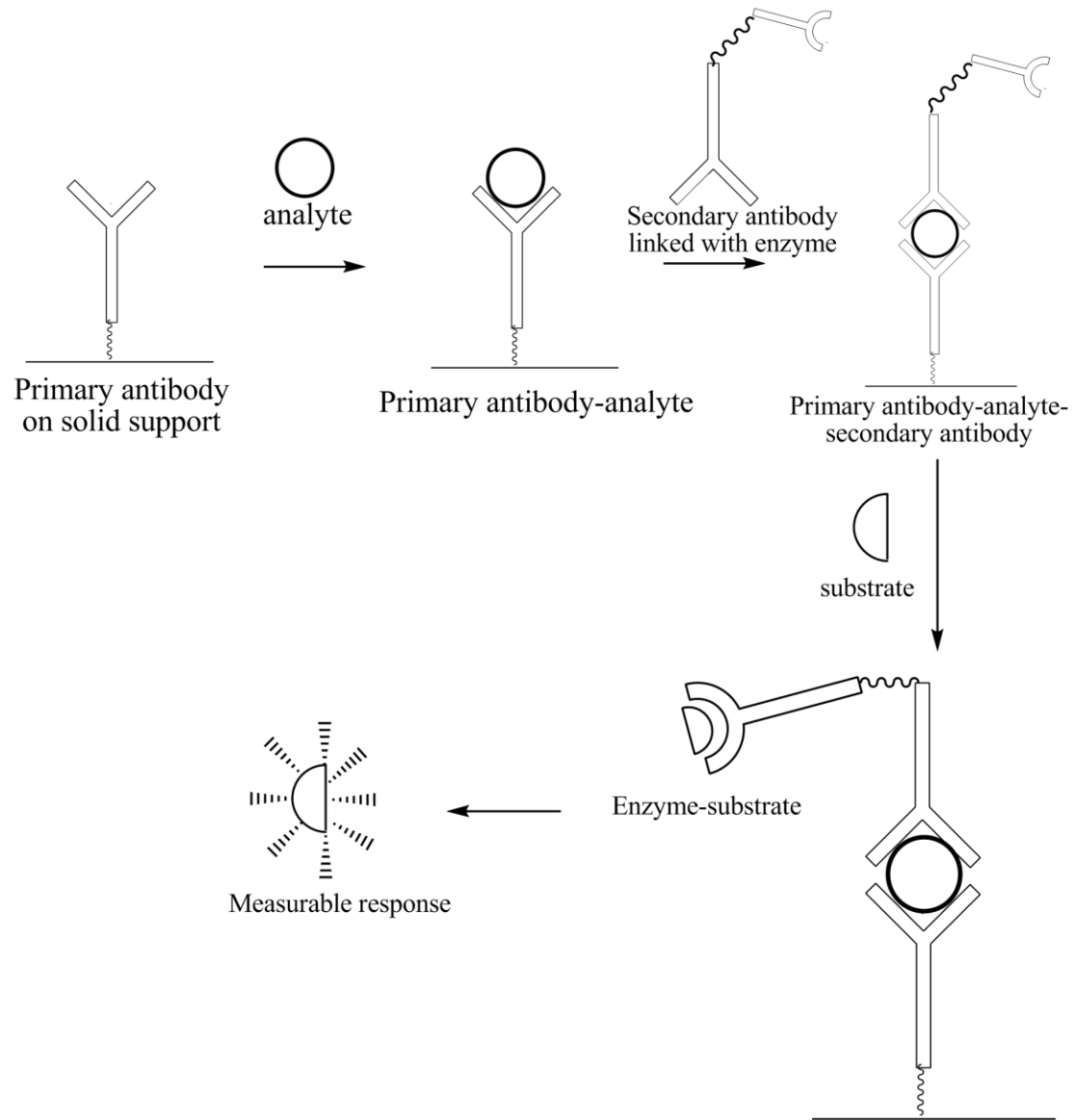
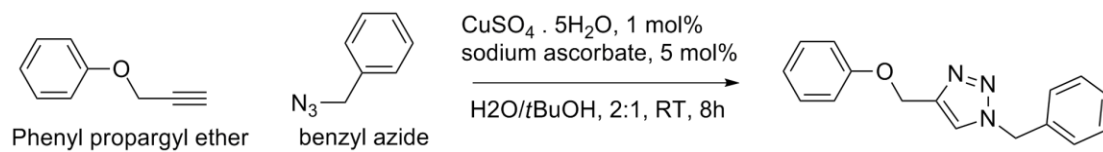
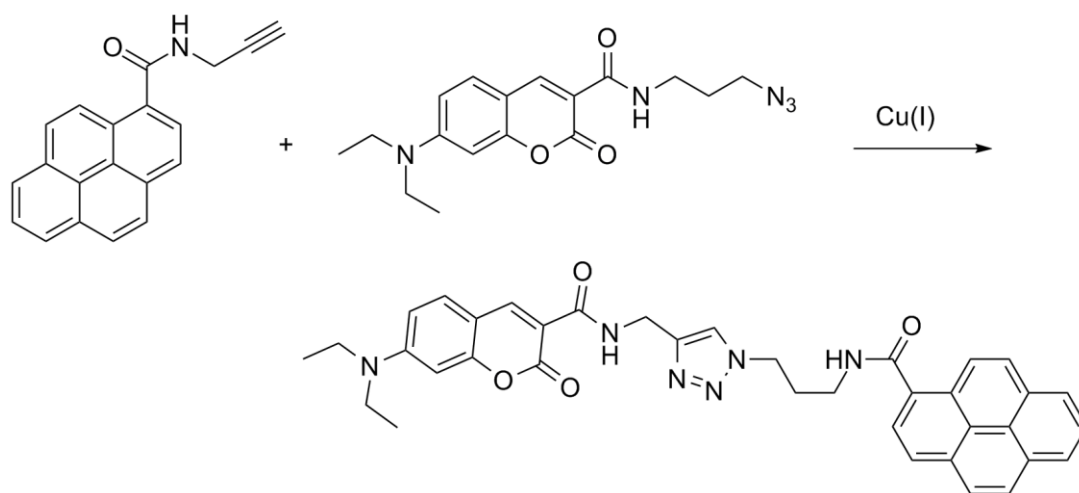


Figure 1.4 Schematic of an enzyme-linked immunosorbent assays (ELISA).¹⁰¹



Scheme 1.8 A Cu (I)-catalyzed Huisgen cycloaddition reaction.¹⁰⁷



Scheme 1.9 A Cu (I)-catalyzed Huisgen cycloaddition reaction for a signal amplifying detection of metal ions.¹⁰⁷

1.6 Strategies for Latent Catalyst

Latent catalysts are catalysts that are only activate under specific conditions, while in normal conditions they remain inactive.¹⁰⁸ Most of the reported latent catalysts are activated by external stimulations like heating,¹⁰⁹⁻¹¹¹ photoirradiation,¹¹²⁻¹¹⁴ ultrasonic wave^{115,116} or addition of reactant.^{117,118} As illustrated in Figure 1.5, the latent catalyst remain inactive in the absence of significant external stimulation. Meanwhile, non-latent catalyst mediates the reaction without stimulation.

The advantages of using latent catalysts over the common catalyst is a more controllable initiation step of the spontaneous catalytic reaction.¹¹⁹ In other words, use of latent catalysts can ensure the chemical reaction initiated under a specific condition. Some polymer synthesis processes have made use of the advantage of latent catalyst in curing¹²⁰⁻¹²² and olefin metathesis^{123,124} to produce functionalized polymer chain¹²⁵ and improve the reaction efficiency.¹²⁶ Although latent catalysts are widely used in polymer synthesis, its application in environmental remediation is less common.

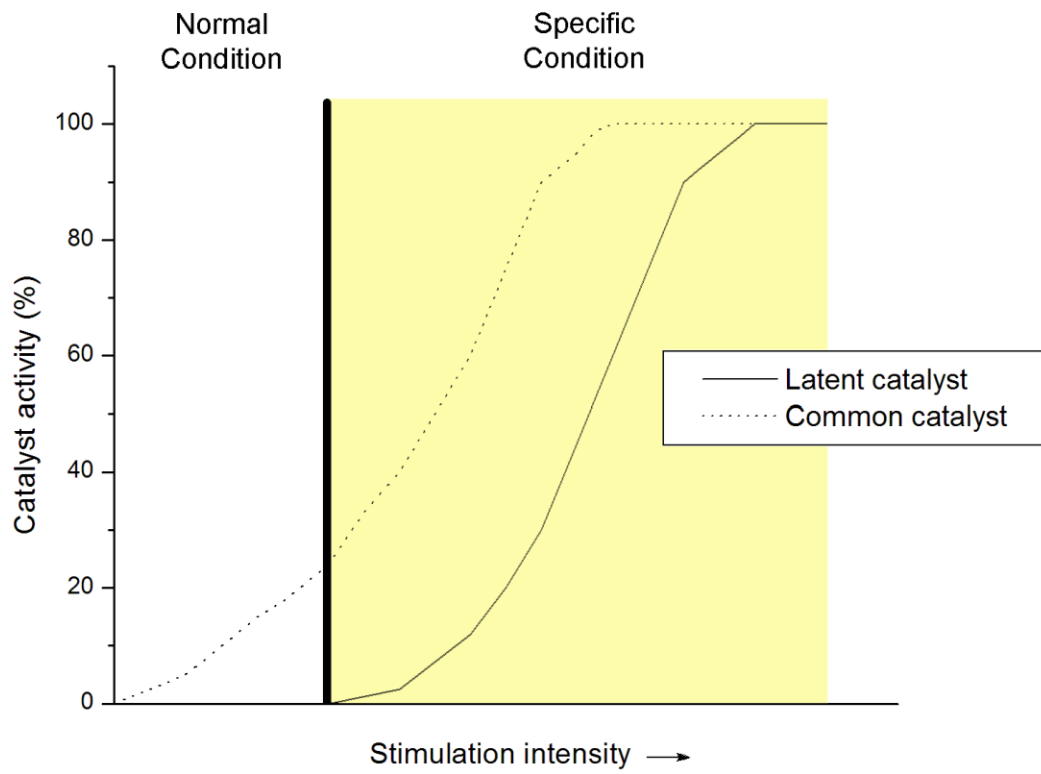


Figure 1.5 Relationship between stimulation intensity and catalyst activity of latent and common catalysts.

1.7 Objectives

Although much effort has been developed to detect or degrade pollutants, only a few techniques have been reported for the simultaneous detection and degradation of pollutants. In the following chapters, we attempt to use bimetallic complexes to develop two sensing and catalytic degradation approaches, i.e. the indicator/catalyst displacement assay (ICDA) and the catalyst displacement assay (CDA). The ICDA approach involved the design of multifunctional molecular devices that feature chemosensing of target analytes, and at the same time catalytically amplify the detection signal and degrade them. As shown in Figure 1.6, the ICDA includes an indicator, which is also a catalyst and is first reversibly bound to a receptor, which is also an inhibitor. When a competitive analyte, such as a toxic pollutant, is introduced into the system, the displacement of the indicator/catalyst from the receptor/inhibitor, in turn, activates both the indicator/catalyst. Ultimately, the analyte concentration can be monitored and catalytically degraded into harmless materials in a one-step process. This design enables the molecular device to degrade the pollutants when their levels reach a certain detection threshold. This approach can reduce the loading of reagents (e.g. H_2O_2), catalysts (transition metal complexes), energy (UV irradiation) and manpower used in traditional Fenton / Photo-Fenton / Fenton-like processes. To the best of our knowledge, there are no existing examples of such multifunctional molecular device.

While the CDA approach, as shown in Figure 1.7, is similar to the ICDA approach, the catalyst is first bound to a receptor which not only inhibits the activity of the catalyst but also introduces latency to the catalysis. The CDA system, therefore, inherits the characteristics of latent catalyst, where reaction conditions to initiate the degradation can be conveniently selected by the inhibitor.

This CDA approach will be useful in the field of environmental remediation and pollutant treatment, where CDA catalyst will remain inactive when pollutants concentration is ignorable, while the degradation of the pollutants will take place when the concentration is over a certain threshold level.

In the following chapters, two examples of ICDA are reported as proof of concept. In Chapter 2, a cyano-bridged bimetallic tetranuclear complex $[\text{Ru}^{\text{II}}(\text{}^t\text{Bubpy})(\text{CN})_4]_2-[\text{Fe}^{\text{III}}(\text{H}_2\text{O})_3\text{Cl}]_2$ (**RuFe 1**) and its anion binding properties are reported. This complex acts as a multifunctional device that features chemosensing, signal amplification and photo-Fenton (PF) catalytic properties of oxalate ($\text{HOOC}-\text{COO}^-$). In Chapter 3, a similar cyano-bridged bimetallic complex $\text{Fe}(\text{}^t\text{Bubpy})(\text{CN})_4-[\text{Cu}(\text{dien})(\text{ClO}_4)]_2$ (**FeCu 1**) is reported and it acts as a multifunctional device that features chemosensing, signal amplification and photo-Fenton catalytic properties toward cyanide (CN^-). Also, CDA based on three cyano-bridged bimetallic complexes, $[\text{Fe}^{\text{II}}(\text{CN})_6]-[\text{Cu}^{\text{II}}(\text{dien})(\text{H}_2\text{O})]_2$ (**FeCu 2**), $[\text{Fe}^{\text{II}}(\text{}^t\text{Bubpy})(\text{CN})_4]-[\text{Cu}^{\text{II}}(\text{dien})\text{Cl}]_2$ (**FeCu 3**) and $\{[\text{Fe}^{\text{II}}(\text{}^t\text{Bubpy})_2(\text{CN})_2]_2-[\text{Cu}^{\text{II}}(\text{dien})]\}_2\text{Cl}_2$ (**FeCu 4**) are reported. Their thermodynamic, kinetic and catalytic properties with cyanide and oxalate are examined. In Chapter 4, a series of new ruthenium (II) complexes with Schiff base 2-(2'-hydroxyphenyl)benzoxazole (PBO) and isocyanide ligands are synthesized and studied in order to understand factors that control the photophysical and electrochemical properties of mixed-ligand ruthenium (II) isocyanide complexes.

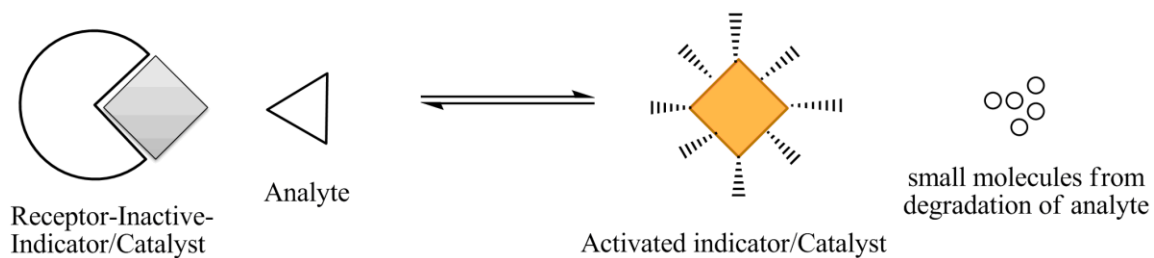


Figure 1.6 A chemosensor/chemodosimeter based on the indicator/catalyst displacement assay (ICDA) approach.

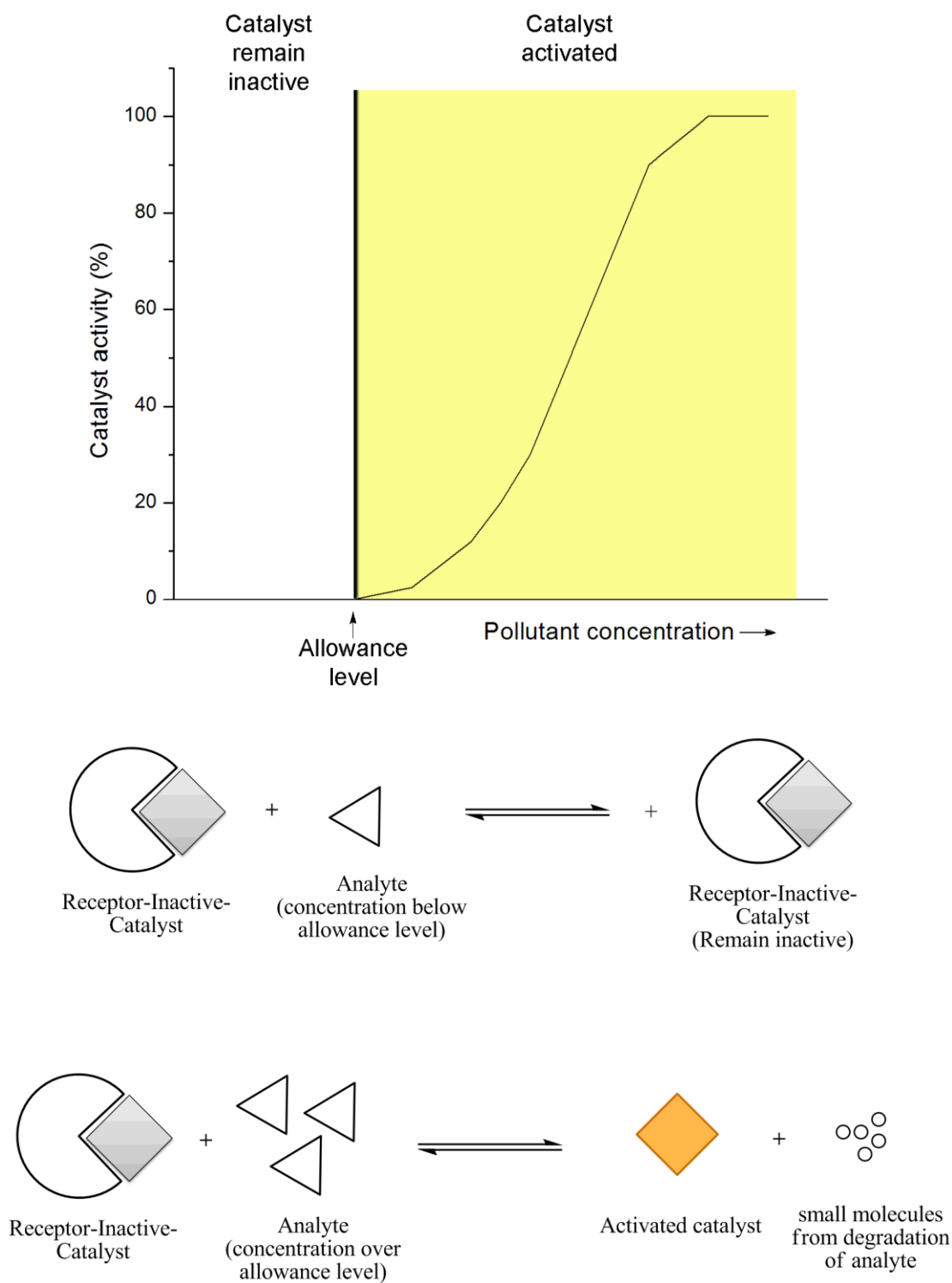


Figure 1.7 A pollution remediation based on catalyst displacement assay (CDA) approach.

Chapter 2: Ru(II)-Fe(III) Bimetallic Complex as a Multifunctional Device for Detection, Signal Amplification, and Degradation of Oxalate

2.1 Introduction

Oxalic acid is a colorless organic acid that dissolves in water. It is found in food, especially in the spinach family and the brassicas, but its concentration seldom causes poisoning in humans.¹²⁷ While high levels of oxalic acid are commonly found in manufacturing processes, such as printing and dyeing processes, pharmaceutical production, rare earth metal extractions and fine chemical synthesis.^{128,129} In 2009, the global demand for oxalic acid was approximately 450,000 tons, whereas the demand in Mainland China alone exceeded 300,000 tons.¹³⁰ Due to its excessive use, several studies have been started to detect the presence of oxalic acid in different freshwater bodies, such as groundwater, rain and snow.¹³¹ Thus, the safe disposal of spent oxalic acid is a challenge to industrial, environmental and public health.

In mammals, oxalic acid has an oral LD₅₀ of up to 600 mg/kg body weight.¹³² However, excessive accumulation of oxalic acid in the human body can cause a variety of health disorders. When oxalic acid is salted out with calcium, the mineral bioavailability decreases and the resulting calcium oxalate is a key component of kidney stones, which induce renal failure, urinary stone disease and pancreatic insufficiency.¹³³⁻¹³⁵

Several methods are available for oxalic acid detection. Zarembski and Hodgkinson have reported a fluorometric determination method of oxalic acid in serum (Scheme 2.1).¹³⁶ In this method, oxalic acid was first extracted by precipitation with calcium sulphate and reduced to glyoxylic acid by zinc spirals, followed by coupling with resorcinol to produce a fluorescent complex. Later on, several methods also based on precipitation of oxalic acid were proposed,^{137,138} whereas these methods have several systematic errors, including incomplete precipitation and reduction, pH dependence and complicate determination method. Others detection method include colorimetric analysis usually include the use of derivatization reagents and most of them suffer from interference by other carboxylic acids.¹³⁹⁻¹⁴³

Several oxalic acid chemosensors were reported, but sensors with high sensitivity and selectivity are seldom reported.¹⁴⁴⁻¹⁴⁶ Fabbrizzi *et al.* have reported a fluorescence chemosensor for carboxylic acid,¹⁴⁷ which consist of a fluorescent Zinc(II) complex with 2,4,6-triamino-1,3,5-trimethoxycyclohexane ligand (ATMCA) (Figure 2.1) and forming ternary ligand/zinc/carboxylic acid complexes with a notable decrease of fluorescence intensity. The detection limit of this method for oxalate anion can be down to sub-mM level. However, this complex was also quenched by nucleotides containing an imide or amide functional group.

Oh *et al.* have reported another fluorescent probe for detection of oxalic acid,¹⁴⁸ which is composed of a fluorescence zinc(II) complex with modified cyclen ligand, oxalic acid will bind in between the enamine group and zinc metal center of the complex result in fluorescence quenching (Scheme 2.2). However the presence of other dicarboxylic acids such as acetic acid and succinic acid will increase the fluorescence intensity.

Hu and Feng have reported a chemosensor of oxalic acid based on IDA, which consists of a Fluorescein/Eosin Y indicator which was first non-covalently bind to a copper-cyclophanes bimetallic complex acceptor (Scheme 2.3). The presence of oxalic acid will competitively bind to the acceptor and indicator released will give color changes and emission. The detection limit of oxalate was found at 0.079 μM .

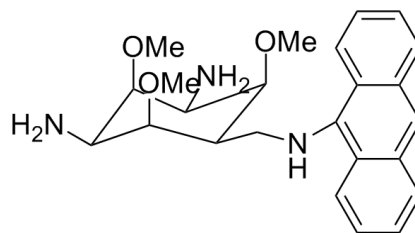
Much work has been done to remediate natural environments contaminated by oxalic acid. Different degradation methods have been investigated, proving that oxalic acid can be destroyed effectively to carbon dioxide.¹⁴⁹⁻¹⁵¹ However, to the best of our knowledge, there have been no chemical devices that detect and degrade oxalic acid simultaneously.

To address the above research gap, we have synthesized a bimetallic $\text{Ru}^{\text{II}}\text{-Fe}^{\text{III}}$ complex, $[\text{Ru}^{\text{II}}(\text{tBubpy})(\text{CN})_4]_2\text{-}[\text{Fe}^{\text{III}}(\text{H}_2\text{O})_3\text{Cl}]_2$ (**RuFe 1**), as an ICDA (Indicator-catalyst displacement assay) system for oxalic acid. In this chapter, **RuFe 1** complex is examined for its sensing and catalytic degradation properties towards oxalic acid. $[\text{Ru}^{\text{II}}(\text{tBubpy})(\text{CN})_4]^{2-}$, as one of the building blocks of **RuFe 1**, is well-known for its solvatochromic and luminescent properties acts as both an indicator and an inhibitor in this system. This Ru(II) complex is firstly allowed to bind with a

Fe(III) receptor/catalyst, for the Fenton degradation of organic substrates. In the absence of a competitive analyte, **RuFe 1** stays inactive. When oxalic acid is introduced to the system, Fe(III) is displaced from Ru(II), as an indicator that provides both chromatic and fluorescence signals. Simultaneously, the Fe(III) receptor released and was catalytically activated to degrade oxalic acid into harmless substances. Most importantly, Fe(III) not only acts as Fenton catalyst, it is also a catalyst which amplifies the chromatic signal by initiating reaction such as the decolorization of the azo dye, which induces intensive colorimetric change detectable with naked-eye, achieving the signal amplification.

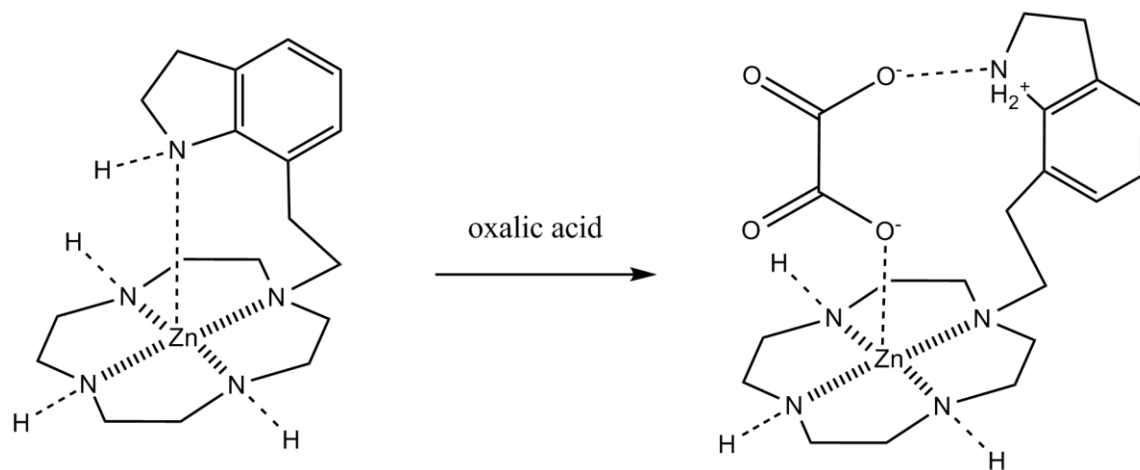


Scheme 2.1 Fluorometric determination of oxalic acid by precipitation of calcium oxalate followed by reducing to glyoxylic acid and coupling with resorcinol.¹³⁶

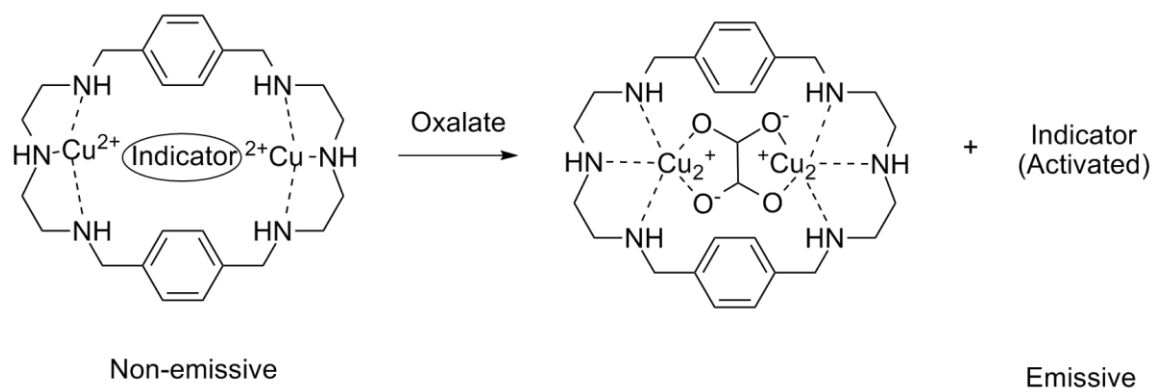


2,4,6-triamino-1,3,5-trimethoxycyclohexane
ATMCA

Figure 2.1 A 2,4,6-triamino-1,3,5-trimethoxycyclohexane ligand that bind to zinc cation for the detection of carboxylic acid.



Scheme 2.2 Chemosensing of oxalic acid based on Zn^{II}-cyclen complex with enamine group



Scheme 2.3 An IDA system consist of copper complex of cyclophane for sensing of oxalate anion.

2.2 Experimental

2.2.1 Materials and Reagents

4,4'-Di-*tert*-butyl-2,2'-bipyridine (^tBubpy), ruthenium (III) chloride hydrate, and potassium salts of acetate, L-tartrate dibasic dehydrate, azide, nitrate, thiocyanate, dihydrogen phosphate, bromide, chloride and sulfate were obtained from Aldrich. Anhydrous ferric chloride, glyoxylic acid monohydrate, pyruvic acid, tetra-*n*-butylammonium hexafluorophosphate and potassium cyanide were obtained from Acros. Potassium oxalate was obtained from Farco Chemical Supplies. $\text{K}_2[\text{Ru}(\text{}^t\text{Bubpy})(\text{CN})_4]$ was synthesized following the method in the literature.¹⁵² All organic solvents used were of analytical grade.

2.2.2 Syntheses

$\{[\text{Ru}(\text{}^t\text{Bubpy})(\text{CN})_4]_2-[\text{Fe}(\text{H}_2\text{O})_3\text{Cl}]_2\} \cdot 2\text{H}_2\text{O}$ (**RuFe 1**)

A solution of $\text{K}_2[\text{Ru}(\text{}^t\text{Bubpy})(\text{CN})_4]$ (0.276 g, 0.5 mmol) was mixed with an equivalent of FeCl_3 (0.081 g, 0.5 mmol) in deionized water to give a total volume of 50 mL. The mixture was stirred at room temperature for 60 min. Blue colored precipitates were isolated by filtration and were subsequently washed by deionized water, acetone, and diethyl ether. The solids were allowed to air-dry overnight. Yield: 0.261 g (76%); IR (KBr): $\nu_{\text{C}\equiv\text{N}} = 2030, 2076, \text{ and } 2114 \text{ cm}^{-1}$; ESI-MS (+ve mode): m/z 620.0 $\{2\text{H}^+ \cdot [\text{Ru}(\text{}^t\text{Bubpy})(\text{CN})_4]_2-[\text{Fe}(\text{H}_2\text{O})_3\text{Cl}]_2\}$ (mass = 1240.1 g mol^{-1} ; charge = +2); Anal. Calc. for $\text{C}_{44}\text{Cl}_2\text{Fe}_2\text{H}_{60}\text{N}_{12}\text{O}_6\text{Ru}_2 \cdot 8\text{H}_2\text{O}$ (**1**): C, 38.24; H, 5.54; N, 12.16; Found: C, 37.98; H, 5.55; N, 12.00.

2.2.3 Physical Measurements and Instrumentation

Infrared spectra in the 500–4000 cm^{-1} range were recorded using a Perkin Elmer Model Frontier FTIR spectrometer using KBr plates. Electrospray mass spectra (ESI-MS) were measured with an AB SCIEX API 2000 LC/MS/MS system. The emission spectra were recorded using a Horiba

FluoroMax-4 spectrofluorometer with a 5 nm slit width and a 0.5 s integration time. Luminescence quantum yields were measured by the optical dilution method¹⁵³ using an aerated aqueous solution of [Ru(bpy)₃]Cl₂ ($\varphi = 0.028$, excitation wavelength at 455 nm)¹⁵⁴ as the standard solution. UV-vis spectra were measured by a Cary 50 ultraviolet visible spectrophotometer. Dissolved organic carbon was measured using a Shimadzu TOC-L CSH High-Sensitivity Total Organic Analyzer. Elemental analyses were performed on a Vario EL CHN analyzer.

2.2.4 Spectroscopic and Spectrofluorimetric Titration

2.2.4.1 General Parameters

Testing solutions were allowed to reach equilibrium prior to measurements. The receptor-substrate interactions were analyzed with the Benesi-Hildebrand equations¹⁵⁵ for the UV-vis spectroscopic titrations (Equations 2.1 and 2.2).

$$\frac{A_0}{A - A_0} = \left(\frac{\epsilon_0}{\epsilon_0 - \epsilon} \right) \left(\frac{1}{K_{\text{overall}} [\text{substrate}]} + 1 \right) \quad (2.1)$$

$$\frac{A_0}{A - A_0} = \left(\frac{\epsilon_0}{\epsilon_0 - \epsilon} \right)^2 \left(\frac{1}{K_{\text{overall}} [\text{substrate}]^2} + 1 \right) \quad (2.2)$$

Where A_0 and A represent the absorbance of the chromogenic reagent in the absence and the presence of the substrate respectively; ϵ_0 and ϵ are the corresponding molar absorption coefficients of the chromogenic reagent in the absence and the presence of the substrate; [substrate] is the concentration of the target analyte.

Receptor-substrate interactions were also analyzed by spectrofluorimetric titrations with the use of Equation 2.3 and 2.4.

$$\frac{I_0}{I - I_0} = \left(\frac{a}{b - a}\right) \left(\frac{1}{K_{\text{overall}} [\text{substrate}] + 1}\right) \quad (2.3)$$

$$\frac{I_0}{I - I_0} = \left(\frac{c}{d - c}\right)^2 \left(\frac{1}{K_{\text{overall}} [\text{substrate}]^2 + 1}\right) \quad (2.4)$$

I_0 and I are the luminescence intensity of the fluorogenic reagent in the absence and the presence of the substrate; a , b , c and d are constants.

2.2.4.2 Binding Constant Determination

Formation constants (K_{overall}) were estimated by the ratio between the y -intercept and the slope of the straight lines obtained by plotting $A_0/(A - A_0)$ or $I_0/(I - I_0)$ vs. $1/[\text{substrate}]$ or $1/[\text{substrate}]^2$ depending on either 1:1 or 1:2 host-guest interactions, respectively. The Gibbs free energy of formation ($\Delta G/\text{kJ mol}^{-1}$) for the donor-acceptor ensembles and the acceptor metal-analyte adducts were evaluated from the corresponding formation constants as stated below (equation 2.5):¹⁵⁵

$$\Delta G = -RT \ln(K_{\text{overall}}) \quad (2.5)$$

Where R is the gas constant and T is the experimental temperature.

2.2.4.3 Binding Constant for $[\text{Ru}^{\text{II}}(\text{tBubpy})(\text{CN})_4]_2-[\text{Fe}^{\text{III}}(\text{H}_2\text{O})_3\text{Cl}]_2$ Adducts

Titration of $\text{K}_2\text{Ru}(\text{tBubpy})(\text{CN})_4$ (4.76×10^{-4} M) with FeCl_3 (0 to 4.76×10^{-4} M) were carried out at a ratio of 2:1 ethanol/pH 1.5 aqueous buffer mixture. Spectral changes of the resultant mixtures were measured. The binding constant for the $[\text{Ru}^{\text{II}}(\text{tBubpy})(\text{CN})_4]_2-[\text{Fe}^{\text{III}}(\text{H}_2\text{O})_3\text{Cl}]_2$ adducts was calculated by fitting the titration curves to the 1:1 Benesi-Hildebrand equation (Equation 2.1).

2.2.4.4 Binding Ratio Determination for $[\text{Ru}^{\text{II}}(\text{tBubpy})(\text{CN})_4]_2-[\text{Fe}^{\text{III}}(\text{H}_2\text{O})_3\text{Cl}]_2$ Adducts by Job's Plot

All the measurements were carried out in deionized water. A series of indicator $\text{K}_2\text{Ru}(\text{tBubpy})(\text{CN})_4$ complex solutions were mixed with FeCl_3 catalyst solutions under the condition that the sum of the concentrations of the indicator and catalyst solutions was constant. Spectral changes (A/A_0) at 606 nm of the resulting mixtures were plotted as a function of the FeCl_3 mole fraction.

2.2.4.5 Binding Constants for $[\text{FeCl}_3]$ -[substrate] Adducts

All titrations were carried out in a pH 1.5 aqueous buffer. Different concentrations of oxalate solutions (0 to 1.67×10^{-3} M) were titrated with a fixed concentration of FeCl_3 solution (1.67×10^{-4} M). Different substrates including glyoxylic acid, L-tartrate, pyruvate, acetate, NCS^- , H_2PO_4^- , Br^- , Cl^- , NO_3^- , N_3^- and SO_4^{2-} (0 to 6.67×10^{-3} M) were also titrated with FeCl_3 (3.33×10^{-4} M). The changes in the absorbance or emission of the resultant mixtures were measured. Binding constants for the $[\text{FeCl}_3]$ -[substrate] adducts were analyzed by fitting the titration curves to the Benesi-Hildebrand equations.

2.2.5 Method Detection Limits of **RuFe 1** toward Oxalate

A series of oxalate solutions (0 to 9.52×10^{-3} M) were mixed with **RuFe 1** solutions (2.17×10^{-4} M). The detection limit studies were carried out in a 2:1 ratio of ethanol/pH 1.5 aqueous buffer mixture at room temperature. Spectroscopic and spectrofluorimetric changes for the resultant mixtures were recorded. The method detection limits were calculated using the corresponding critical concentrations via the Hubaux and Vos methods, as outlined in Equation 2.6.¹⁵⁶

$$X_c = \frac{t_{(0.05, n-2)} \times S_{y/x}}{b} \times \sqrt{\frac{1}{K} + \frac{1}{I \times J} + \frac{\bar{x}^2}{J \times \sum_{i=1}^I (x_i - \bar{x})^2}} \quad (2.6)$$

Where X_c is the critical concentration, $S_{y/x}$ is the standard error of regression, b is the slope of the calibration curve, K is the number of preparations for each unknown sample, I is the number of calibration points, and J is the number of preparations for each calibration point.

2.2.6 Photocatalytic Degradation of Organic Substrates by **RuFe 1**

All experiments were conducted in a 125 mL conical flask with a 200 W Hg(Xe) ultraviolet–visible lamp (Newport) as the irradiation source. The whole setup was shielded to block out surrounding light. The distance between the lamp and the test solution was 10 cm. Mixtures of the **RuFe 1** complex (1.79×10^{-4} M) with organic substrates such as oxalate, glyoxylic acid, pyruvate, L-tartrate, and acetate (1.79×10^{-3} M) were prepared to 100 mL with the pH value adjusted to 1.5. Dissolved organic carbon (DOC) of the mixture was obtained at regular intervals and analyzed to evaluate catalytic efficiency.

2.2.7 Catalytic Signal Amplification of **RuFe 1** toward Oxalate

A series of oxalate solutions [0 to 2.17×10^{-3} M (0 to 400 ppm)] were mixed with **RuFe 1** (2.17×10^{-4} M) and a methyl orange (2.17×10^{-5} M) mixture. The studies were carried out in a pH 1.5 aqueous buffer at room temperature. Each solution was irradiated for 180 min using the 200 W Hg(Xe) ultraviolet–visible lamp (Newport). The whole setup was shielded from surrounding light. The distance between the lamp and the test solution was 30 cm. The UV-vis absorption spectra and their intensities at 510 nm were recorded at fixed time intervals.

2.2.8 *In Vivo* Toxicity Assay for **RuFe 1**

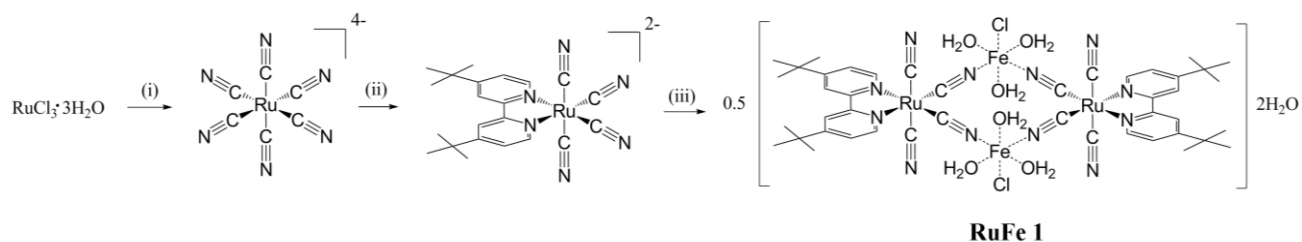
Medaka embryos were obtained from Dr. Doris W. T. Au (City University of Hong Kong). Hatched larvae were maintained in an embryo rearing medium (pH 7.2),¹⁵⁷ and fed with finely ground Otohime BETA1 (Nisshin Co., Japan). Larvae (~4–5 mm in length) were fasted for 5 h and then exposed to **RuFe 1** on the fifth day-post-hatch (dph) using multi-well cell culture plates. Each of the cell culture wells held seven medaka larvae, which were incubated in 7 mL of embryo rearing medium at room temperature with a suspension of a known **RuFe 1** concentration (i.e., 0 (as a control), 1, 10 and 100 mg/mL) and were continuously fed every other day for up to 7 days. Due

to the low complex **RuFe 1** specific gravity relative to water, the complex solid floated in the embryo-rearing medium rather than sunk to the bottom of the wells. Vitality of larvae was checked every 24 h. Data was processed with SPSS 21.0 software.

2.3 Results and Discussion

2.3.1 Synthesis of Tetranuclear Bimetallic Complex **RuFe 1**

$K_2[Ru^{II}(\text{'Bubpy})(CN)_4]$ is a well-known strong luminescent complex and metallic coordinating donor; it can be synthesized according to the method in the literature.¹⁵⁸ The complex was well characterized by infrared spectrometry, elementary analysis, electrospray mass spectrometry, and 1H -NMR. All of them gave satisfactory results compared with the literature.^{152,159}



Scheme 2.4 Synthetic scheme for **RuFe 1**. Reaction condition: (i) reflux with excess amount of KCN in water, (ii) reflux with 1 eq of 'Bubpy in aqueous methanol (pH 2), (iii) stirring 1 eq of $FeCl_3$ in deionized water in room temperature.

Bimetallic complex **RuFe 1** was formed by simply stirring equal equivalents of $K_2[Ru^{II}(\text{'Bubpy})(CN)_4]$ complex and $FeCl_3$ in deionized water in open atmosphere and at room temperature (Scheme 2.4). It was isolated as an air-stable blue colored solid with satisfactory yield. The complex was slightly soluble in polar organic solvents such as DMSO, DMF, methanol, and ethanol but insoluble in acetone and water. Integrity of the tetranuclei state of **RuFe 1** in ethanol was demonstrated by electrospray-MS showing peaks at m/z 620.0 m/z representing $\{2H^+ \cdot [Ru(\text{'Bubpy})(CN)_4]_2 - [Fe(H_2O)_3Cl]_2\}$ (mass = 1240.1 $gmol^{-1}$; charge = +2). Figure 2.2 depicts the electrospray mass spectra for **RuFe 1** in a methanol/DMSO mixture with 0.1% hydrochloric acid.

According to the elementary analysis, eight water molecules were found in **RuFe 1**. It is commonly found that in cyano-bridged bimetallic complexes, water molecules trends to coordinate with

cyano-bridged bimetallic complexes, and the porous crystalline structure also tends to trap water molecules in the unit cell during synthesis.¹⁶⁰⁻¹⁶² Therefore the composition of the **RuFe 1** was tentatively assigned as $\{[\text{Ru}(\text{tBubpy})(\text{CN})_4]_2-[\text{Fe}(\text{H}_2\text{O})_3\text{Cl}]_2\} \cdot 2\text{H}_2\text{O}$, with six coordinated to unsaturated Fe (III) and two non-coordinated water molecules.

The binding ratio of $\text{K}_2[\text{Ru}^{\text{II}}(\text{tBubpy})(\text{CN})_4]$ and FeCl_3 in complex **RuFe 1** was also confirmed by Job's plot titration. By plotting the UV absorbance of solution $\text{K}_2[\text{Ru}^{\text{II}}(\text{tBubpy})(\text{CN})_4]$ against the mole fraction of FeCl_3 shown in Figure 2.3, the maximum of the plot at 0.5 implicated that the two species is in equal stoichiometry.

Formation of the cyano-bridged bimetallic complex was also confirmed by IR spectroscopic studies where the $\nu_{\text{C}=\text{N}}$ of $\text{K}_2[\text{Ru}(\text{tBubpy})(\text{CN})_4]$ at 2042, 2058, and 2093 cm^{-1} was shifted to 2030, 2076, and 2114 cm^{-1} after binding with Fe(III). The band red shifted was assigned as terminal cyano,¹⁶³ whereas bands blue shifted were assigned to be bridging cyano. This blue shift was attributed to the kinematic coupling placing a mechanical constraint upon the bridging cyano by the second metal, the second metal withdraw charge from the nitrogen resulting in the strengthening of back-bonding.¹⁶⁴⁻¹⁶⁶

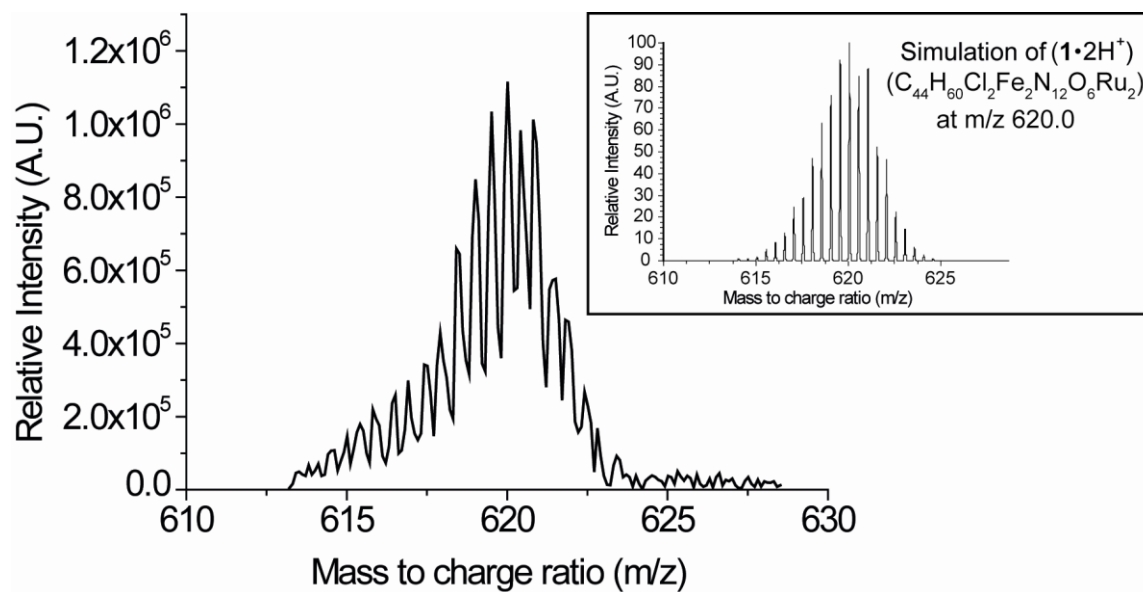


Figure 2.2 Electropray mass spectrum of the isotopic distribution for **RuFe 1**: and (*inset*) its simulation for $\{[\text{Ru}(\text{}^t\text{Bubpy})(\text{CN})_4]_2-[\text{Fe}(\text{H}_2\text{O})_3\text{Cl}]_2\cdot 2\text{H}\}^{2+}$ peak at 620.0. Mass spectrometry was performed in a methanol/DMSO mixture with 0.1% of HCl.

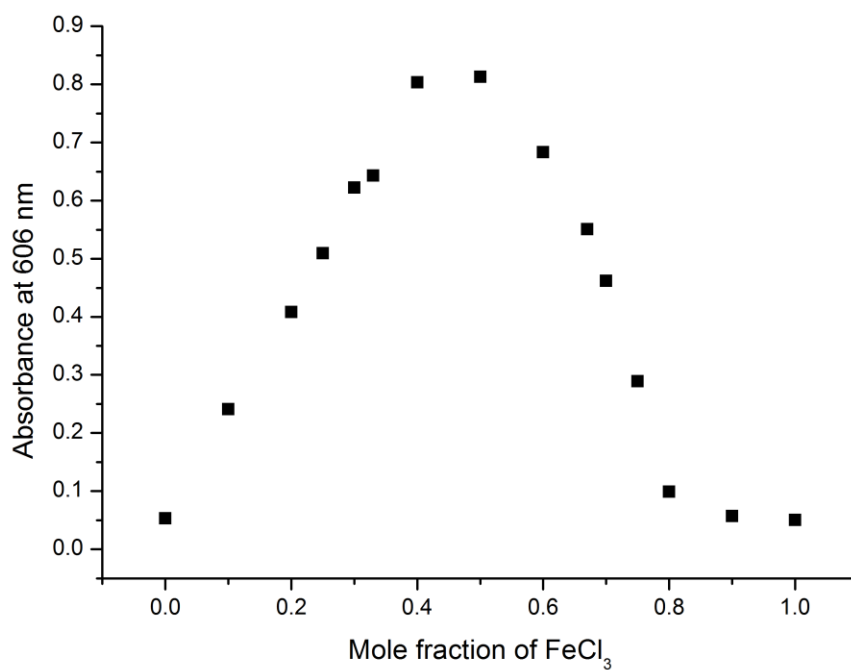


Figure 2.3 Job's plot of $\text{K}_2[\text{Ru}(\text{Bubpy})(\text{CN})_4]$ by FeCl_3 showing that the maximum response of the complex **RuFe 1** occurs at a mole ratio of 2:2. The experiment was performed in deionized water at 298 K.

2.3.2 Electronic Absorption and Luminescent Properties of **RuFe 1**

The absorption spectra for **RuFe 1** and its precursors are shown in Figure 2.4. The **RuFe 1** complex shows an increase in the absorption coefficient compared with its precursors $\text{K}_2[\text{Ru}(\text{tBubpy})(\text{CN})_4]$ and FeCl_3 . The increase from 200 to 465 nm is due to the superposition of the absorption of two precursors. The broad absorption band which is dominant in the visible range at ~500–750 nm is assigned as mixed valent species,¹⁶⁷ the formation of a metal-metal charge transfer (MMCT) band,¹⁶⁸ resulted, form a class II mixed valent species and the suggested direction as $\text{Ru}(\text{II}) \rightarrow \text{Fe}(\text{III})$.⁴⁷

Figure 2.5 shows the triplet state metal-to-ligand charge transfer (³MLCT) emission spectra for $\text{K}_2[\text{Ru}(\text{tBubpy})(\text{CN})_4]$ and **RuFe 1** at 298 K in aqueous ethanol at pH 1.5. The $\text{K}_2[\text{Ru}(\text{tBubpy})(\text{CN})_4]$ complex has a low-energy emission band at ~550–750 nm. With reference to previous works this low-energy emission band is assigned to the $[\pi^*(\text{diimine}) \rightarrow d\pi(\text{Ru})]$ ³MLCT emission.¹⁶⁹ Upon coordination of the FeCl_3 acceptor, the emission intensity decreased as the paramagnetic $\text{Fe}(\text{III})$ quenched the $\text{Ru}(\text{II})$ -diimine chromophore.^{47,170}

Figure 2.6 shows the spectra change upon the UV-vis spectroscopic and spectrofluorimetric titrations of $\text{K}_2\text{Ru}(\text{tBubpy})(\text{CN})_4$ with FeCl_3 . The formation constant for the $[\text{Ru}^{\text{II}}(\text{tBubpy})(\text{CN})_4]_2-[\text{Fe}^{\text{III}}(\text{H}_2\text{O})_3\text{Cl}]_2$ adducts was determined by fitting the titration curves with the 1:1 Benesi-Hildebrand equation giving the linear relationship. The binding constant ($\log K_{\text{overall}}$) between $\text{K}_2[\text{Ru}(\text{tBubpy})(\text{CN})_4]$ and FeCl_3 was found to be $3.15 \pm 0.005 \text{ M}^{-1}$.

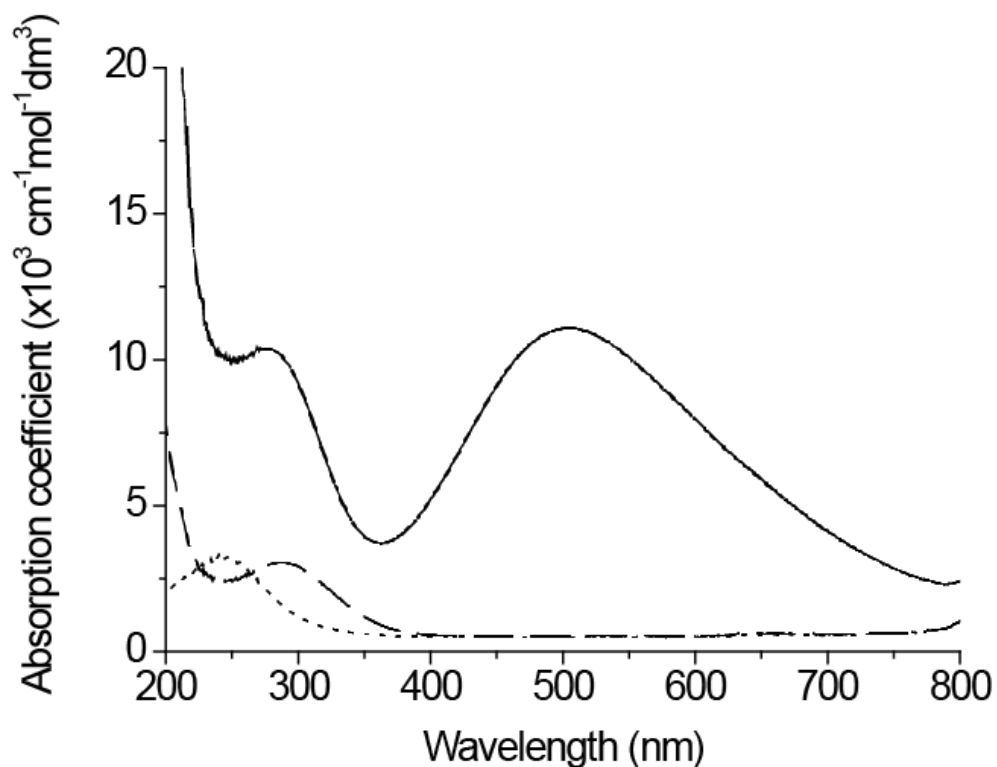


Figure 2.4 (a) Absorption spectra for **RuFe 1** (—), $\text{K}_2\text{Ru}(\text{tBubpy})(\text{CN})_4$ (---) and FeCl_3 (···) in aqueous ethanol (1:2 v/v) (1.00 mL of aqueous KCl/HCl buffer at pH 1.5 + 2.00 mL of ethanol) at 298 K.

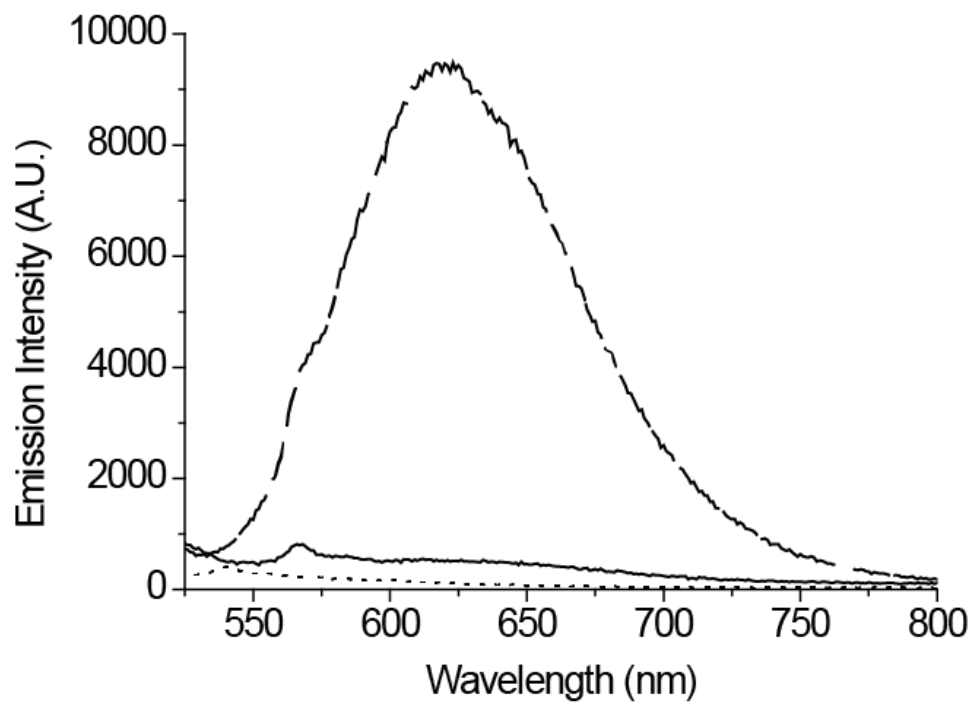


Figure 2.5 Luminescent spectra for **RuFe 1** (—), $\text{K}_2\text{Ru}(\text{}^4\text{Bubpy})(\text{CN})_4$ (---) and FeCl_3 (···) in aqueous ethanol (1:2 v/v) (1.00 mL of aqueous KCl/HCl buffer at pH 1.5 + 2.00 mL of ethanol) at 298 K. Luminescent spectra were obtained with 467 nm excitation.

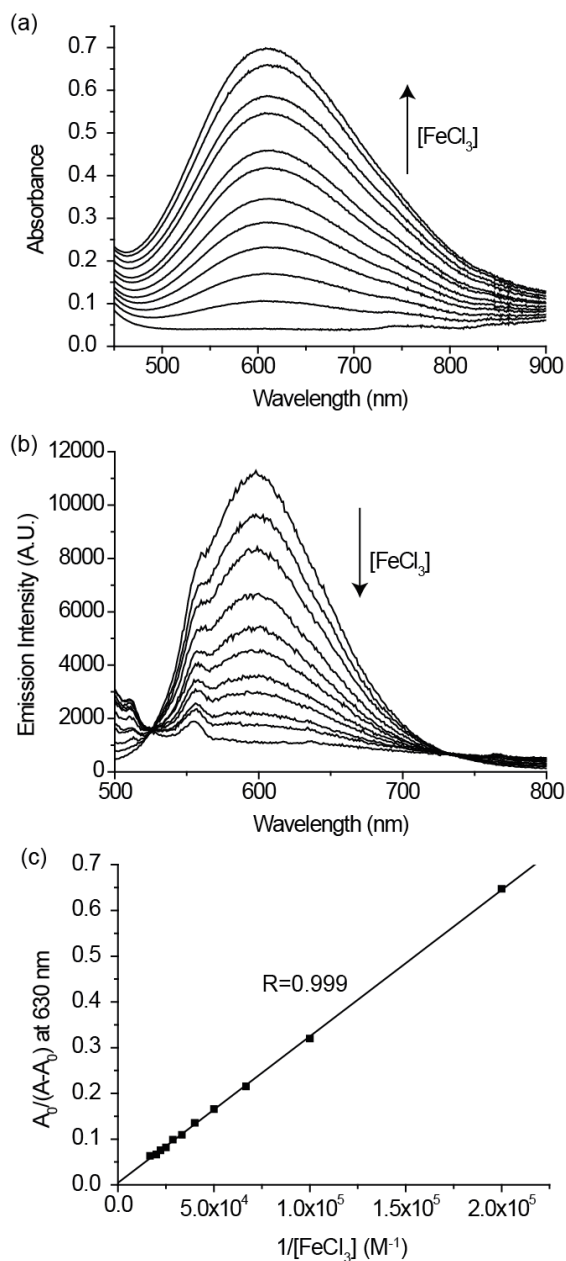


Figure 2.6 (a) UV-vis spectroscopic, (b) spectrofluorimetric titrations for $\text{K}_2\text{Ru}(\text{tBubpy})(\text{CN})_4$ (1.00×10^{-4} M) with FeCl_3 (0 to 1.00×10^{-4} M). (c) The slope and y-intercept are 3.20×10^{-6} and 4.56×10^{-3} respectively of the best fitted $A_0/(A-A_0)$ versus $1/[\text{FeCl}_3]$ plot with $\log K = 3.15 \pm 0.005$ M^{-1} at 630 nm. All titrations were carried out in aqueous KCl/HCl buffer at pH 1.5 at 298 K. Excitation $\lambda_{\text{ex}} = 468$ nm.

2.3.3 Detection of Oxalate Anions

2.3.3.1 Chemodosimetric Properties of **RuFe 1** toward Oxalate

With the addition of oxalate (HC_2O_4^-) to **RuFe 1** in an aqueous ethanol solution at pH 1.5, the intensity of its MMCT band declined and resulted in a blue to pale yellow colorimetric response. Meanwhile, the addition also perturbed the $^3\text{MLCT}$ transition in **RuFe 1** with a significant enhancement in intensity resulting in an intense orange colored emission. Figure 2.7 shows the colorimetric and luminescent responses of **RuFe 1** to oxalate. The spectrofluorimetric titration for **RuFe 1** with different anions (glyoxylic acid, pyruvic acid, potassium tartrate, potassium acetate, K_2SO_4 , KH_2PO_4 , KNO_3 , KCN , KSCN , KN_3 , and KBr) in aqueous ethanol solution at pH 1.5 is summarized in Figure 2.8. Among these anions, only oxalate is able to induce significant luminescent/colorimetric responses. These results reveal that **RuFe-1** has selectivity toward oxalate and other anions do not interfere with the signaling responses of **RuFe 1** toward the detection of oxalate. Moreover, the spectrofluorometric responses of **RuFe 1** toward a mixture of oxalate and other anions showed emission enhancements similar to those toward oxalate alone as shown in Figure 2.9. This indicates that the detection of oxalate by **RuFe 1** has no interference from other analytes.

Through the UV-vis spectroscopic and spectrofluorometric methods, the method detection limits (MDL) of **RuFe 1** toward oxalate were found as 78.7 and 5.5 ppm, respectively, via the Hubaux and Vos method. From Figure 2.10 and Figure 2.11, qualitative analysis of oxalate by naked eye was about 100 ppm and can be distinguished from other common anions.

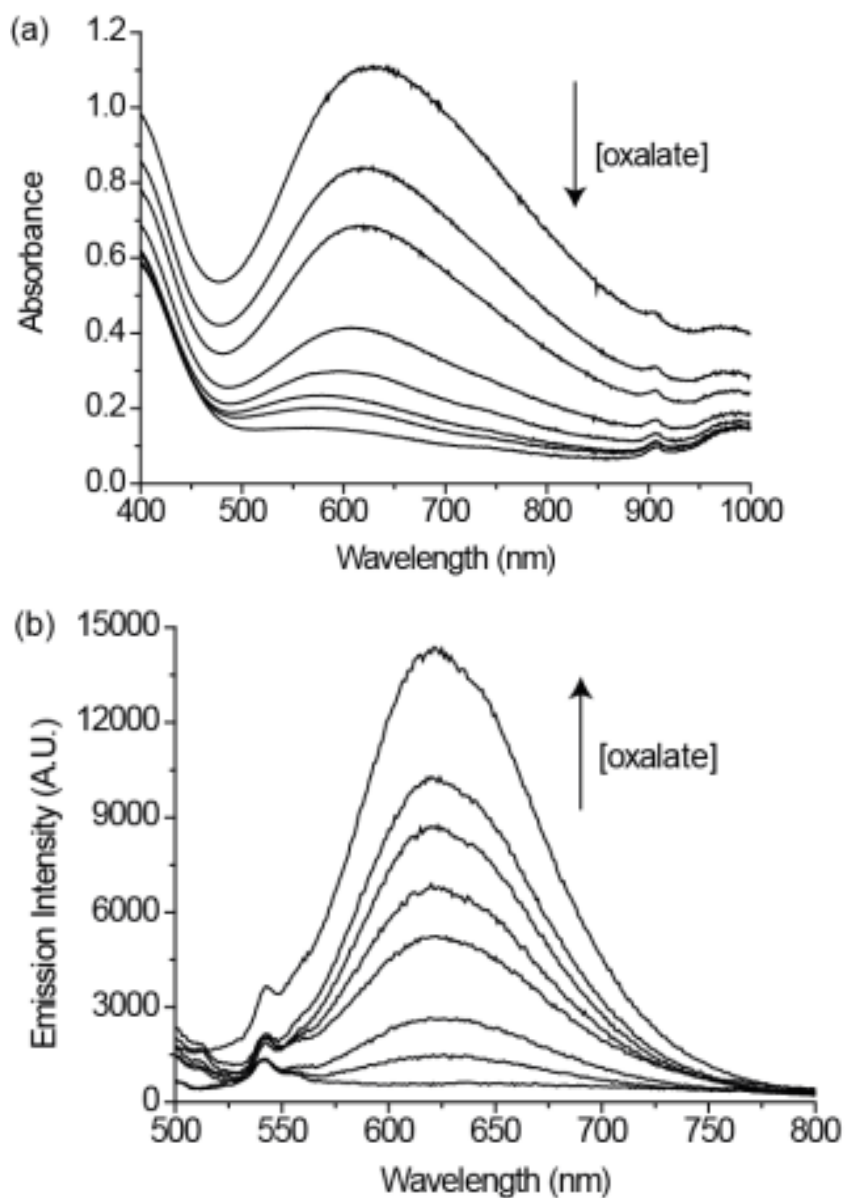


Figure 2.7 (a) UV-vis spectroscopic and (b) spectrofluorimetric titrations for **RuFe 1** (1.08×10^{-4} M) with oxalate (0 to 3.24×10^{-2} M). All titrations were carried out in aqueous ethanol (1:2 v/v) (1.00 mL of aqueous KCl/HCl buffer at pH 1.5 + 2.00 mL of ethanol) at 298 K. Excitation λ was 468 nm.

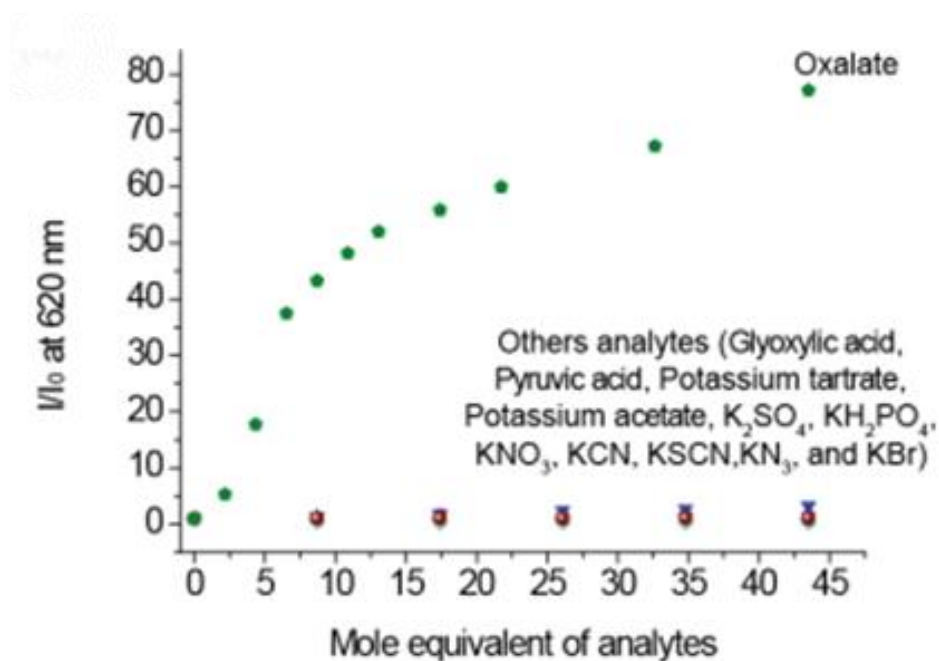


Figure 2.8 Summary of spectrofluorometric titration (I/I_0 at 620 nm) for **RuFe 1** (2.17×10^{-4} M) with various analytes monitored as a function of the increase in emission intensity. All titrations were carried out in aqueous ethanol (1:2 v/v) (1.00 mL of aqueous KCl/HCl buffer at pH 1.5 + 2.00 mL of ethanol) at 298 K. Excitation λ was 468 nm.

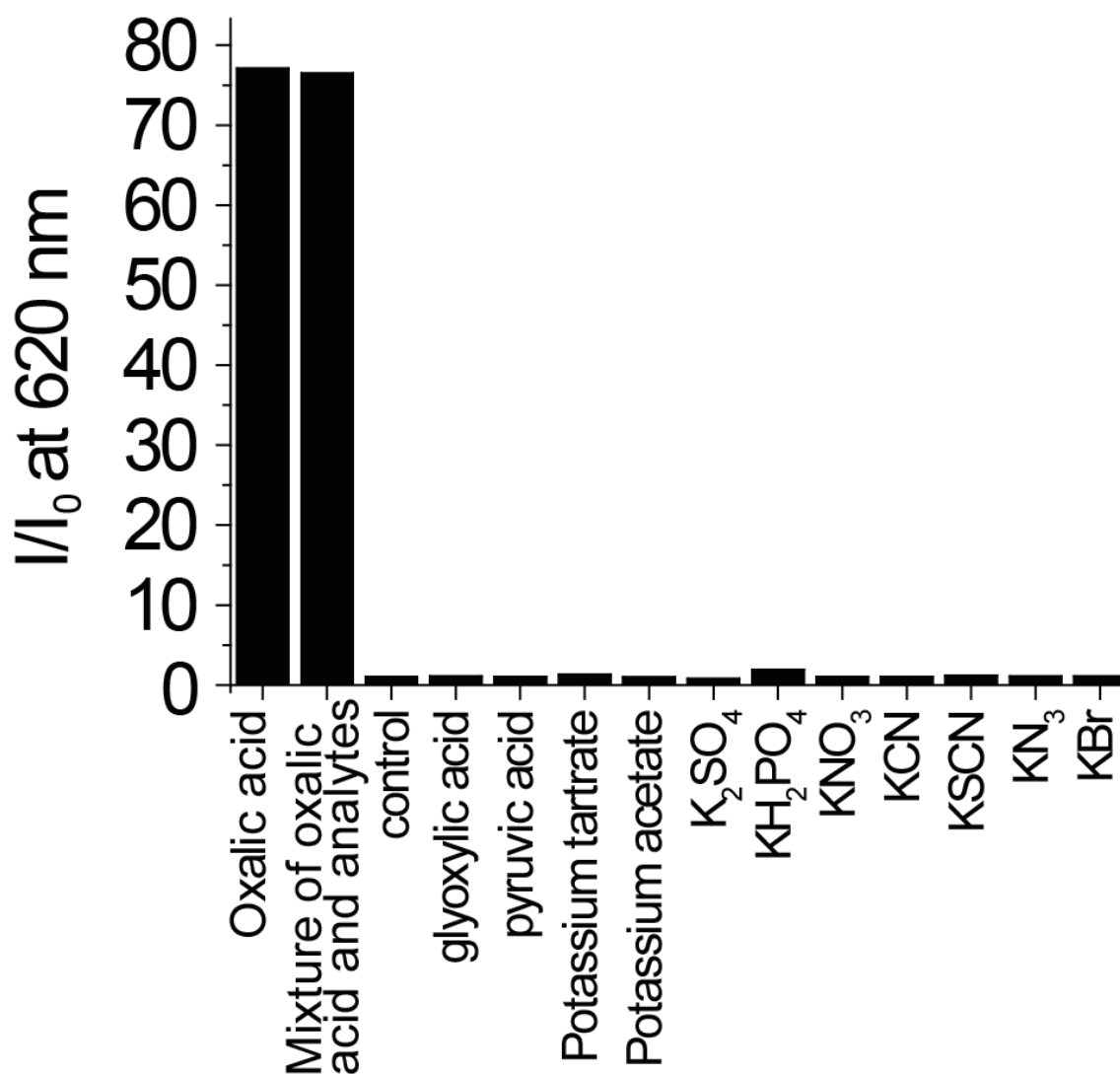


Figure 2.9 Bar chart showing the spectrofluorometric responses of **RuFe 1** (2.17×10^{-4} M) in the presence of oxalic acid and various analytes (concentration of each of the analyte 8.68×10^{-3} M: glyoxylic acid, pyruvic acid, potassium tartrate, potassium acetate, K_2SO_4 , KH_2PO_4 , KNO_3 , KCN, KSCN, KN_3 and KBr) at aqueous ethanol (1:2 v/v) (1.00 mL of aqueous KCl/HCl buffer at pH 1.5 + 2.00 mL of ethanol) at 298 K. Luminescent spectra were obtained with 467 nm excitation.



Figure 2.10 Photos of the colorimetric responses of complex **RuFe 1** (2.17×10^{-4} M) to 40 molar equivalent of different anions (8.68×10^{-3} M) : (1) **RuFe 1** + oxalate, (2) **RuFe 1** only; (3-13) **RuFe 1** + glyoxylic acid, pyruvic acid, potassium tartrate, potassium acetate, K_2SO_4 , KH_2PO_4 , KNO_3 , KCN , $KSCN$, KN_3 , and KBr . Recorded in aqueous ethanol (1:2 v/v) (1.00 mL of aqueous KCl/HCl buffer at pH 1.5 + 2.00 mL of ethanol) at 298 K.

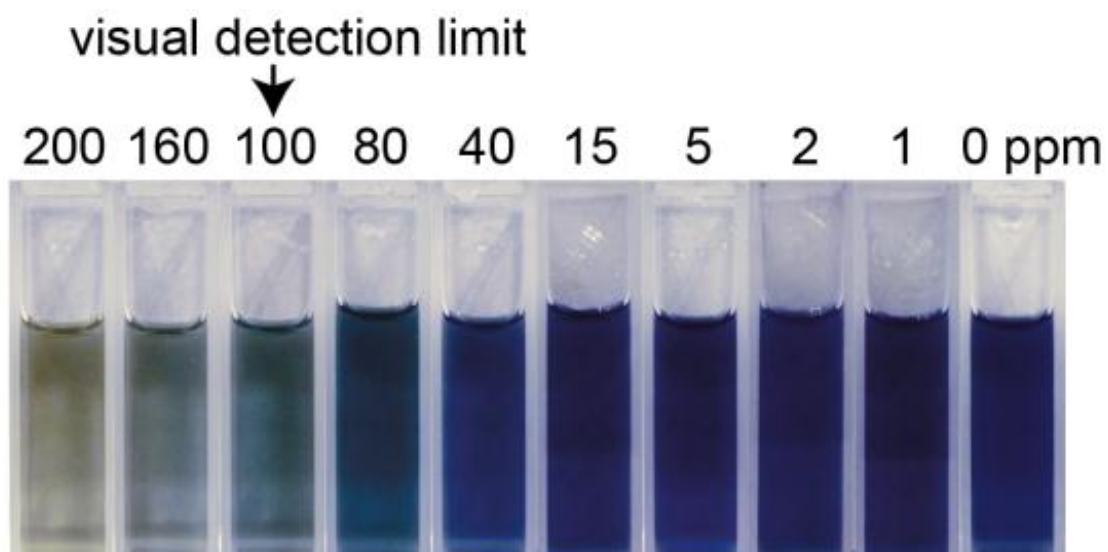


Figure 2.11 Photos of colorimetric response of **RuFe 1** to oxalate in aqueous ethanol (1:2 v/v) (1.00 mL of aqueous KCl/HCl buffer at pH 1.5 + 2.00 mL of ethanol) at 298 K.

2.3.3.2 Binding Constant and Binding Mechanism of **RuFe 1** with Oxalate

Figure 2.12 shows the fitting of UV-vis spectroscopic responses of **RuFe 1** to oxalate in 1:2 to the Benesi–Hildebrand equation.¹⁵⁶ The binding constant, $\log K_{\text{overall}}$, for **RuFe 1** and oxalate was found to be $3.43 \pm 0.03 \text{ M}^{-1}$, indicating that each Fe(III) center in the tetranuclear complex binds one molecule of oxalate.

Figure 2.13 shows the electrospray-MS for the mixture of **RuFe 1** and oxalate. The m/z 512.9 $[\text{M} + \text{K}]^-$ was attributed to $[\text{Ru}(\text{tBubpy})(\text{CN})_4]^{2-}$ suggesting that all the cyanide bridges between Ru(II) and Fe(III) in the tetranuclear complex are cleaved following oxalate molecule binding to the Fe(III) centers. The close resemblances in the UV-vis and luminescent responses for the “**RuFe 1**-oxalate-mixture” to those for $\text{K}_2\text{Ru}(\text{tBubpy})(\text{CN})_4$ also implicate the cleavage of cyanide bridges.

The substrate selectivity of the binding-induced dissociation is most probably attributable to the relative stability of the Ru(II)-Fe(III) complex compared with that of the Fe^{III} -analyte adducts. Table 2.1 summarizes the binding constants and Gibbs free energy change ($-\Delta G$) for the complexation of FeCl_3 to various anions. Only Fe^{III} -oxalate exhibits a ΔG° smaller than that of **RuFe 1**, indicating that the driving force for the cleavage of **RuFe 1** by oxalate is due to the formation of more stable Fe(III)-oxalate species.

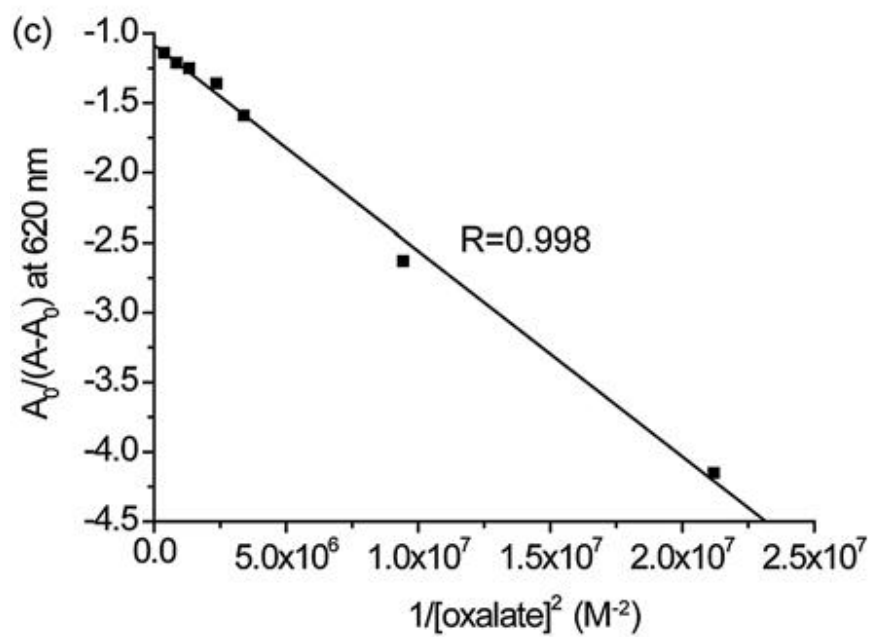


Figure 2.12 Fitting of UV-vis spectroscopic responses of **RuFe 1** to oxalate in 1:2 Benesi–Hildebrand equation.

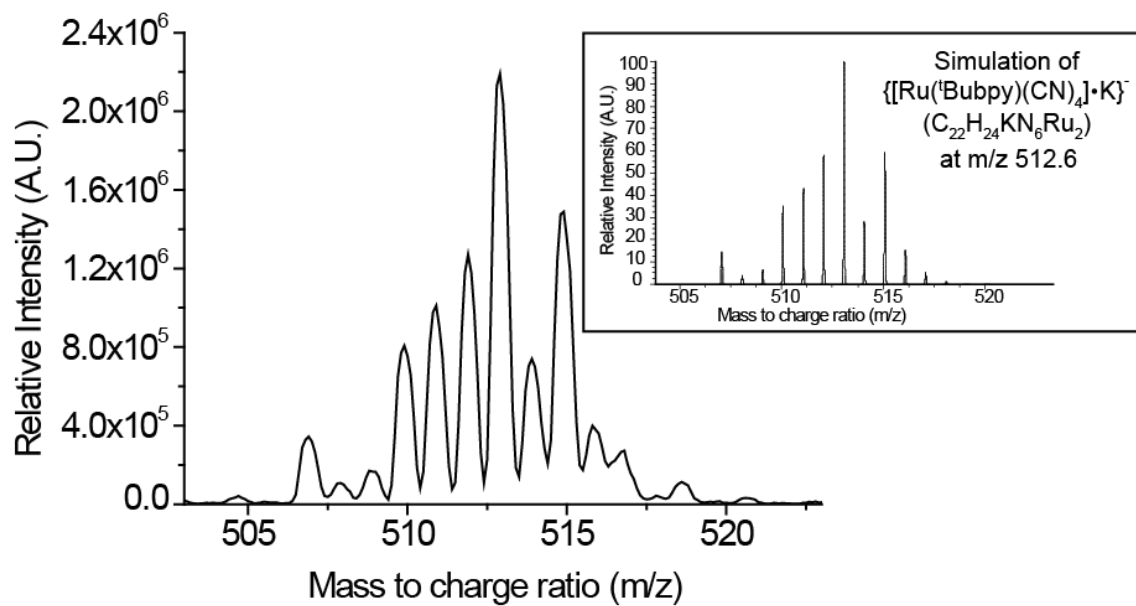


Figure 2.13 Electrospray mass spectrum of the isotopic distribution of “**RuFe 1-oxalate-mixture**”: and (*inset*) its simulation of $\{[\text{Ru}(\text{Bubpy})(\text{CN})_4]\text{K}\}^-$ peak at 512.6. The mass spectrum was performed in methanol/water mixture.

Table 2.1 Binding constants ($\log K_{\text{overall}}$) and Gibbs free energy changes (ΔG_0) for the complexation of various analytes and $\text{K}_2\text{Ru}(\text{}^t\text{Bubpy})(\text{CN})_4$ by FeCl_3 .

	Acceptor	Donor	$\log K_{\text{overall}}^t$	ΔG° /kJmol ⁻¹
1	FeCl_3	Oxalate	3.52	-20.1
2	FeCl_3	$\text{K}_2\text{Ru}(\text{}^t\text{Bubpy})(\text{CN})_4$	3.15	-18.0
3	FeCl_3	Pyruvic acid	2.55 ^b	-14.5
4	FeCl_3	KH_2PO_4	2.33	-13.3
5	FeCl_3	KCN	1.91	-10.9
6	FeCl_3	KN_3	1.47 ^c	-8.16
7	FeCl_3	Potassium tartrate	1.36	-7.7
8	FeCl_3	Potassium acetate	0.96	-5.5
9	FeCl_3	KSCN	0.75	-4.3
10	FeCl_3	Glyoxylic acid	0.54	-3.1
11	FeCl_3	K_2SO_4	0.24	-1.4
12	FeCl_3	KNO_3	--- ^d	--- ^d
13	FeCl_3	KBr	--- ^d	--- ^d

^aBinding strengths were measured by UV spectroscopic titration and calculated with Benesi-Hildebrand 1:1 equation. ^bBinding strengths were measured by spectrofluorimetric titration and calculated with Benesi-Hildebrand 1:2 equations. ^cBinding strengths were measured by UV spectroscopic titration and calculated with Benesi-Hildebrand 1:2 equations. ^{a-c}All the titrations were conducted in aqueous KCl/HCl buffer at pH 1.5 at 298 K. ^dToo small to be determined.

2.4 Photocatalytic degradation of Oxalate by **RuFe 1**

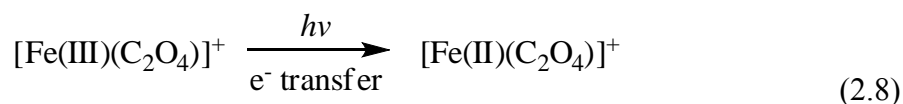
The photocatalytic properties of **RuFe 1** in oxalate degradation were studied by treating the same concentration of oxalate solution (4.16×10^{-4} M) in various working conditions. The results are summarized in Figure 2.14. The concentration of oxalate was determined by monitoring the change of DOC content, where influence of dissolved carbon dioxide was eliminated by baseline correction, and assumption was made that the dissolved carbon dioxide in reaction mixture was equal to the control setup. The change of DOC can be contributed by degradation of **RuFe 1** complex or intermediates (e.g. formic acid) of the reaction, therefore may not be a good method to study the reaction rate. Instead of reaction rate, time or ability to reach 95% mineralization (DOC_{95}) was measured in different reaction conditions to study the reaction mechanism.

The DOC content of **RuFe 1** in oxalate solution decreased rapidly in the first 250 min and achieved DOC_{95} at approximately 360 min [Figure 2.14 curve (●)] under UV-vis irradiation at room temperature. Similar experiments were conducted in the presence of FeCl_3 and $\text{K}_2\text{Ru}(\text{tBubpy})(\text{CN})_4$, with only mixtures containing FeCl_3 showing a DOC decrease with a similar pattern as that of **RuFe 1** [Figure 2.14 curve (■)], while the DOC content of the $[\text{K}_2\text{Ru}(\text{tBubpy})(\text{CN})_4]$ -oxalate mixture did not have significant changes following 7 h of treatment [Figure 2.14 curve (◆)]. These results indicate that the remediation of oxalate by **RuFe 1** is due to the release of Fe(III) complexes, and the decrease of DOC content indicates that oxalate was degraded into CO_2 in this process.

The degradation mechanism was further investigated by treating a series of oxalate solutions in the presence of **RuFe 1** under the following conditions: (i) dark, (ii) dark with heat (50°C), and (iii) nitrogen atmosphere; all three conditions showed no significant DOC change [Figure 2.14 curves (×), (◀), and (★) respectively]. Hence, the degradation of oxalate is most probably due to the generation of a superoxide ion radical, O_2^- , and/or the hydroxyl radical via the photo-assisted Fenton mechanism with the help of UV-vis irradiation.¹⁷¹⁻¹⁷³

The photodegradation of Fe(III)-oxalate complexes has been widely studied, the existing mechanism involve the electron transfer from the oxalate ligand to the ferric ion with assist of radiation, following by the formation of ferrous ion and oxalate radical (Equation 2.7 to 2.9).

The oxalate radical further react with atmospheric O₂ to produce O₂⁻ and finally produce H₂O₂ and regenerate the ferric ion (Equation 2.10 to 2.13).^{94,174} The mechanism is in agreement with the deactivation of Fe(III) catalyst when there is absent of radiation and atmospheric oxygen. The probable reaction pathways are shown below:



To investigate the selectivity of **RuFe 1** in oxalate photo-degradation, organic carboxylic acids/carboxylates were used as organic interferences. Figure 2.15 summarizes the changes in the DOC content of oxalate, glyoxylic acid, pyruvic acid, potassium tartrate, and potassium acetate against time in the presence of **RuFe 1** under UV-vis irradiation exposure at room temperature and under open atmosphere. Among all the organic carboxylic acids, only the mixture of oxalate with **RuFe 1** shows a significant decrease in its DOC content, whereas the other substances were nearly unchanged. These selective degradation properties are similar to the chemosensing properties of **RuFe 1** toward oxalate as stated before. The introduction of oxalate to the **RuFe 1** system caused the breakage of cyano-linkages and the release of the Fe(III) catalyst. Meanwhile, the cyano-bridged Fe(III) catalyst remained inactive when other analytes were introduced and could not initiate the photo-degradation reaction.

The reproducibility of **RuFe 1** to degrade oxalate degradation by **RuFe 1** was investigated as shown in Figure 2.16. The experiments were performed six times with oxalate continuously added to the [**RuFe 1**-oxalate] mixture after reacted for 240 min. Afterwards, the efficiency still reached 85.0%, indicating that the catalyst exhibited repeatable efficiency.

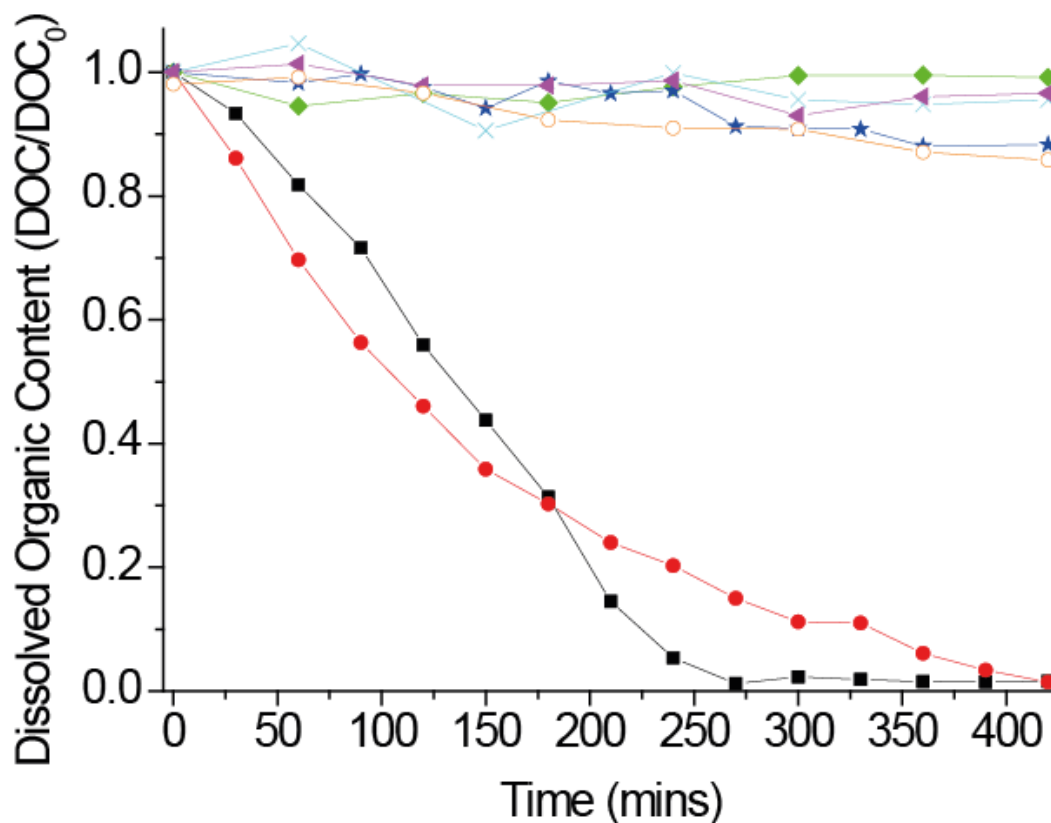


Figure 2.14 DOC during the degradation of oxalate under various conditions. (●) In the presence of **RuFe 1** (1.90×10^{-4} M), (■) FeCl_3 (1.90×10^{-4} M) and (◆) $\text{K}_2\text{Ru}(\text{Bubpy})(\text{CN})_4$ (1.90×10^{-4} M) under UV irradiation at room temperature. In the presence of **RuFe 1** (1.90×10^{-4} M) under (×) dark condition at room temperature, (◀) dark condition at 50 °C, and (★) under UV irradiation at room temp with saturation of N_2 (○). Control experiment was conducted at pH 1.5 with oxalate (4.16×10^{-4} M) under UV at room temperature and open atmosphere.

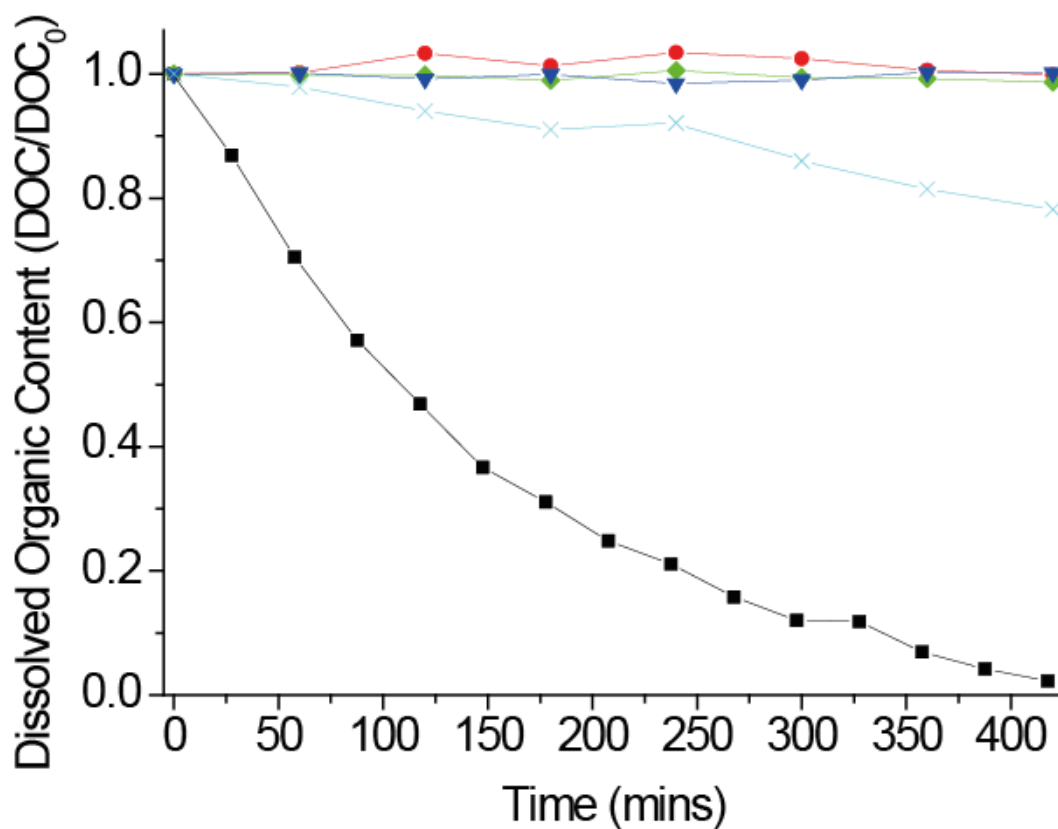


Figure 2.15 Selective degradation properties of **RuFe 1** (1.90×10^{-4} M) toward different organic carboxylate (4.16×10^{-4} M), (■) potassium oxalate, (●) potassium acetate, (▼) potassium tartrate, (◆) pyruvic acid, and (×) glyoxylic acid. All experiments were performed at pH 1.5 under UV at room temperature.

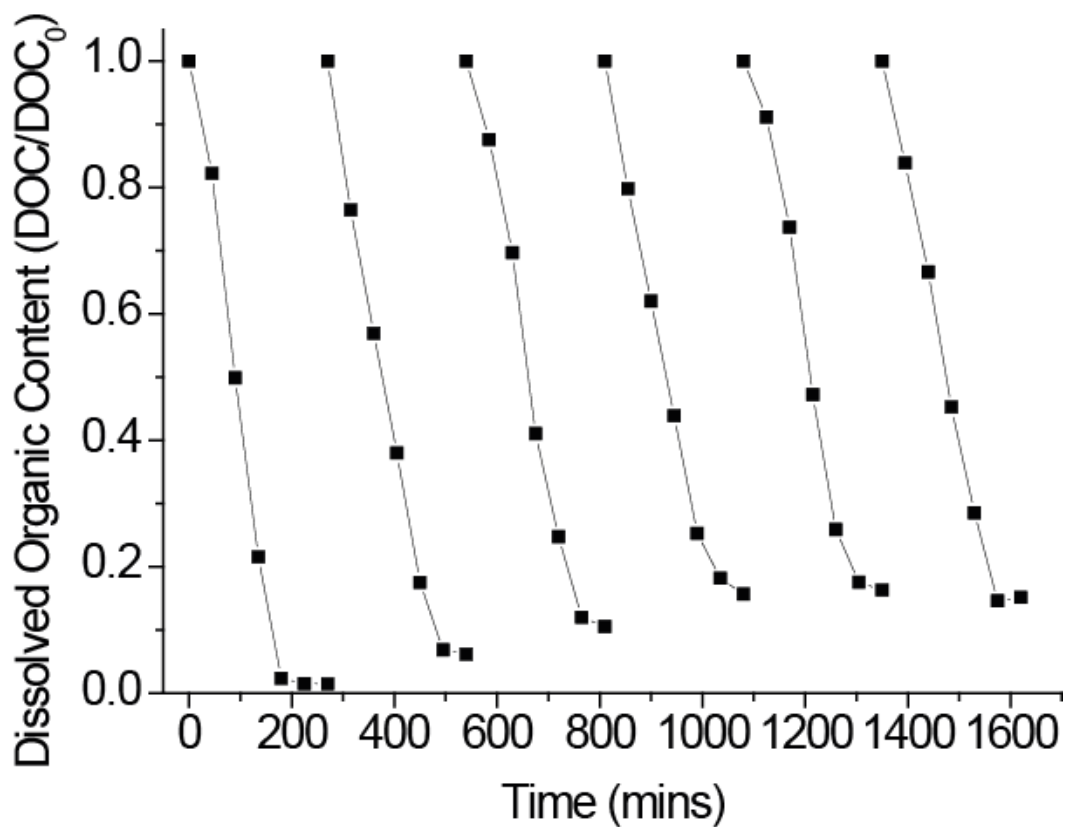


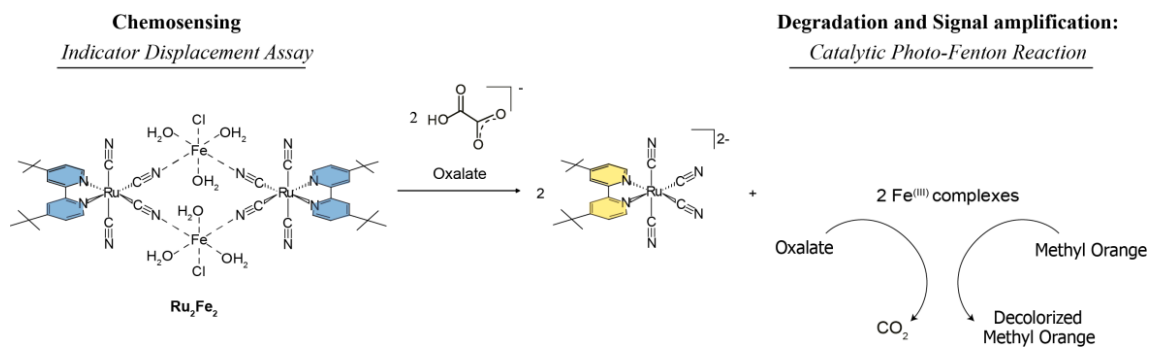
Figure 2.16 Repeatability of **RuFe 1** (1.90×10^{-4} M) toward potassium oxalate (4.16×10^{-4} M). All experiments were performed at pH 1.5 under UV at room temperature.

2.4.1 Catalytic Signal Amplification of **RuFe 1** towards Oxalate

To amplify the detection signal of **RuFe 1** towards oxalate, methyl orange was introduced to the system as the coloring agent. Methyl orange is an organic chromophore that is decolorized and destroyed in the photoassisted Fenton reaction through a reaction with hydroxyl radicals.^{175,176} Scheme 2.5 shows the mechanism for **RuFe 1** as ICDA toward oxalate in detection, degradation, and signal amplification, where Fe(III)-oxalate complex formed was known to be catalyst of the photodegradation of methyl orange.

Figure 2.17 shows the UV-vis spectroscopic changes of the [**RuFe 1**-oxalate-methyl orange] solution with UV-vis irradiation as a function of time. The results show that the color of methyl orange (λ_{abs} at 510 nm) fades with time, resulting in a more contrasting color change compared with that in the absence of methyl orange. The complete decolorization (95% of λ_{abs} at 510 nm) of the [**RuFe 1**-oxalate-methyl orange] solution can be achieved in 180 min with an initial oxalate concentration of 15 ppm. The decolorization rate became faster when the initial oxalate concentration increased as shown in Figure 2.17. Complete decolorization was achieved in 100 min when the initial oxalate concentration was increased to 80 ppm. The increase of rate is in trend with the increase of **RuFe 1**:oxalate mole ratio, where more Fe(III)-oxalate complex formed which catalyze the decolorization of methyl orange.

With this amplification, the visual detection limit of oxalate by **RuFe 1** improved to 2 ppm for an irradiation period of 180 min as shown in Figure 2.18. Compared to the colorimetric responses before the amplification, the sensitivity of **RuFe 1** towards oxalate was amplified ~50 times.



Scheme 2.5 Proposed ICDA of **RuFe 1** toward oxalate. The mechanism is composed of chemosensing, degradation, and signal amplification with the addition of methyl orange.

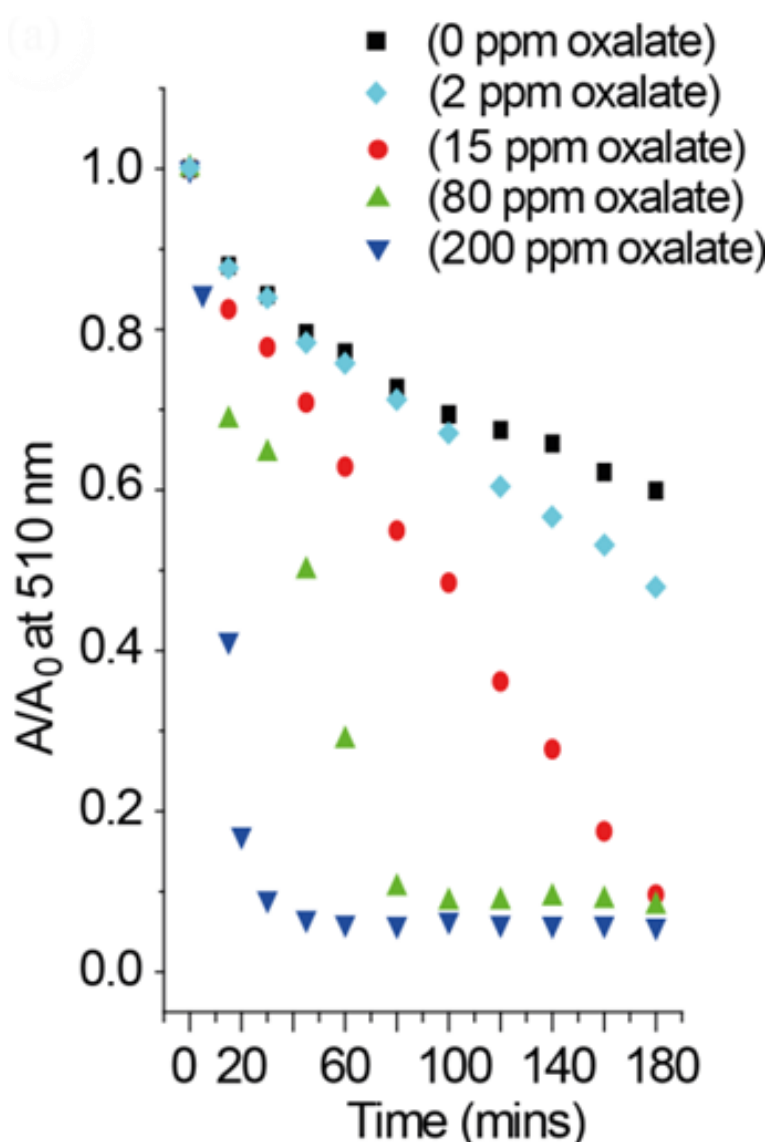


Figure 2.17 Spectroscopic changes with time of **RuFe 1** solution added with methyl orange (1:1 mol/mol) in the presence of oxalate (0 ppm to 200 ppm). All titrations were conducted in aqueous buffer (pH 1.5) under UV-vis at room temperature.

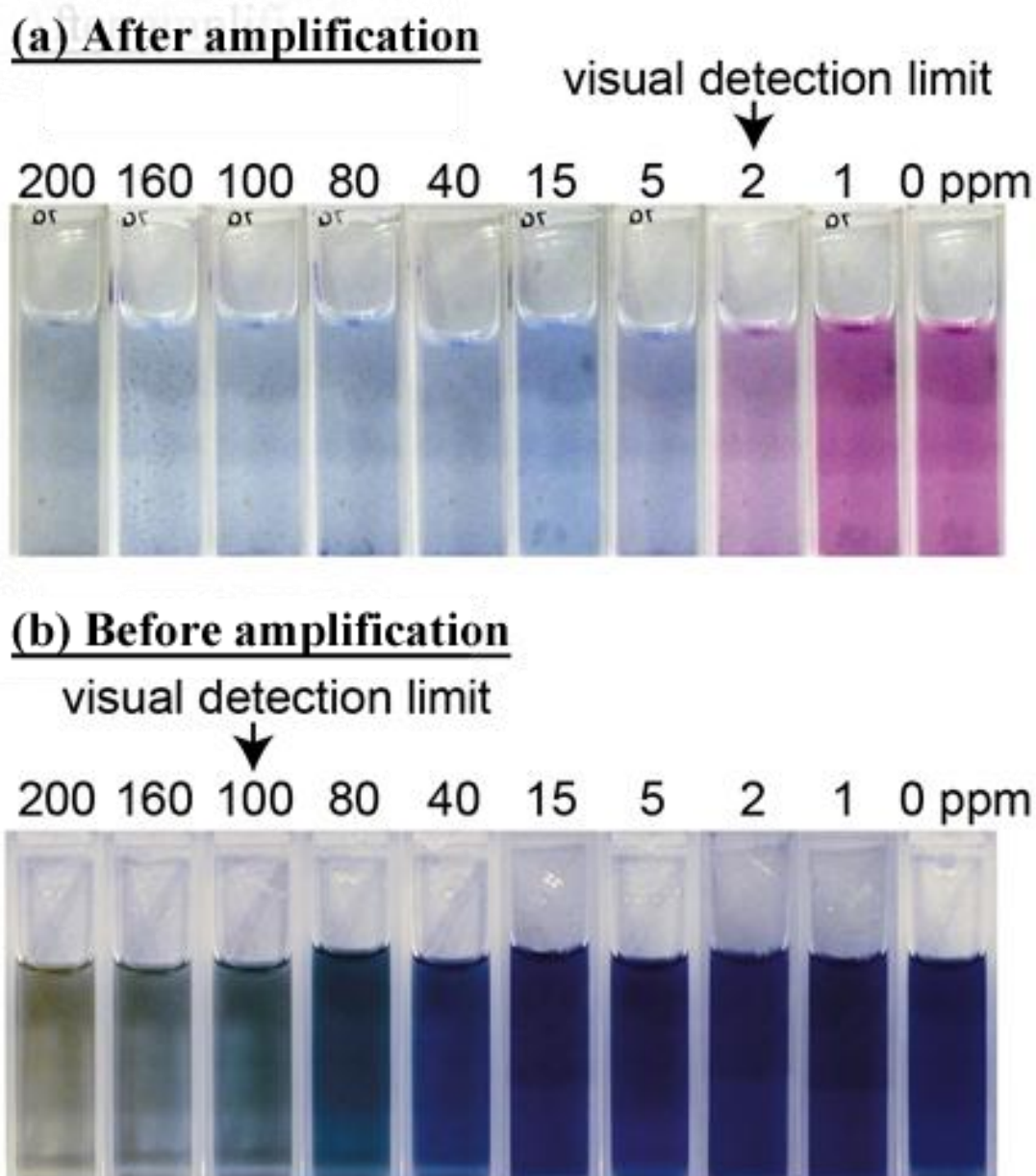


Figure 2.18 Photos of colorimetric response of **RuFe 1** (a) added with methyl orange (1:1 mol/mol) in the present of oxalate (0 ppm to 200 ppm) in aqueous buffer (pH 1.5) under irradiation at 298 K compare with (b) oxalate detection by **RuFe 1** without amplification.

2.4.2 Detection, Amplification, and Photo-degradation of Oxalate in Real Water Samples by **RuFe 1**

To verify the practical application of **RuFe 1** to actual environmental situations, water samples were spiked with **RuFe 1** and oxalate. Water sample sources included lake, river, and underground water collected in Hong Kong, China to simulate different contaminated water bodies. The samples were filtered through 0.45 μm pore-size membrane filters (Pall Corporation) to remove insoluble substances and used without any further treatment.

For spectrofluorometric detection of oxalate by **RuFe 1** in the real samples, all samples were spiked with the same amount of oxalate (33.3 ppm) and analyzed by **RuFe 1** under the same conditions as of the developed calibration curve shown in Figure 2.19. The analytical results show a good recovery and relative standard deviation (RSD, %) of 92.4%–115.8% and 2.24%–2.76%, respectively, suggesting that **RuFe 1** can function properly as a molecular detector for practical water sources.

For photo-degradation of oxalate by **RuFe 1** in the water samples, the samples were spiked with 767 ppm oxalate and tuned to pH 1.5 to simulate heavily polluted water bodies. With the addition of **RuFe 1** and exposure of 200 W UV-vis irradiation, oxalate degraded rapidly in the first 2 h with respect to a decrease in the DOC content. Figure 2.20 shows the DOC content of the samples against time. The times required for the 95% mineralization (DOC_{95}) of all water samples were within 200 min, indicating that the photocatalytic properties of **RuFe 1** can function properly for practical water sources.

A small amount of oxalate was added to river (3.3 ppm), lake (10.0 ppm), and underground (13.3 ppm) water samples. With the addition of **RuFe 1** and methyl orange, the oxalate concentrations were determined using the developed calibration curve shown in Figure 2.21. Under the amplification mechanism, the results show that **RuFe 1** achieved good recovery and relative standard deviation. Table 2.2 summarizes results for the detection, amplification, and degradation of oxalate by **RuFe 1** in actual water samples.

Toxicity tests were conducted to further validate the application of **RuFe 1** to real environmental situations. Figure 2.22 shows the results for an *in vivo* toxicity assay for the complex towards Japanese Medaka (*Oryzias latipes*). The test was performed with four different **RuFe 1** concentrations (0, 1, 10, and 100 mg/mL). Medaka larvae (~4–5 mm in length) were exposed to the **RuFe 1** complex for 7 days. Neither abnormal behavior, nor mortality of the fish was observed within the 7 day exposure period. The results indicate that **RuFe 1** does not cause any apparent adverse effects to the organism.

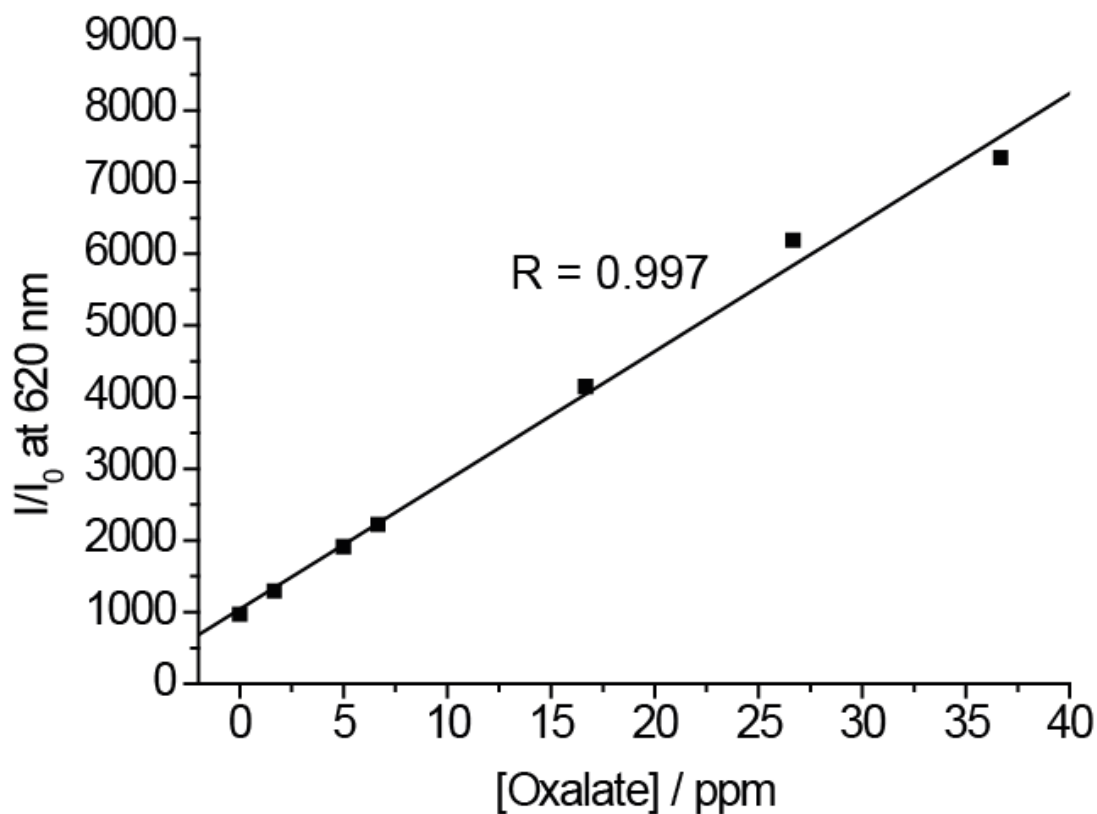


Figure 2.19 Calibration curve developed from the spectrofluorometric titrations of **RuFe 1** (3.33×10^{-5} M) with oxalate (0 to 36.67 ppm). The slope and y-intercept are 179.9 and 1041.4 ppm respectively of the best fitted I/I_0 versus [oxalate] plot at 620 nm. All titrations were carried out in a 2:1 ratio of ethanol/pH 1.5 aqueous buffer mixture at room temperature. Excitation $\lambda_{\text{ex}} = 468$ nm.

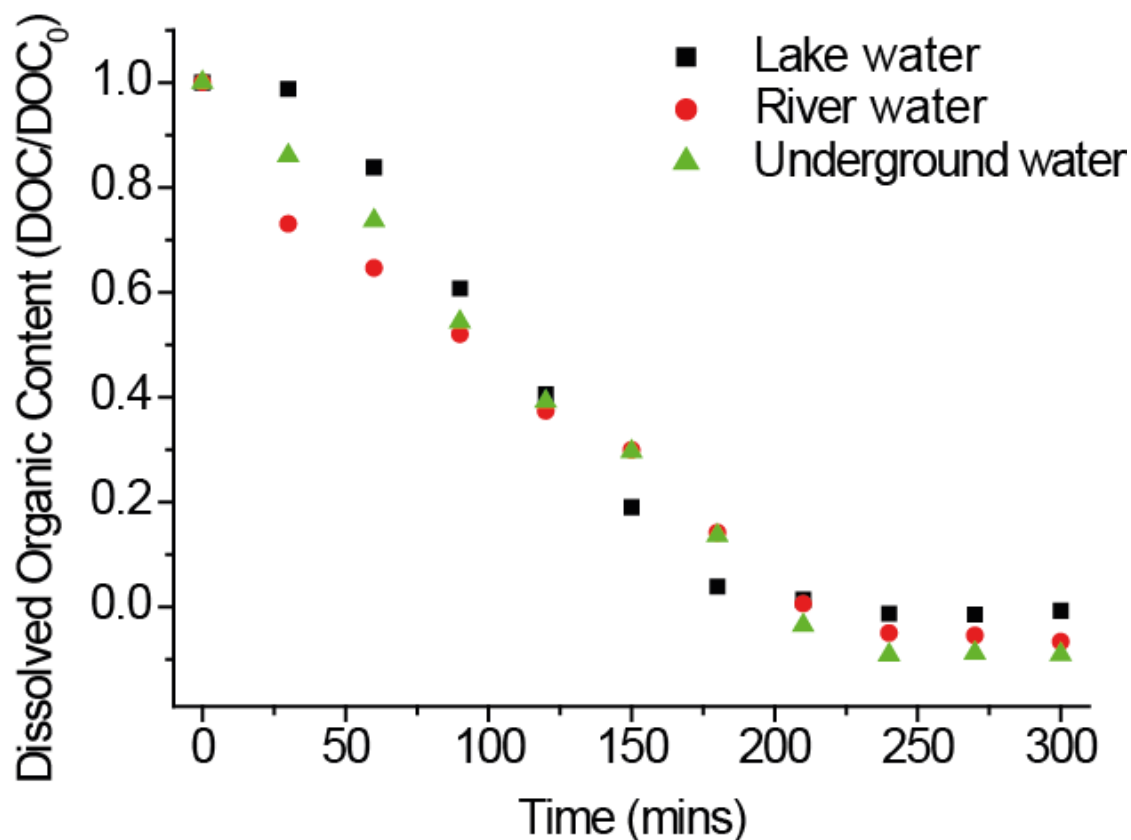


Figure 2.20 DOC during the course of the photo-degradation of oxalate by **RuFe 1** (1.79×10^{-4} M) in the different water bodies within 300 min. (■) lake water, (●) river water, and (▲) underground water. All the experiments were conducted at pH 1.5 with spiked oxalate (767 ppm) under 200W Hg(Xe) irradiation at room temperature and open atmosphere.

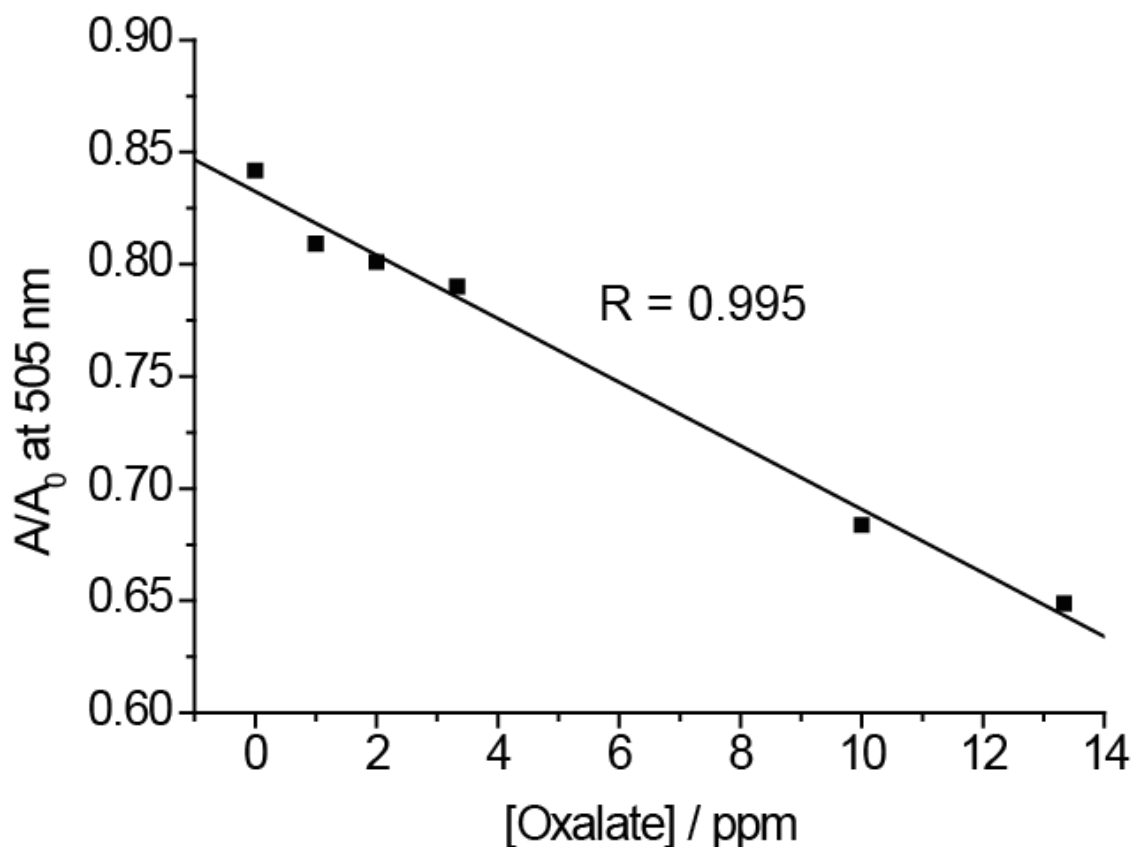


Figure 2.21 Calibration curve developed from the spectroscopic titrations of **RuFe 1** (8.61×10^{-6} M), methyl orange (1.63×10^{-5} M) with oxalate (0 to 13.33 ppm). The slope and y-intercept are -1.42×10^{-2} and 8.32×10^{-1} ppm respectively of the best fitted A/A_0 versus [oxalate] plot at 505 nm. All titrations were carried out in a 2:1 ratio of ethanol/pH 1.5 aqueous buffer mixture under UV-vis irradiation for 2 h.

Table 2.2 Results of oxalate detecting/degrading/signal amplifying lake, river, and underground water samples with **RuFe 1**.

Detection				
Water samples	Oxalate added ($\mu\text{g/L}$)	Oxalate found (ppm)	Recovery (%)	RSD (%)
lake	33.3	31.5 ± 0.9	94.6	2.76
river	33.3	38.6 ± 1.0	115.8	2.60
underground	33.3	30.8 ± 0.7	92.4	2.24
Degradation				
Water samples	Oxalate added ($\mu\text{g/L}$)	Oxalate left (ppm)	DOC ₉₅ (min)	
lake	767.0	0.0	175	
river	767.0	0.0	205	
underground	767.0	0.0	200	
Amplification				
Water samples	Oxalate added ($\mu\text{g/L}$)	Oxalate found (ppm)	Recovery (%)	RSD (%)
lake	10.0	10.1 ± 0.07	101.4	6.42
river	3.3	3.5 ± 0.09	103.9	9.18
underground	13.3	12.7 ± 0.07	95.1	6.89

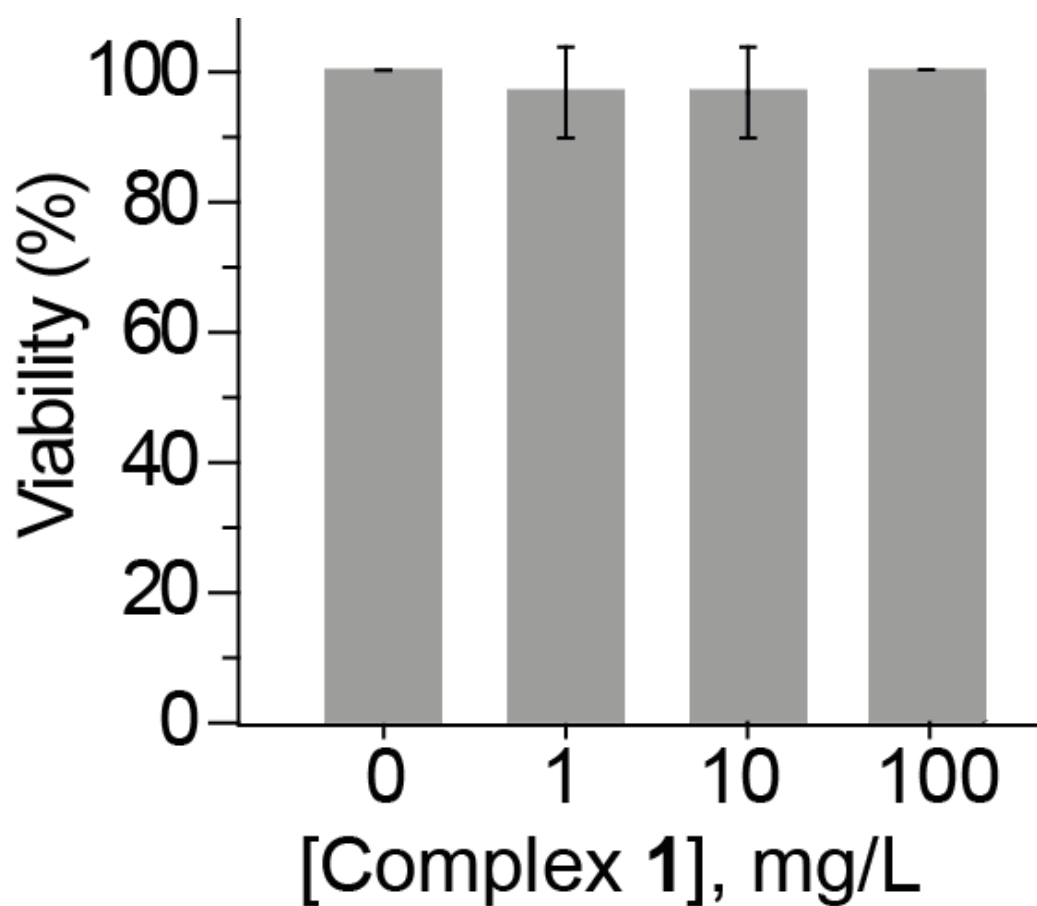


Figure 2.22 *In vivo* toxicity studies of the solid powders of complex **RuFe 1** on Japanese medaka. Larvae were exposed to culture medium with different concentration of the solid powder from 0 to 100 mg/L, and were fed once every other day, continuously for up to 7 days.

2.5 Conclusions

A new tetranuclear bimetallic Ru(II)-Fe(III) donor-acceptor complex has been synthesized and characterized. To the best of our knowledge, the **RuFe 1** complex is the first multifunctional device that can simultaneously contribute to detection, signal amplification, and degradation of oxalate in practical water samples. **RuFe 1** demonstrated the concept of the indicator/catalyst displacement assay (ICDA), in which one metal center acts as an indicator as well as an inhibitor, and is bridged to another metal center responsible for signal amplification and degradation. In the next chapter, we employed the present ICDA concept to synthesize a new molecular device, $\text{Fe}(\text{tBubpy})(\text{CN})_4\text{-}[\text{Cu}(\text{dien})(\text{ClO}_4)]_2$ (**FeCu 1**), for the detection, degradation, and signal amplification of an analyte other than oxalate.

Chapter 3: A Multifunctional Bimetallic Molecular Device for Ultrasensitive Detection, Naked-Eye Recognition and Elimination of Cyanide Ions

3.1 Introduction

Cyanide pollutants can cause serious environmental problems due to their high toxicity. Exposure to low concentrations of cyanide as low as 1.5 mg kg^{-1} can cause fatal poisoning.¹⁷⁷ There are more than 1.4 million tons of hydrogen cyanide produced per year from different industries such as mining and manufacturing industries. Although cyanide substances are highly regulated, their excessive use by the different industries makes accidental cyanide spills difficult to avoid.^{178,179}

Cyanide concentration monitoring in water has been investigated extensively, methods include titration,¹⁸⁰ spectrometric,¹⁸¹⁻¹⁸⁴ flow injection analysis,¹⁸⁵⁻¹⁸⁷ electrochemical detection¹⁸⁸⁻¹⁹⁰ and biosensor.¹⁹¹⁻¹⁹³ Most of the existing cyanide chemosensors focus on achieving high selectivity and sensitivity in aqueous condition, the measurement of cyanide can down to sub- $\mu\text{g L}^{-1}$ level.¹⁹⁴

Niamnont et al. have designed and synthesized three fluorescent probes for detection of cyanide (Figure 3.1), which contain diphenylacetylene as fluorogenic units and salicylaldehyde as a receptor (Scheme 3.1).¹⁹⁵ Upon the addition of cyanide to the assays, fluorescence intensity enhanced with the detection limit down to μM level. The sensor was also dropped on filter paper strips as paper-based sensors, where the signal was found to be naked eye detectable with 5 nmol cyanide.

A fluoro-chromogenic probe which is a subphthalocyanide derivative for detection of cyanide was reported by Ros-Lis *et al.* (Figure 3.2), in the presence of cyanide the probe will change color from magenta to colorless.¹⁹⁶ It shows a rather poor selectivity in aqueous condition but is overcome when acetonitrile introduced to the solvent system. The detection limit of this probe can as low as sub-ppm level, depending on the pH of the testing environment.

Lou et al. have reported a cyanide chemosensor based on IDA, which composed of a rhodamine-based dye bind with copper(II) ion.¹⁹⁷ The magenta complex solution will be decolorized with the introduction of cyanide, which captures the copper ions from the complex and results in a color change (Scheme 3.2). The detection limit of this assay can as low as 0.013 ppm.

Another example of cyanide sensor using displacement is reported by Kaushik *et al.* which based on a copper complex of coumarin (Scheme 3.3).¹⁹⁸ The non-emissive copper complex will “turn-on” when there is presence of cyanide. The detection limit of this probe is down to 5.77 μM in water and 14.4 μM in fresh mouse serum. Chung et al. also reported a fluorescence cyanide detection probe based on copper ion displacement.¹⁹⁹ This probe is a fluorescein derivative which exhibits less fluorescence when bind with copper ion and is recovered when cyanide anion introduce into the system (Scheme 3.4). The probe can detect cyanide in μM level and can apply in *in vivo* imaging.

Various remediation methods of water contaminated by cyanide exist include physical, complexation, adsorption and oxidation methods.²⁰⁰ The copper-catalyzed hydrogen peroxide oxidation process is one of the most frequently applied method in treating cyanidation wastes, the advantages of this method include simple to operate and mild reaction condition, but high reagent cost and requires accurate measurement for chemical dose control made this method unflavored.²⁰¹ In addition, over-treatment in remediation process can result in excessive cost and waste of energy. The overdose of chemical for wastewater treatment can case inefficient degradation,²⁰²⁻²⁰⁴ environmental pollutions and toxicities to aqua organisms.²⁰⁵⁻²⁰⁷ Moreover, continuous monitoring of pollutant concentration is needed to notice the need for remediation is also undesirable. Therefore chemosensor that can simultaneously detect and catalyze the degradation of cyanide into less toxic substances and which catalytic properties only initiate under a specific set of conditions is favorable.

Pramanik and Aprahamian have reported a hydrazone switch-based negative feedback loop which only catalyzes the formation of imine complex when the concentration of zinc(II) reach threshold (Scheme 3.5).²⁰⁸ This system only activates when the reaction mixture has zinc(II) concentration up to 20 mol %. Based on the previous chapter proposed ICDA system, herein we establish a catalyst displacement assay (CDA) which only catalyze the remediation process

when cyanide reaches the threshold. The CDA system is formed by non-covalently binding a catalyst with an inhibitor. This assay retained the features of ICDA which can selectively recognize a target analyte and at the same time readily re-activate to catalyze the degradation of the analyte, and also provide a new function that re-activation will only happen when the analyte concentration reaches a certain threshold. Such device can reduce the use of chemicals and can remove pollutant automatically without additional monitoring.

In this chapter, a series of Fe(II)-Cu(II) cyano-bridged bimetallic complex, **FeCu 1-4**, was designed and synthesized for the detection and degradation of cyanide anion. The **FeCu 1** complex $[\text{Fe}^{\text{II}}(\text{tBubpy})(\text{CN})_4]-[\text{Cu}^{\text{II}}(\text{dien})\text{ClO}_4]_2$ shows high selectivity and sensitivity for the cyanide anion in aqueous condition, and with the addition of phenolphthalin, the complex also serves as a signal amplifier that improves the detection limit to the ppb level making it suitable for naked-eye recognition. Moreover, this complex effectively degrades cyanide into the cyanate ion, which is a chemical 1500 times less toxic than cyanide.²⁰⁹ While **FeCu 2-4** complexes were synthesized based on **FeCu 1** with different Fe^{II} subunits, including $[\text{Fe}^{\text{II}}(\text{CN})_6]-[\text{Cu}^{\text{II}}(\text{dien})(\text{H}_2\text{O})]_2$ (**FeCu 2**), $[\text{Fe}^{\text{II}}(\text{tBubpy})(\text{CN})_4]-[\text{Cu}^{\text{II}}(\text{dien})\text{Cl}]_2$ (**FeCu 3**) and $\{[\text{Fe}^{\text{II}}(\text{tBubpy})_2(\text{CN})_2]_2-[\text{Cu}^{\text{II}}(\text{dien})]\}\text{Cl}_2$ (**FeCu 4**). The catalytic properties of Fe(II)-Cu(II) bimetallic complexes are temporarily deactivated, however, once the cyanide concentration reached a certain threshold, a catalytic oxidation reaction of the cyanide is initiated and turns cyanide into less toxic cyanate. The threshold is found to be controlled by both thermodynamic and kinetic properties of the donor-acceptor formation in the bimetallic complexes.

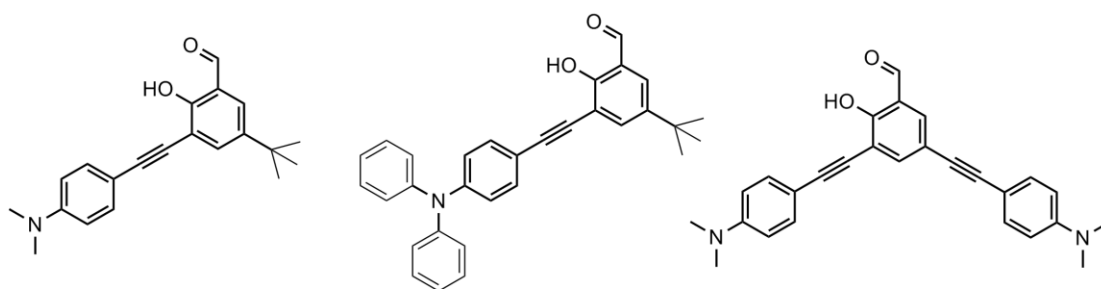
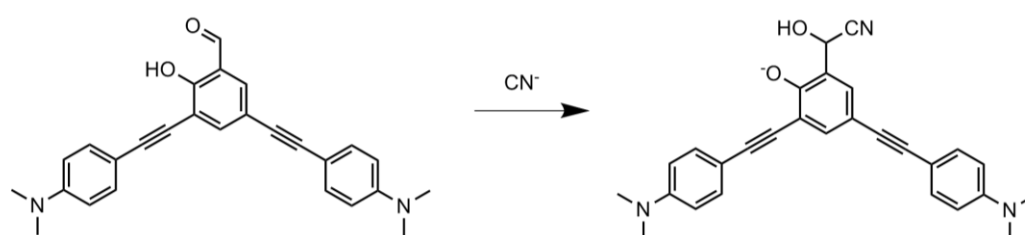


Figure 3.1 Molecular structures of the three fluorescent probes composed of salicylaldehyde and diphenylacetylene groups for detection of cyanide.¹⁹⁵



Scheme 3.1 Reaction scheme for the fluorescent probe to detect cyanide.¹⁹⁵

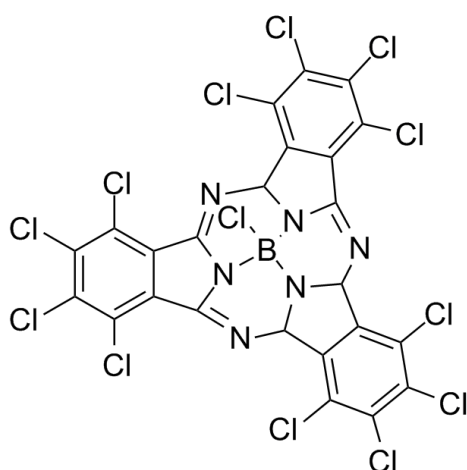
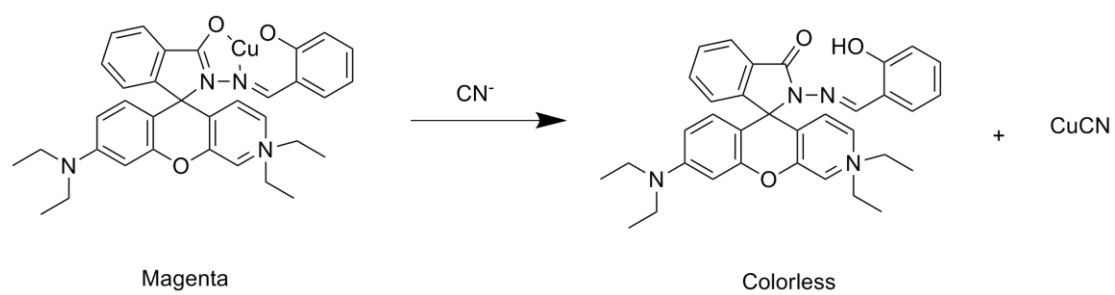
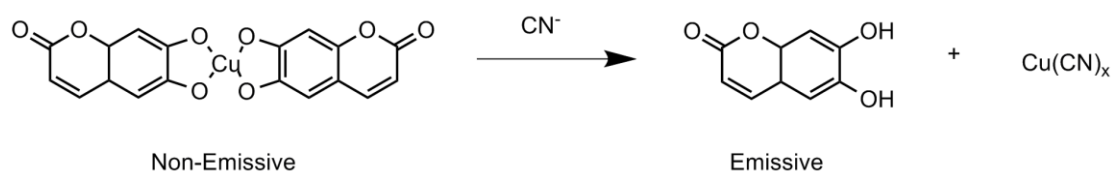


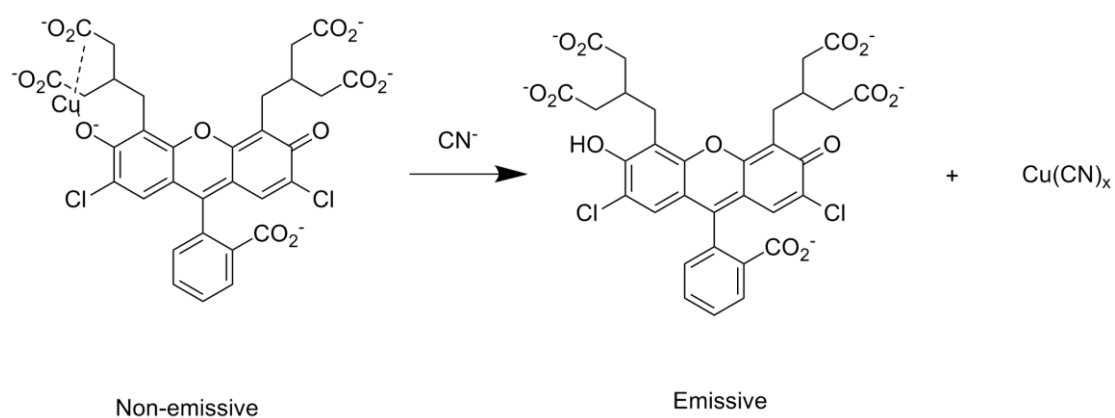
Figure 3.2 A subphthalocyanide derivative as fluoro-chromogenic probe for the detection of cyanide.¹⁹⁶



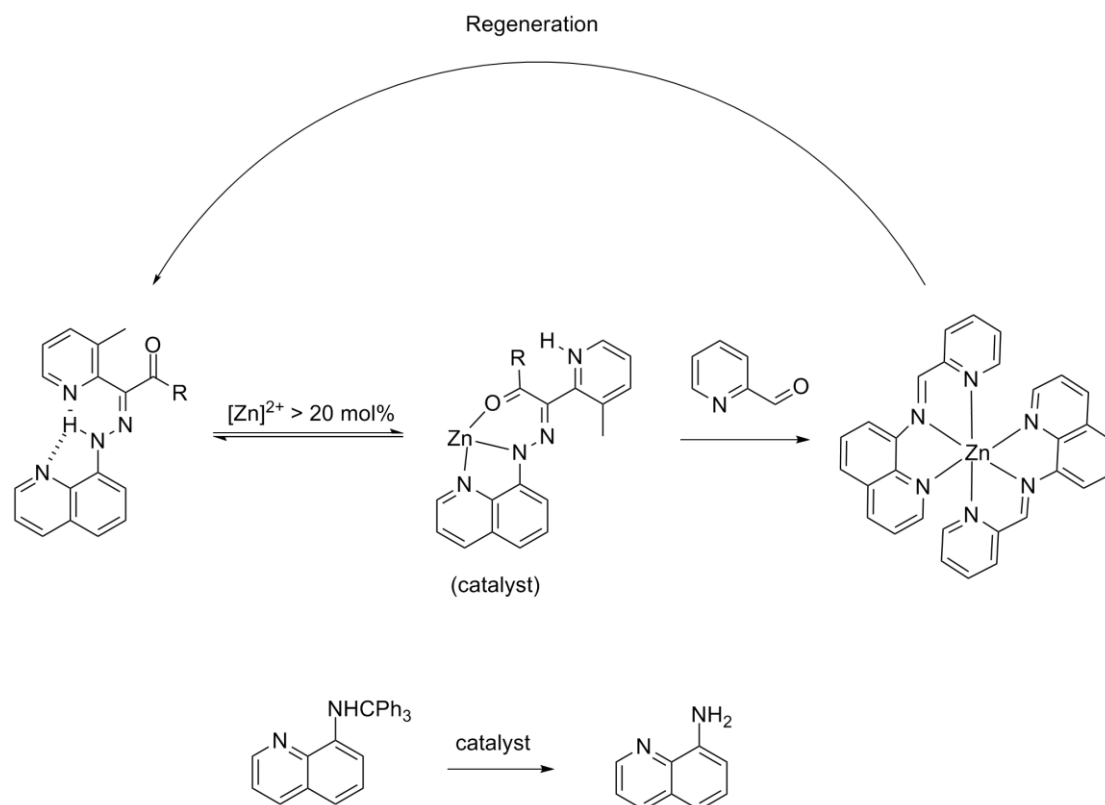
Scheme 3.2 A chemosensor of cyanide anion composed of rhodamine based copper complex.¹⁹⁶



Scheme 3.3 A chemosensor of cyanide anion composed of 6,7-dihydroxycoumarin copper complex.¹⁹⁸



Scheme 3.4 A chemosensor for cyanide detection based on a copper complex of fluorescein derivative.¹⁹⁹



Scheme 3.5 A hydrazone switch-based negative feedback loop which only catalyze the formation of imine complex when concentration of zinc(II) over 20 mol%.²⁰⁸

3.2 Experimental

3.2.1 Materials and Reagents

4,4'-Di-*tert*-butyl-2,2'-bipyridine (^tBubpy), diethylenetriamine (dien), K₄[Fe(CN)₆], potassium oxalate, copper (II) perchlorate hexahydrate, ammonium iron (II) sulfate hexahydrate, and potassium salts of acetate, azide, nitrate, thiocyanate, dihydrogen phosphate, bromide, chloride, and sulfate, were obtained from Aldrich. Potassium cyanide was obtained from Acros and potassium oxalate was obtained from Farco chemical supplies. Complexes Fe^{II}(^tBubpy)₂(CN)₂, K₂[Fe(^tBubpy)(CN)₄] and Cu(dien)(ClO₄)₂ were synthesized according to the method in the literature.^{210,211} All organic solvents used were of analytical grade.

3.2.2 Synthesis



A mixture of K₂[Fe(^tBubpy)(CN)₄] (0.253 g, 0.5 mmol) and Cu(dien)(ClO₄)₂ (0.366 g, 1 mmol) was stirred in a solvent mixture of water/methanol (1:1 v/v, 10 mL) at room temperature for 30 min and then allowed to stand overnight. Brown precipitates were obtained by centrifugation and were washed with deionized water and acetone and then air-dried. Yield: 0.414 g (86.4%); IR (KBr): $\nu_{\text{C}\equiv\text{N}} = 2052, 2076, 2096, 2118 \text{ cm}^{-1}$; ESI-MS (MeCN, +ve mode): m/z 380.1 {Fe(^tBubpy)(CN)₄[Cu(dien)]₂}²⁺ (mass = 760.2 g mol⁻¹; charge = +2); Anal. calc. for C₃₀Cl₂Cu₂FeH₅₀N₁₂O₈·CH₃C(O)CH₃ (FeCu 1): C, 38.91; H, 5.54; N, 16.50; Found: C, 39.02; H, 5.61; N, 16.84.



A mixture of K₄[Fe^{II}(CN)₆] (1.00 g, 2.37 mmol) and Cu(dien)Cl₂ (0.56 g, 2.37 mmol) was stirred in a water/methanol (1:1) mixture 12.5 mL/12.5 mL (v/v), overnight at room temperature. FeCu 2 was obtained as green solid by filtration, which was washed with deionized water and acetone and allowed to air-dry. Yield: 1.04 g (81.4%); IR (KBr): $\nu_{\text{C}\equiv\text{N}} = 2039, 2047, 2103 \text{ cm}^{-1}$; ESI-MS (MeOH, +ve mode): m/z 544.8 {[Fe(CN)₆]-[Cu(dien)]₂}H⁺

(mass = 544.0 g mol⁻¹; charge = +1); Anal. calc. for C₁₄Cu₂FeH₂₆N₁₂·4H₂O (**FeCu 2**): C, 27.23; H, 5.55; N, 27.22; Found: C, 27.29; H, 5.52; N, 26.95.

[Fe^{II}(^tBubpy)(CN)₄]-[Cu^{II}(dien)Cl]₂ (**FeCu 3**)

The synthetic procedure was similar to that of **FeCu 1** except that [Cu^{II}(dien)Cl]₂ (0.05 g, 0.2 mmol) was used instead of [Cu(dien)(ClO₄)₂]. Yield: 0.069 g (83.1%). IR (KBr): ν_{C≡N} = 2059, 2084, 2103, 2114 cm⁻¹; ESI-MS (MeCN, +ve mode): m/z 380.1 {[Fe(^tBubpy)(CN)₄]-[Cu(dien)]₂}²⁺ (mass = 760.2 g mol⁻¹; charge = +2); Anal. calc. for C₃₀Cl₂Cu₂FeH₅₀N₁₂ (**FeCu 3**): C, 43.27; H, 6.05; N, 20.19; Found: C, 43.22; H, 6.10; N, 20.10.

{[Fe^{II}(^tBubpy)₂(CN)₂]₂-[Cu^{II}(dien)]}Cl₂ (**FeCu 4**)

A mixture of Fe^{II}(^tBubpy)₂(CN)₂ (0.10 g, 0.16 mmol) and Cu(dien)Cl₂ (0.038 g, 0.16 mmol) was stirred in 25 mL methanol overnight at room temperature. Reddish brown solid was collected after evaporation and was washed by chloroform, deionized (DI) water, and acetone and then air-dried. Yield: 0.0745 g (61.1%); IR (KBr): ν_{C≡N} = 2068, 2082 cm⁻¹; ESI-MS (MeOH, +ve mode): m/z 726.9 {[Fe(^tBubpy)₂(CN)₂]₂-[Cu(dien)]}²⁺ (mass = 1454.70 g mol⁻¹; charge = +2); Anal. calc. for C₈₀Cl₂Cu₁Fe₂H₁₀₉N₁₅·CH₃C(O)CH₃ (**FeCu 4**): C, 62.81; H, 7.62; N, 11.94; Found: C, 63.52; H, 7.62; N, 11.73.

3.2.3 Physical Measurements and Instrumentation

Electrospray (ES) mass spectrometry was performed by means of an AB SCIEX API 2000 LC/MS/MS system. IR spectra in the range of 500–4000 cm⁻¹ with KBr pellets were recorded on a PerkinElmer Model Frontier FTIR spectrometer. Emission spectra were recorded using a Horiba FluoroMax-4 spectrofluorometer with a 1 nm slit width and a 0.5 s integration time. UV/Vis spectra were measured on a Cary 50 UV/Vis spectrophotometer. Elemental analyses were conducted on a Vario EL CHN analyzer.

3.2.4 UV-vis Spectroscopic Titration

3.2.4.1 General Parameters

With the exception of DMF which was purified by distillation before use, all solvents used in the UV-vis spectroscopic titrations were of analytical grade and used without purification. The HEPES buffer used was 10 mM at pH 7.4. All spectroscopic titrations were carried out in aqueous DMF (1:1 v/v) (1.50 mL of aqueous HEPES buffer at pH 7.4 with 1.50 mL DMF) except titrations with **FeCu 2** and its corresponding precursor complex, which were performed in aqueous HEPES buffer at pH 7.4. Signal amplification titrations were carried out in DI water with pH 14 adjusted by potassium hydroxide. Receptor-substrate interaction was analyzed according to either 1:1 or 1:2 Benesi–Hildebrand equations¹⁵⁵ for the UV-vis spectroscopic titrations.

3.2.4.2 Binding Constant Determination

For the binding determinations for **FeCu 1**, $K_2[Fe(tBubpy)(CN)_4]$ solutions (1.0×10^{-4} M) of a fixed concentration were mixed with $Cu(dien)(ClO_4)_2$ solutions of various concentrations (0 to 1.0×10^{-4} M). The absorption intensity of the resultant mixtures was measured at 505 nm and $A_0/(A-A_0)$ was plotted as a function of $\{1/[Cu(dien)(ClO_4)_2]\}^2$

3.2.4.3 Spectroscopic UV-vis Titrations of **FeCu 1-4** by Cyanide and Common Anions

Binding constants ($\log K_{overall}$) and formation energies ($\Delta G/kJ\ mol^{-1}$) of **FeCu 1-4** toward cyanide were calculated according to either 1:1 or 1:2 Benesi–Hildebrand equations using the ratio between the y -intercept and the slope of the best fitted straight line. Fixed concentrations of the complex (2.0×10^{-4} M) were prepared and titrated with different concentrations of cyanide solution (0 to 4.0×10^{-4} M) in aqueous DMF.

3.2.5 Spectroscopic UV-vis Titrations of **FeCu 1** by Common Anions

Fixed concentrations of **FeCu 1** solutions (2.00×10^{-4} M) were mixed with 10 equivalents of various analytes (CN^- , SO_4^{2-} , HCO_3^- , HPO_4^{2-} , N_3^- , CH_3COO^- , NCS^- , NO_3^- , and Cl^-) (0 to 2.00

$\times 10^{-3}$ M). The absorbances at 505 nm were plotted as a function of the analyte mole ratios. The colorimetric responses of **FeCu 1** to the analytes were also obtained by digital photography.

3.2.5.1 Signal Amplification by **FeCu 1** in Cyanide Detection

All signal amplification testing solutions were adjusted to pH 14 by potassium hydroxide and investigations were conducted at room temperature. Different amounts of cyanide (0 to 4.61×10^{-5} M, i.e. 0 to 1.2 ppm) were added to mixtures of **FeCu 1** (2.50×10^{-6} M) and phenolphthalin (2.52×10^{-4} M). Each solution was allowed to stand for 15 min prior to measurement. UV-vis absorption spectra were recorded at fixed time intervals and absorbance changes at 551 nm were plotted against cyanide concentrations. Responses after amplification were also obtained by digital photography.

3.2.5.2 Oxidation of Cyanide to Cyanate with **FeCu 1-4** as the Catalyst

All experiments were conducted in a 40 mL boiling tube in the absence of light. A 15.00 mL test solution was stirred during the experiments. Testing solutions were composed of varied concentration of CN^- from 0 to 1000 μM and fixed concentration of H_2O_2 (6.53×10^{-4} M) and **FeCu** complexes, where the total Cu^{II} concentration maintained at 0.2 mM. At regular time intervals, concentrations of CN^- and NCO^- in the test solution were measured by analytical method reported in the literature.²¹² Fixed volume of testing solution (1 mL) was added to a solution of 2-aminobenzoic acid solution (0.1M, 1 mL) and incubated at 40°C for 10 mins, followed by addition of HCl solution (12N, 1 mL) and boiled in a water bath for 1 min. After cooled to room temperature, emission intensity at 330 nm were measured with excitation at 310 nm. Concentration of cyanate was found with a developed calibration curve. Analyses were conducted immediately to avoid errors due to further reactions.

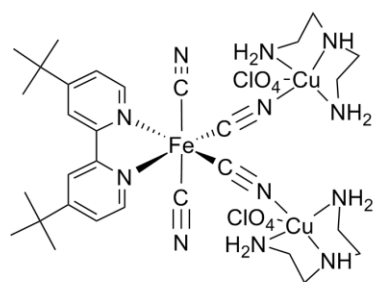
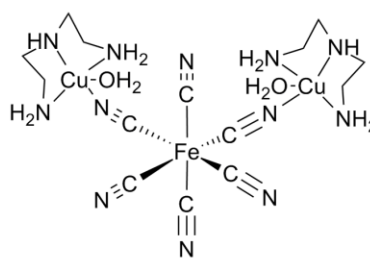
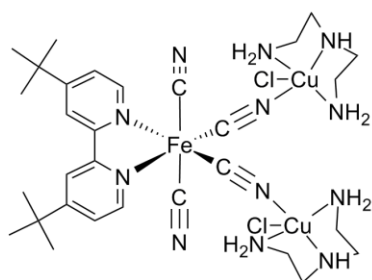
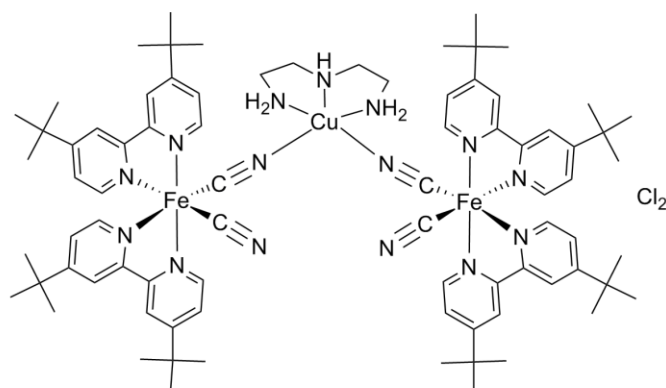
3.3 Results and Discussion

3.3.1 Syntheses and Characterization

The building blocks of all the bimetallic complexes are well-known donor and acceptor coordination complexes. $K_2[Fe^{II}('Bubpy)(CN)_4]$, $[Fe^{II}('Bubpy)_2(CN)_2]$, and $[Cu^{II}(dien)]^{2+}$ were synthesized according to methods in the literature while $K_4[Fe^{II}(CN)_6]$ is commercially available. The Fe^{II} and Cu^{II} complexes were well characterized by electrospray mass spectrometry, infrared spectrometry, and elementary analysis. All of the characterization results are in good accordance with the literature.^{210,211}

All the bimetallic complexes were formed by stirring equal equivalents of $[Cu^{II}(dien)Cl_2]$ with corresponding cyano-ferrous complexes. The structures of **FeCu1-4** were shown in Scheme 3.6. All these complexes were isolated as an air-stable solid. Surprisingly, even the Fe^{II} and Cu^{II} ratio was set as 1:1 during synthesis, the composition **FeCu 4** still changed to 2:1 while others in 1:2. The integrity of their trinuclear state were demonstrated by electrospray-MS showing a peak at m/z 380.1, 544.8, 380.1 and 726.9 corresponding to $[FeCu 1-Cl_2]^{2+}$, $[FeCu 2-H]^+$, $[FeCu 3-Cl_2]^{2+}$, and $[FeCu 4-Cl_2]^{2+}$, respectively. Figure 3.3 to Figure 3.6 depict the electrospray mass spectra of **FeCu 1-4 respectively** in aqueous methanol. All the structures were also verified by CHN elemental analysis and gave satisfactory results.

Formation of Fe-CN-Cu bridges in the new complexes was also confirmed by IR spectroscopic studies. All the $\nu_{C\equiv N}$ stretching frequencies of **FeCu 1-4** were red shifted with respect to their cyano-ferrous precursors as shown in Table 3.1, which indicated the formation of cyano-bridge in the complexes. Differences in degree of the shifts could be attributed to the electron density differences of the cyano-ferrous precursors, with respect to their different net charges (varies from -4, to -2, and 0 respectively). The larger the negative charges, the greater π back bonding from the Fe^{II} to the CN π^* antibonding orbital, result in the decrease of wavenumber shifts amount three complexes.²¹³

**FeCu 1****FeCu 2****FeCu 3****FeCu 4**Scheme 3.6 Structures of complexes **FeCu 1-4**.

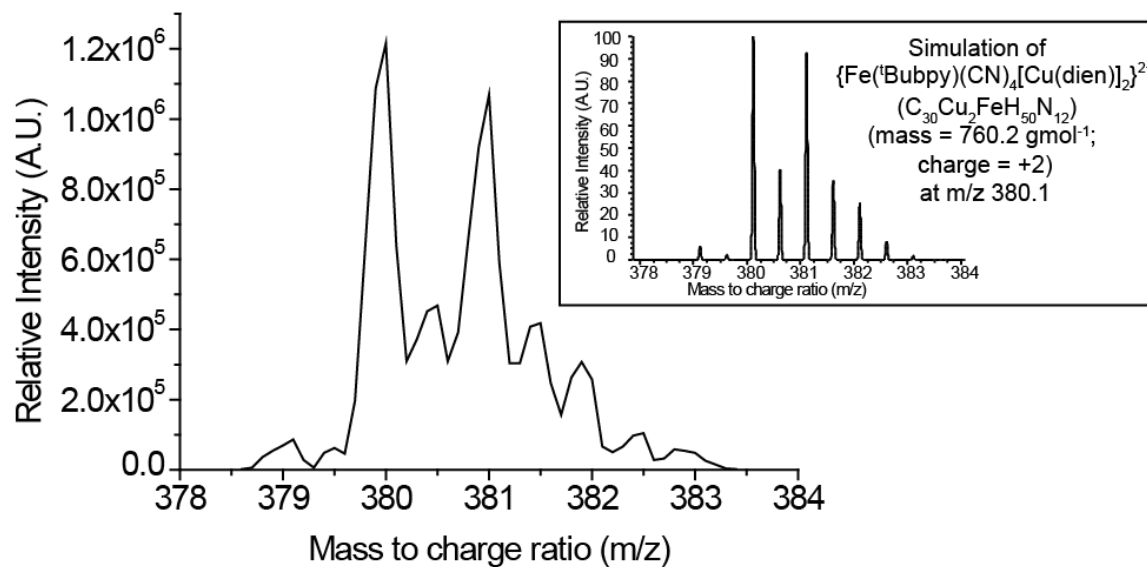


Figure 3.3 Isotopic distribution and its simulation (*inset*) of **FeCu 1**: $[M-Cl_2]^{2+}$ peak at m/z 380.1. The mass spectrum was obtained in methanol.

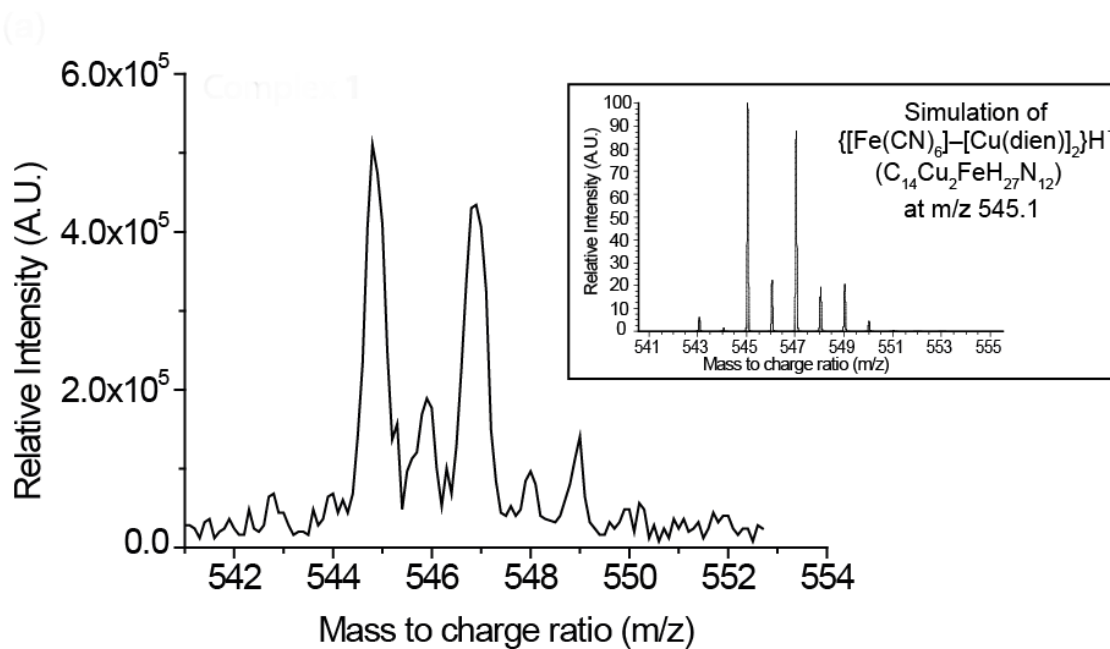


Figure 3.4 Isotopic distribution of ESI-MS spectrum of the m/z 545 peak of $\{[\text{Fe}^{\text{II}}(\text{CN})_6]-[\text{Cu}(\text{dien})]_2\}\text{H}^+$ (**FeCu 2**+H⁺) and (*inset*) simulations based on its molecular formula. Spectrum was obtained in DI water/methanol.

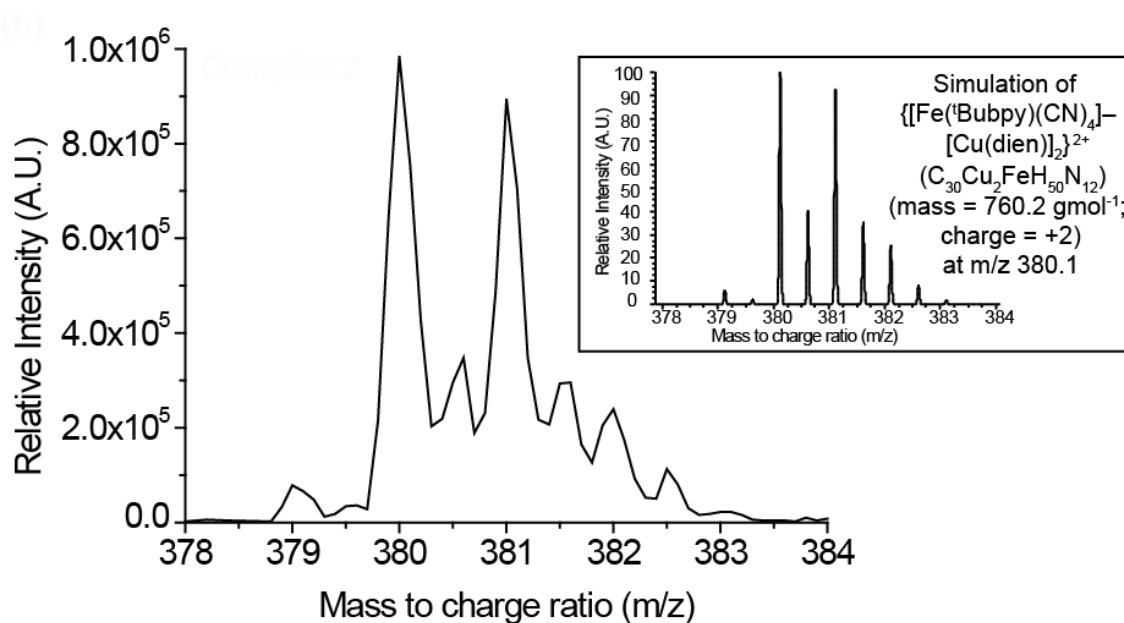


Figure 3.5 Isotopic distribution of ESI-MS spectrum of the m/z 380 peak of $\{[\text{Fe}^{\text{II}}(\text{tBubpy})(\text{CN})_4]-[\text{Cu}(\text{dien})_2]\}^{2+}$ (FeCu 3-Cl_2) $^{2+}$ and (*inset*) simulations based on its molecular formula. Spectrum was obtained in DI water/methanol.

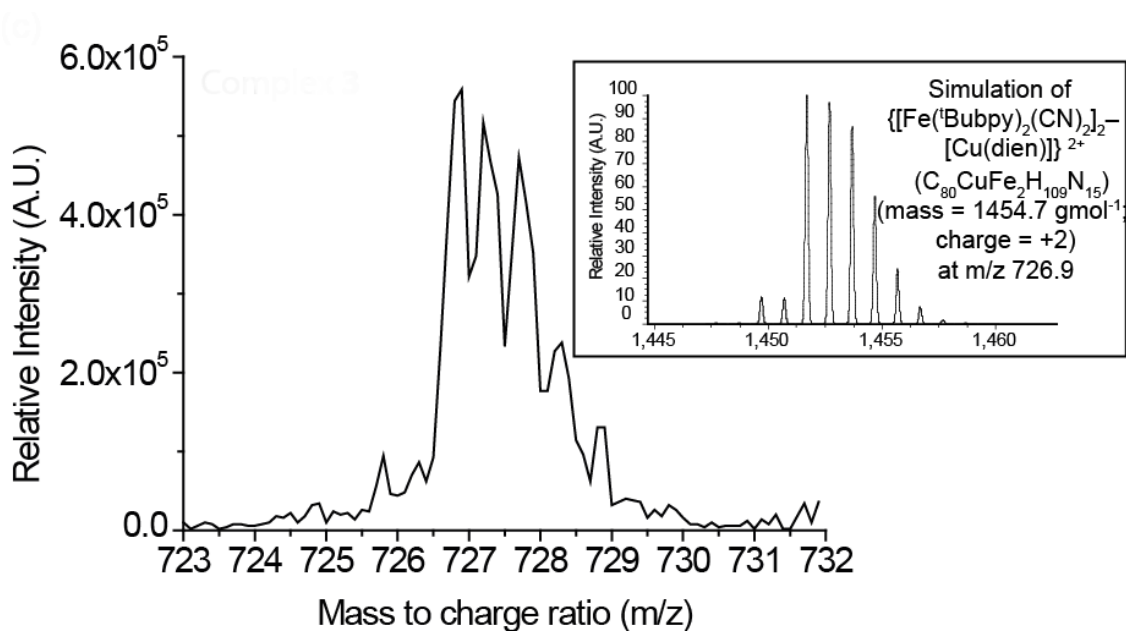


Figure 3.6 Isotopic distribution of ESI-MS spectrum of the m/z 727 peak of $\{[\text{Fe}^{\text{II}}(\text{tBubpy})_2(\text{CN})_2]_2-[\text{Cu}(\text{dien})]\}^{2+}$ (**FeCu 4-Cl₂**)²⁺ and (*inset*) simulations based on its molecular formula. Spectrum was obtained in DI water/methanol.

Table 3.1 IR spectroscopic study of the cyano-stretching frequency ($\nu_{\text{C}\equiv\text{N}}$) of **FeCu 1-4** and their ferrous precursors.

Entry	Complexes	$\nu_{\text{C}\equiv\text{N}}$ (cm^{-1})
1	$[\text{Fe}^{\text{II}}(\text{}^t\text{Bubpy})(\text{CN})_4]-[\text{Cu}^{\text{II}}(\text{dien})\text{ClO}_4]_2$ (FeCu 1)	2052, 2076, 2095, 2118
2	$[\text{Fe}^{\text{II}}(\text{CN})_6]-[\text{Cu}^{\text{II}}(\text{dien})]_2$ (FeCu 2)	2047, 2059, 2103
3	$[\text{Fe}^{\text{II}}(\text{}^t\text{Bubpy})(\text{CN})_4]-[\text{Cu}^{\text{II}}(\text{dien})\text{Cl}]_2$ (FeCu 3)	2059, 2084, 2103, 2114
4	$\{[\text{Fe}^{\text{II}}(\text{}^t\text{Bubpy})_2(\text{CN})_2]_2-[\text{Cu}^{\text{II}}(\text{dien})]\}_2\text{Cl}_2$ (FeCu 4)	2068, 2082
5	$\text{K}_4[\text{Fe}^{\text{II}}(\text{CN})_6]$	2030, 2043
6	$\text{K}_2[\text{Fe}^{\text{II}}(\text{}^t\text{Bubpy})(\text{CN})_4]$	2053, 2067, 2085
7	$\text{Fe}^{\text{II}}(\text{}^t\text{Bubpy})_2(\text{CN})_2$	2080

3.3.2 Electronic Absorption Properties

The precursor complex, $K_2[Fe(^tBubpy)(CN)_4]$, shows a low energy absorption band from ~430 to 600 nm. Referencing the literature, the low-energy absorption bands are assigned to $Fe(d\pi) \rightarrow ^tBubpy(\pi^*)$ metal-to-ligand charge transfer absorption (MLCT).²¹⁰

Figure 3.7 shows the MLCT absorption for $K_2[Fe(^tBubpy)(CN)_4]$ before and after bridging with the $[Cu(dien)(ClO_4)_2]$ complex in aqueous DMF at 298 K, where the **FeCu 1** formed is reddish brown in color with respect to its reddish purple precursor. The λ_{max} for the $Fe(d\pi) \rightarrow ^tBubpy(\pi^*)$ MLCT transitions of $K_2[Fe(^tBubpy)(CN)_4]$ was 523 nm, and with the coordination of the $[Cu(dien)(ClO_4)_2]$, the MLCT transition shifted from 523 nm to 498 nm, and the absorption coefficient was increased from 1450 to 4530 $cm^{-1}mol^{-1}dm^3$.

Spectroscopic titration was performed to further confirm the trinuclear state of **FeCu 1-4**. As shown in Figure 3.8 to Figure 3.11, a good linear relationship for the plot of $A_0/(A-A_0)$ versus $1/\{[Cu^{II}(dien)(ClO_4)_2]\}^2$ and $A_0/(A-A_0)$ versus $1/\{[Cu^{II}(dien)(ClO_4)_2]\}^{0.5}$ was obtained by fitting to the 1:2 and 2:1 Benesi–Hildebrand equation, indicating that the **FeCu 1-3** system possess a 1:2 whereas **FeCu 4** possesses a 2:1 binding stoichiometry of Fe^{II}/Cu^{II} . The binding constant (K_B) for **FeCu 1-4** was summarized in Table 3.2.

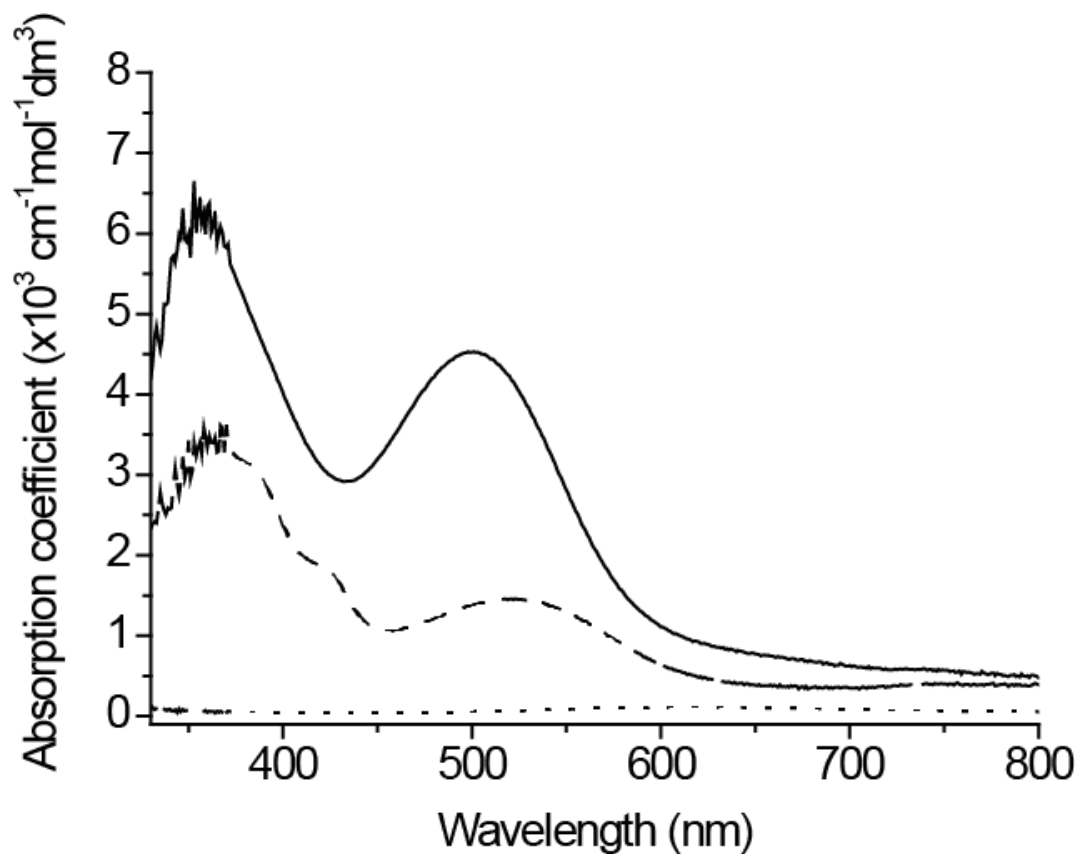


Figure 3.7 Absorption spectra of **FeCu 1** (—) and its precursors $\text{K}_2\text{Fe}^{\text{II}}(\text{}^t\text{Bubpy})(\text{CN})_4$ (---) and $\text{Cu}^{\text{II}}(\text{dien})(\text{ClO}_4)_2$ (⋯). Spectra were obtained in aqueous DMF (1:1 v/v) (1.50 mL of aqueous HEPES buffer at pH 7.4 + 1.50 mL of DMF) at 298 K.

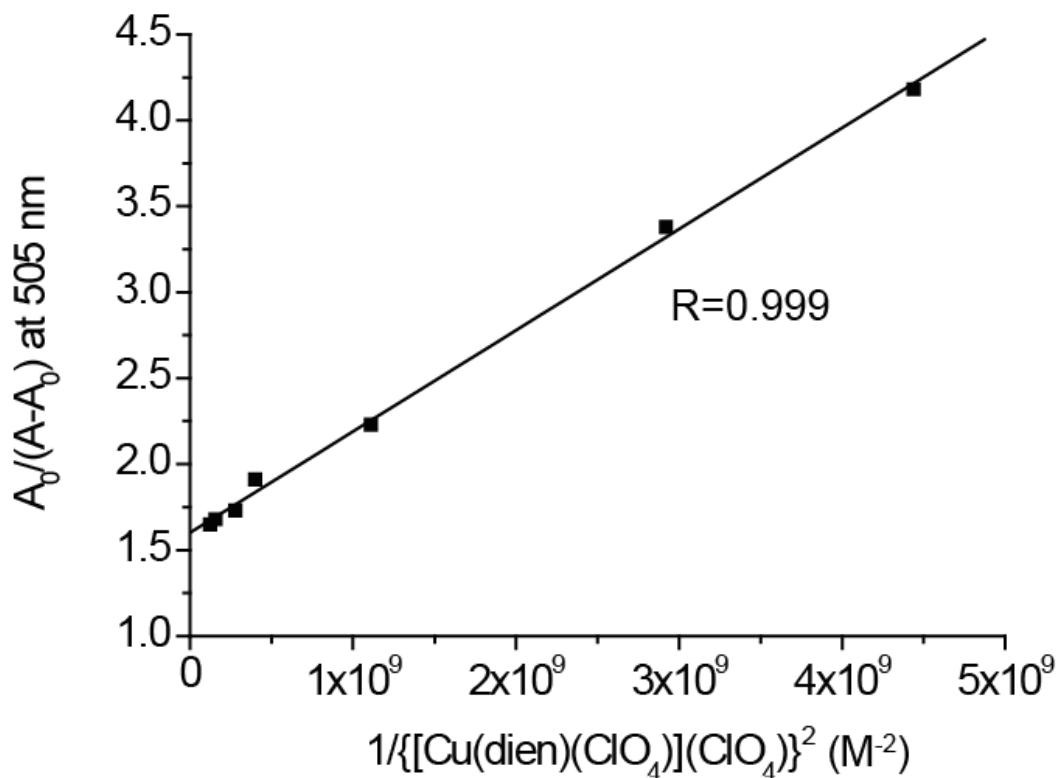


Figure 3.8 Results of spectroscopic titration for $\text{K}_2[\text{Fe}(\text{tBubpy})(\text{CN})_4]$ (1.00×10^{-4}) by $[\text{Cu}(\text{dien})(\text{ClO}_4)_2]$. All the titrations were performed in aqueous DMF (1:1 v/v) (1.50 mL of aqueous HEPES buffer at pH 7.4 + 1.50 mL of DMF) at 298 K. From fitting the curve with the 1:2 Benesi-Hildebrand equation, slope and y-intercept are $5.89 \times 10^{-10} \text{ M}^2$ and 1.60 respectively with the best fitted $A_0/(A-A_0)$ at 505 nm versus $1/\{[\text{Cu}^{\text{II}}(\text{dien})(\text{ClO}_4)_2]\}^2$, $\log K = 4.72 \pm 0.003 \text{ M}^{-1}$. The solvated form of **FeCu 1** is deduced as 1:2 ratio of $[\text{Fe}(\text{II})]:[\text{Cu}(\text{II})]$.

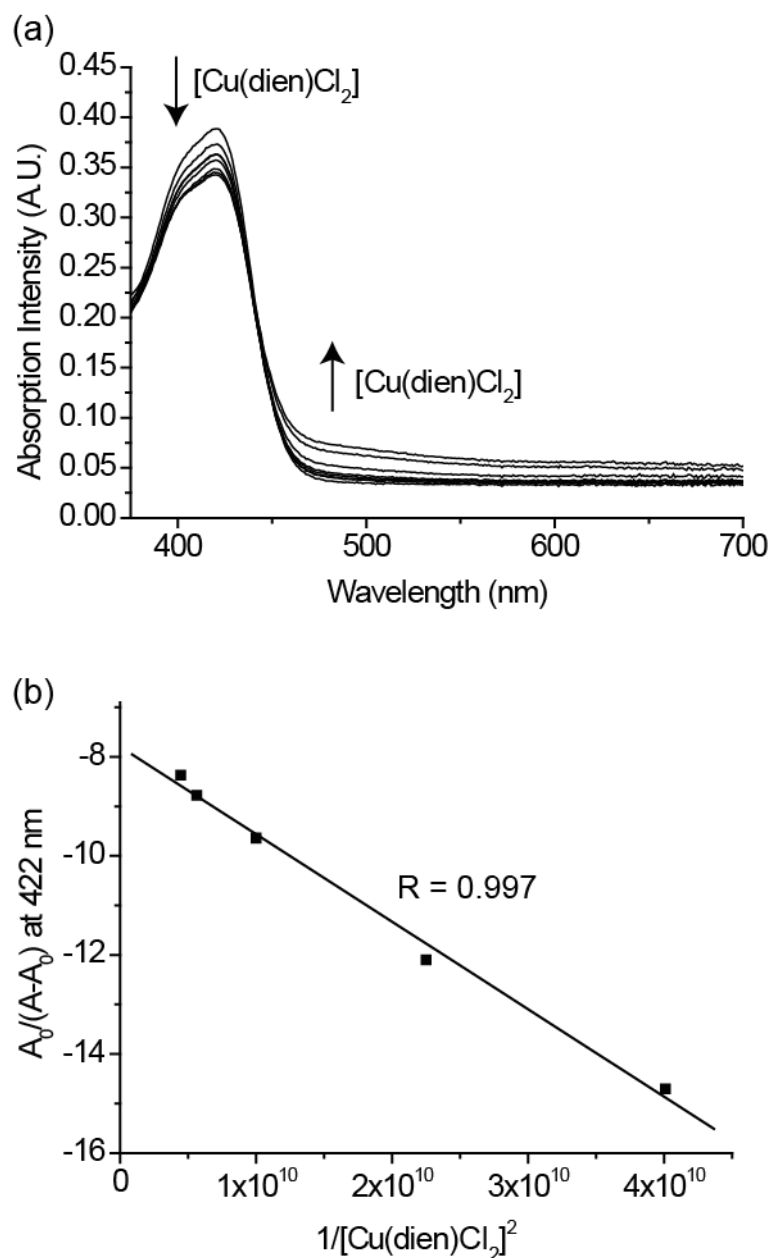


Figure 3.9 (a) UV-vis spectroscopic titrations of $\text{K}_4[\text{Fe}^{\text{II}}(\text{CN})_6]$ by $\text{Cu}^{\text{II}}(\text{dien})\text{Cl}_2$ (b) The best fitted 1:2 Benesi-Hildebrand equation with $A_0/(A-A_0)$ versus $1/\{\text{Cu}^{\text{II}}(\text{dien})\text{Cl}_2\}^2$ plot at 422 nm. The slope and y-intercept are -1.77×10^{-10} M and -7.79 respectively, with $\log K = 5.32 \pm 0.008$ M^{-1} . The solvated form of the complex is deduced as 1:2 ratio of $[\text{Fe}^{\text{II}}:\text{Cu}^{\text{II}}]$. All the titrations were performed in HEPES buffer at pH 7.4 at 298 K.

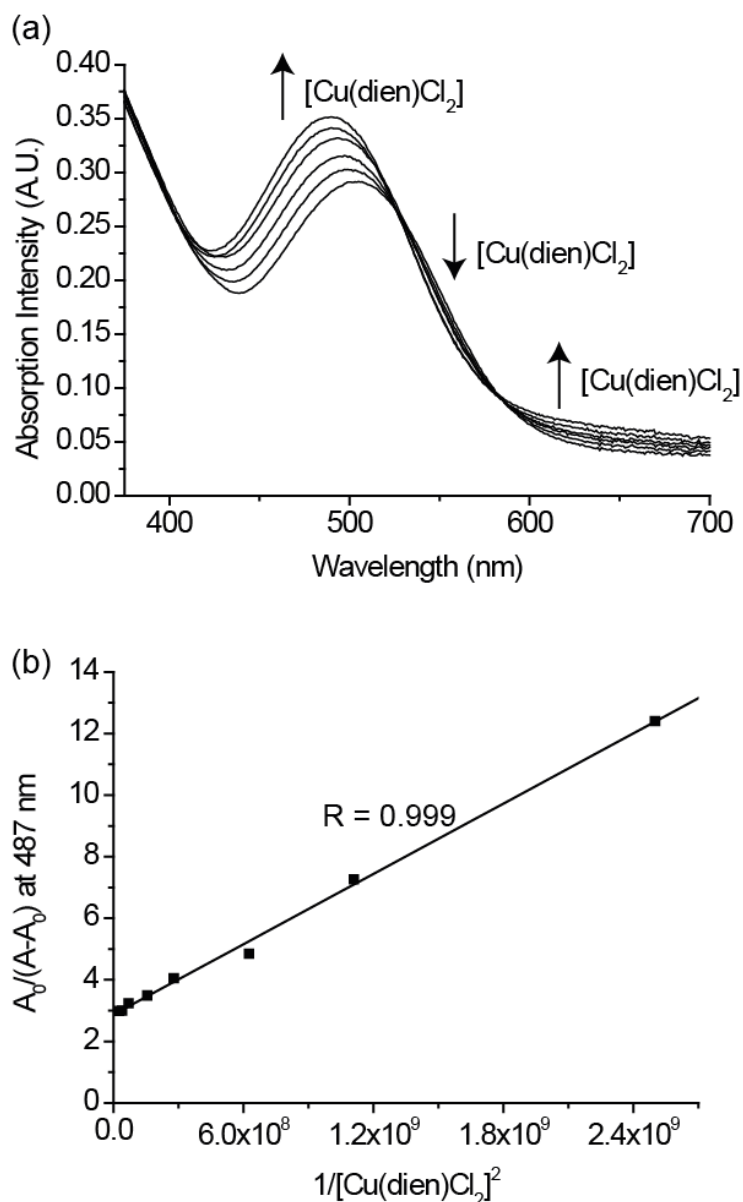


Figure 3.10 (a) UV-vis spectroscopic titrations of $K_2[Fe^{II}(4Bubpy)(CN)_4]$ by $Cu^{II}(dien)Cl_2$ (b) The best fitted 1:2 Benesi-Hildebrand equation with $A_0/(A-A_0)$ versus $1/\{[Cu^{II}(dien)Cl_2]\}^2$ plot at 487 nm. The slope and y-intercept are 3.80×10^{-9} M and 2.88 respectively, with $\log K = 4.44 \pm 0.001$ M⁻¹. The solvated form of the complex is deduced as 1:2 ratio of $[Fe^{II}:Cu^{II}]$. All the titrations were performed in aqueous DMF (1:1 v/v) (1.50 mL of aqueous HEPES buffer at pH 7.4 + 1.50 mL of DMF) at 298 K.

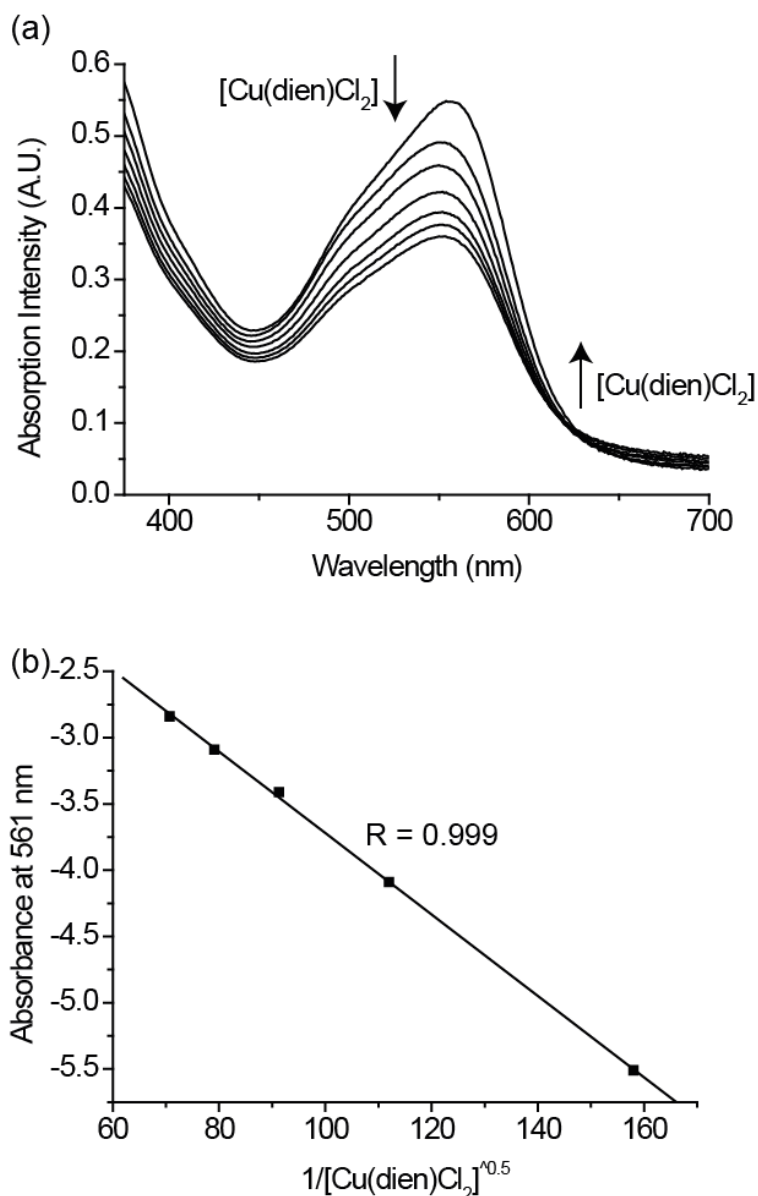


Figure 3.11 UV-vis spectroscopic titrations of $\text{Fe}^{\text{II}}(\text{tBubpy})_2(\text{CN})_2$ by $\text{Cu}^{\text{II}}(\text{dien})\text{Cl}_2$ (b) The slope and y-intercept of the best fitted $A_0/(A-A_0)$ versus $1/\{[\text{Cu}^{\text{II}}(\text{dien})\text{Cl}_2]^{0.5}\}$ plot are $-3.07 \times 10^{-2} \text{ M}$ and 6.51×10^{-1} respectively with $\log K = 2.65 \pm 0.001 \text{ M}^{-1}$ at 561 nm. Curve was fitted by the ratio 0.5:1 Benesi-Hildebrand equation with good linear relationship, the solvated form of the complex is deduced as 1:2 ratio of $[\text{Fe}^{\text{II}}:\text{Cu}^{\text{II}}]$. All the titrations were performed in aqueous DMF (1:1 v/v) (1.50 mL of aqueous HEPES buffer at pH 7.4 + 1.50 mL of DMF) at 298 K.

Table 3.2 Binding constant (log K) and Gibbs free energy change for the formation of complexes **FeCu 1 – 4**.

	Fe ^{II} subunit	log K^a	$\Delta G^{0a}/\text{kJ mol}^{-1}$
FeCu 1	$\text{K}_2[\text{Fe}^{\text{II}}(\text{}^t\text{Bubpy})(\text{CN})_4]$	4.72	-27.0
FeCu 2	$\text{K}_4[\text{Fe}^{\text{II}}(\text{CN})_6]$	5.32	-30.4
FeCu 3	$\text{K}_2[\text{Fe}^{\text{II}}(\text{}^t\text{Bubpy})(\text{CN})_4]$	4.44	-25.3
FeCu 4	$\text{Fe}^{\text{II}}(\text{}^t\text{Bubpy})_2(\text{CN})_2$	2.65 ^b	-15.1 ^b

Binding strengths were measured by means of UV spectroscopic titrations and was calculated by using the ^a1:2 and ^b2:1 Benesi–Hildebrand equation. The titrations were conducted in aqueous DMF (1:1, v/v; aqueous HEPES buffer (1.50 mL, pH 7.4)+DMF (1.50 mL)) at 298 K.

3.3.3 Chemodosimetric Responses of **FeCu 1** toward Cyanide and Different Anions

Addition of cyanide anion into an aqueous DMF solution of **FeCu 1** shifted the MLCT transition from 498 nm to 523 nm with a significant decrease of absorption intensity. Figure 3.12 shows the restoration of $[\text{Fe}(\text{tBubpy})(\text{CN})_4]^{2-}$ characteristic spectroscopic properties for a mixture of **FeCu 1** and cyanide in DMF solution. Figure 3.13 summarizes the UV-vis spectroscopic titrations for **FeCu 1** with common anions (CN^- , SO_4^{2-} , HCO_3^- , HPO_4^{2-} , N_3^- , CH_3COO^- , NCS^- , NO_3^- , and Cl^-). Only cyanide produces a colorimetric response of **FeCu 1** among these anions.

Through the UV-vis spectroscopic methods, the method detection limit (MDL) of **FeCu 1** toward cyanide was found to be 0.5 ppm using the Hubaux and Vos method.¹⁵⁶ From Figure 3.14 and Figure 3.15, semi-quantitative analysis of cyanide by the naked eye was about 16 ppm and can be used to distinguish from other common anions.

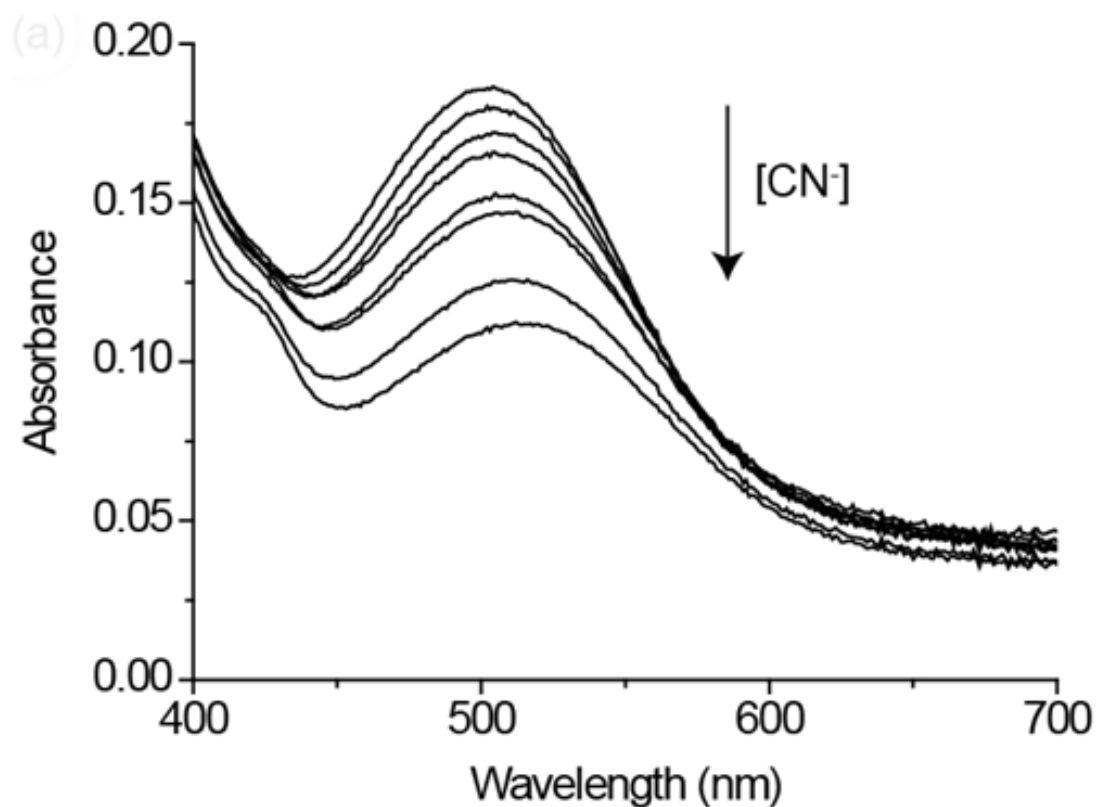


Figure 3.12 UV-vis spectroscopic titration of **FeCu 1** (5.0×10^{-5} M) with CN^- (0 to 2.0×10^{-4} M). All spectra were obtained in aqueous DMF (1:1 v/v, 1.50 mL of aqueous HEPES buffer at pH 7.4 + 1.50 mL of DMF) at 298 K.

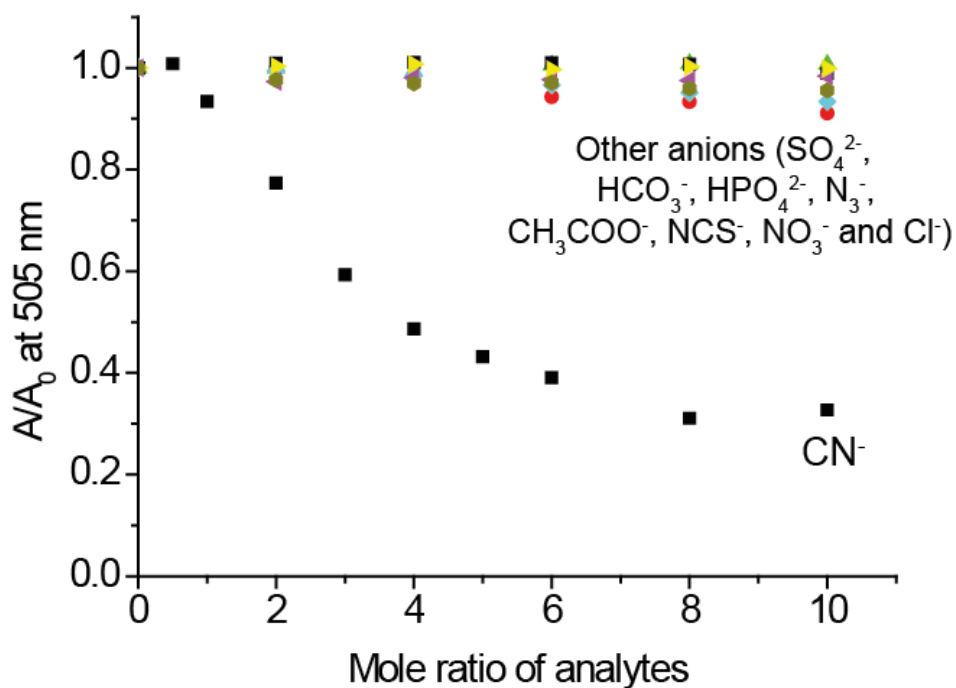


Figure 3.13 Summary of UV-vis spectroscopic titrations for **FeCu 1** (2.0×10^{-4} M) with the anions monitored as a function of the decrease in absorbance (A/A_0) at 505 nm. All titrations were carried out in aqueous DMF (1:1 v/v, 1.50 mL of aqueous HEPES buffer at pH 7.4 + 1.50 mL of DMF) at 298 K.

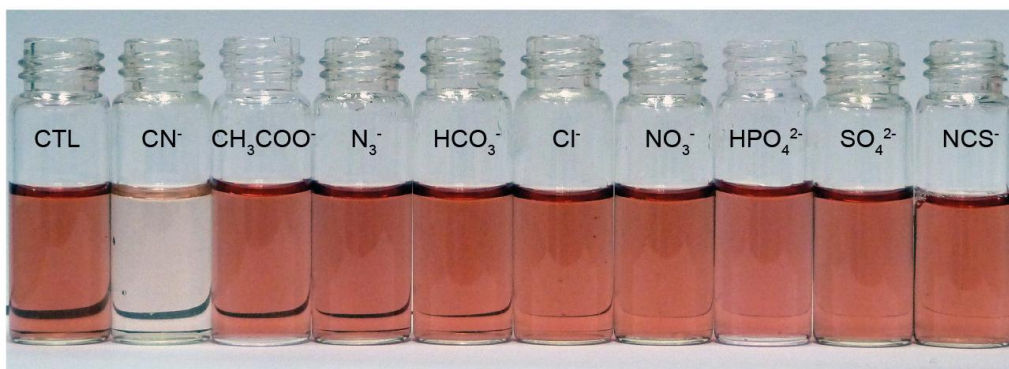


Figure 3.14 Photographs of the colorimetric responses of **FeCu 1** (2.0×10^{-4} M) toward common anions (2.0×10^{-4} M) in aqueous DMF (1:1 v/v, 1.50 mL of aqueous HEPES buffer at pH 7.4 + 1.50 mL of DMF) at 298 K: (CTL = control, **FeCu 1** alone).

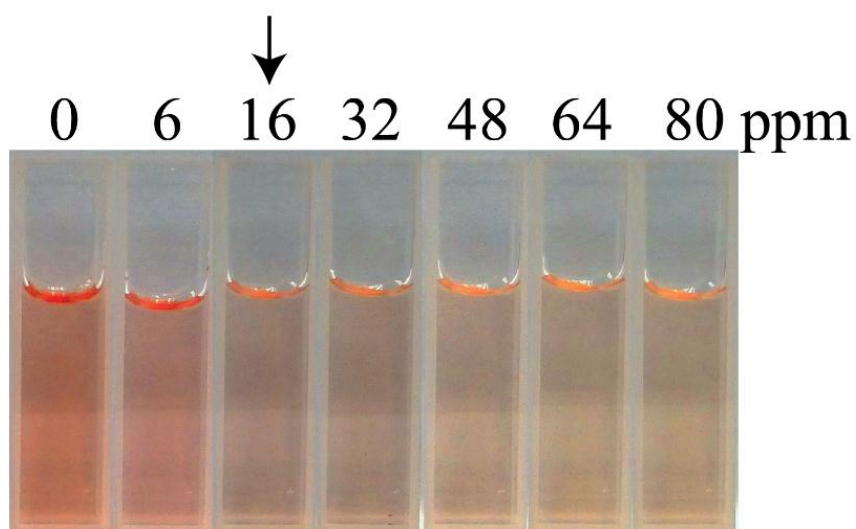


Figure 3.15 Photographs of colorimetric response for **FeCu 1** to cyanide in aqueous DMF (1:1 v/v, 1.50 mL of aqueous HEPES buffer at pH 7.4 + 1.50 mL of DMF) at 298 K. Visual detection limit was about 16 ppm.

3.3.4 Binding Constant and Binding Mechanism of **FeCu 1** with Cyanide

Binding constant between **FeCu 1** and CN^- was found by spectroscopic titrations. A series of solutions with fixed concentration of complexes were titrated with varies cyanide concentrations (0 to 2.0×10^{-4} M) in aqueous DMF at 298 K and with pH 7.4 HEPES buffer solution. The binding stoichiometry of **FeCu 1** and cyanide were analyzed by the 1:2 Benesi–Hildebrand equation (the detail mathematic derivation is discussed in chapter 2). Table 3.3 summarizes the binding constants and Gibbs free energy (ΔG°) between Fe^{II} and Cu^{II} of **FeCu 1** as well as the adducts between cyanide and $\text{Cu}^{\text{II}}(\text{dien})^{2+}$. The results show that except cyanide, the $\text{K}_2[\text{Fe}^{\text{II}}(\text{tBubpy})(\text{CN})_4]$ form most stable adduct with $[\text{Cu}^{\text{II}}(\text{dien})]^{2+}$ with the most negative ΔG° value (-30.4 kJmol^{-1}). Therefore only introduction of cyanide into these three bimetallic systems would cause cyanide bridge cleavage and formation of more stable $[\text{Cu}^{\text{II}}(\text{dien})(\text{CN})]^+$ adducts.

A mixture of **FeCu 1** and cyanide was analyzed by electrospray-MS, as shown in Figure 3.16. The presence of $[\text{Fe}(\text{tBubpy})(\text{CN})_4]^{2-}$ (m/z 467.1 $[\text{M} + \text{K}]^-$) in the mixture suggests that cyanide bridges between Fe^{II} and Cu^{II} in **FeCu 1** are cleaved when Cu^{II} centers bind cyanide.

Table 3.3 Binding constants ($\log K$) and Gibbs free energy changes (ΔG^0) for the complexation of various anions and $K_2Fe^{II}(^tBubpy)(CN)_4$ by $[Cu^{II}(dien)(ClO_4)](ClO_4)$.^a

	Acceptor	Donor	$\log K^a$	ΔG^0 ^a / kJmol^{-1}
1	$[Cu^{II}(dien)(ClO_4)](ClO_4)$	CN^-	6.64	-37.9
2	$[Cu^{II}(dien)(ClO_4)](ClO_4)$	$K_2[Fe^{II}(^tBubpy)(CN)_4]$	4.72 ^b	-27.0 ^b
3	$[Cu^{II}(dien)(ClO_4)](ClO_4)$	SO_4^{2-}	4.67	-26.6
4	$[Cu^{II}(dien)(ClO_4)](ClO_4)$	HCO_3^-	3.72	-21.2
5	$[Cu^{II}(dien)(ClO_4)](ClO_4)$	$HC_2O_4^-$	3.59	-20.5
6	$[Cu^{II}(dien)(ClO_4)](ClO_4)$	HPO_4^{2-}	2.60	-14.8
7	$[Cu^{II}(dien)(ClO_4)](ClO_4)$	N_3^-	2.26	-12.9
8	$[Cu^{II}(dien)(ClO_4)](ClO_4)$	CH_3COO^-	1.77	-10.1
9	$[Cu^{II}(dien)(ClO_4)](ClO_4)$	NCS^-	1.72	-9.8
10	$[Cu^{II}(dien)(ClO_4)](ClO_4)$	NO_3^-	0.35	-2.0
11	$[Cu^{II}(dien)(ClO_4)](ClO_4)$	Cl^-	0.35	-2.0

^a $\log K$ and ΔG^0 data are cited from reference. ^bBinding strengths were measured by UV spectroscopic titration and calculated using the 1:2 Benesi-Hildebrand equation. All the titrations were conducted in aqueous DMF (1:1 v/v) (1.50 mL of aqueous HEPES buffer at pH 7.4 + 1.50 mL of DMF) at 298 K.

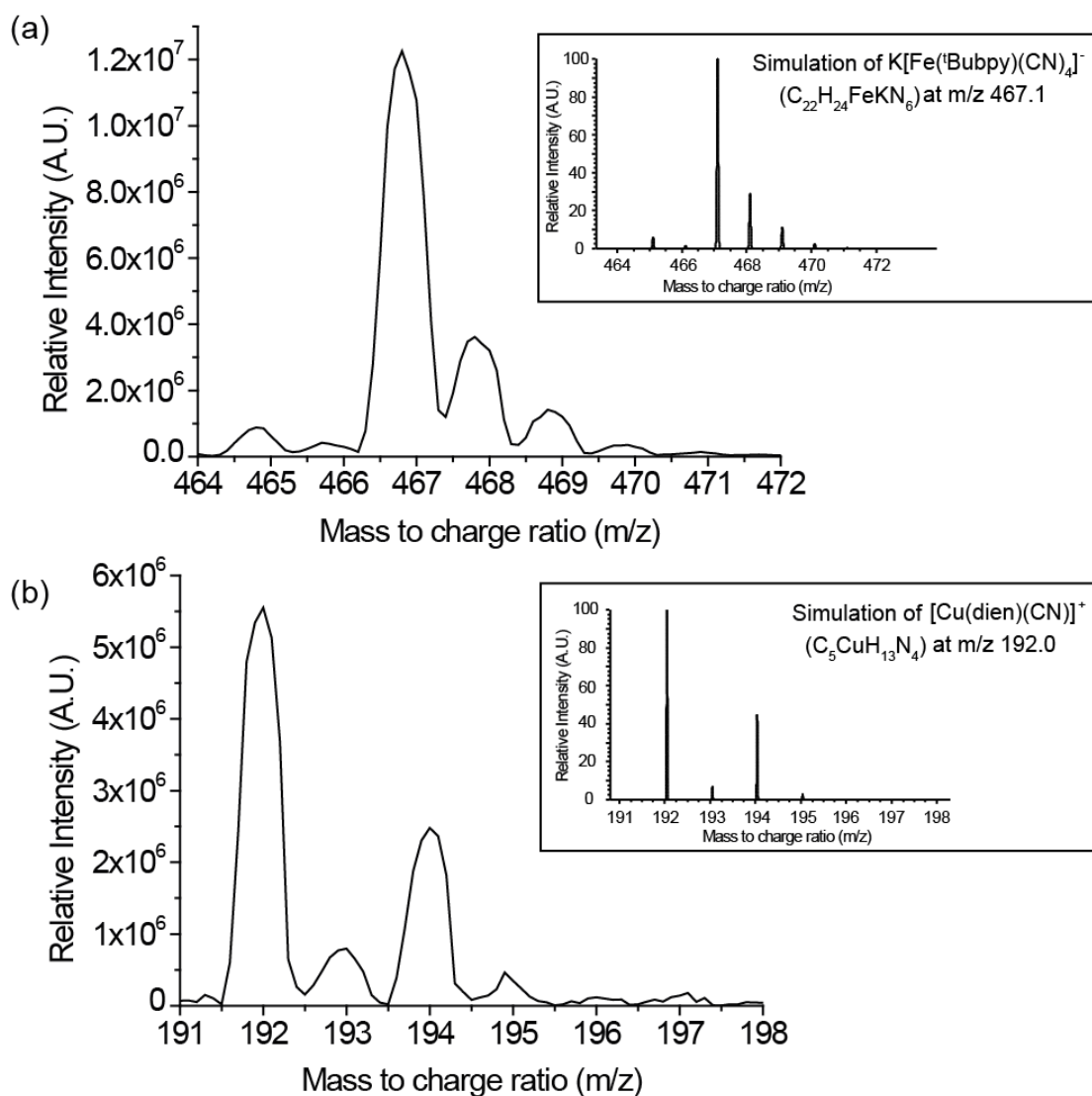


Figure 3.16 Electro spray mass spectra of “FeCu 1-cyanide-mixture”: and (*inset*) the simulation of (a) $\{K[Fe^{II}(tBubpy)(CN)_4]\}^-$ (m/z 467.1) and (b) $[Cu^{II}(dien)(CN)]^+$ (m/z 192.0). The mass spectra were performed in methanol.

3.3.5 Elimination of Cyanide by catalytic oxidation with **FeCu 1** as the catalyst

Hydrogen peroxide can oxidize copper or other weakly complexed metal cyanide and forming less toxic cyanate:⁹²



The copper subunit in **FeCu 1** is supposed to be catalyst for cyanide oxidation. The mechanism of catalytic oxidation of cyanide to cyanate with **FeCu 1** was studied with different working conditions (Figure 3.17). With the presence of **FeCu 1** and H_2O_2 , the concentration of cyanide decreased rapidly in the first 90 min [Figure 3.17 curve (\blacktriangle)] with resulting increase of cyanate concentration, and cyanate concentration reached its maximum at 180 min [Figure 3.17 curve (\blacksquare)]. The cyanide consumption is disproportionate to cyanate formation at first 180 min, where cyanide first forming Cu-cyanide adduct and then cyanogen as shown below:²¹⁴



The copper(II) ions released from **FeCu 1** were first reduced to copper(I) with the formation of cyanogen, which then complex with the copper ion to form $\text{Cu}(\text{CN})_2$. The cyanogen is then subsequently oxidized into cyanate. These stepwise reactions result in the time lag between cyanide consumption and cyanate formation.

A similar experiment was conducted with the absence of **FeCu 1**, where both concentrations of cyanide and cyanate remained unchanged after 240 min of treatment [Figure 3.17 curve (Δ) and (\square)]. This catalytic property of **FeCu 1** that oxidizes cyanide to the much less toxic cyanate is due to the release of the $[\text{Cu}(\text{dien})]^{2+}$ catalyst in the presence of H_2O_2 .²¹⁴⁻²¹⁷ Figure 3.18 demonstrates the repeatability for the oxidation of cyanide to cyanate by **FeCu 1**. The repeatability was examined by recycling the catalyst four times and the efficiency was found to be $> 99.0\%$.

The cyanide oxidation to cyanate by **FeCu 2 – 4** with H_2O_2 as the oxidant were also investigated and result were summarizes in Figure 3.19 . The complexes **FeCu 2**(♦), **FeCu 3** (■), and **FeCu 4** (▲) when mixed with cyanide and H_2O_2 in a mole ratio of 1:10:65, showed similar catalytic properties in oxidizing cyanide into cyanate with control experiments [without H_2O_2 (●)/without complexes (▼)] no cyanide was oxidized to cyanate throughout the 150 min period.

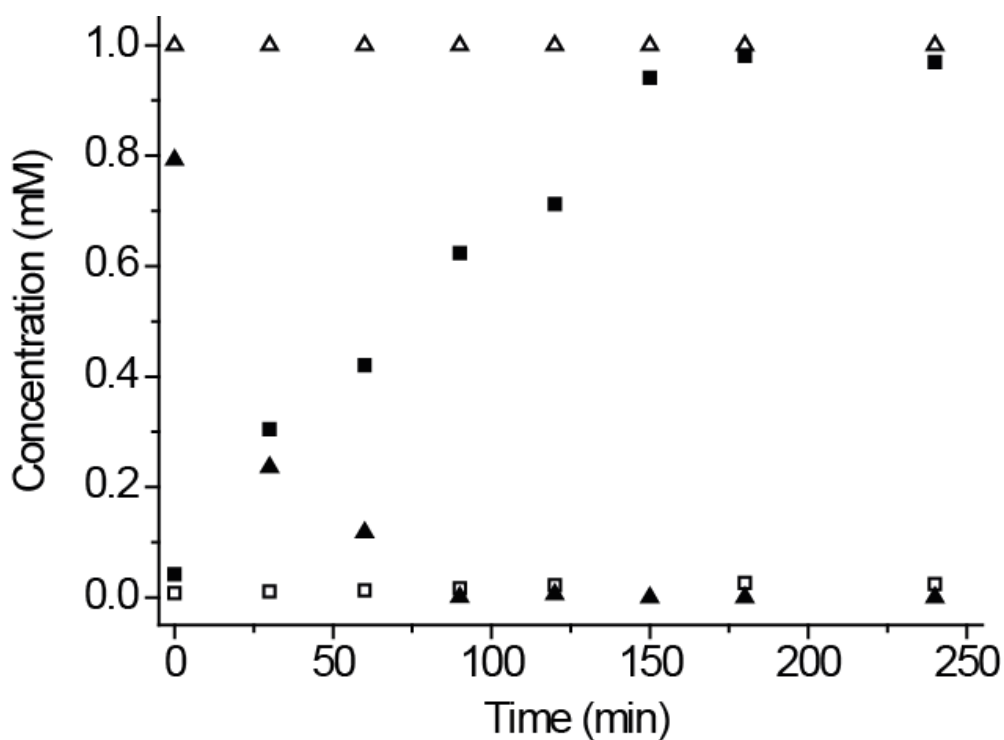


Figure 3.17 Cyanide (▲) and cyanate (■) concentration during the presence of **FeCu 1** (1.00×10^{-4} M) and cyanide (△) and cyanate (□) concentration in the absence of **FeCu 1**. The initial concentrations of cyanide and cyanate were 1.0 and 0 mM, respectively. All experiments were performed in DI water with H_2O_2 (6.53×10^{-4} M) at room temperature under an open atmosphere.

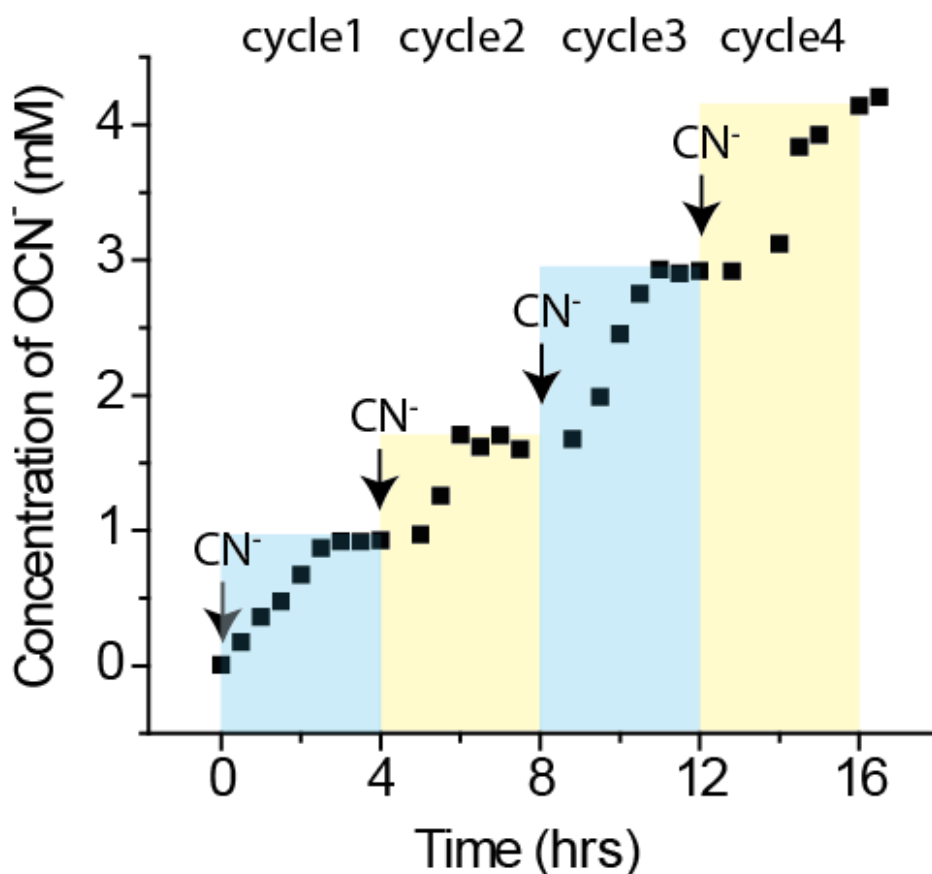


Figure 3.18 Repeatability of performance in oxidation of cyanide by **FeCu 1** (1.00×10^{-4} M) with H_2O_2 (6.53×10^{-3} M) with concentration of cyanate plotted as a function of the reaction time. The initial concentration of cyanide was 1.0 M and at every subsequent 4 hours additional cyanide (each addition as 1.00×10^{-3} M) was added. All experiments were conducted in DI water, in a dark at room temperature and under an open atmosphere.

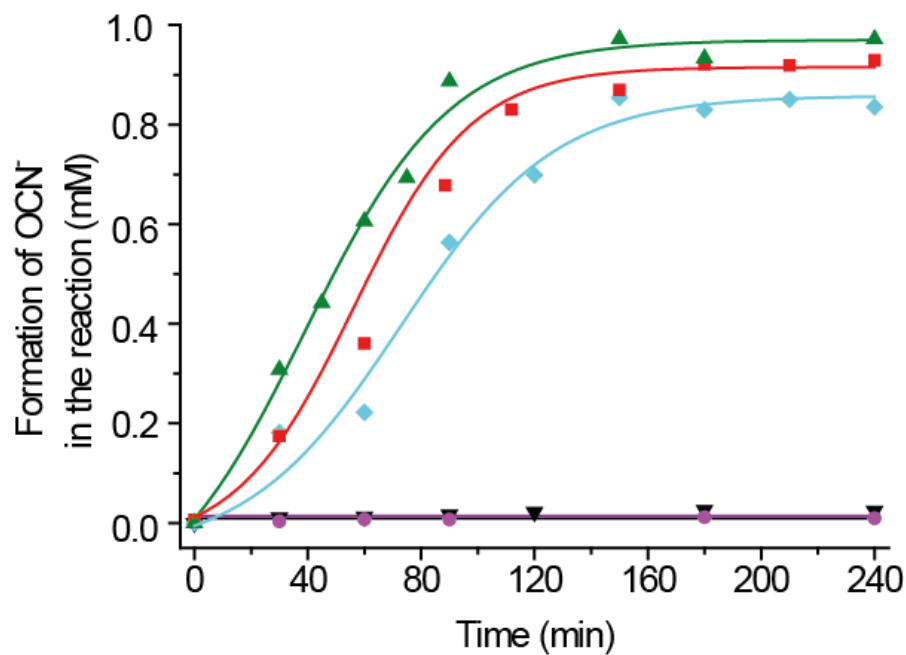


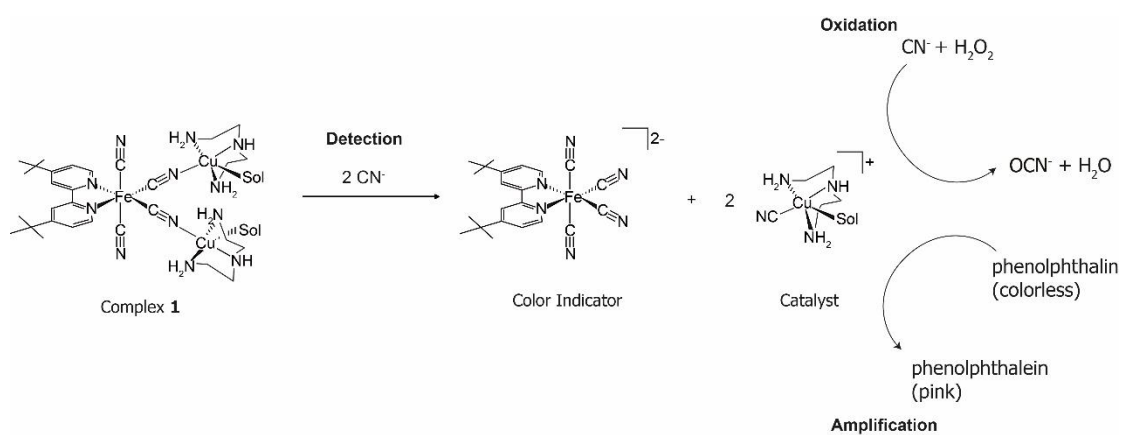
Figure 3.19 Formation of cyanate from the oxidation of cyanide (1 mM) in the presence of **FeCu 2** (\blacklozenge), **FeCu 3** (\blacksquare), and **FeCu 4** (\blacktriangle) against time. The formation of cyanate is ignorable in the absence of H_2O_2 (\bullet) or catalyst (\blacktriangledown). All the experiments were performed with cyanide, H_2O_2 and the $\text{Cu}^{\text{II}}(\text{dien})^{2+}$ of **FeCu 2**, **FeCu 3**, or **FeCu 4** in the mole ratio 10:65:1 at room temperature under and open to atmosphere.

3.3.6 Catalytic Signal Amplification by **FeCu 1** in Cyanide Detection

To amplify the colorimetric cyanide detection signal of **FeCu 1**, oxidation of phenolphthalin by Cu^{II} was applied. The signaling mechanism of **FeCu 1** is proposed in Scheme 3.7. The presence of cyanide cleaves the cyanide bridge in **FeCu 1** resulting in the release of $[\text{Cu}(\text{dien})]^{2+}$ (catalyst), which sequentially catalyzes the oxidation of phenolphthalin to phenolphthalein,²¹⁷ and develops a more contrasting pink color (λ_{abs} at 551 nm), resulting in a sharp magnified color change as shows in Figure 3.20.

The **FeCu 1** added in the amplifying testing solutions were 80-fold lower (2.0×10^{-4} to 2.50×10^{-6} M) than the non-amplifying one, which give a nearly clear control solution. When initial cyanide concentration as low as 0.4 ppm is introduced, a naked-eye detectable responses is induced, which is around 80-fold lower than the visual detection before amplification. Spectroscopic titration of **FeCu 1** with cyanide had a suitably linear dynamic range of 0–2000 ppb of cyanide as shown in Figure 3.21 with a MDL of 9.5 ppb estimated by the Hubaux and Vos method¹⁵⁶.

To investigate the selectivity of **FeCu 1** after amplification, various anions (4 molar equivalents of CN^- , 40 molar equivalents of SO_4^{2-} , NO_3^- , PO_4^{3-} , N_3^- , CH_3COO^- , NCS^- , NO_3^- , and Cl^-) were used as interferences in titrations with **FeCu 1**. The results are summarized in Figure 3.22. Only the solutions containing cyanide show significant spectroscopic changes.



Scheme 3.7 Proposed cyanide detection, signaling, and oxidation mechanism by **FeCu 1**.

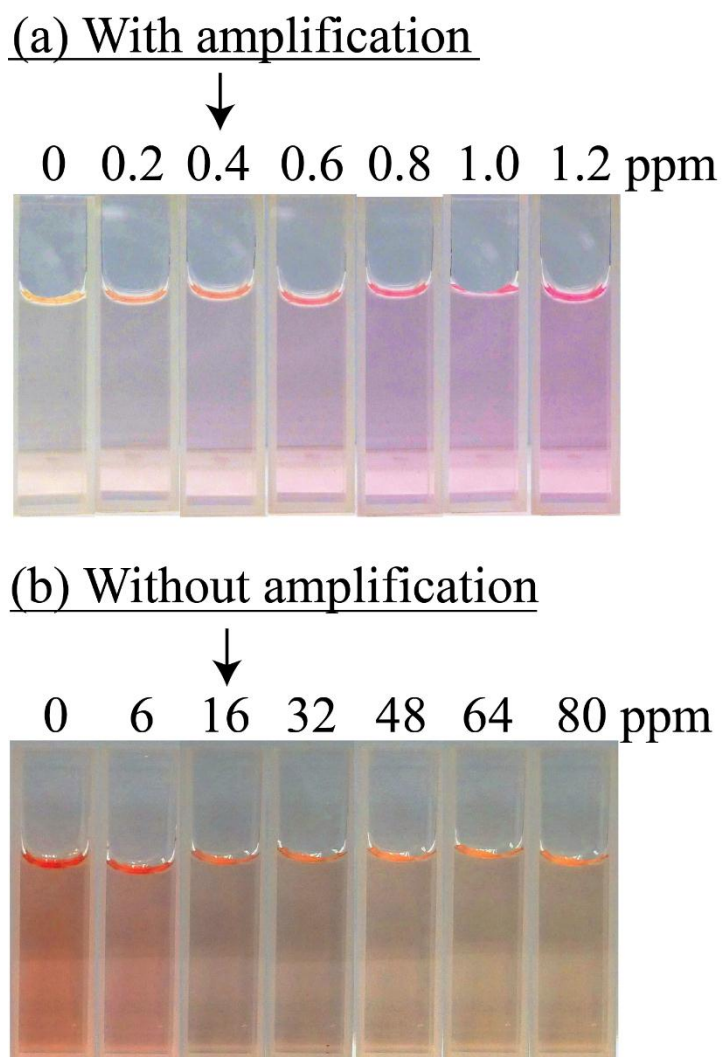


Figure 3.20 Photographs of colorimetric response for **FeCu 1** to cyanide (a) with and (b) without addition of phenolphthalin in aqueous DMF (1:1 v/v, 1.50 mL of aqueous HEPES buffer at pH 7.4 + 1.50 mL of DMF) at 298 K. Visual detection limits (a) after and (b) before signal amplification were about 0.4 and 16 ppm, respectively.

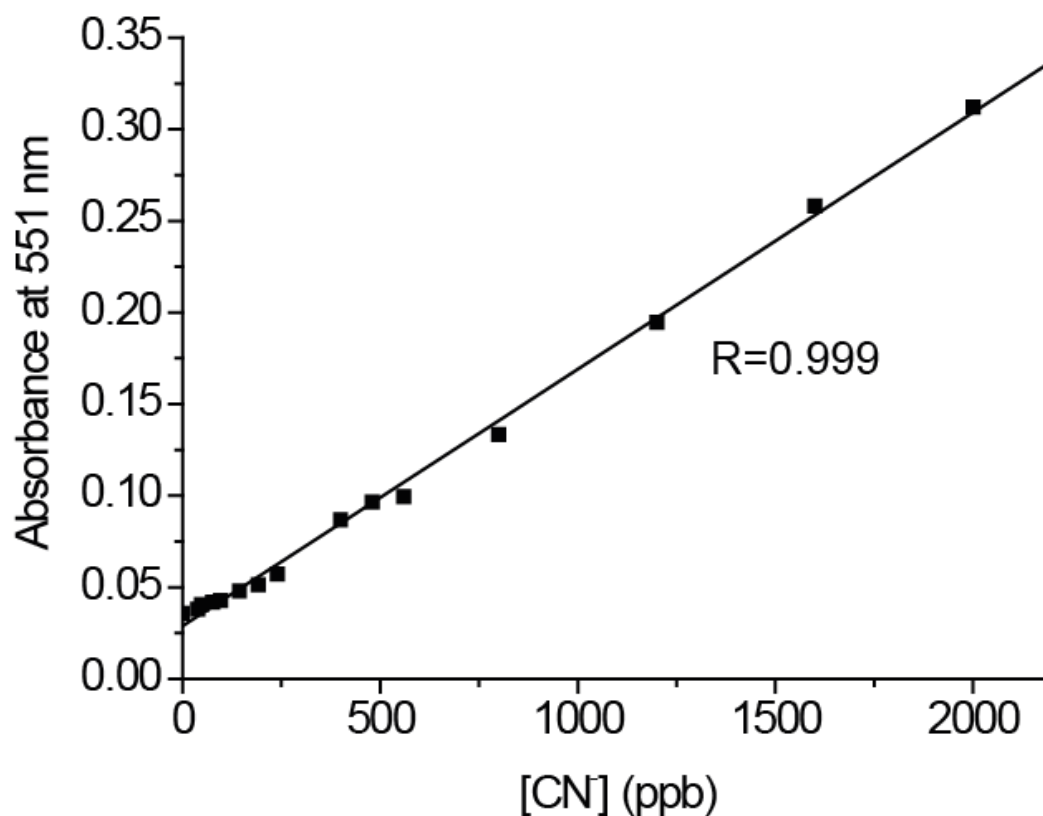


Figure 3.21 Linear curve developed from the UV–vis spectroscopic titrations (absorbance at 551 nm) of **FeCu 1** (2.50×10^{-6} M) with addition of phenolphthalin (1:10 mol/mol) towards increasing concentration of cyanide (0 to 2000 ppb). The slope and y-intercept are 1.40×10^{-4} and 2.89 ppb respectively. All titrations were carried out in pH 14 aqueous solution at room temperature.

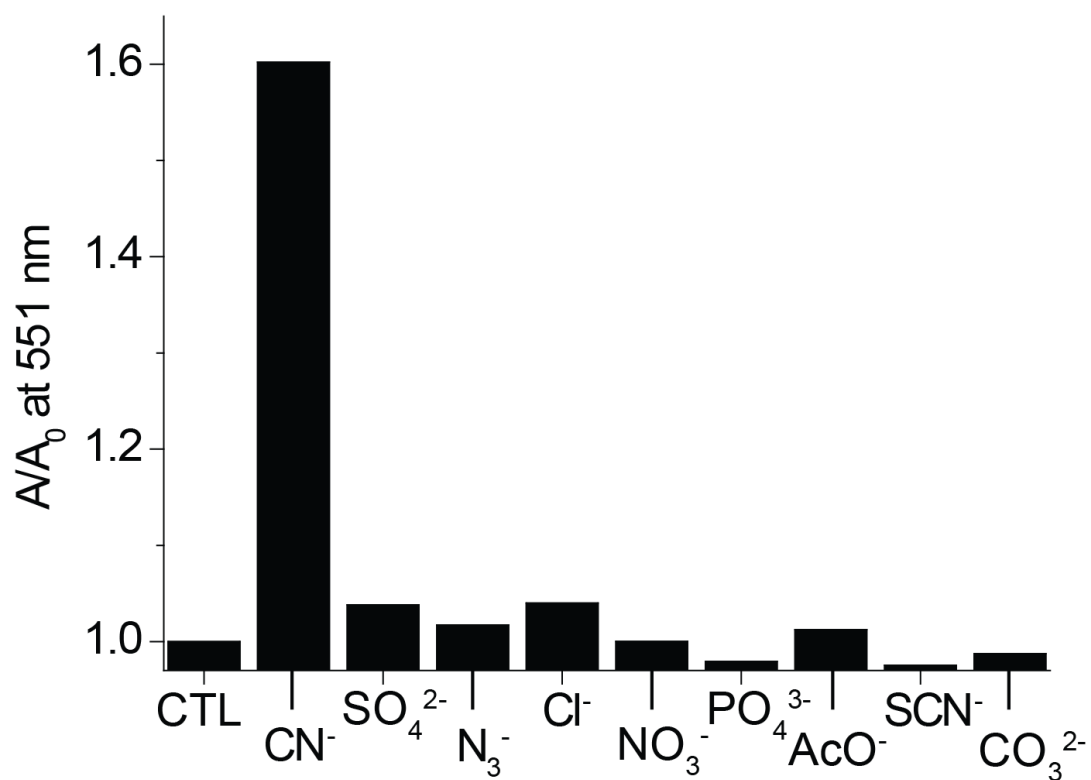


Figure 3.22 Summary of UV-vis spectroscopic titrations (A/A_0 at 551 nm) of **FeCu 1** (2.5×10^{-6} M) with various anions, except cyanide in 4 molar equivalents, 40 molar equivalents of anions were added respectively. All experiments were carried out at room temperature in aqueous solutions at pH 14. (CTL = control)

3.3.7 Application of **FeCu 1** to Practical Water Samples

Verification of **FeCu 1** application to practical environmental situations was investigated by applying **FeCu 1** to real water samples. Four kinds of water samples (tap, lake, river, and underground water) were collected in Hong Kong. Samples were filtered through 0.45 μm pore-size membrane filters (Pall Corporation) to remove insoluble substances and used without further treatment. Table 3.4 summarizes the results of detection, signal amplification, and photo-degradation of cyanide by **FeCu 1** for water samples.

Spectroscopic detections of cyanide in water samples were done by spiking 0.60 ppm of cyanide into all samples and the spiked cyanide concentrations were determined by **FeCu 1** with its calibration curve developed under the same working conditions. The analytical results show good recovery and relative standard deviation (RSD, %) as 93.9–105.9% and 5.72–10.61%, respectively. These results indicate that trivial organic and inorganic substrates in water samples do not affect the function of **FeCu 1** as a chemodosimeter.

Oxidation of cyanide by **FeCu 1** with assistance from H_2O_2 was also studied in water samples. All the samples were spiked with 1mM cyanide. With the addition of **FeCu 1** and H_2O_2 , the cyanate content of the samples increased rapidly and reached a maximum within 210 min. The results indicate that **FeCu 1** functions effectively as a catalyst in the oxidation of cyanide to less toxic cyanate in practical water samples.

Small amounts of cyanide were added to tap (48 ppb), lake (48 ppb), underground (150 ppb), and river (150 ppb) water samples, and the samples were analyzed following the addition of **FeCu 1** and phenolphthalin in a 1:100 mole ratio. The concentrations of cyanide in water samples were determined and analyzed with a developed calibration curve. The results show that **FeCu 1** achieves an excellent recovery (87.0–109.4%) with good RSD (3.22–11.38%), demonstrating the suitability and practicality of **FeCu 1** for cyanide detection in drinking water with a maximum allowable level of 50–200 ppb suggested by world health organization (WHO).²¹⁸

Table 3.4 Results for cyanide detection/oxidation/signal amplification in tap, lake, river, and underground water samples by complex 1.

Cyanide Detection				
Water samples	Cyanide added (ppm)	Cyanide found (ppm)	Recovery (%)	RSD (%)
tap	0.60	0.56 ± 0.03	93.9	5.72
lake	0.60	0.65 ± 0.05	105.9	8.48
river	0.60	0.62 ± 0.07	103.7	10.61
underground	0.60	0.63 ± 0.05	104.6	7.72
Cyanide Detection with Signal Amplification Process				
Water samples	Cyanide added (ppb)	Cyanide found (ppb)	Recovery (%)	RSD (%)
tap	48.0	52.5 ± 5.0	109.4	9.59
lake	48.0	48.6 ± 1.6	101.3	3.22
river	150.0	130.5 ± 14.9	87.0	8.31
underground	150.0	139.4 ± 11.6	92.9	11.38
Cyanide Elimination				
Water samples	Cyanide added (mM)	Cyanate generated (mM)	Recovery (%)	
tap	1.00	0.96	95.9	
lake	1.00	0.95	95.0	
river	1.00	0.95	94.5	
underground	1.00	1.03	86.5	

3.4 Kinetic Investigations of Catalyst Displacement Assay with **FeCu 2-4**

Two kinetic studies of the bimetallic complexes were investigated. Firstly, the rate of cyanide bridge cleavage in between the Fe^{II} donor and Cu^{II} acceptor of the bimetallic systems by cyanide was investigated. Data obtained were analyzed using pseudo-first order technique. For this cyanide bridge cleavage measurement, the rate law for the cleavage can be written as equation 3.1, where the brackets around a chemical species refer to concentration of that species in the mixture depend on time:

$$\frac{d[FeCu]}{dt} = -k[FeCu][CN^-] \quad (3.1)$$

$$\frac{d[FeCu]}{dt} = -k_{obs}[FeCu] \quad (3.2)$$

$$k' = k[CN^-]_o \quad (3.3)$$

With cyanide in excess of the **FeCu 2-4** complexes, the rate law can be expressed in the pseudo-first-order form of equation 3.2, where k' is defined by equation 3.3 and can be assumed constant. The kinetic plot of the apparent association rate constant k_{obs} (s^{-1}) versus cyanide concentration were shown in Figure 3.23, where the k' were calculated from the slopes of the curves. The rate constants of cyanide bridge cleavage in **FeCu 2**, **FeCu 3**, and **FeCu 4** complexes were found as 18.8, 32.0 and 58.3 $M^{-1}s^{-1}$, respectively. Which is in line with the decrease of ΔG^0 of the formation of complexes (Table 3.2).

According to Sarla *et al.* work, the oxidation of cyanide to cyanate with assist of H_2O_2/Cu^{2+} was calculated to be $249.5 M^{-1}s^{-1}$.²¹⁵ The results revealed that the cleavage of cyanide bridges was the rate-determining step in the overall CDA process rather than the oxidation process. Therefore, we believe that not only the thermodynamic properties, but also the kinetic properties of the systems affect the initiation of the catalytic properties.

Figure 3.24 summarizes the cyanate formation in solutions with different initial cyanide concentrations. Concentrations of the complexes and H_2O_2 were same under different cyanide working solutions. However, oxidation processes only occurred in solutions when cyanide

concentrations reached the thresholds (0.2 mM for **FeCu 2**, 0.1 mM for **FeCu 3**, and 0.02 mM for **FeCu 4**). These results revealed that in addition to thermodynamic properties, kinetic properties also affect the breakage of cyano-bridges and the release of Cu^{II} catalysts. Mechanism for the latent catalyst to catalyze the oxidation process is proposed in Scheme 3.8.

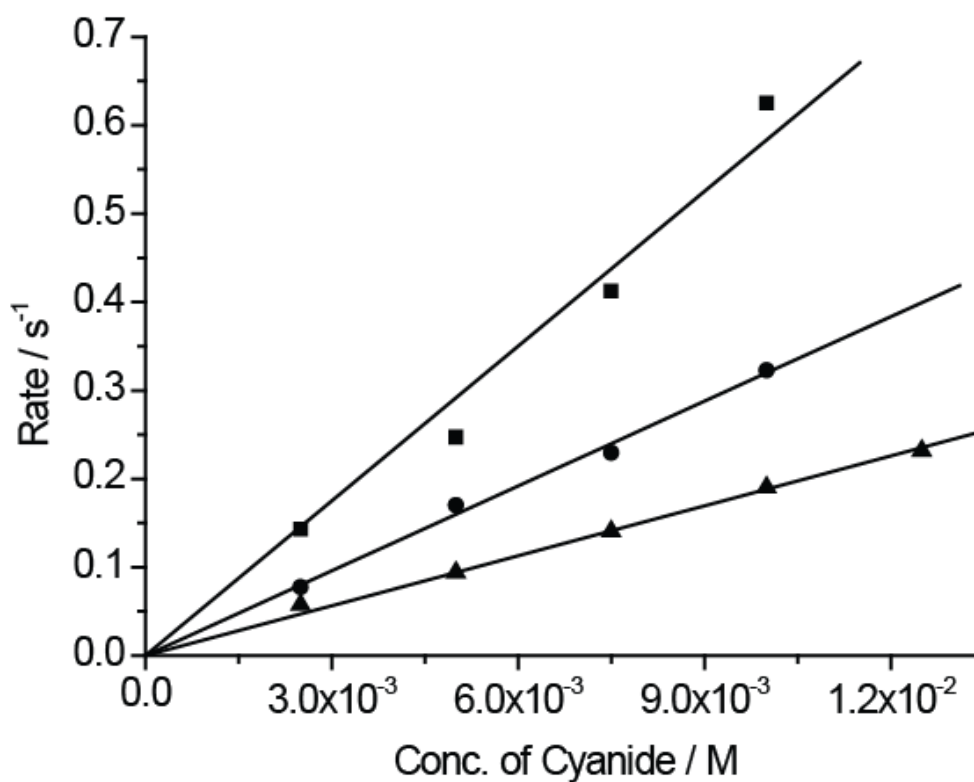


Figure 3.23 Kinetic plot of apparent association rate constant k_{obs} (s^{-1}) versus cyanide concentration. The rate constant values (**FeCu 2** (▲) = $18.8 M^{-1}s^{-1}$, **FeCu 3** (●) = $32.0 M^{-1}s^{-1}$, and **FeCu 4** (■) = $58.3 M^{-1}s^{-1}$) were calculated from the slopes of the curves ($y=mx$).

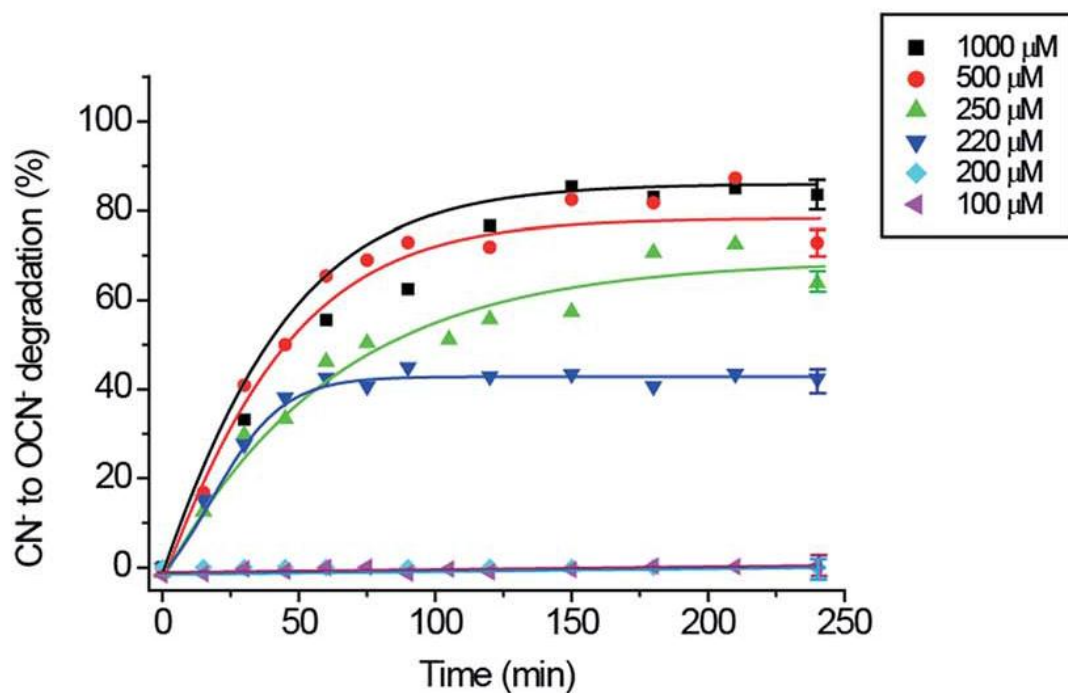


Figure 3.24a Formation of cyanate in the presence of **FeCu 2** (0.1 mM) with respect to the different initial concentration of cyanide (100 to 1000 μM) against time. All the experiments were performed with H_2O_2 (6.53mM) and the $\text{Cu}^{\text{II}}(\text{dien})^{2+}$ of **FeCu 2** in the mole ratio 65:2 at room temperature under an open atmosphere.

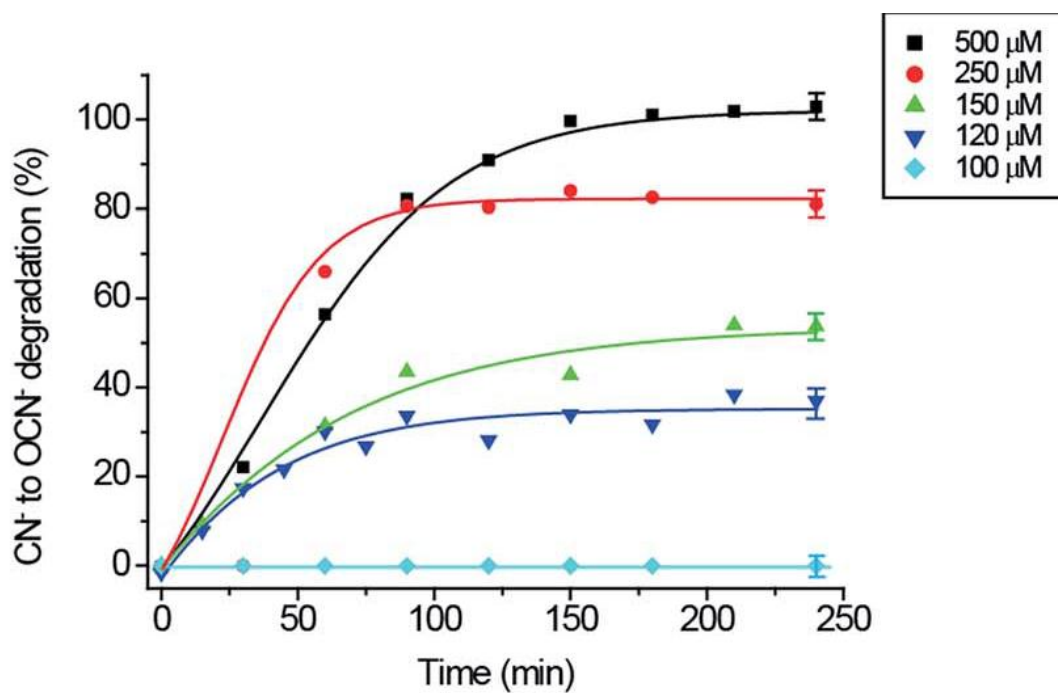


Figure 3.24b Formation of cyanate in the presence of **FeCu 3** (0.1 mM) with respect to the different initial concentration of cyanide (100 to 500 μM) against time. All the experiments were performed with H_2O_2 (6.53mM) and the $\text{Cu}^{\text{II}}(\text{dien})^{2+}$ of **FeCu 3** in the mole ratio 65:2 at room temperature under an open atmosphere.

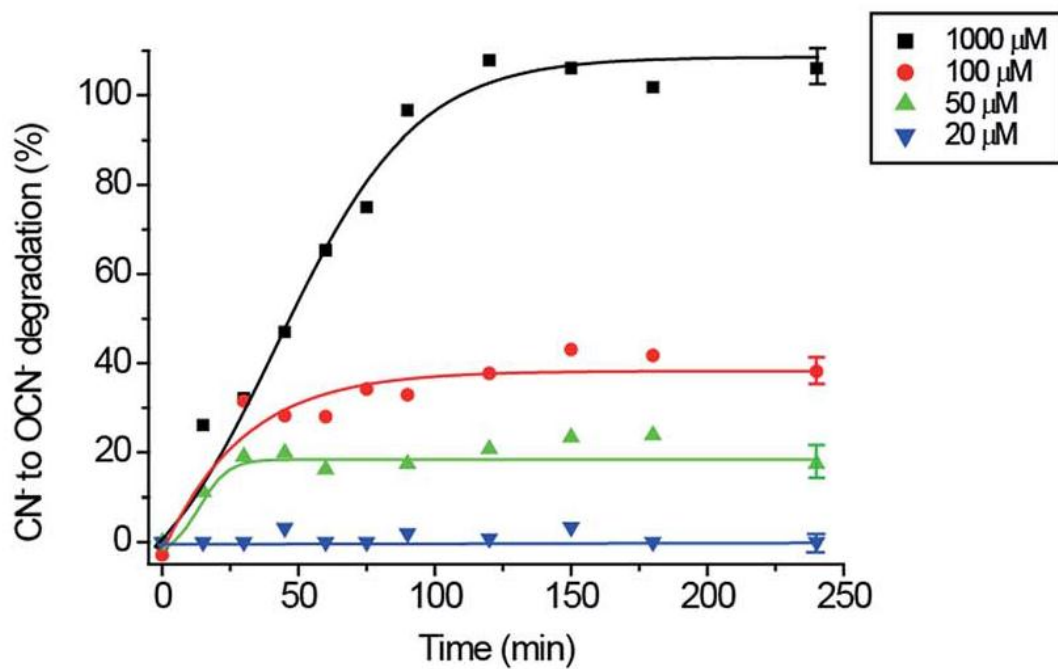
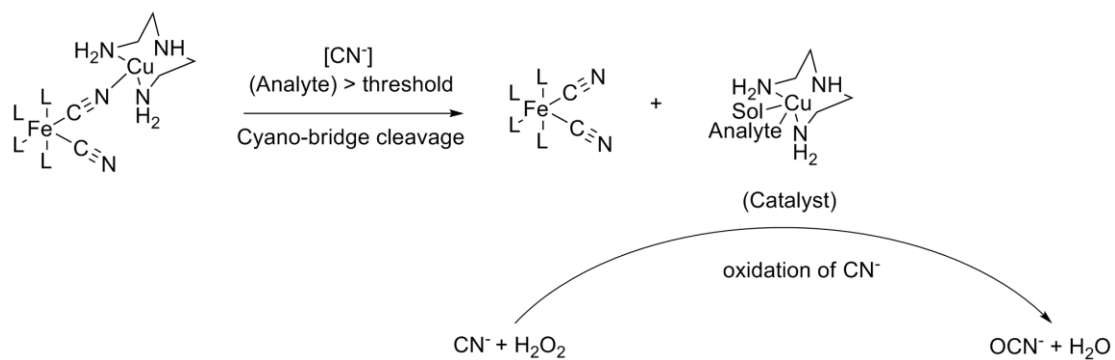


Figure 3.24c Formation of cyanate in the presence of **FeCu 4** (0.2 mM) with respect to the different initial concentration of cyanide (20 to 1000 μM) against time. All the experiments were performed with H_2O_2 (6.53mM) and the $\text{Cu}^{\text{II}}(\text{dien})^{2+}$ of **FeCu 4** in the mole ratio 65:2 at room temperature under an open atmosphere.



Scheme 3.8 Proposed scheme for the overall CDA process. Activated catalysts release when cyanide concentration reach threshold, which then catalyze the oxidation of free cyanide to cyanate.

3.4.1 Degradation of Cyanide in Practical Wastewater Samples by the CDA system

The verification of the CDA applications in wastewater treatment was performed by applying **FeCu 4** in wastewater samples. The wastewater samples from a domestic wastewater treatment plant (level I, untreated) and an industrial effluent were collected in Hong Kong, China. Samples were filtered through 0.45 μm pore-size membrane filters (Pall Corporation) to remove insoluble substances and used without further treatment. All the wastewater samples were spiked with 10, 20, or 30 μM of cyanide with respect to the maximum allowable levels for cyanide in wastewater (20 μM) suggested by World Health Organization (WHO).

Figure 3.25 shows the results of degradation of cyanide in wastewater by **FeCu 4** and was analyzed as summarized in Table 3.5. From the above-mentioned studies, the threshold concentration of cyanide for initiating **FeCu 4** catalytic properties was 20 μM . No cyanide was oxidized to cyanate in samples with cyanide concentration of 10 μM (concentration less than the threshold); while cyanide was intelligently oxidized to cyanate when 20 and 30 μM of cyanide was spiked in the water samples. Control experiments were also done in the absence **FeCu 4**, in which concentrations of cyanide and cyanate show no observable changes. The results indicated that the CDA system is also able to function in practical domestic and industrial wastewater samples without interference from organic and inorganic matter.

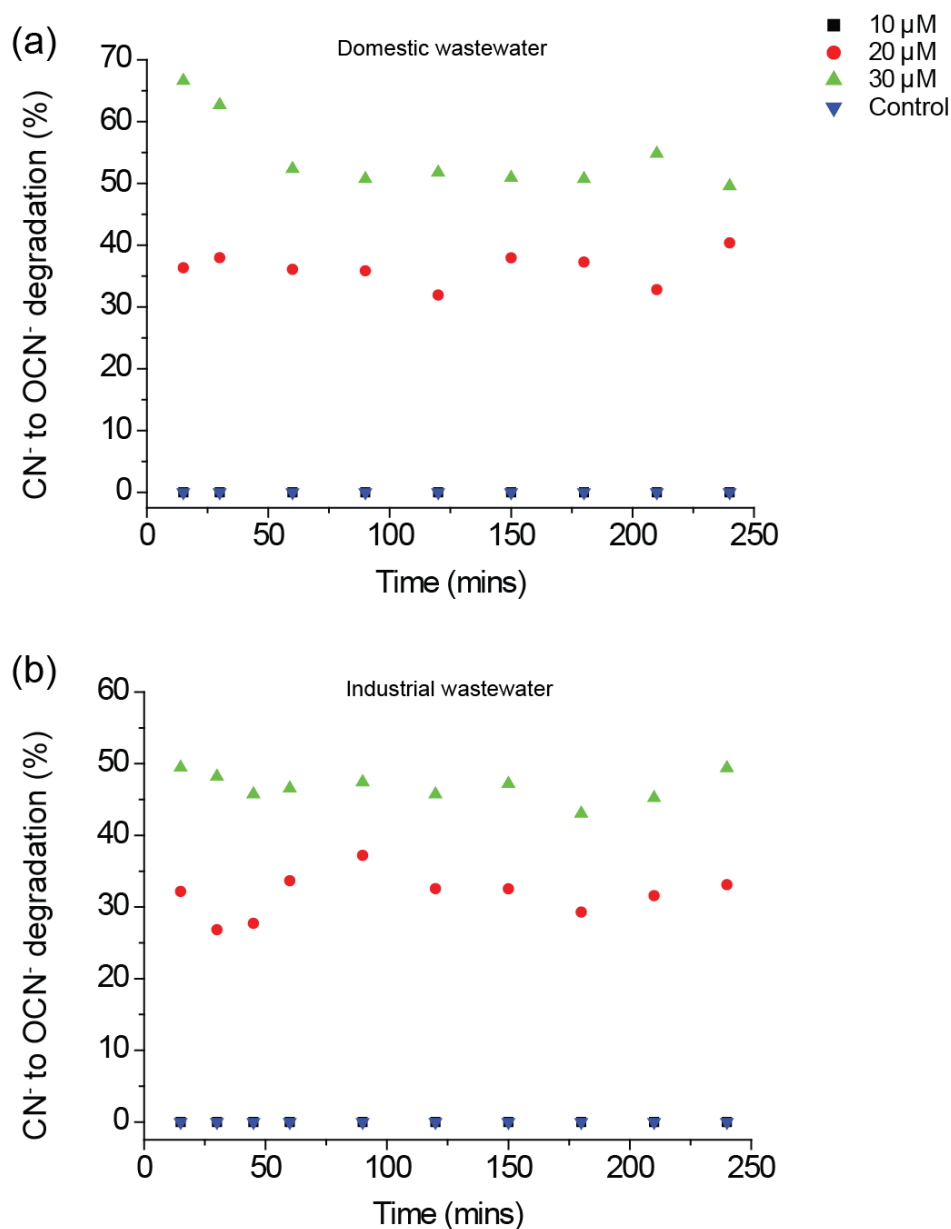


Figure 3.25 Degradation of cyanide to cyanate in practical sample of (a) domestic wastewater (level I, untreated) and (b) industrial effluent by **FeCu 4** ($2.0 \times 10^{-4}\text{M}$) in the presence of H_2O_2 ($6.53 \times 10^{-4}\text{M}$) and spiked with (●) 20 μM and (▲) 30 μM of cyanide. Control experiments (▼) were run in the absence of **FeCu 4**, with the presence of H_2O_2 ($6.53 \times 10^{-4}\text{M}$) and cyanide (10 μM).

Table 3.5 Summaries of cyanide degradation in domestic (level I, untreated) and industrial wastewater samples by **FeCu 4**.

Wastewater samples	Cyanide added (μM)	Cyanate generated (μM)	Conversion after 4 h (%)
Domestic (level I, untreated)	10	0	0
	20	6.1	40.4
	30	12.9	42.9
Industrial	10	0	0
	20	6.6	33.1
	30	14.8	49.4

3.5 Conclusions

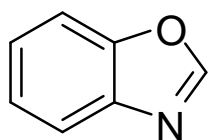
A series of Fe-Cu bimetallic complexes were synthesized, characterized and prove can be functioned simultaneously as a chemodosimeter, a signal amplifier, and an oxidation catalyst in the detection and remediation of cyanide in practical water samples. The concept of a catalyst displacement assay (CDA) was also demonstrated as a versatile way of designing new smart catalysts with fine-tunable initiation conditions. The crucial factors that affect the displacement of catalysts were found to be controlled not only by thermodynamic properties but also by kinetic properties.

In the next chapter, a series of ruthenium complexes were synthesized and characterized for the studies of their photophysical properties.

Chapter 4: Synthesis, structure and photophysical properties of isocyano Ruthenium (II) 2-(2-hydroxyphenyl)benzoxazole complexes

4.1 Introduction

Benzoxazole is a class of aromatic organic compound with benzene-fused heterocyclic oxazole ring structure as shown in Figure 4.1. Derivatives of benzoxazole can be found in nature and displays a wide range of biological properties including antifungal, antioxidant, antiallergic, antitumoral and antiparasitic properties. They are also commercially important as herbicides^{219,220} and fluorescent whitening dyes²²¹.



Benzoxazole

Figure 4.1 Structure of benzoxazole group.

There have been a number of studies related to 2-(2-hydroxyphenyl)benzoxazole (HPBO), which is a derivative of benzoxazole, and is well known because of its excited state intramolecular proton transfer (ESIPT) property. The ESIPT photophysical process of HPBO is shown in Figure 4.2, where HPBO undergo tautomerization and rotamerization when excited by light.²²² This photophysical property make HPBO exhibit remarkable large Stokes shift (up to *ca.* 180 nm) and therefore can avoid self-absorption in fluorescence analysis such as molecular sensing²²³⁻²²⁶ and DNA modeling.²²⁷⁻²²⁹

Different complexes with HPBO ligand were studied and found to have interesting photophysical properties. Rai, V.K. *et al.* have reported [Zn(PBO)₂] complex which give blue fluorescent with $\lambda_{em} = 450$ nm.²³⁰ Two gallium PBO complexes, Me₂GaPBO and Et₂GaPBO were reported by Pal *et. at.* and were found to be emissive in room temperature with $\lambda_{em} = 450$ nm and 440 nm respectively.²³¹ Du *et. al.* has reported an iridium (III) complex Ir(ppy)₂PBO (ppy = 2-phenylpyridine), which is a yellowish-green emitter with $\lambda_{em} = 526$ nm.²³² Massue *et, al.* have reported a borate (III) complex B(PBO)F₂ with with $\lambda_{em} = 401$ nm. All of these

complexes were found to be an efficient electroluminescent layer for the construction of white organic light-emitting diodes (WOLEDs) and were potential electroluminescent devices for energy transfer.

Although lots of PBO complexes have been extensively studied, only a limited number of its ruthenium complexes have been reported. Ruthenium complexes of 2-(2-hydroxyphenyl)benzoxazole and its derivative are reported to have special photophysical and electrochemical properties, where noninnocent redox behavior and rich visible-NIR spectroscopy were reported.²³³⁻²³⁶ The phenolate oxygen of the ligand is also a good sigma donor^{237,238} which stabilize the metal center with higher oxidation state in catalysis. Keyes *et al.* have reported two $[\text{Ru}(\text{L-L})_2\text{PBO}](\text{PF}_6)$ complexes, where L-L is 2,2-bipyridine and 2,2-biquinoline,²³⁵ Novales *et al.* synthesized the complexes *trans*- $[\text{Ru}(\text{tolyterpy})(\text{PBO})(\text{Cl})](\text{PF}_6)$, *cis*- $[\text{Ru}(\text{tolyterpy})(\text{PBO})(\text{H}_2\text{O})](\text{PF}_6)_2$ and *cis*- $[\text{Ru}(\text{tolyterpy})(\text{PBO})(\text{NMI})](\text{PF}_6)$ (Figure 4.3).^{228,234} Małeck J. G. *et al.* have reported $[(\text{C}_6\text{H}_6)\text{RuCl}(\text{PBO})]$,²³⁹ $[\text{RuCl}_2(\text{PBO})(\text{PPh}_3)_2]$ and $[\text{RuCl}(\text{CO})(\text{PBO})(\text{PPh}_3)_2]$ (Figure 4.4),²⁴⁰ All these complexes show rich visible-NIR spectroscopy and therefore are potential candidates in developing solar energy conversion device.

Isocyanide ($\text{R-N}\equiv\text{C}$) is a strong σ -donor and also a weak π -acceptor. It forms readily complexes with low-valent metals.²⁴¹⁻²⁴⁵ A large number of isocyano metal complexes have been reported. Their photophysical and electrochemical properties can be varied by changing the substituent(s) on isocyanide, resulting in a modified M–C bond distance.²⁴⁶⁻²⁵⁰ Therefore, the readily tunable steric and electronic nature of isocyanide ligands could be utilized for designing metal complexes with desirable electrochemical and photophysical properties.

Interesting photoluminescence properties were reported recently for Ru isocyano complexes bearing quinoline-based ligands.^{245,251} Ruthenium bis-isocyano complex bearing 8-quinolinolate $\text{Ru}(\text{Q})_2(\text{CNR})_2$ was reported by Lau and coworkers²⁵¹ and exhibit metal-to-ligand charge transfer (MLCT) luminescence, which is dependent on the isomeric, i.e. *cis,cis,trans*- and *trans,trans,trans*-, forms and the electronic properties of the isocyanide (Figure 4.5). Leung and Ko have later reported a series of ruthenium complexes containing quinoline-8-thiolate (SQ) and isocyanide ligands $\text{Ru}(\text{SQ})_2(\text{CNR})(\text{PPh}_3)$ (Figure 4.6).²⁴⁵ The complexes display red

to near-IR MLCT luminescence at room temperature, which varies also with the π -accepting ability of the isocyanide ligands and the isomeric forms (*cis*, *trans*- and *cis*, *cis*-) of the complexes.

In this chapter, a series of ruthenium complexes bearing HPBO and isocyanide ligands have been synthesized and characterized. By the reactions of $\text{Ru}(\text{PBO})_2(\text{PPh}_3)_2$ with the phenyl isocyanide with varied substituents, the complexes *trans*, *trans*, *trans*- (**1**), *trans*, *cis*- $\text{Ru}(\text{PBO})_2(\text{CNR})(\text{PPh}_3)$ (**2**) and *cis*, *trans*, *cis*- $\text{Ru}(\text{PBO})_2(\text{CNR})_2$ (**3**) have been isolated. The structures of complexes **1b**, **1e**, **2c** and **3b** have been determined. The influence of the electronic properties of the isocyanides and the isomeric forms on the photophysical and electrochemical properties of the complexes were studied to investigate the possibility of the Ru-PBO complexes in developing electroluminescent and solar energy conversion device

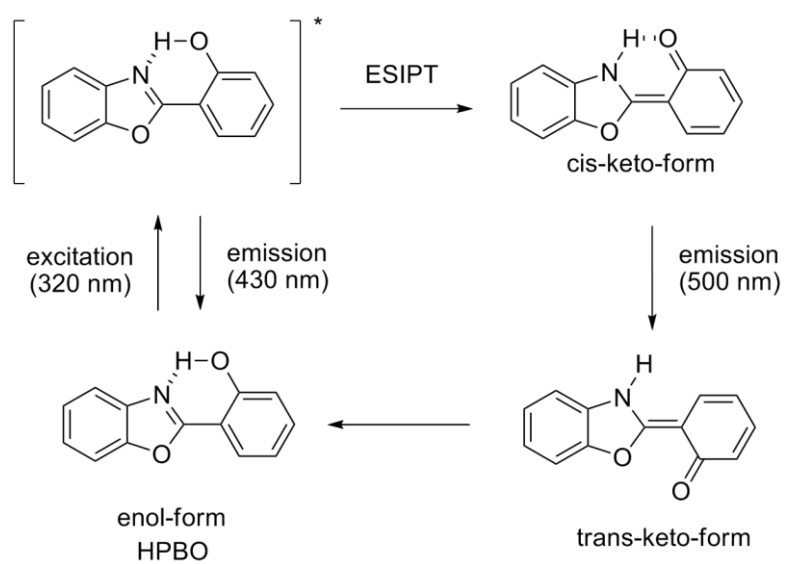


Figure 4.2 ESIPT of HPBO.²⁵²

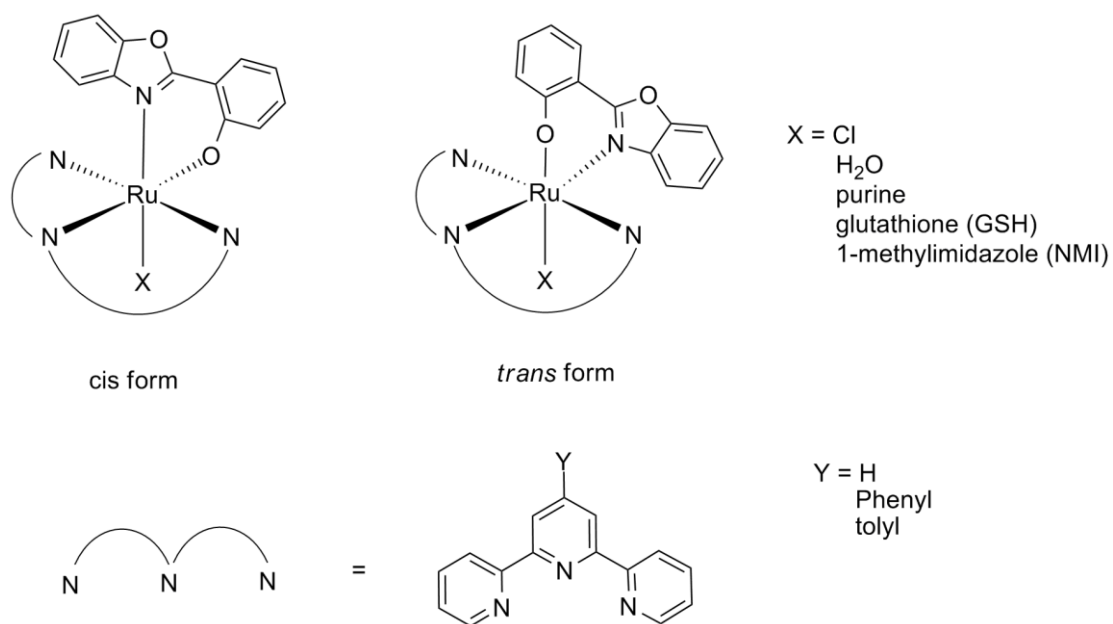


Figure 4.3 Structure of ruthenium complexes with polypyridyl and PBO ligands.^{228,234}

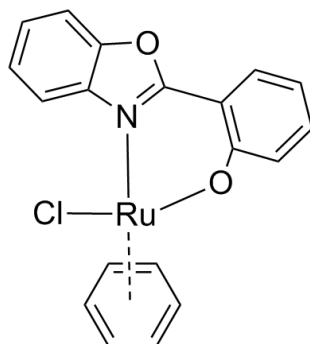


Figure 4.4 Structure of $[(C_6H_6)RuCl(HPBO)]^{240}$

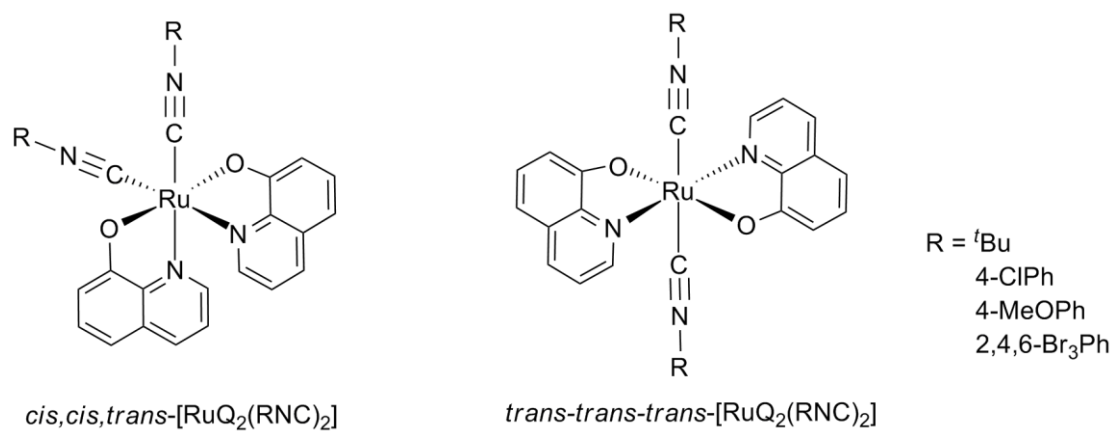


Figure 4.5 Structure for *cis,cis,trans*- and *trans,trans,trans*-[Ru^{II}Q₂(CNR)₂].²⁵¹

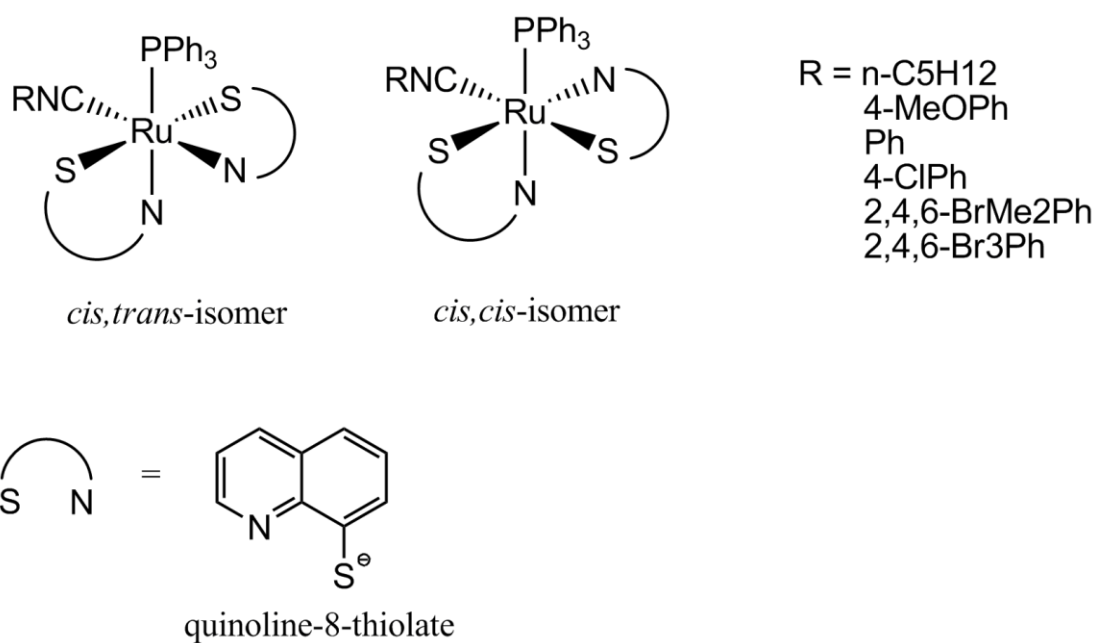


Figure 4.6 Structure for *cis,trans*- and *cis,cis*-[Ru^{II}(SQ)₂(PPh₃)(CNR)].²⁴⁵

4.2 Experimental

4.2.1 Materials and Reagents

2-(2-hydroxyphenyl)benzoxazole was obtained from Acros. Ruthenium (III) chloride hydrate and triphenylphosphine were purchased from Strem Chemical Company. $[\text{Ru}(\text{PPh}_3)_3\text{Cl}_2]$ ^{253,254} and isocyanide ligands²⁵⁵ were synthesized according to literature procedures. All reagents and organic solvents used were of analytical grade and were used without further purification.

4.2.2 Syntheses

Synthesis of $[\text{Ru}(\text{PBO})_2(\text{PPh}_3)_2]$

$[\text{Ru}(\text{PPh}_3)_3\text{Cl}_2]$ (480 mg, 0.5 mmol) was suspended in ethanol (30 mL) under an argon atmosphere. To the suspension, HPBO (212 mg, 1 mmol) and 2,6-lutidine (0.1 mL) were added. The mixture was then heated to reflux for 1 hr. The reaction mixture was cooled to room temperature. The dark reddish-purple crystalline solid was collected by filtration. The solid was washed with three portions of ethanol (2 mL) and then with diethyl ether (2 mL) and dried in air. Yield: 0.348 g (66.4%).

Synthesis of isocyanide ligands

Isocyanide ligands were prepared by slight modification of a literature procedure.²⁵⁶ To 100 mL diluted DCM solution of the corresponding aromatic amine (22 mmol), a 50 wt % aqueous NaOH with 1 mol % tetrabutylammonium bromide and 2.6 mL CHCl_3 (1.5 eq, 33 mmol) were added. The reaction mixture was stirred for 6 hrs at room temperature, and diluted with 200 mL of H_2O . Organic layer was separated by separating funnel and was dried over MgSO_4 . Solvent was removed under reduced pressure at room temperature. Product was further purified by column chromatography on silica gel using DCM-hexane (1:4 v/v) as eluent.

Synthesis of *trans,trans,trans*- $[\text{Ru}(\text{PBO})_2(\text{CNR})_2]$ (**1**)

Isocyanide ligand (0.126 mmol) was added to a suspension of $[\text{Ru}(\text{PBO})_2(\text{PPh}_3)_2]$ (60 mg, 0.057 mmol) in ethanol (15 mL) under argon atmosphere in the presence of Zn/Hg. The resulting mixture was refluxed for 4 hrs, during which the solution gradually turned orange and precipitate formed. Solid was collected by filtration and was purified by column

chromatography on silica gel using dichloromethane (DCM) as eluent. The first major band (**1**) was collected and dried in vacuo.

Synthesis of *cis,trans*-[Ru(PBO)₂(PPh₃)(CNR)] (**2**)

Complex **2** was synthesized by procedure similar to **1** except reaction mixture was refluxed for overnight. An orange yellow solution and precipitate was formed after cooling down to room temperature. Product was purified by column chromatography on silica gel using dichloromethane and ethyl acetate 10:1 as eluent. The last yellow band (**2**) was collected and dried in vacuo. Recrystallization from diethyl ether in dark gave the analytically pure complex as orange yellow microcrystalline solids.

Synthesis of *cis,trans,cis*-[Ru(PBO)₂(CNR)₂] (**3**)

Complexes **3** was synthesized by procedure similar to **2** except large excess of isocyanide (10 eq) were added and the analogues with 2,6-Cl₂PhNC and 2,4,6-Br₃PhNC were refluxed in toluene. The resulting mixture was refluxed overnight and a clear yellow solution was formed. Product was purified by column chromatography on neutral alumina using dichloromethane and ethyl acetate 10:1 as eluent. The last yellow band (**3**) was collected and dried in vacuo. Recrystallization from diethyl ether in dark gave the analytically pure complex as yellow microcrystalline solids.

trans,trans,trans-[Ru(PBO)₂(MeOPhNC)₂] (**1a**)

Yield: 23.5 mg (52.0%). ¹HNMR (300 MHz, (CD₃)₂CO): δ 8.73 (dd, J = 8.0, 1.4 Hz, 2H, PBO), 7.85 (dd, J = 8.1, 1.9 Hz, 2H, PBO), 7.66 (dd, J = 7.4, 1.6 Hz, 2H, PBO), 7.48 – 7.37 (m, 4H, PBO), 7.15 (ddd, J = 8.7, 6.8, 1.9 Hz, 2H, PBO), 7.05 – 6.95 (m, 4H, PBO+MeOPhNC), 6.87 – 6.78 (m, 6H, PBO+MeOPhNC), 6.48 (ddd, J = 8.0, 6.8, 1.1 Hz, 2H, PBO), 3.75 (s, 6H, MeOPhNC). IR (KBr, cm⁻¹): 2087 ν(C≡N). UV/vis (CH₂Cl₂) λ_{max}, nm (ε, M⁻¹ cm⁻¹): 326 (31780), 445sh (4290). ESI-MS: m/z 787 [M]⁺.

trans,trans,trans-[Ru(PBO)₂(PhNC)₂] (**1b**)

Yield: mg (%). ¹HNMR (300 MHz, (CD₃)₂CO): δ 8.75 (dd, J = 7.7, 1.7 Hz, 2H, PBO), 7.87 (dd, J = 8.1, 1.9 Hz, 2H, PBO), 7.67 (dd, J = 7.3, 1.4 Hz, 2H, PBO), 7.53–7.29 (m, 11H, PBO+PhNC), 7.16 (ddd, J = 8.7, 6.8, 1.9 Hz, 2H, PBO), 7.11–7.02 (m, 4H, PBO+PhNC), 6.85 (dd, J = 8.6, 1.1 Hz, 2H, PBO), 6.50 (ddd, J = 8.0, 6.8, 1.2 Hz, 2H, PBO). IR (KBr, cm⁻¹): 2080

$\nu(\text{C}\equiv\text{N})$. UV/vis (CH_2Cl_2) λ_{max} , nm (ϵ , $\text{M}^{-1} \text{cm}^{-1}$): 331 (24350), 444sh (4202). ESI-MS: m/z 728 $[\text{M}]^+$.

trans,trans,trans-[Ru(PBO)₂(CIPhNC)₂] (**1c**)

Yield: 29.6 mg (64.8%). ¹HNMR (400 MHz, CDCl_3): δ 8.43 (dd, $J = 8.0, 1.3$ Hz, 2H, PBO), 7.90 (dd, $J = 8.0, 1.9$ Hz, 2H, PBO), 7.54 (dt, $J = 7.9, 0.8$ Hz, 2H, PBO), 7.42–7.29 (m, 4H, PBO), 7.24–7.15 (m, 6H, PBO+CIPhNC), 6.94 (d, $J = 8.6$ Hz, 2H, PBO), 6.89–6.81 (m, 4H, PBO+CIPhNC), 6.58 (t, $J = 7.4$ Hz, 2H, PBO). IR (KBr, cm^{-1}): 2069 $\nu(\text{C}\equiv\text{N})$. UV/vis (CH_2Cl_2) λ_{max} , nm (ϵ , $\text{M}^{-1} \text{cm}^{-1}$): 337 (24990), 449 sh(4600). ESI-MS: m/z 796 $[\text{M}]^+$.

trans,trans,trans-[Ru(PBO)₂(Cl₂PhNC)₂] (**1d**)

Yield: mg (%). ¹HNMR (400 MHz, CDCl_3): δ 8.71 (d, $J = 8.2$ Hz, 1H, PBO), 7.95 (m, 4H, CNPhCl₂), 7.88 (d, $J = 8.4$ Hz, 1H, PBO), 7.53 (d, $J = 7.0$ Hz, 1H, BPO), 7.41–7.29 (m, 4H, PBO), 7.22–7.08 (m, 9H, PBO+ Cl₂PhNC), 7.07–6.99 (m, 1H, PBO), 6.88 (d, $J = 8.6$ Hz, 1H, PBO), 6.50 (t, $J = 7.3$ Hz, 1H, BPO). IR (KBr, cm^{-1}): 2065 $\nu(\text{N}\equiv\text{C})$. UV/vis (CH_2Cl_2) λ_{max} , nm (ϵ , $\text{M}^{-1} \text{cm}^{-1}$): 323 (30220), 354sh (22860), 420 (12390). ESI-MS: m/z 866 $[\text{M}]^+$.

trans,trans,trans-[Ru(PBO)₂(Br₃PhCN)₂] (**1e**)

Yield: 25.9 mg (37.6%). ¹HNMR (400 MHz, CDCl_3): δ 8.74 (d, $J = 7.9$ Hz, 2H, PBO), 7.87 (d, $J = 8.0$ Hz, 2H, PBO), 7.53 (d, $J = 5.9$ Hz, 6H, PBO+Br₃PhNC), 7.33 (dt, $J = 19.5, 7.4$ Hz, 4H, PBO), 7.12 (t, $J = 7.5$ Hz, 2H, PBO), 6.89 (d, $J = 8.6$ Hz, 2H, PBO), 6.48 (t, $J = 7.5$ Hz, 2H, PBO). IR (KBr, cm^{-1}): 2041 $\nu(\text{N}\equiv\text{C})$. UV/vis (CH_2Cl_2) λ_{max} , nm (ϵ , $\text{M}^{-1} \text{cm}^{-1}$): 329 (28420), 375 (22950), 430 (14424). ESI-MS: m/z 1201 $[\text{M}]^+$.

cis,trans-[Ru(PBO)₂(PPh₃)(MeOPhNC)] (**2a**)

Yield: 18.6 mg (35.4%) ¹HNMR (400 MHz, CD_2Cl_2): δ 7.98 (d, $J = 7.9$ Hz, 1H, PBO), 7.85 (dd, $J = 8.0, 1.9$ Hz, 1H, PBO), 7.58 (dd, $J = 8.4, 2.0$ Hz, 1H, PBO), 7.40 (d, $J = 8.2$ Hz, 3H, PBO), 7.38–6.80 (m, 19H, PBO+PPh₃+MeOPhNC), 6.75–6.66 (m, 1H, PBO), 6.48–6.40 (m, 1H, PBO), 6.35–6.28 (m, 2H, PBO), 6.14 (dd, $J = 8.5, 1.1$ Hz, 1H, PBO), 3.79 (d, $J = 1.7$ Hz, 3H, MeOPhNC). IR (KBr, cm^{-1}): 2066 $\nu(\text{N}\equiv\text{C})$. UV/vis (CH_2Cl_2) λ_{max} , nm (ϵ , $\text{M}^{-1} \text{cm}^{-1}$): 334 (13130), 387sh (7130), 431sh (5570). ESI-MS: m/z 917 $[\text{M}]^+$.

cis,trans-[Ru(PBO)₂(PPh₃)(PhNC)] (**2b**)

Yield: 22.7 mg (44.6%) $^1\text{H NMR}$ (400 MHz, CD_2Cl_2): δ 8.01 (dd, $J = 8.1, 1.2$ Hz, 1H, PBO), 7.86 (dd, $J = 8.0, 1.8$ Hz, 1H, PBO), 7.60 (dd, $J = 8.4, 1.8$ Hz, 1H, PBO), 7.49 – 6.84 (m, 27H, PBO+ PPh_3 +PhNC), 6.72 (t, $J = 8.2, 7.4, 1.1$ Hz, 1H, PBO), 6.45 (t, $J = 7.9, 6.9, 1.2$ Hz, 1H, PBO), 6.37 – 6.29 (m, 2H, PBO), 6.16 (d, $J = 8.6, 1.2$ Hz, 1H, PBO). IR (KBr, cm^{-1}): 2057 $\nu(\text{N}\equiv\text{C})$. UV/vis (CH_2Cl_2) λ_{max} , nm ($\epsilon, \text{M}^{-1} \text{cm}^{-1}$): 335 (18800), 432sh (8850). ESI-MS: m/z 887 $[\text{M}]^+$.

cis,trans-[Ru(PBO) $_2$ (PPh $_3$)(ClPhNC)] (**2c**)

Yield: 29.6 mg (56.0%) $^1\text{H NMR}$ (400 MHz, CD_2Cl_2): δ 7.95 (d, $J = 7.9$ Hz, 1H, PBO), 7.85 (dd, $J = 7.9, 1.9$ Hz, 1H, PBO), 7.59 (dd, $J = 8.4, 1.9$ Hz, 1H, PBO), 7.51–6.81 (m, 26H, PBO+ PPh_3 +ClPhNC), 6.71 (t, 1H, PBO), 6.45 (t, $J = 8.0, 6.8, 1.2$ Hz, 1H, PBO), 6.37–6.29 (m, 2H, PBO), 6.14 (dd, $J = 8.5, 1.1$ Hz, 1H, PBO). IR (KBr, cm^{-1}): 2013 $\nu(\text{N}\equiv\text{C})$. UV/vis (CH_2Cl_2) λ_{max} , nm ($\epsilon, \text{M}^{-1} \text{cm}^{-1}$): 328 (18680), 384sh (11700), 434sh (7030). ESI-MS: m/z 921 $[\text{M}]^+$.

cis,trans-[Ru(PBO) $_2$ (PPh $_3$)(Cl $_2$ PhNC)] (**2d**)

Yield: 28.0 mg (51.1%) $^1\text{H NMR}$ (400 MHz, CD_2Cl_2): δ 8.52 (d, $J = 7.7, 1.5$ Hz, 1H, PBO), 7.86 (dd, $J = 8.0, 1.9$ Hz, 1H, PBO), 7.53 (dd, $J = 8.1, 1.8$ Hz, 1H, PBO), 7.41 (d, 1H, PBO), 7.35 (d, $J = 8.2$ Hz, 1H, PBO), 7.31–7.20 (m, 4H, PBO), 7.19–6.80 (m, 22H, PBO+ PPh_3 +Cl $_2$ PhNC), 6.58 (t, $J = 8.3, 7.4, 1.1$ Hz, 1H, PBO), 6.42 (t, $J = 8.0, 7.0, 1.2$ Hz, 1H, PBO), 6.37–6.24 (m, 2H, PBO), 6.10 (dd, $J = 8.5, 1.2$ Hz, 1H, PBO). IR (KBr, cm^{-1}): 1986 $\nu(\text{N}\equiv\text{C})$. UV/vis (CH_2Cl_2) λ_{max} , nm ($\epsilon, \text{M}^{-1} \text{cm}^{-1}$): 335 (25240), 389sh (13830), 434sh (10360). ESI-MS: m/z 955 $[\text{M}]^+$.

cis,trans-[Ru(PBO) $_2$ (PPh $_3$)(Br $_3$ PhNC)] (**2e**)

Yield: 31.5 mg (48.9%) $^1\text{H NMR}$ (400 MHz, CD_2Cl_2): δ 8.54 (d, 1H, PBO), 7.85 (dd, $J = 8.0, 1.9$ Hz, 1H, PBO), 7.60 (s, 2H, Br $_3$ PhNC), 7.53 (dd, $J = 7.9, 1.8$ Hz, 1H, PBO), 7.42 (d, 1H, PBO), 7.34 (d, $J = 8.1$ Hz, 1H, PBO), 7.31–7.20 (m, 2H), 7.19–6.79 (m, 8H, PBO+ PPh_3), 6.59 (t, $J = 8.4, 7.4, 1.1$ Hz, 1H, PBO), 6.42 (t, $J = 8.0, 6.8, 1.1$ Hz, 1H), 6.34–6.26 (m, 2H, PBO), 6.08 (dd, $J = 8.5, 1.1$ Hz, 1H, PBO). IR (KBr, cm^{-1}): 1957 $\nu(\text{N}\equiv\text{C})$. UV/vis (CH_2Cl_2) λ_{max} , nm ($\epsilon, \text{M}^{-1} \text{cm}^{-1}$): 301 (50000), 344 (40700), 433 (15100). ESI-MS: m/z 1123 $[\text{M}]^+$.

cis,trans,cis-[Ru(PBO) $_2$ (MeOPhNC) $_2$] (**3a**)

Yield: 18.5 mg (41.0%) $^1\text{H NMR}$ (300 MHz, CD_2Cl_2): δ 8.13 – 8.04 (m, 2H, PBO), 7.90 (dd, $J = 8.0, 1.9$ Hz, 2H, PBO), 7.70 – 7.61 (m, 2H, PBO), 7.49 – 7.38 (m, 4H, PBO), 7.11 – 6.98 (m,

6H, PBO+MeOPhNC), 6.85 – 6.75 (m, 4H, PBO+MeOPhNC), 6.51 (t, $J = 8.0, 6.8, 1.1$ Hz, 2H, PBO), 6.33 (dd, $J = 8.6, 1.2$ Hz, 2H, PBO), 3.77 (s, 6H, MeOPhNC). IR (KBr, cm^{-1}): 1949, 2057, 2119 $\nu(\text{N}\equiv\text{C})$. UV/vis (CH_2Cl_2) λ_{max} , nm (ϵ , $\text{M}^{-1} \text{cm}^{-1}$): 325 (40500), 421 (16700). ESI-MS: m/z 788 $[\text{M}]^+$.

cis,trans,cis-[Ru(PBO)₂(PhNC)₂] (**3b**)

Yield: 20.5 mg (49.1%) ¹HNMR (300 MHz, CD_2Cl_2): δ 8.08 (d, $J = 9.2$ Hz, 2H, PBO), 7.90 (d, $J = 6.8$ Hz, 2H, PBO), 7.67 – 7.62 (m, 2H, PBO), 7.47 – 7.39 (m, 4H, PBO), 7.35 – 7.24 (m, 6H, PBO+ PhNC), 7.14 – 6.99 (m, 6H, PBO+ PhNC), 6.52 (t, $J = 7.4$ Hz, 2H, PBO), 6.35 (d, $J = 8.6$ Hz, 2H, PBO). IR (KBr, cm^{-1}): 2005, 2063, 2127 $\nu(\text{N}\equiv\text{C})$. UV/vis (CH_2Cl_2) λ_{max} , nm (ϵ , $\text{M}^{-1} \text{cm}^{-1}$): 324 (31500), 420 (15300). ESI-MS: m/z 728 $[\text{M}]^+$.

cis,trans,cis-[Ru(PBO)₂(ClPhNC)₂] (**3c**)

Yield: 16.9 mg (37.0%) ¹HNMR (400 MHz, CD_2Cl_2): δ 8.03 – 7.97 (m, 2H, PBO), 7.90 (dd, $J = 8.0, 1.8$ Hz, 2H, PBO), 7.68–7.62 (m, 2H, PBO), 7.46 – 7.38 (m, 4H, PBO), 7.31 – 7.24 (m, 4H, PBO+ClPhNC), 7.09 – 6.98 (m, 6H, PBO+ClPhNC), 6.54 (t, $J = 8.0, 6.8, 1.2$ Hz, 2H, PBO), 6.36 (dd, $J = 8.7, 1.2$ Hz, 2H, PBO). IR (KBr, cm^{-1}): 2012, 2047, 2112 $\nu(\text{N}\equiv\text{C})$. UV/vis (CH_2Cl_2) λ_{max} , nm (ϵ , $\text{M}^{-1} \text{cm}^{-1}$): 321sh (22420), 419 (9040). ESI-MS: m/z 797 $[\text{M}]^+$.

cis,trans,cis-[Ru(PBO)₂(Cl₂PhNC)₂] (**3d**)

Yield: 18.9 mg (38.1%) ¹HNMR (400 MHz, CD_2Cl_2): δ 8.04 (d, $J = 8.2$ Hz, 2H, PBO), 7.90 (m, 6H, PBO+CNPhCl₂), 7.70–7.61 (m, 2H, PBO), 7.32–7.08 (m, 9H, PBO+ Cl₂PhNC), 7.07–6.99 (m, 1H, PBO), 6.88 (d, $J = 8.6$ Hz, 1H, PBO), 6.50 (t, $J = 7.3$ Hz, 1H, BPO). IR (KBr, cm^{-1}): 2005, 2055, 2110 $\nu(\text{N}\equiv\text{C})$. UV/vis (CH_2Cl_2) λ_{max} , nm (ϵ , $\text{M}^{-1} \text{cm}^{-1}$): 328sh (15700), 418sh (9470). ESI-MS: m/z 866 $[\text{M}]^+$.

cis,trans,cis-[Ru(PBO)₂(Cl₂PhNC)₂] (**3e**)

Yield: 25.6 mg (37.2%) ¹HNMR (400 MHz, CD_2Cl_2): δ 8.04 (d, $J = 7.9$ Hz, 2H, PBO), 7.87 (d, $J = 8.0$ Hz, 2H, PBO), 7.53 (d, $J = 5.9$ Hz, 6H, PBO+Br₃PhNC), 7.33 (dt, $J = 19.5, 7.4$ Hz, 4H, PBO), 7.07 (t, $J = 7.5$ Hz, 2H, PBO), 7.01 (d, $J = 8.6$ Hz, 2H, PBO), 6.78 (t, $J = 7.5$ Hz, 2H, PBO). IR (KBr, cm^{-1}): 1986, 2098 $\nu(\text{N}\equiv\text{C})$. UV/vis (CH_2Cl_2) λ_{max} , nm (ϵ , $\text{M}^{-1} \text{cm}^{-1}$): 340sh (33150), 419sh (19200). ESI-MS: m/z 1202 $[\text{M}]^+$.

4.2.3 Physical Measurement and Instrumentation

Infrared spectra in the 500–4000 cm^{-1} range were recorded using a Perkin Elmer Model Frontier FTIR spectrometer using KBr plates. Electrospray mass spectra (ESI-MS) were obtained with an AB SCIEX API 2000 LC/MS/MS system. The emission spectra and lifetime were measured using a Horiba FluoroMax-4 spectrofluorometer with a 5 nm slit width and a 0.5 s integration time in ethanol/methanol (4:1) at 77K. UV-vis spectra were measured by a Cary 50 ultraviolet visible spectrophotometer.

4.2.3.1 General Parameter

Electrochemical studies were conducted in HPLC grade dichloromethane (DCM). Cyclic voltammetric (CV) measurements were performed on a CH Instruments, Inc. model CHI 620 Electrochemical Analyser in DCM solution with 0.1 M *n*-tetrabutylammonium hexafluorophosphate (TBAP) as a supporting electrolyte at room temperature, by using a Ag/AgCl reference electrode, a glassy carbon working electrode and a platinum-wire counter electrode. Solutions for electrochemical studies were deaerated with pre-purified argon (Ar) gas and kept under an Ar atmosphere during the measurements. TBAP was recrystallized from hot ethanol for three times and dried overnight at 120 °C under vacuo before use. Ferrocene (Fc) was used as the internal reference in all measurements.

4.2.4 Crystallographic Studies

Single crystals of **1b**, **1e** and **2c** were obtained by slow evaporation of dichloromethane solution of the complexes in dark at room temperature. All crystallographic determinations of the complexes were performed by Dr. Ken S. M. Yiu at The City University of Hong Kong. X-ray diffraction data were collected at 173K on an Oxford CCD diffractometer using graphite-monochromated Cu-K α ($\lambda = 1.54178 \text{ \AA}$) in the ω -scan mode. The structures were solved by the direct method, and expanded using Fourier techniques. Hydrogen atoms are included but not refined. All calculations were performed using the Crystal Structure crystallographic software package from Molecular Structure Corporation.

Table 4.1a Summary of Crystal and Structural Determination Data for the Complexes **1b** and **1e**.

	1b	1e
Empirical formula	C ₄₀ H ₂₆ N ₄ O ₄ Ru	C ₅₁ H ₃₅ ClN ₃ O ₄ PRu
Formula weight	727.73	921.34
$\lambda(\text{\AA})$	1.54178	1.54178
T(°C)	-100.15	-100.15
Space group	P-1	P-1
$a(\text{\AA})$	9.1694(4)	11.4670(4)
$b(\text{\AA})$	10.3740(5)	12.2915(4)
$c(\text{\AA})$	17.4722(6)	17.3141(6)
$\alpha(^{\circ})$	87.052(3)	71.483(3)
$\beta(^{\circ})$	83.125(3)	74.534(3)
$\gamma(^{\circ})$	81.125(4)	69.357(3)
$V(\text{\AA}^3)$	1629.39(12)	2132.29(14)
Z value	2	1
D_{calc} (g cm ⁻³)	1.483	1.500
F_{000}	740.0	980.00
$\mu(\text{Cu-K}\alpha)(\text{mm}^{-1})$	4.299	4.901
R^a	0.0291(5057)	0.0308(7164)
$R\omega^b$	0.0791(5856)	0.0814(7767)
Goodness of fit	1.088	1.058

$$^a R = \sum ||F_o| - |F_c|| / \sum |F_o|.$$

$$^b R\omega = [\sum \omega(|F_o| - |F_c|)^2 / \sum \omega(F_o)]^{1/2}.$$

Table 4.1b Summary of Crystal and Structural Determination Data for the Complexes **2c** and **3b**.

	2c	3b
Empirical formula	C ₄₁ H ₂₂ Br ₆ N ₄ O ₄ RuCl ₂	C ₄₀ H ₂₆ N ₄ O ₄ Ru
Formula weight	1279.52	727.72
λ (Å)	1.54178	1.54178
T(°C)	-100.15	-100.15
Space group	P 1 21/n 1	P-1
a (Å)	9.5891(2)	10.1816(5)
b (Å)	23.2714(6)	11.8343(4)
c (Å)	18.9365(5)	14.3853(6)
α (°)	90	81.530(3)
β (°)	101.210(2)	80.893(3)
γ (°)	90	69.568(3)
V (Å ³)	4145.09(18)	1595.83(11)
Z value	4	2
D_{calc} (g cm ⁻³)	2.061	1.514
F_{000}	2464	740
μ (Cu-K α)(mm ⁻¹)	11.424	4.389
R^a	0.0533(6198)	0.0290(5474)
$R\omega^b$	0.1447(7596)	0.0791(5816)
Goodness of fit	1.083	1.027

$$^a R = \sum ||F_o| - |F_c|| / \sum |F_o|.$$

$$^b R\omega = [\sum \omega(|F_o| - |F_c|)^2 / \sum \omega(F_o)]^{1/2}.$$

4.3 Results and Discussion

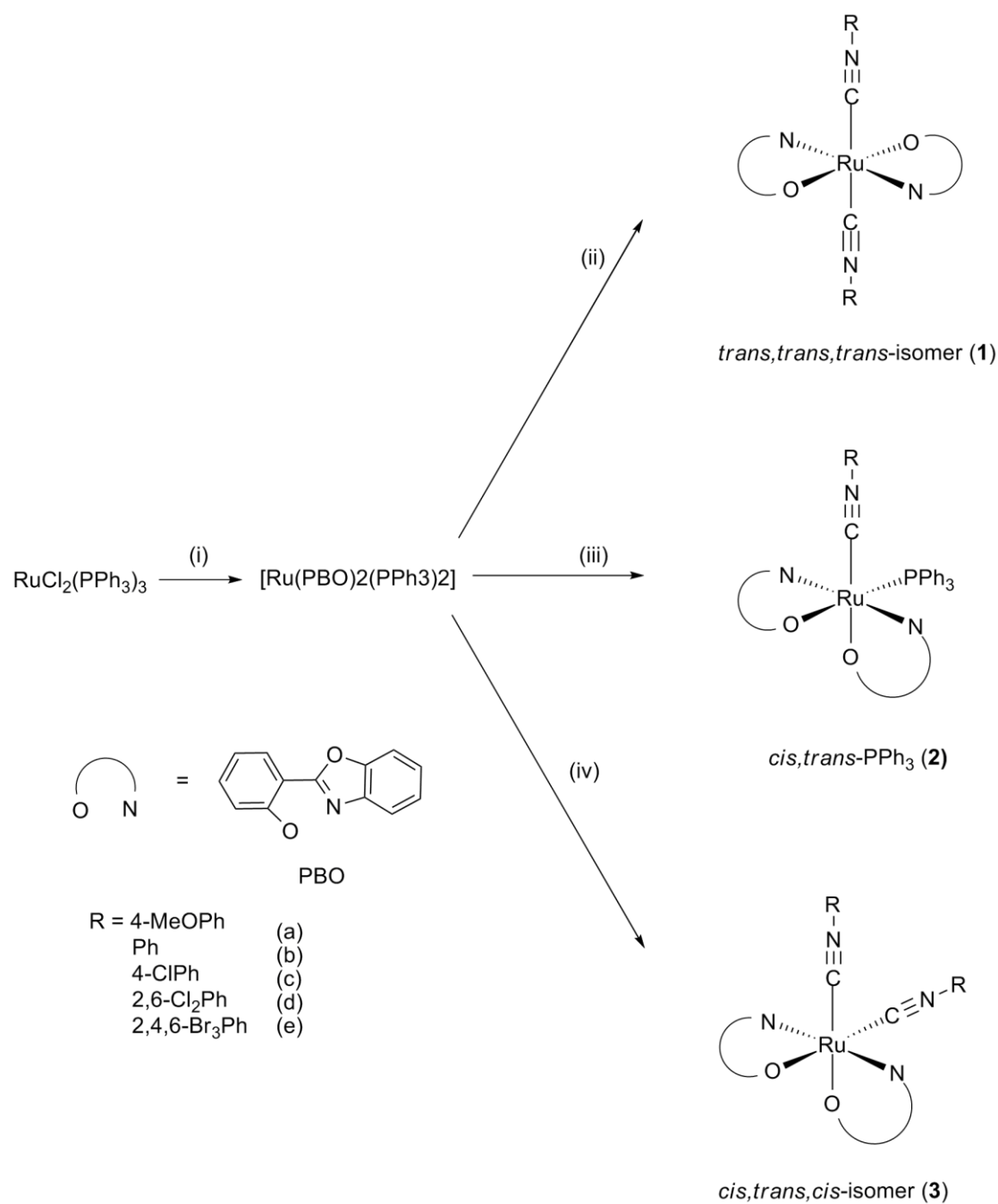
4.3.1 Synthesis and Characterization

Complexes **1-3** were prepared by reacting $[\text{Ru}(\text{PBO})_2(\text{PPh}_3)_2]$ with different equivalents of RNC and reaction time as shown in Scheme 4.1. The reaction of $[\text{Ru}(\text{PBO})_2(\text{PPh}_3)_2]$ with 2.2 mole equivalents of RNC in refluxing ethanol in the presence of Zn/Hg under argon produces *trans,trans,trans*- $[\text{Ru}(\text{PBO})_2(\text{RNC})_2]$ (**1**) and *cis,trans*- $[\text{Ru}(\text{PBO})_2(\text{RNC})(\text{PPh}_3)]$ (**2**), where the ratio of product vary with refluxing time and $[\text{Ru}(\text{PBO})_2(\text{RNC})(\text{PPh}_3)]$ become major product if the reaction mixtures were allowed to reflux overnight. The product can be readily separated by column chromatography on silica gel using dichloromethane as eluent. The complexes were soluble in non-polar organic solvents but only slightly soluble in polar organic solvents such as methanol, ethanol and acetonitrile. By reacting $[\text{Ru}(\text{PBO})_2(\text{PPh}_3)_2]$ with 10 moles equivalents of CNR overnight under the same conditions, *cis,trans,cis*- $[\text{Ru}(\text{PBO})_2(\text{RNC})_2]$ (**3a-c**) were isolated (R = 4-MeOPh, Ph and 4-ClPh), and by replacing ethanol with toluene, the **3d** and **3e** analogues were obtained.

By varying the reaction time, complex with different spatial arrangement of PBO were obtained, which indicated that a thermal *trans*-to-*cis* isomerization had occurred during reaction. The distorted planar PBO ligand in complexes **2** and **3** also suggest bond rupture between PBO and Ru may be involved in the reaction. Complexes **2** and **3** were formed when reflux overnight, and complex **3** could only be obtained when CNR were in large excess, suggesting that the PPh_3 is competing ligand when prolonged heating.

All complexes were characterized and checked for purity by infrared spectrometry, elementary analysis, electrospray mass spectrometry, and $^1\text{H-NMR}$. Results show good agreement to simulations. The coordination of isocyanide ligands were confirmed by the IR spectroscopy (Figure 4.7 to Figure 4.9), Complexes *trans,trans,trans*- $[\text{Ru}(\text{PBO})_2(\text{RNC})_2]$ show a strong $\nu_{\text{N}\equiv\text{C}}$ in the range of $2087 - 2044 \text{ cm}^{-1}$ (KBr) [**1a** (2084 cm^{-1}) > **1b** (2080 cm^{-1}) > **1c** (2069 cm^{-1}) > **1d** (2065 cm^{-1}) > **1e** (2041 cm^{-1})], which is in an order inverse to the π -accepting ability of the isocyanides ($\text{Br}_3\text{PhNC} > \text{Cl}_2\text{PhNC} > \text{ClPhNC} \geq \text{PhNC} > \text{MeOPhNC}$), which increasingly favor π -back bonding between the isocyanide ligands and the ruthenium(II) metal center. Similar

variations of the $\nu_{\text{N}\equiv\text{C}}$ with the π -accepting ability of the isocyanides were also observed for compounds **2** and **3** (Table 4.2). The $\nu_{\text{N}\equiv\text{C}}$ for the *cis,trans*- and *cis,trans,cis*- complexes occur at substantially lower energies than those for the *trans,trans,trans*- complexes, indicating the decreased bond order effected by the greater back-donation from the metal and triphenylphosphine group. The integrities of the complexes in dichloromethane were also demonstrated by electrospray mass spectrum showing peaks of $[\text{M}]^+$ as shown in Figure 4.10 to Figure 4.12.



Scheme 4.1 Synthetic scheme for compounds **1-3**. Reaction condition: (i) reflux with 2 eq of HPBO with 2,6-lutidine (0.12 mL) in ethanol, (ii) reflux with 2.2 eqv of RNC in ethanol and Hg/Zn for 4 hrs. (iii) reflux with 2.2 eqv of RNC in ethanol and Hg/Zn overnight. (iv) reflux with 10 eqv of RNC overnight.

Table 4.2 IR spectroscopic study of the cyano-stretching frequency ($\nu_{\text{N}\equiv\text{C}}$) (cm^{-1}) of complexes 1-3.

Entry	1	2	3
a	2084 (s)	2066 (s)	1949 (s) 2057 (s) 2119 (s)
b	2080 (s)	2057 (s)	2005 (s) 2062 (s) 2127 (s)
c	2069 (s)	2008 (s)	2012 (s) 2047 (s) 2113 (s)
d	2065 (s)	1986 (s)	2005 (s) 2055 (s) 2110 (s)
e	2041 (s)	1957 (s)	1986 (s) 2098 (s)

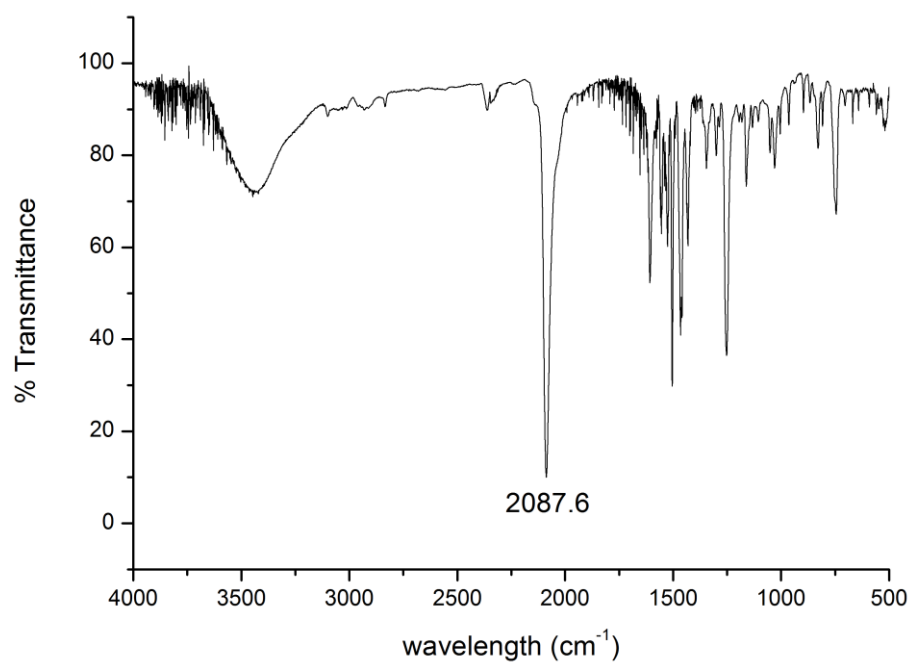


Figure 4.7a IR spectrum of **1a**.

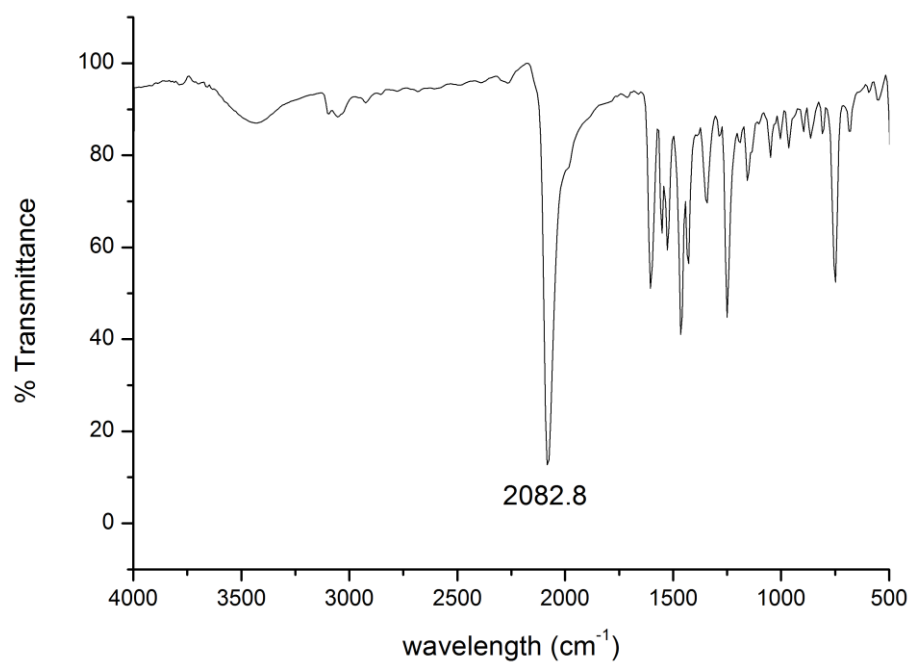


Figure 4.7b IR spectrum of **1b**.

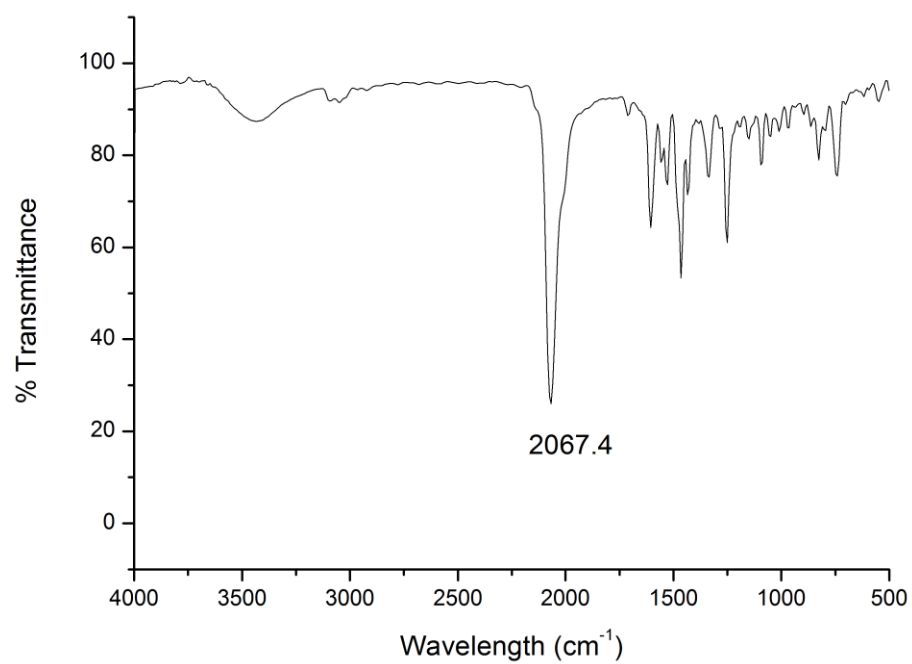


Figure 4.7c IR spectrum of **1c**.

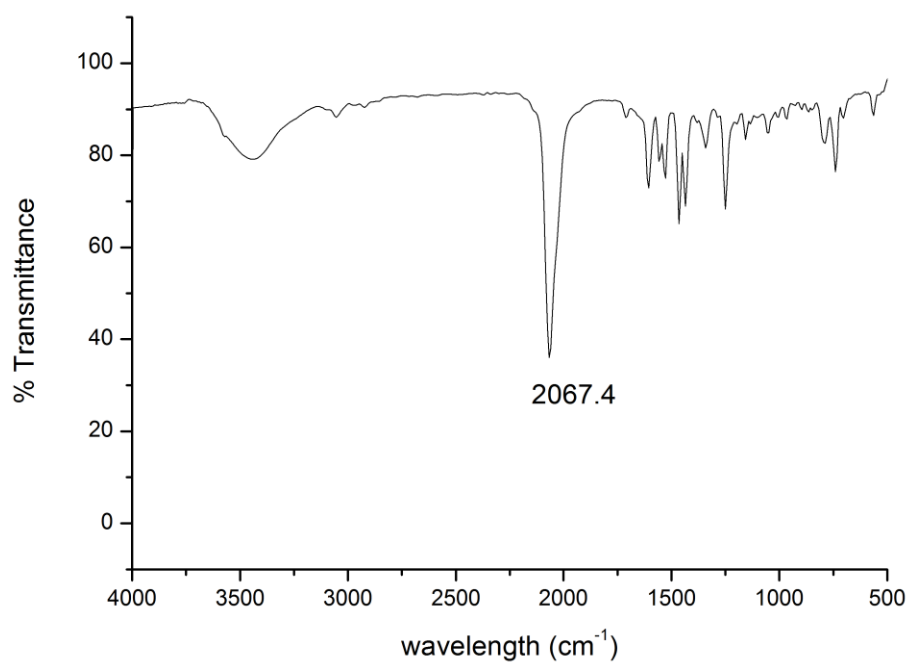


Figure 4.7d IR spectrum of **1d**.

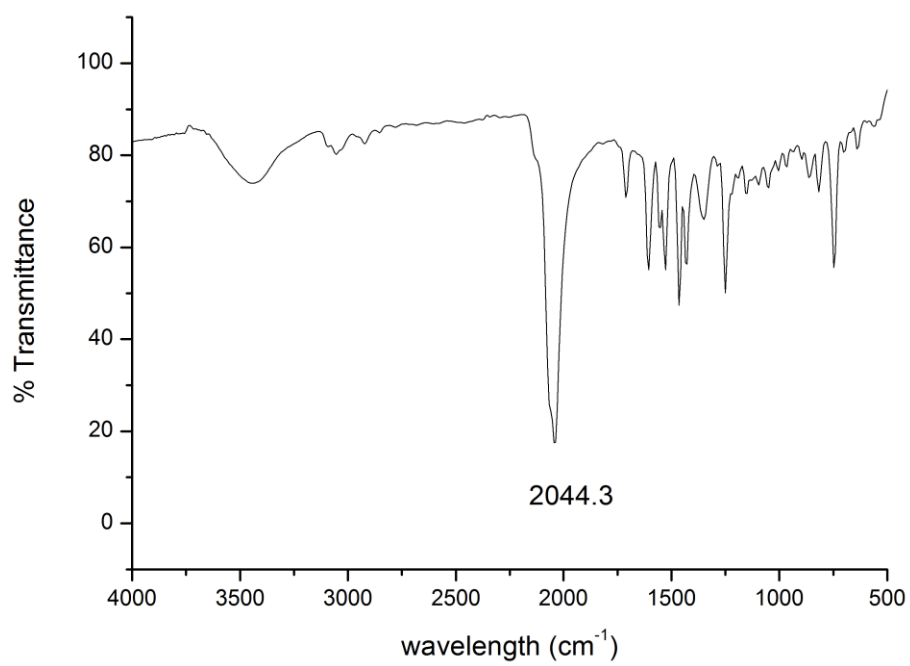


Figure 4.7e IR spectrum of **1e**.

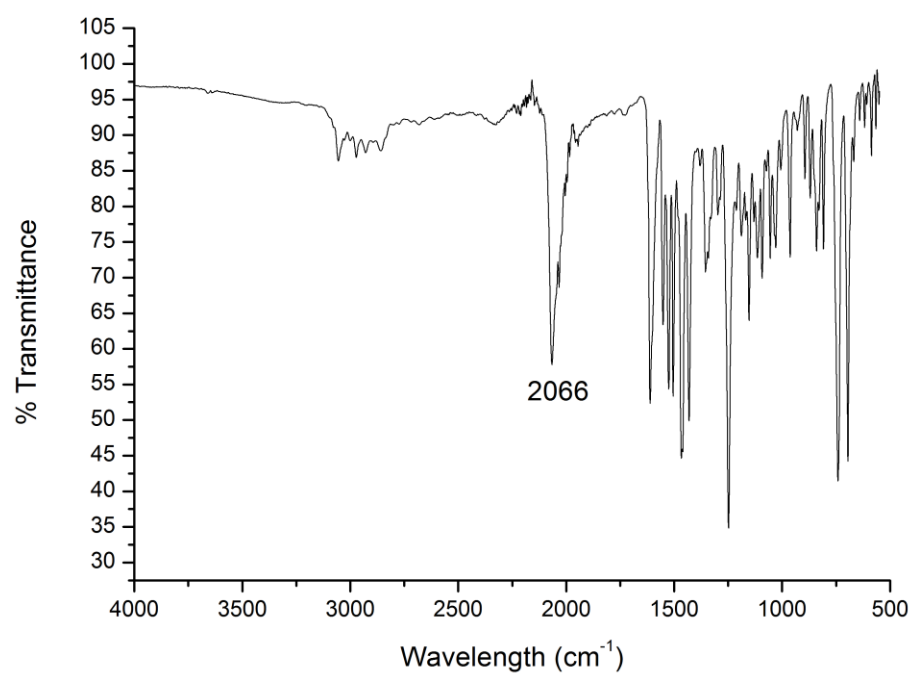


Figure 4.8a IR spectrum of **2a**.

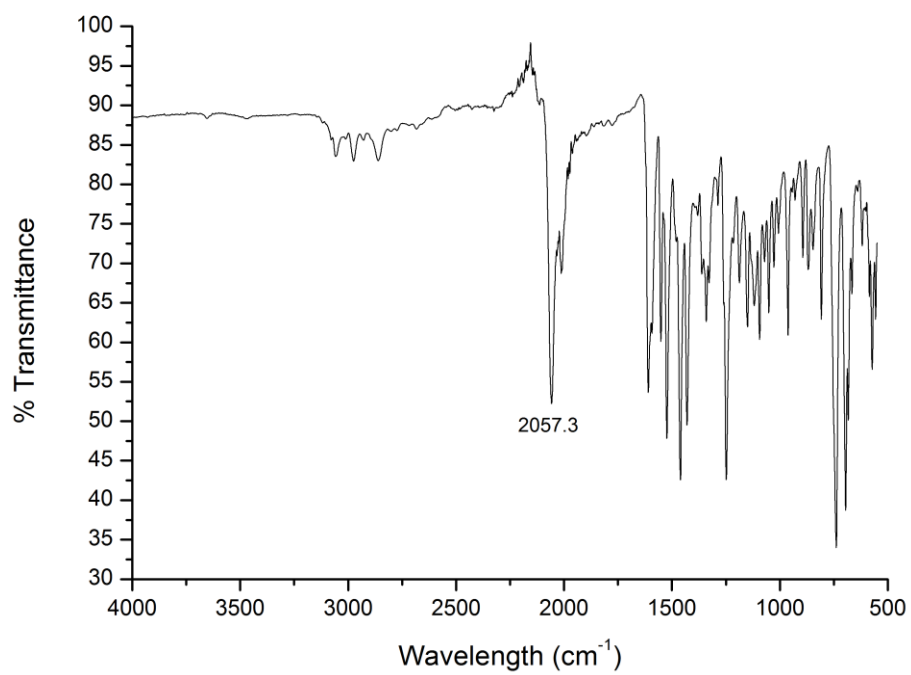


Figure 4.8b IR spectrum of **2b**.

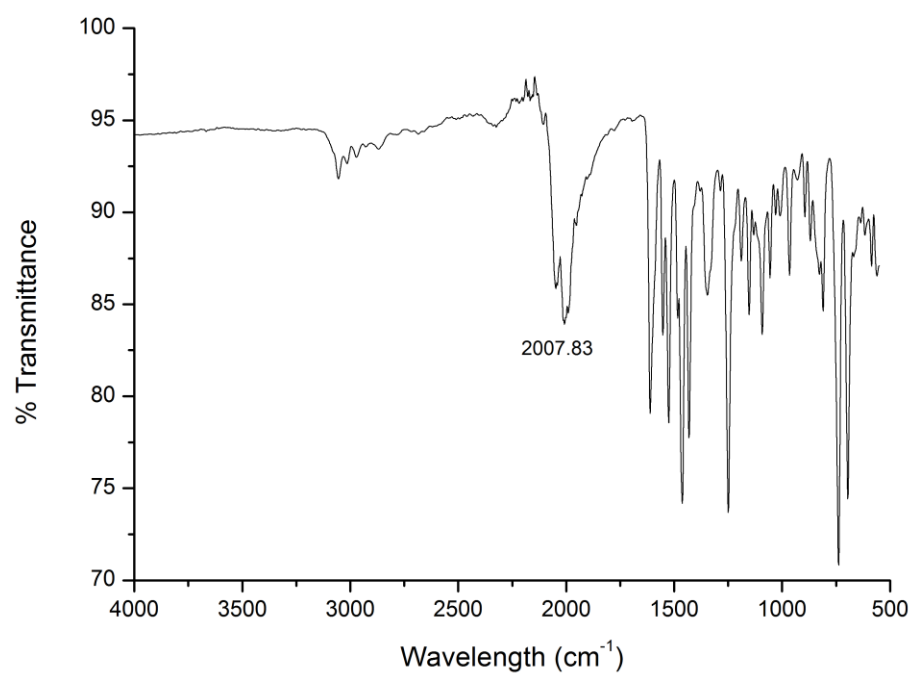


Figure 4.8c IR spectrum of **2c**.

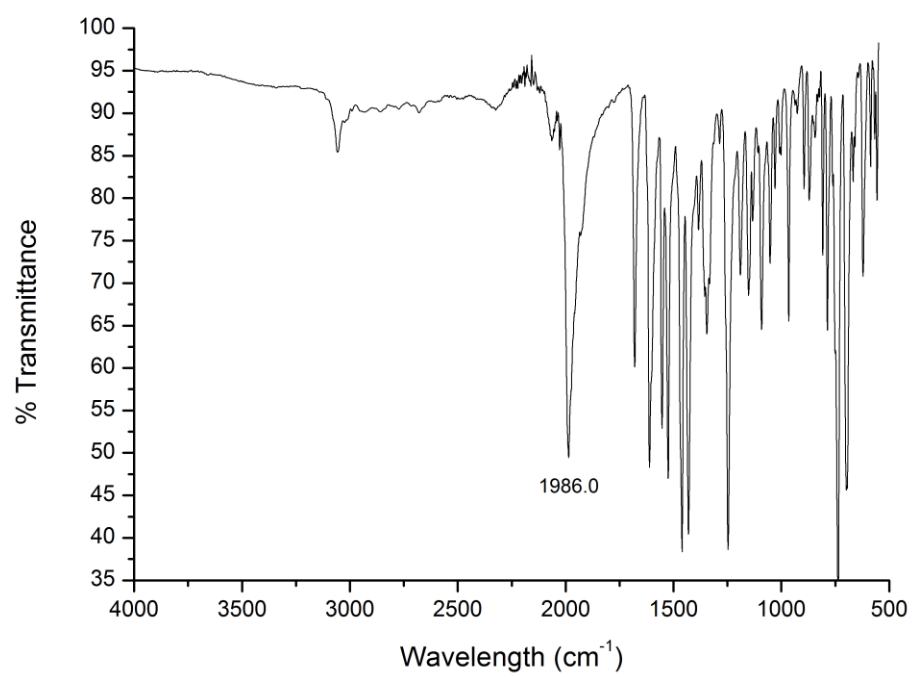


Figure 4.8d IR spectrum of **2d**.

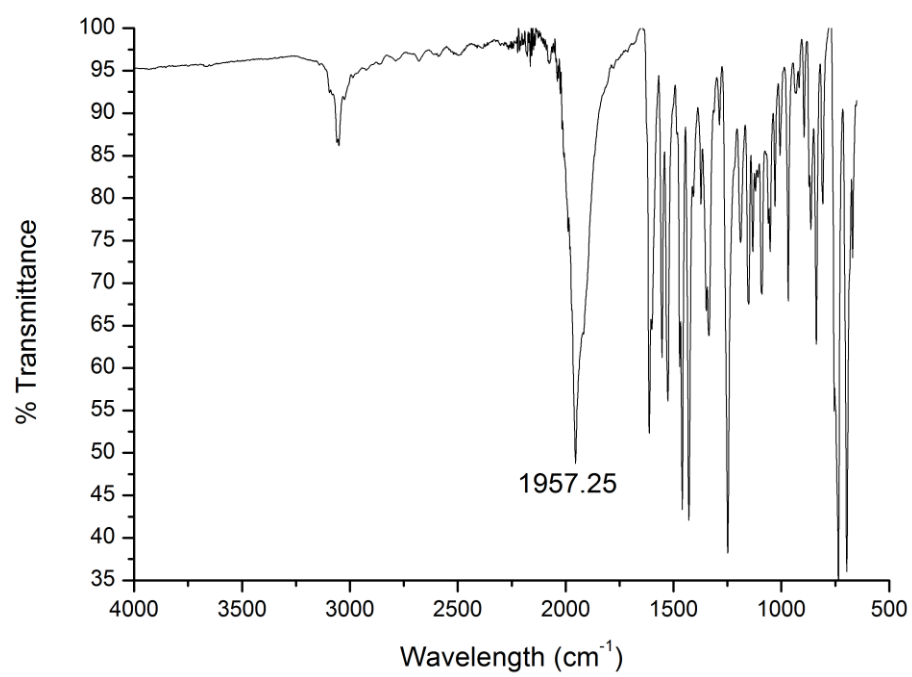


Figure 4.8e IR spectrum of **2e**.

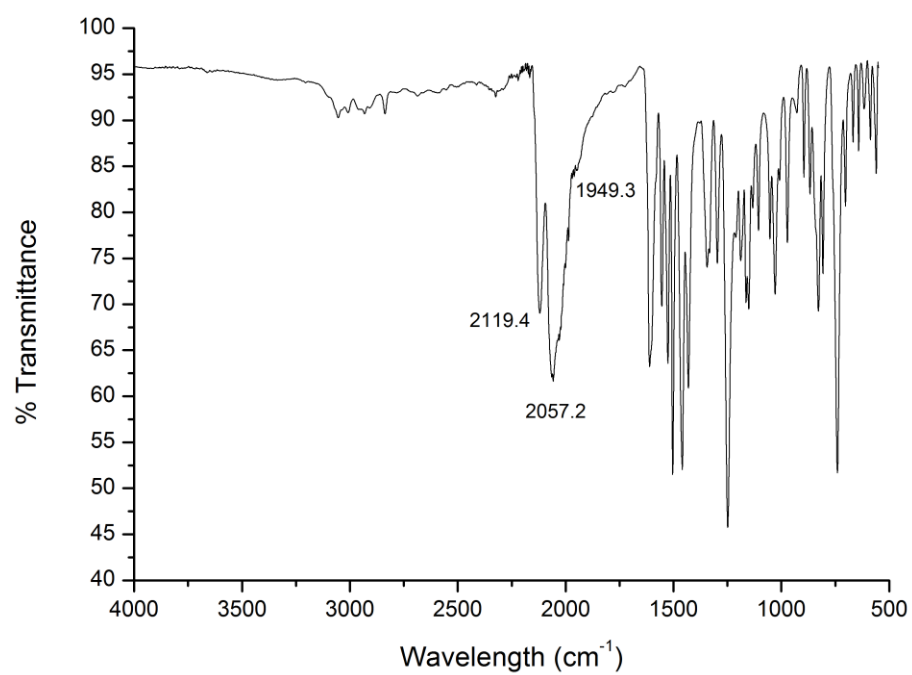


Figure 4.9a IR spectrum of **3a**.

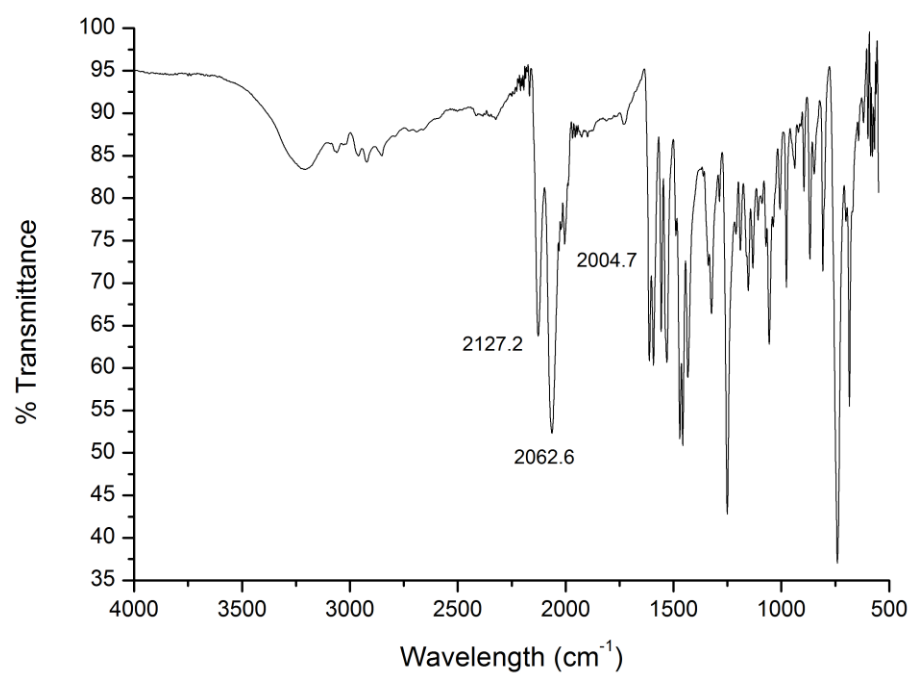


Figure 4.9b IR spectrum of **3b**.

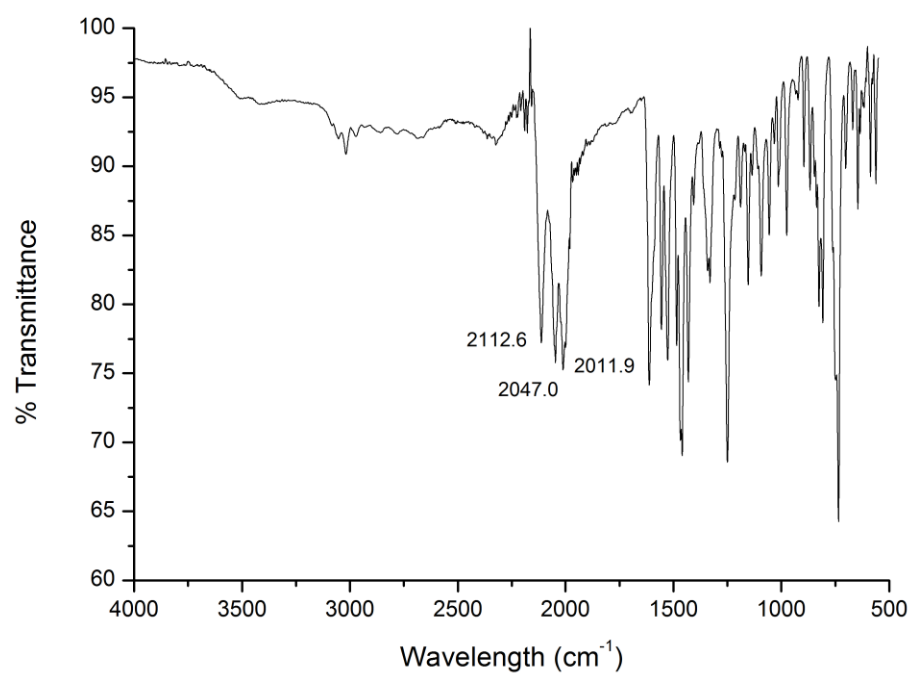


Figure 4.9c IR spectrum of **3c**.

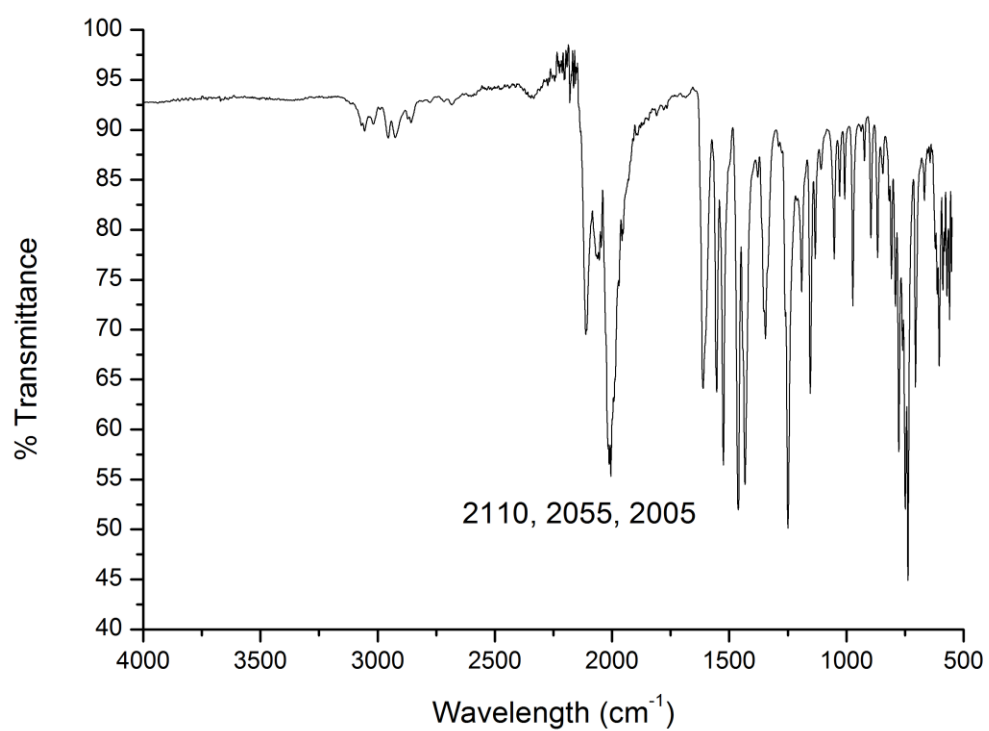


Figure 4.9d Figure IR spectrum of **3d**.

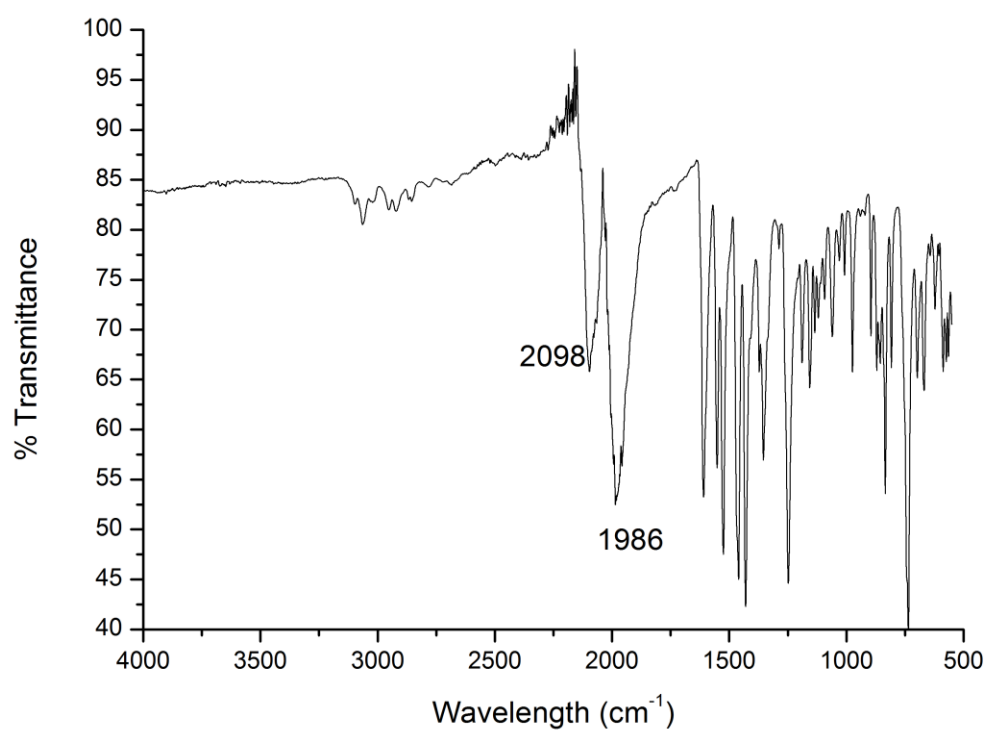


Figure 4.9e IR spectrum of **3e**.

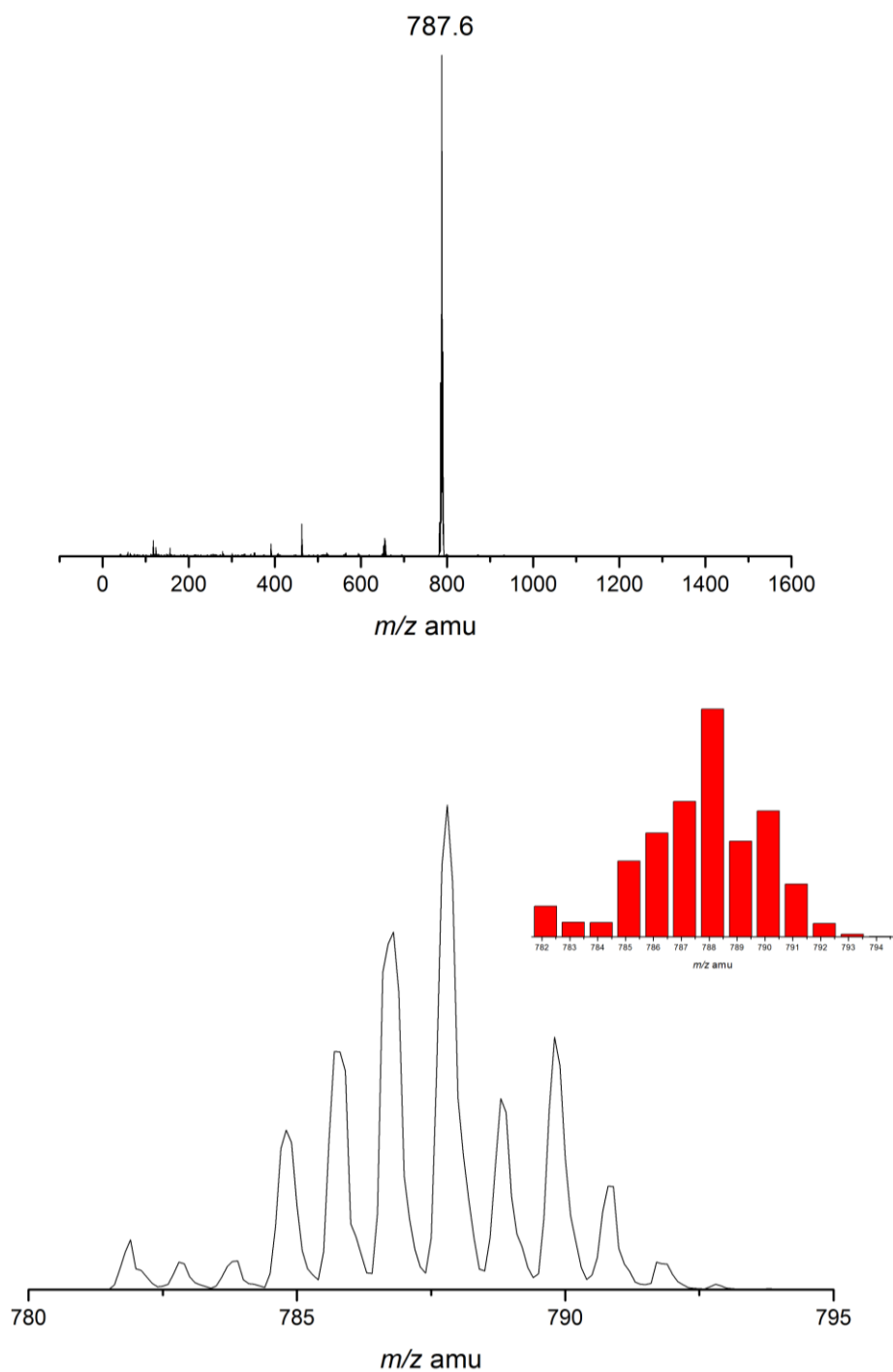


Figure 4.10a ESI-mass spectrum (+ve mode) of *trans,trans,trans*-[Ru^{II}(PBO)₂(MeOPhNC)₂] (**1a**) in dichloromethane. (below: experimental isotopic distribution patterns of $m/z = 787$; insert: simulated isotopic patterns at $m/z = 787$.)

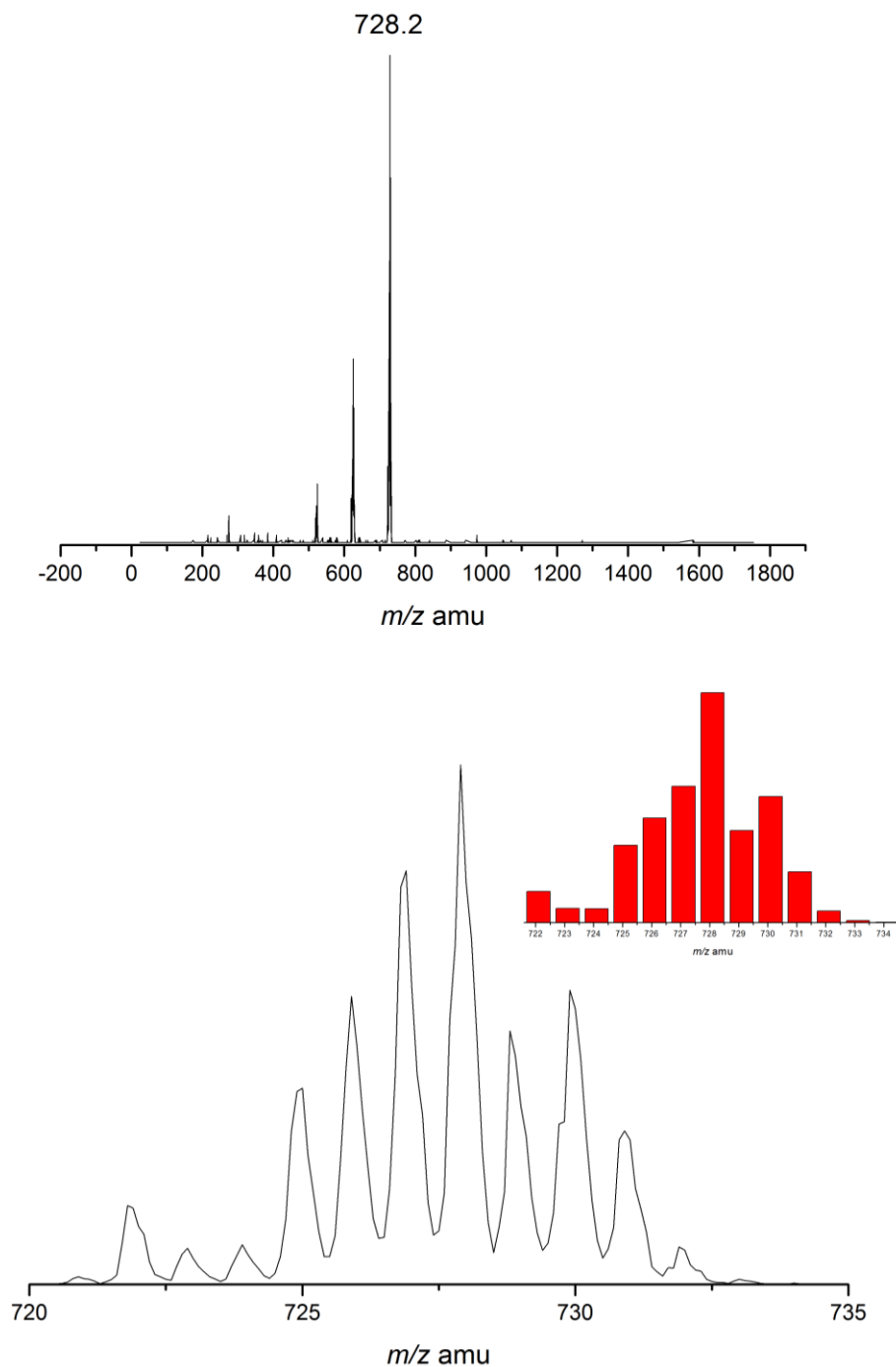


Figure 4.10b ESI-mass spectrum (+ve mode) of $\text{trans,trans,trans-[Ru}^{\text{II}}(\text{PBO})_2(\text{PhNC})_2]$ (**1b**) in dichloromethane. (below: experimental isotopic distribution patterns of $m/z = 728$; insert: simulated isotopic patterns at $m/z = 728$.)

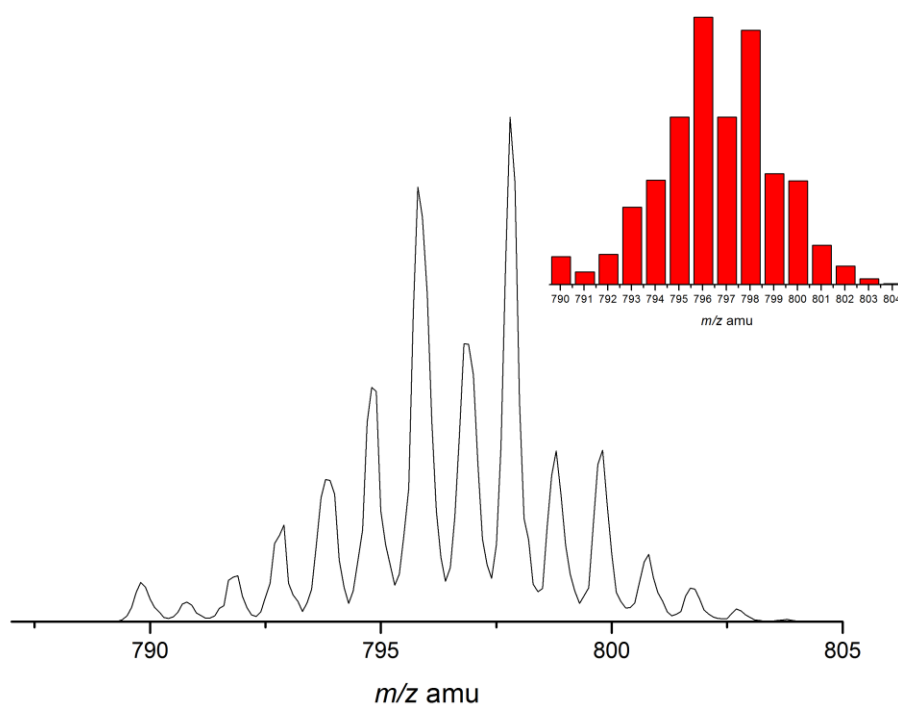
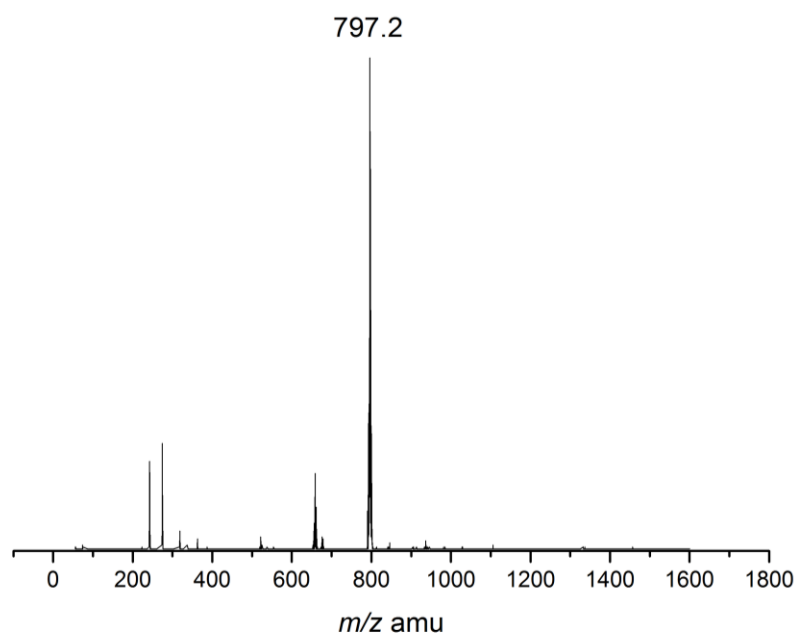


Figure 4.10c ESI-mass spectrum (+ve mode) of $\text{trans,trans,trans-[Ru}^{\text{II}}(\text{PBO})_2(\text{CIPhNC})_2]$ (**1c**) in dichloromethane. (below: experimental isotopic distribution patterns of $m/z = 796$; insert: simulated isotopic patterns at $m/z = 796$.)

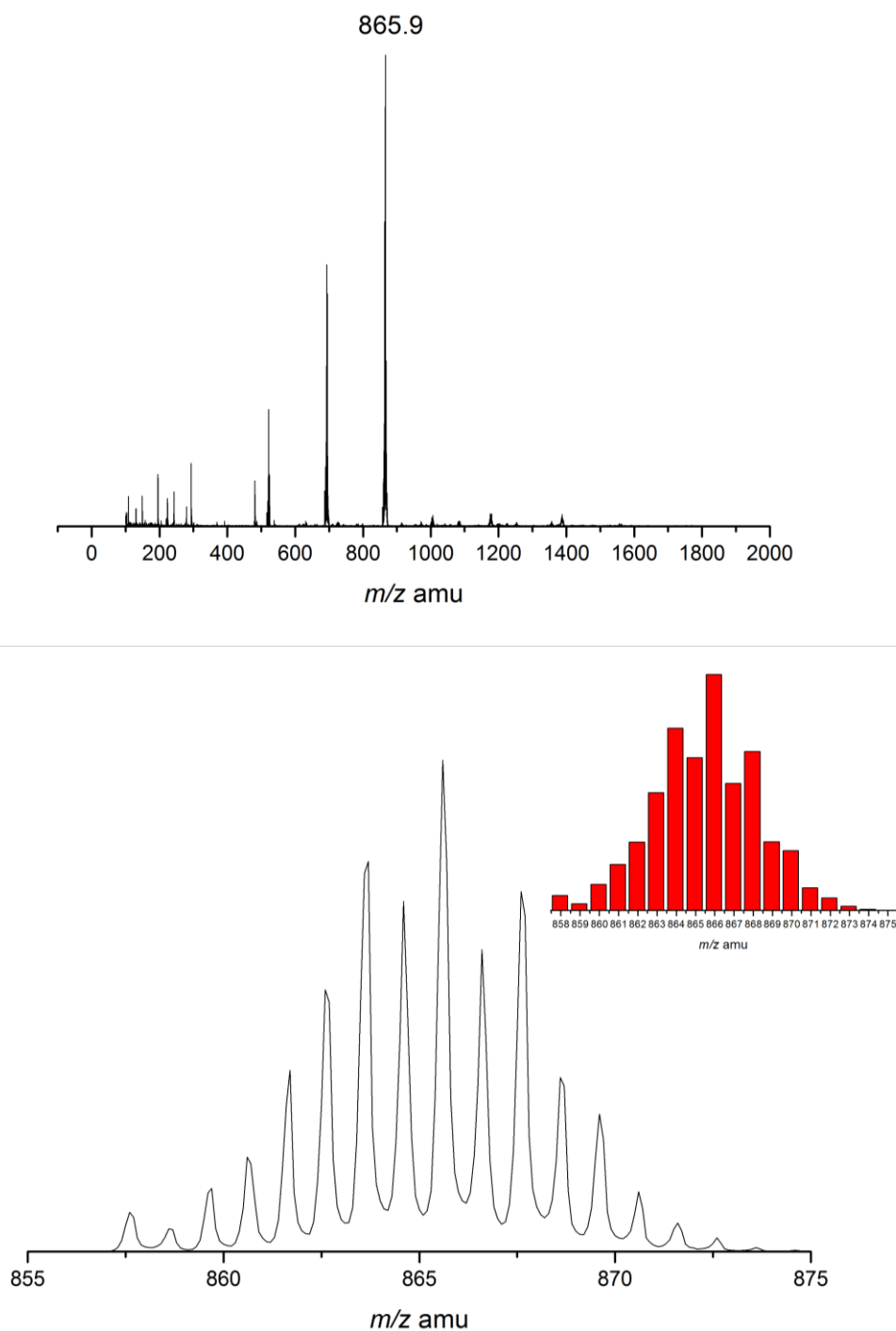


Figure 4.10d ESI-mass spectrum (+ve mode) of $\text{trans,trans,trans-[Ru}^{\text{II}}(\text{PBO})_2(\text{Cl}_2\text{PhNC})_2]$ (**1d**) in dichloromethane. (below: experimental isotopic distribution patterns of $m/z = 866$; insert: simulated isotopic patterns at $m/z = 866$.)

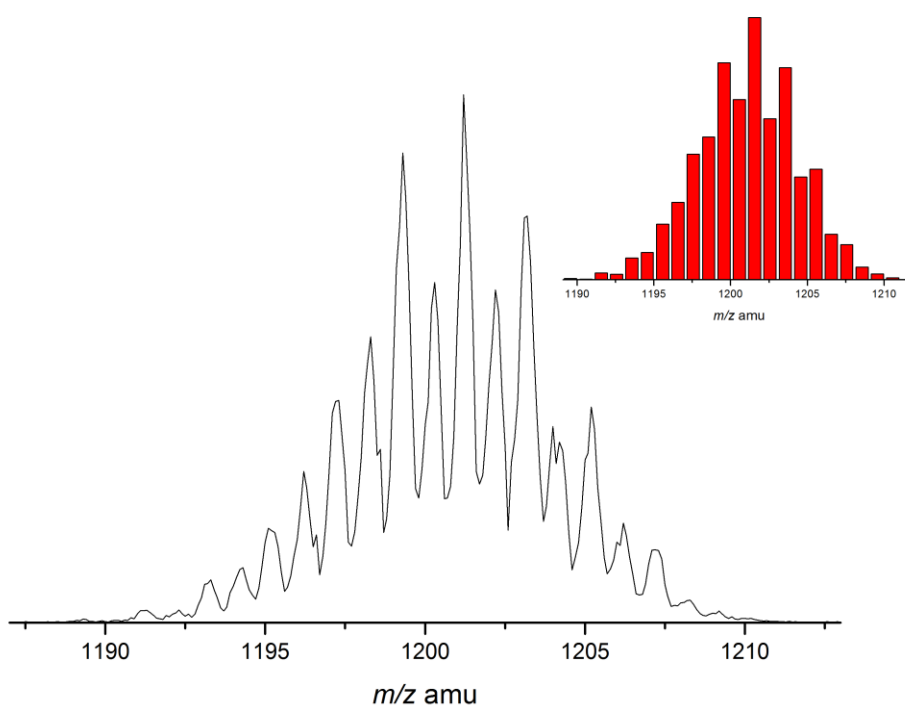
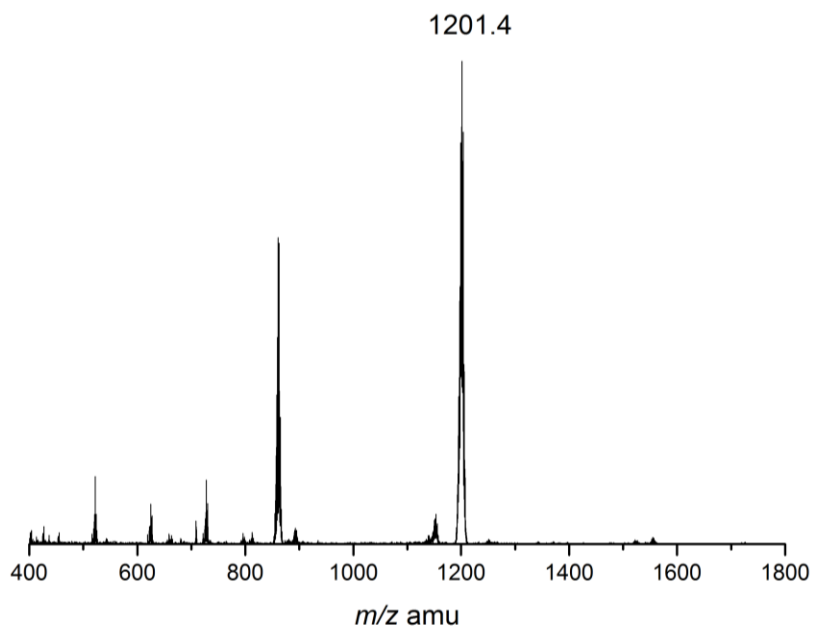


Figure 4.10e ESI-mass spectrum (+ve mode) of $\text{trans,trans,trans-[Ru}^{\text{II}}(\text{PBO})_2(\text{Br}_3\text{PhNC})_2]$ (**1e**) in dichloromethane. (below: experimental isotopic distribution patterns of $m/z = 1201$; insert: simulated isotopic patterns at $m/z = 1201$.)

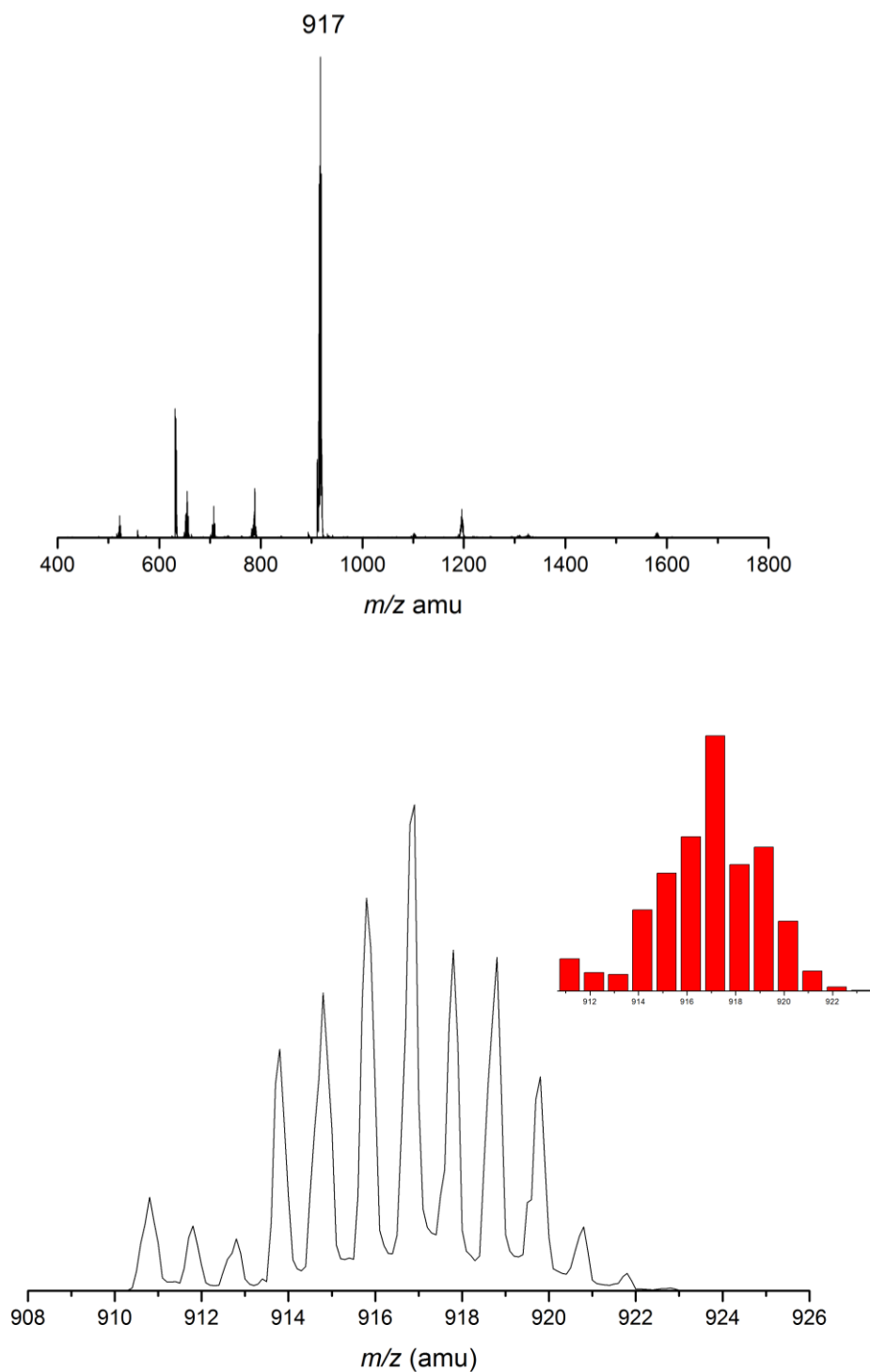


Figure 4.11a ESI-mass spectrum (+ve mode) of *cis,trans*-[Ru(PBO)₂(PPh₃)(MeOPhNC)] (**2a**) in dichloromethane. (below: experimental isotopic distribution patterns of *m/z* = 917; insert: simulated isotopic patterns at *m/z* = 917.)

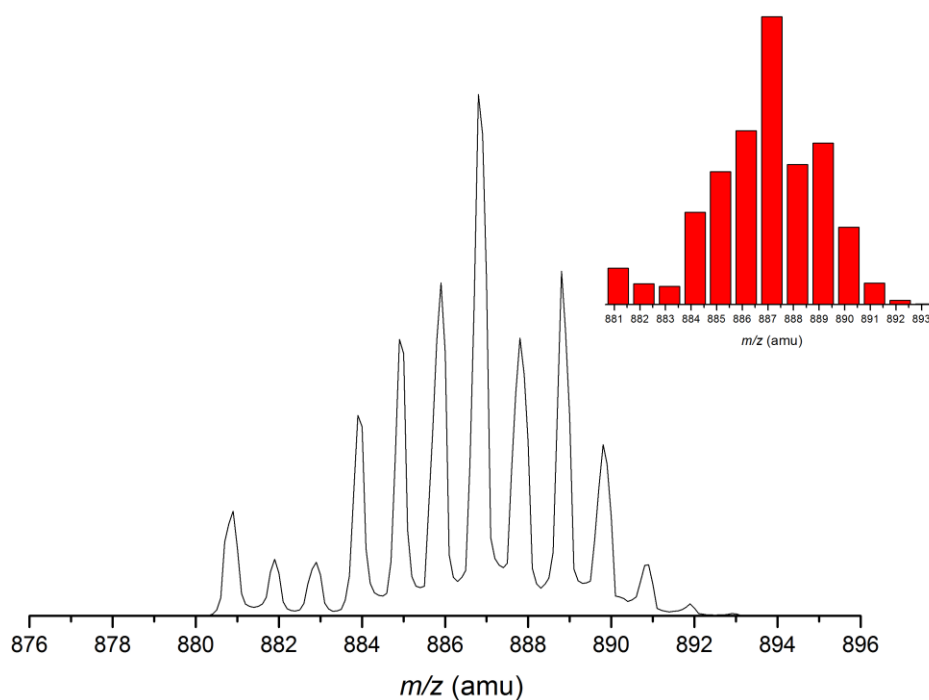
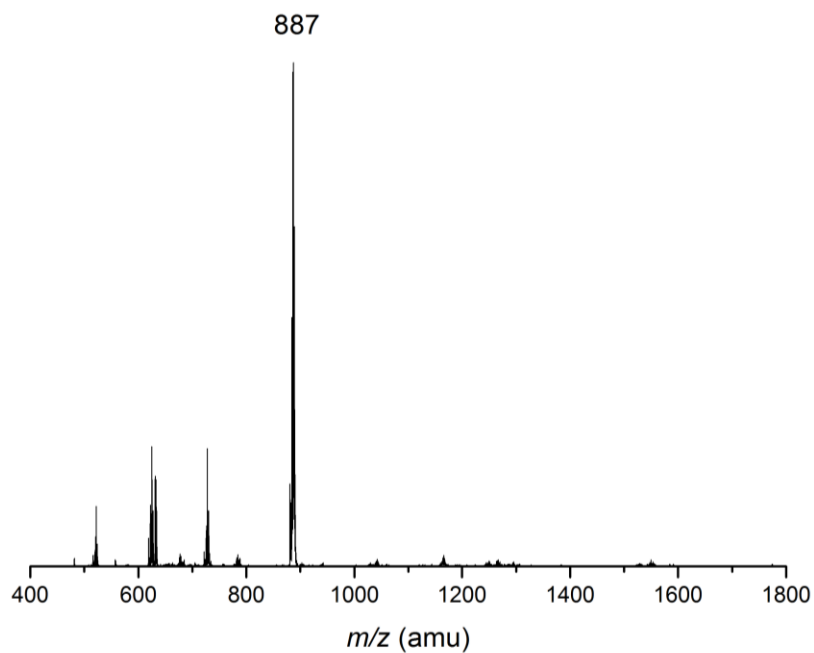


Figure 4.11b ESI-mass spectrum (+ve mode) of *cis,trans*-[Ru(PBO)₂(PPh₃)(PhNC)] (**2b**) in dichloromethane. (below: experimental isotopic distribution patterns of m/z = 887; insert: simulated isotopic patterns at m/z = 887.)

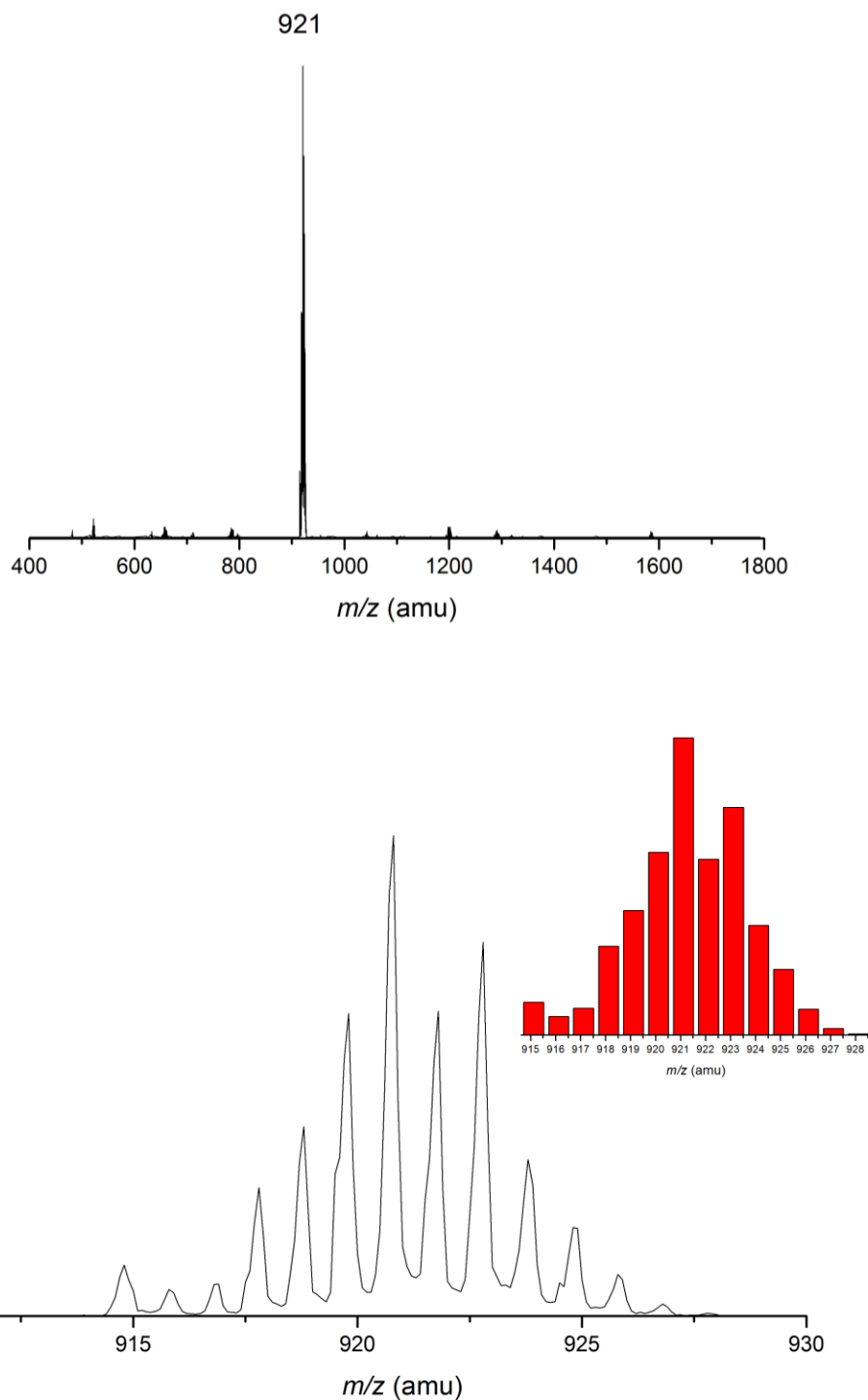


Figure 4.11c ESI-mass spectrum (+ve mode) of *cis,trans*-[Ru(PBO)₂(PPh₃)(ClPhNC)] (**2c**) in dichloromethane. (below: experimental isotopic distribution patterns of m/z = 921; insert: simulated isotopic patterns at m/z = 921.)

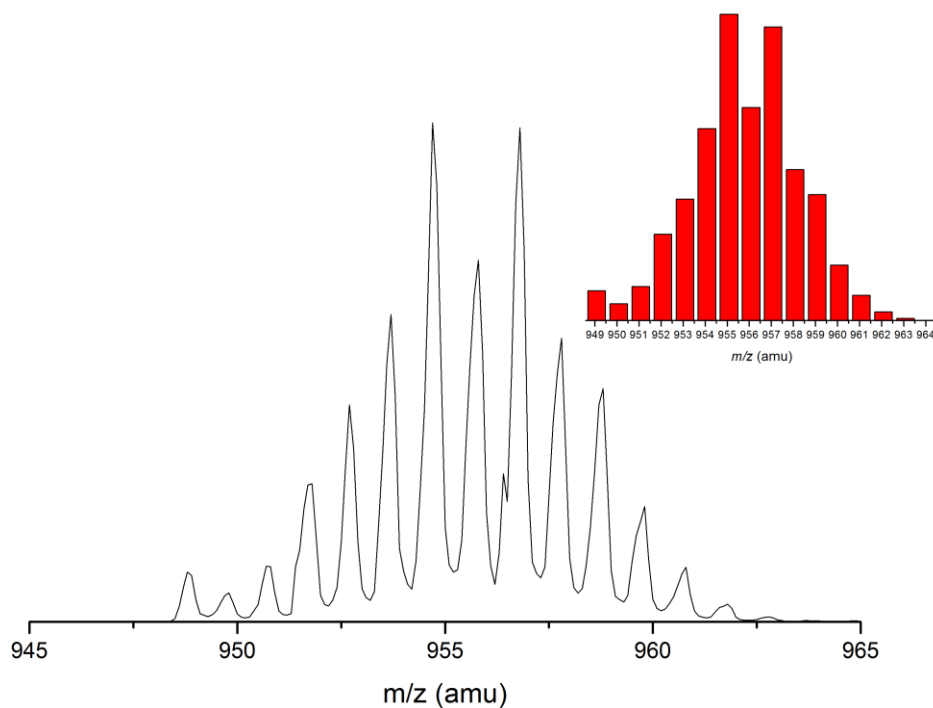
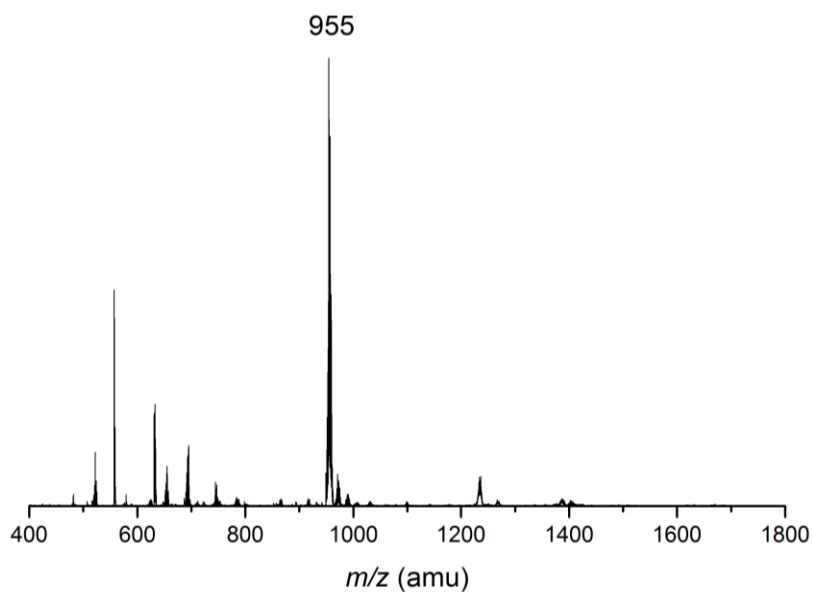


Figure 4.11d ESI-mass spectrum (+ve mode) of *cis,trans*-[Ru(PBO)₂(PPh₃)(Cl₂PhNC)] (**2d**) in dichloromethane. (below: experimental isotopic distribution patterns of $m/z = 955$; insert: simulated isotopic patterns at $m/z = 955$.)

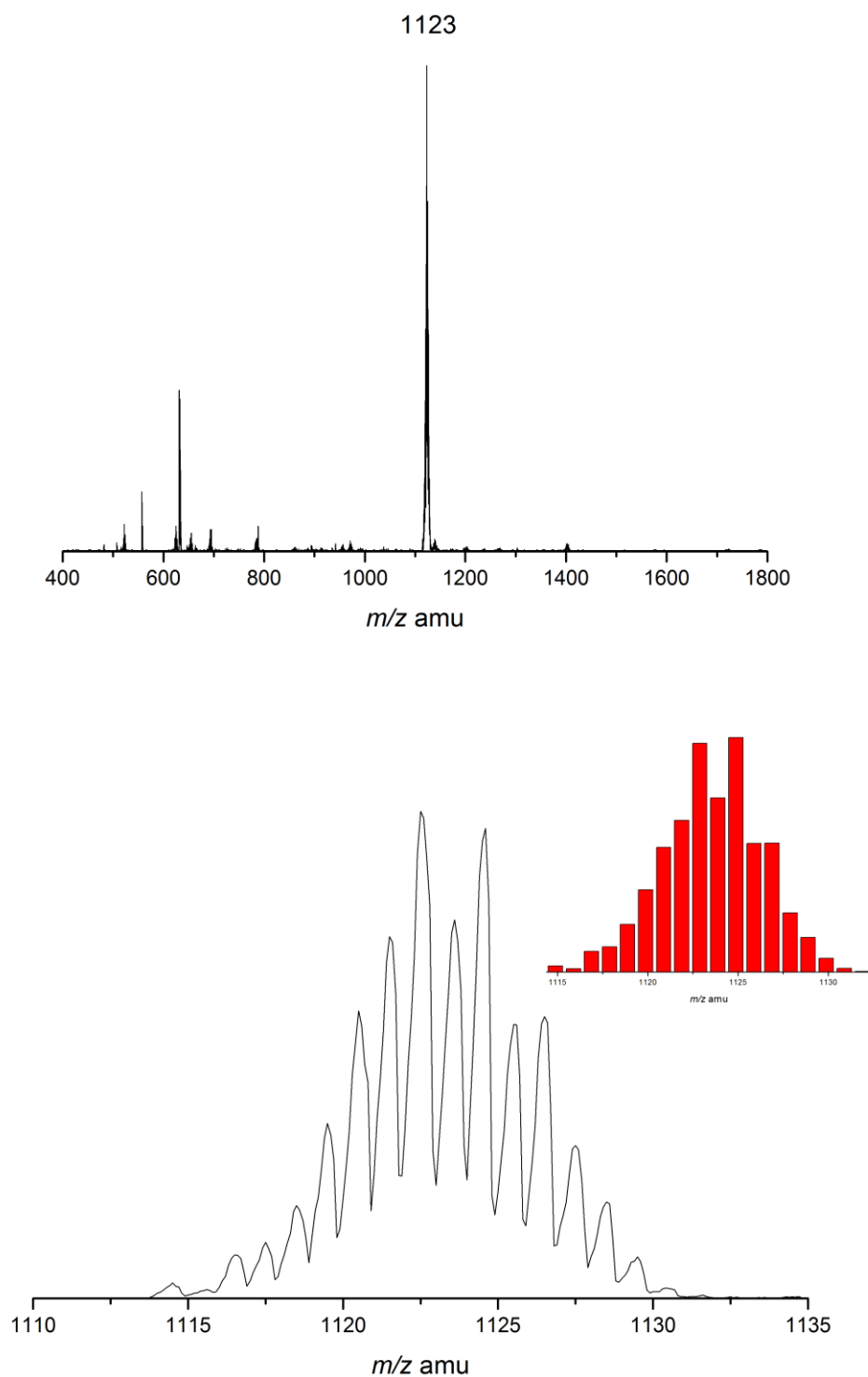


Figure 4.11e ESI-mass spectrum (+ve mode) of $cis,trans$ -[Ru(PBO)₂(PPh₃)(Br₃PhNC)] (**2e**) in dichloromethane. (below: experimental isotopic distribution patterns of $m/z = 1123$; insert: simulated isotopic patterns at $m/z = 1123$.)

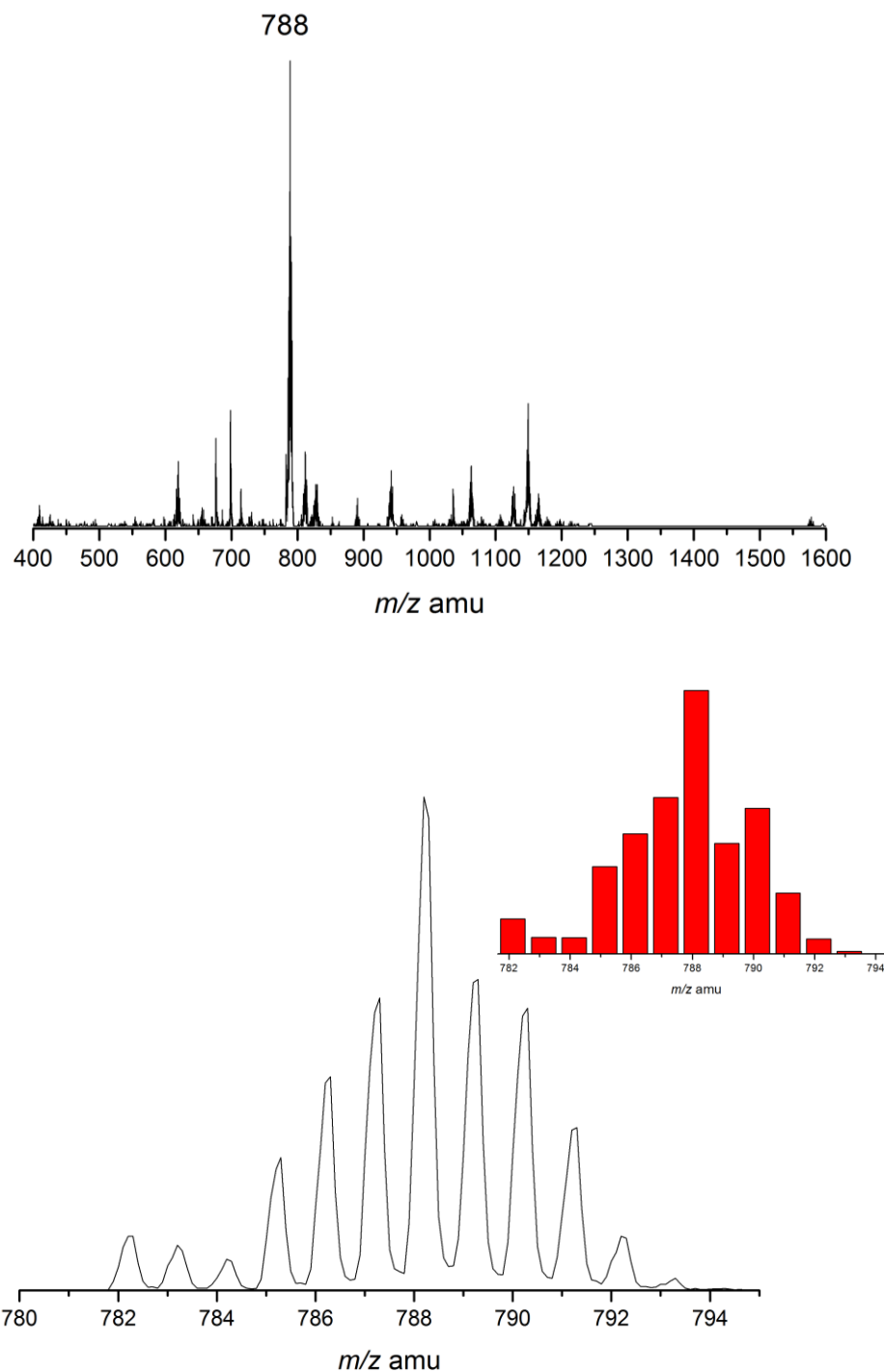


Figure 4.12a ESI-mass spectrum (+ve mode) of *cis,trans,cis*-[Ru(PBO)₂(MeOPhNC)₂] (**3a**) in dichloromethane. (below: experimental isotopic distribution patterns of $m/z = 788$; insert: simulated isotopic patterns at $m/z = 788$.)

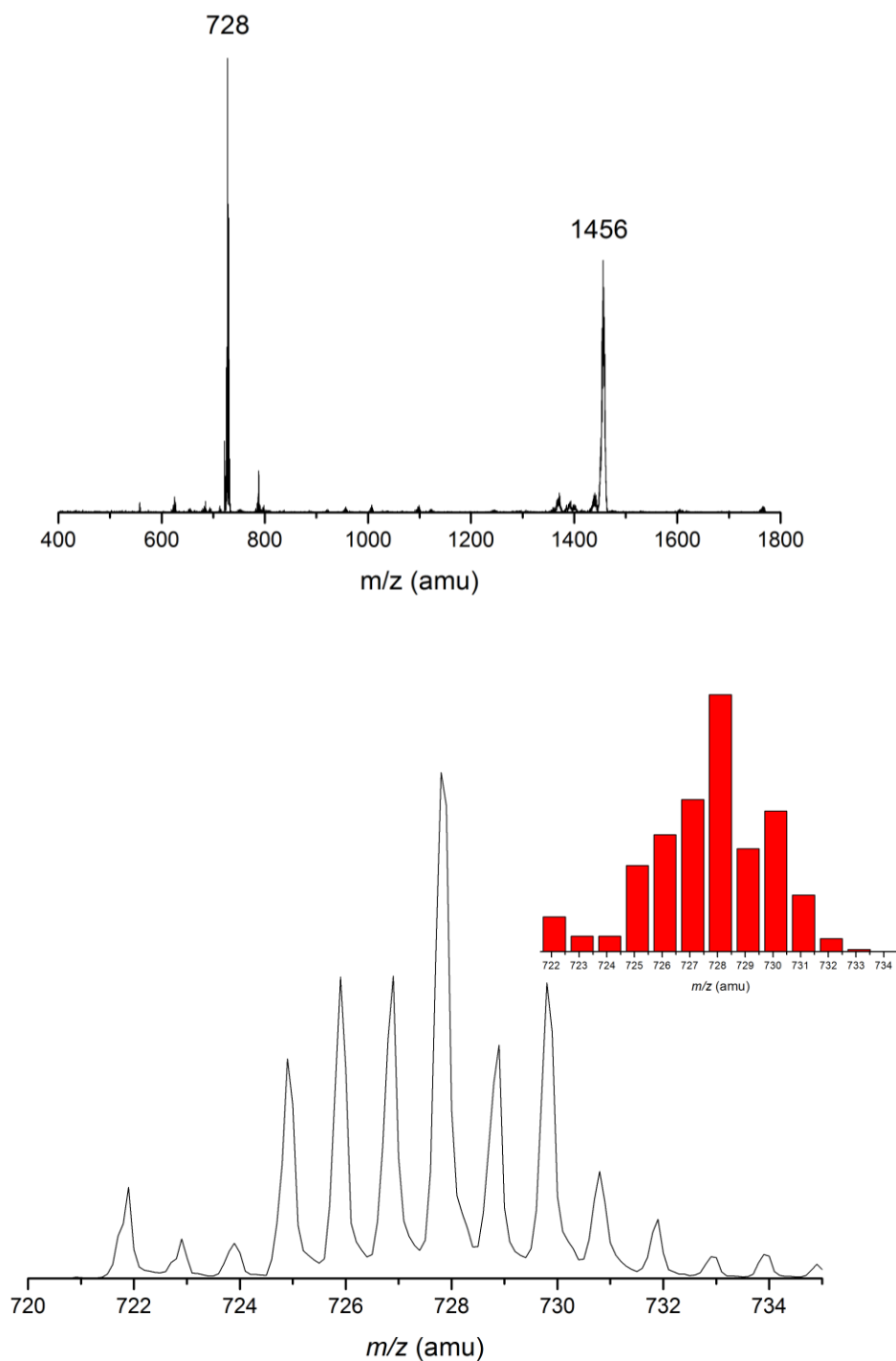


Figure 4.12b ESI-mass spectrum (+ve mode) of *cis,trans,cis*-[Ru(PBO)₂(PhNC)₂] (**3b**) in dichloromethane. (below: experimental isotopic distribution patterns of $m/z = 728$; insert: simulated isotopic patterns at $m/z = 728$.)

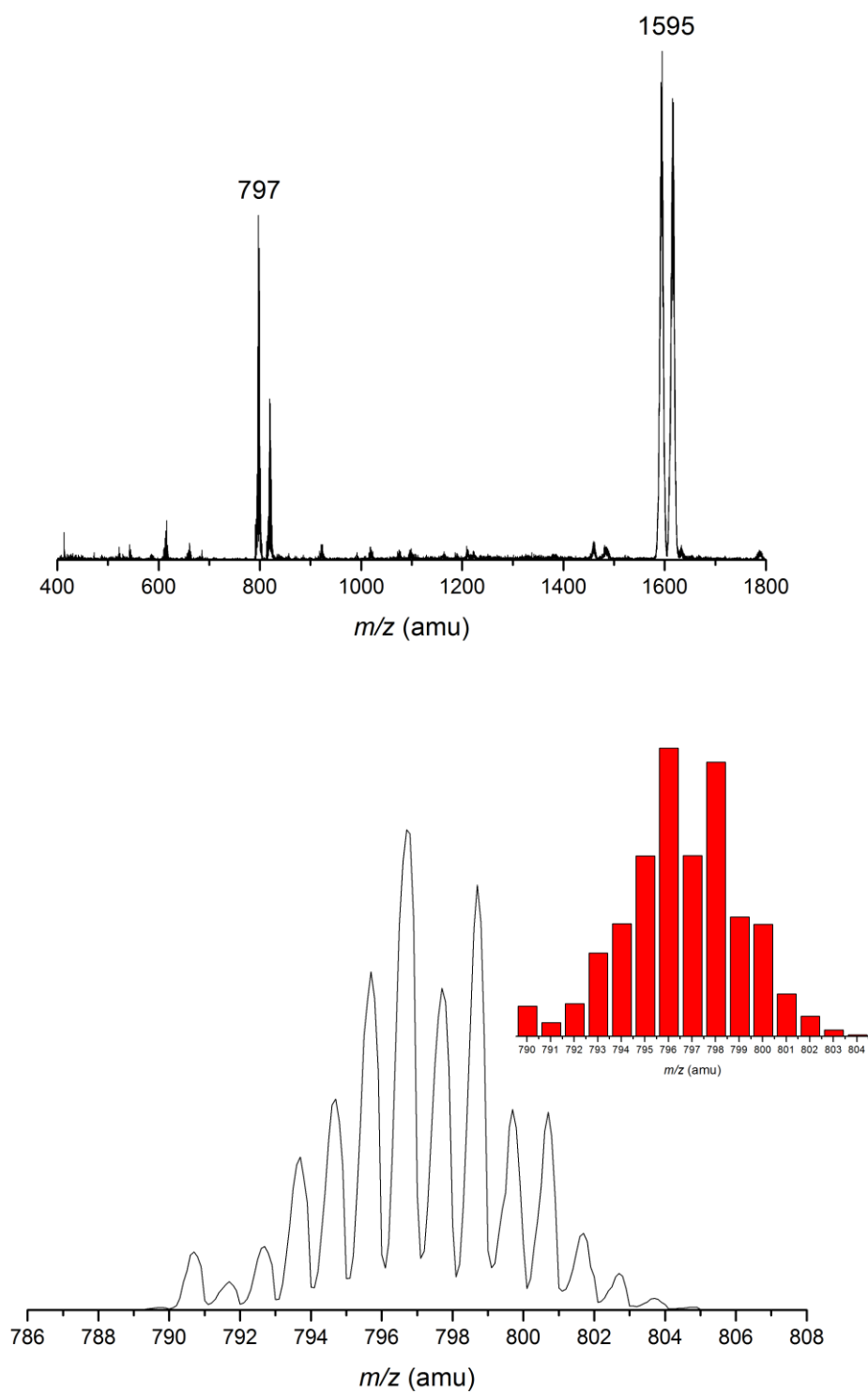


Figure 4.12c ESI-mass spectrum (+ve mode) of *cis,trans,cis*-[Ru(PBO)₂(ClPhNC)₂] (**3c**) in dichloromethane. (below: experimental isotopic distribution patterns of $m/z = 797$; insert: simulated isotopic patterns at $m/z = 797$.)

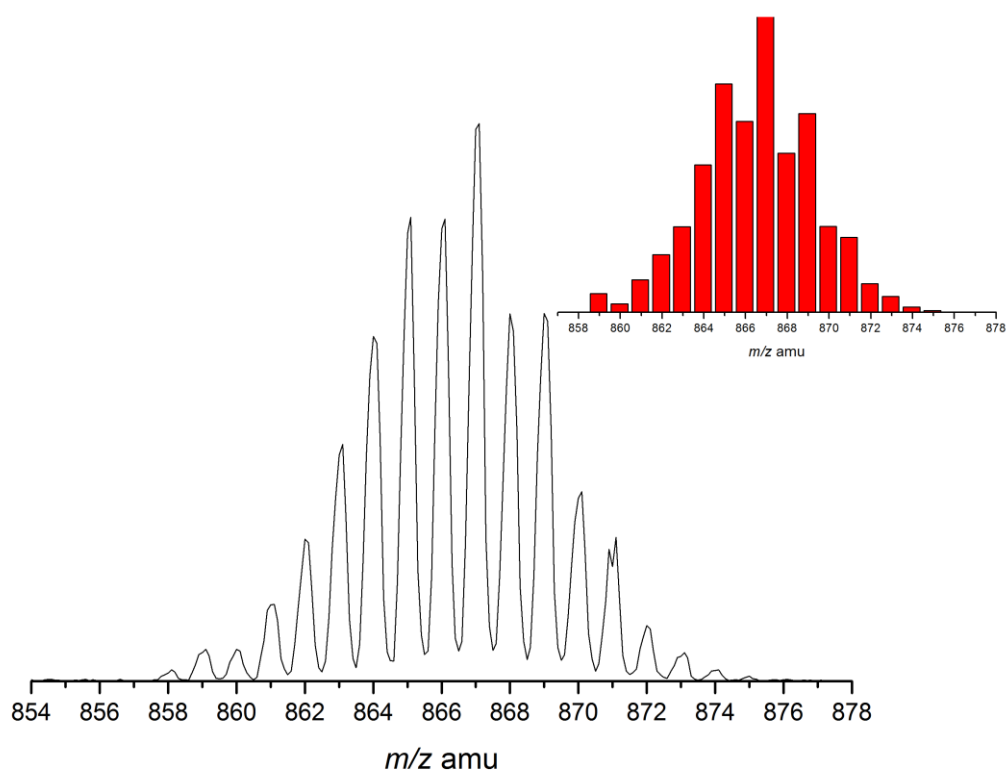
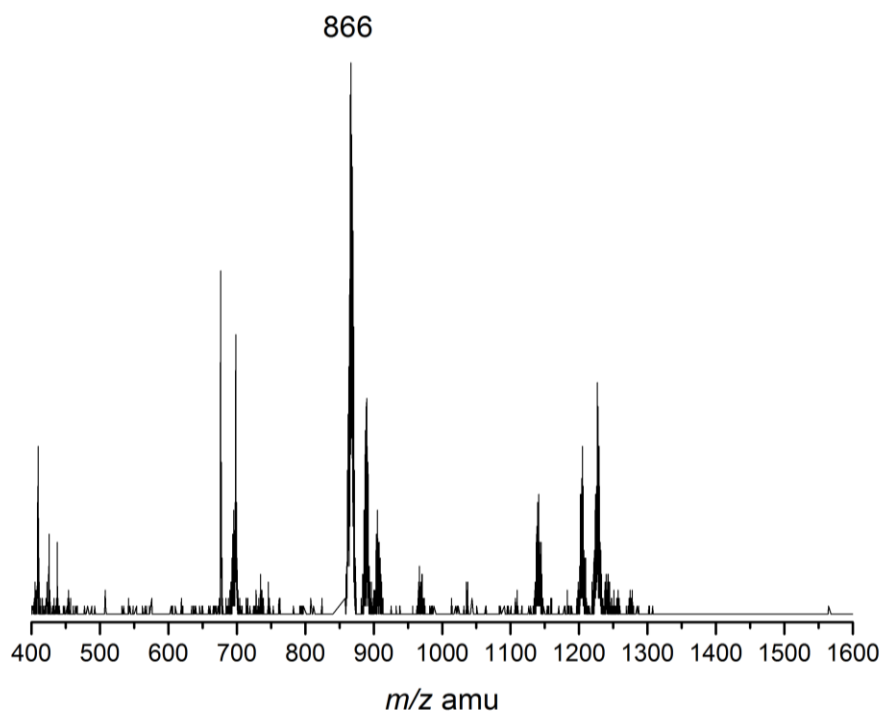


Figure 4.12d ESI-mass spectrum (+ve mode) of *cis,trans,cis*-[Ru(PBO)₂(Cl₂PhNC)₂] (**3c**) in dichloromethane. (below: experimental isotopic distribution patterns of $m/z = 866$; insert: simulated isotopic patterns at $m/z = 866$.)

4.3.2 X-ray Crystallography

Single crystals of **1b**, **1e**, **2c** and **3b** were obtained by recrystallization from of dichloromethane/*n*-hexane at room temperature in dark. The structures of the complexes were determined by X-ray crystallography. The crystal data and experimental details for are summarized in Table 4.1. Selected bond lengths and angles for complexes are given in Table 4.3 and their ORTEP drawings were shown in Figure 4.13.

As shown in their ORTEP drawings, ruthenium centers in **1b** and **1e** exhibit a slightly distorted octahedral geometry. The PBO ligands in the complexes are arranged in a *cis*-C, *cis*-N, *cis*-O configuration. The Ru–O and Ru–N bond lengths are in agreement with those in other Ru-PBO complexes, e.g. *trans*-[Ru(tolyterpy)(PBO)(Cl)](PF₆) (1.9623(6) Å),²²⁸ [Ru(terpy)(PBO)]Cl (2.101(4) Å)²³⁴ and [Ru(bpy)₂(PBO)](PF₆) (2.0569(18) Å).²³⁵ The Ru–C(isocyanide) (1.990(6) – 1.994(3) Å) and C≡N distances in (1.137(8) – 1.153(4) Å) are similar to that in *trans,trans,trans*-Ru(Q)₂(CNR)₂ (1.975(10) and 1.157(12) Å respectively, R = 2,4,6-Br₃Ph).

Ruthenium center in **2c** and **3b** exhibit also a distorted octahedral geometry. The two PBO ligands are arranged in the *trans*-N, *cis*-O configuration, while the isocyanide and phosphine are positioned *trans* to the O of the two auxiliary PBO ligands. Ru–C and C≡N distance in **2c** (1.871(2) and 1.181(3) Å respectively) and **3b** (1.887(2) and 1.175(3) Å respectively) are comparable to those in Ru(SQ)₂(PPh₃)(CNR) (1.862(4) – 1.901(3) Å and 1.166(8) – 1.182(4) Å respectively).²⁴⁵ In all the above complexes, the non-linear C≡N–C (166.7–179.4°) is attributed to the π-back bonding from the electron-rich Ru^{II} center to the anti-bonding π*-orbital of the C≡N triple bond.

Table 4.3a Selected bond lengths (Å) and bond angles (°) of **1b**.

bond lengths (Å) and bond angles (°)	
Ru(1)-C(1)	1.994(3)
Ru(1)-O(1)	2.0661(18)
Ru(1)-N(2)	2.089(2)
C(1)-N(1)	1.153(4)
N(1)-C(2)	1.399(3)
Ru(1)-C(1)-N(1)	173.6(2)
O(1)-Ru(1)-N(2)	88.11(8)
C(1)-N(1)-C(2)	175.8(3)

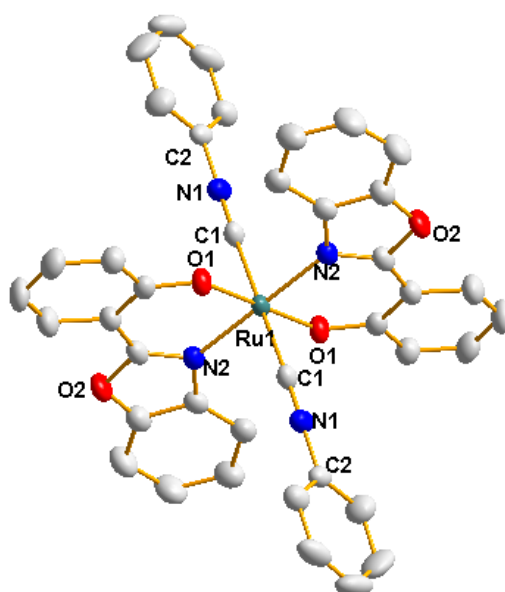


Figure 4.13a ORTEP drawing of **1b**. Thermal ellipsoids are drawn at the 50% probability (hydrogen atoms are omitted for clarity).

Table 4.3b Selected bond lengths (Å) and bond angles (°) of **1e**.

bond lengths (Å) and bond angles (°)	
Ru(1)-O(1)	2.079(4)
Ru(1)-O(3)	2.066(4)
Ru(1)-N(1)	2.069(5)
Ru(1)-N(2)	2.062(5)
Ru(1)-C(27)	1.993(6)
Ru(1)-C(34)	1.990(6)
C(27)-N(3)	1.137(8)
C(34)-N(4)	1.138(8)
N(3)-C(28)	1.385(7)
N(4)-C(35)	1.380(8)
Ru(1)-O(1)	2.079(4)
N(1)-Ru(1)-O(1)	87.9(18)
N(2)-Ru(1)-O(3)	87.13(19)
Ru(1)-C(34)-N(4)	178.5(5)
Ru(1)-C(27)-N(3)	176.3(6)
C(27)-N(3)-C(28)	175.2(7)
C(34)-N(4)-C(35)	179.4(6)

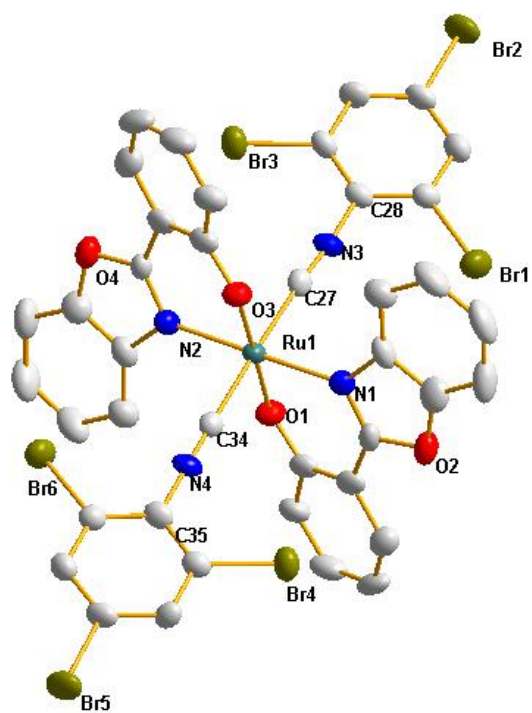


Figure 4.13b ORTEP drawing of **1e**. Thermal ellipsoids are drawn at the 50% probability.

Table 4.3c Selected bond lengths (Å) and bond angles (°) of **2c**.

bond lengths (Å) and bond angles (°)	
Ru(1)-O(1)	2.0944(16)
Ru(1)-N(1)	2.0804(19)
Ru(1)-P(1)	2.3231(6)
Ru(1)-C(27)	1.871(2)
Ru(1)-N(2)	2.0930(19)
Ru(1)-O(3)	2.1014(16)
N(3)-C(27)	1.181(3)
N(1)-Ru(1)-O(1)	87.63(7)
N(2)-Ru(1)-O(3)	84.36(7)
Ru(1)-C(27)-N(3)	175.9(2)
C(27)-N(3)-C(28)	166.7(2)

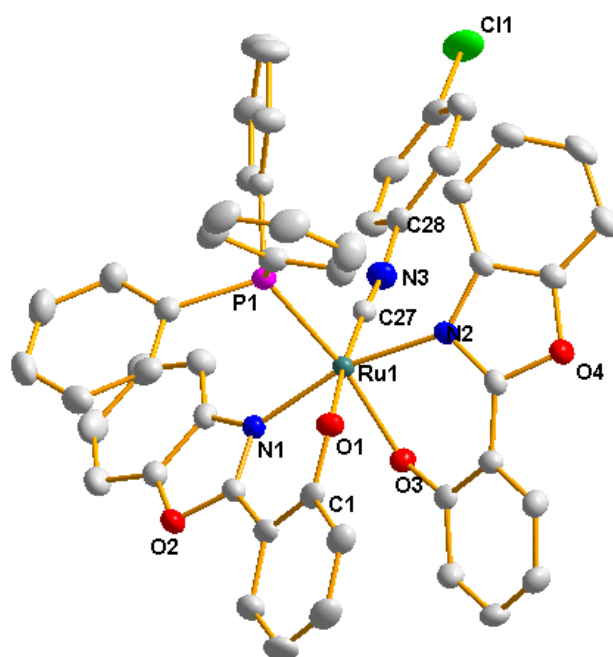


Figure 4.13c ORTEP drawing of **2c**. Thermal ellipsoids are drawn at the 50% probability.

Table 4.3d Selected bond lengths (Å) and bond angles (°) of **3b**.

	bond lengths (Å) and bond angles (°)
Ru(1)-C(1)	1.887(2)
Ru(1)-C(2)	1.900(2)
Ru(1)-N(3)	2.0759(8)
Ru(1)-O(1)	2.0695(16)
Ru(1)-O(3)	2.0710(15)
Ru(1)-N(4)	2.0669(18)
N(1)-C(3)	1.369(3)
N(2)-C(9)	1.386(3)
C(1)-N(1)	1.175(3)
C(2)-N(2)	1.162(3)
Ru(1)-C(1)-N(1)	173.8(2)
Ru(1)-C(2)-N(2)	176.4(2)
O(1)-Ru(1)-N(3)	88.43(7)
O(3)-Ru(1)-N(4)	88.35(7)
C(1)-N(1)-C(3)	161.7(2)
C(2)-N(2)-C(9)	174.1(2)

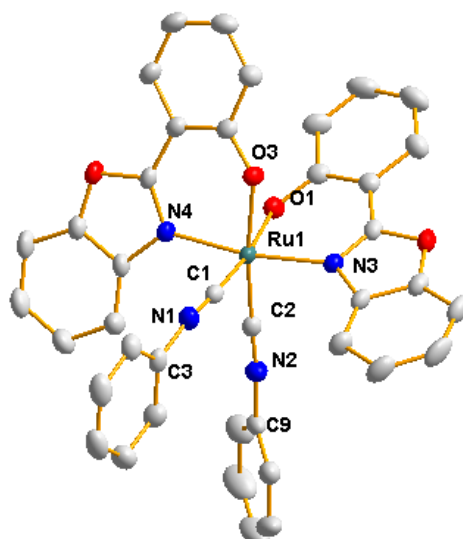


Figure 4.13d ORTEP drawing of **3b**. Thermal ellipsoids are drawn at the 50% probability.

4.3.3 Electronic Absorption and Luminescent Properties of **1**, **2** and **3**

The absorption spectra for **1** – **3** are shown in Figure 4.14 and their photophysical data are summarized in Table 4.4. The electronic spectra of the *trans, trans, trans*- diisocyano complexes (**1a** – **e**) exhibit a higher energy absorption at approx. 330 nm with a ϵ of $10^5 \text{ M}^{-1} \text{ cm}^{-1}$ which is assigned tentatively as the ligand-centered π -to- π^* transition of the BPO and isocyanides. A broad shoulder peak (ϵ of $10^4 \text{ M}^{-1} \text{ cm}^{-1}$) is observed at lower energy region (444 – 449 nm) for **1a** – **c**. The lower-energy peak become more distinct (ϵ of $10^5 \text{ M}^{-1} \text{ cm}^{-1}$) and blue-shifted (420 and 430 nm respectively), when more electrophilic isocyanide ligands, i.e. 2,6-dichloro- and 2,4,6-tribromophenisocyanide (**1d** and **1e**), were introduced. Two closely located bands are observed for the *trans, cis*- isocyano phosphine complexes (**2a** – **e**) at the range of 320 – 344 and 384 – 389 nm respectively, probably resulted from the mixed ligand-centered absorption of the triphenylphosphine, BPO and isocyanides. A moderate absorption, which is insensitive to electronic properties of the isocyanide ligands, is observed at 430 nm. The *cis, trans, cis*- diisocyano complexes (**3a** – **e**) exhibit a ligand-centered absorption (ϵ of $10^5 \text{ M}^{-1} \text{ cm}^{-1}$) peaking similarly at 320 – 325 nm are also observed. The absorption at 420 nm is also insensitive to electronic properties of the isocyanide ligands, as in **2a** – **e**.

The emission characteristics of **1-3** in EtOH/MeOH (4:1) glass at 77K were summarized in Table 4.4 with normalized emission spectra shown in Figure 4.15. The emission characteristics of the *cis, trans, cis*- (**3a** – **c**) and *trans, trans, trans*- (**1a** – **e**) diisocyano complexes in EtOH-MeOH glass (77K) are shown in the above tables. The emission maxima of the *cis, trans, cis*- and *trans, trans, trans*- isomers with identical substituents are very similar. The emission peaks for the complexes with stronger electron withdrawing substituents are slightly blue-shifted

compared to the electron donating ones. The emission lifetime of the three *cis*, *trans*, *cis*- isomers are similar, which is slightly longer for the electron withdrawing substituents. In contrast, the lifetime (and the emission intensity) of the *trans*, *trans*, *trans*- isomer increases significantly when the substituents is changed from electron donating substituents to electron withdrawing ones. For *trans*, *cis*- isocyano phosphine complexes with less electron withdrawing isocyanide substituents (**2a – c**), there are also strong structured emissions at similar wavelengths with the diisocyano complexes, and the emission lifetimes are comparable to those observed for the *cis*- isomers.

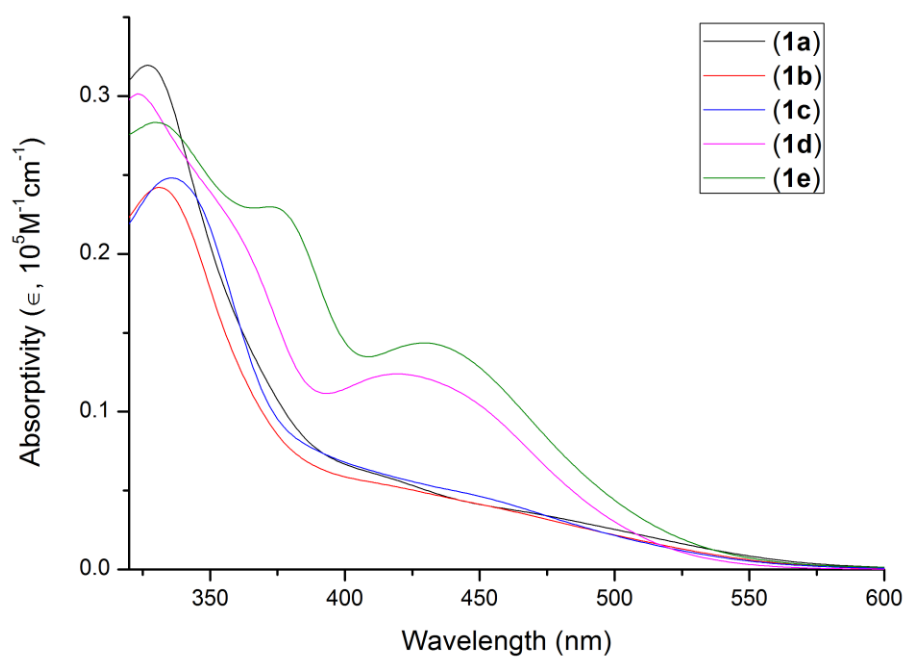


Figure 4.14a UV-Vis spectrum of complexes **1a** – **e** in dichloromethane at 298 K.

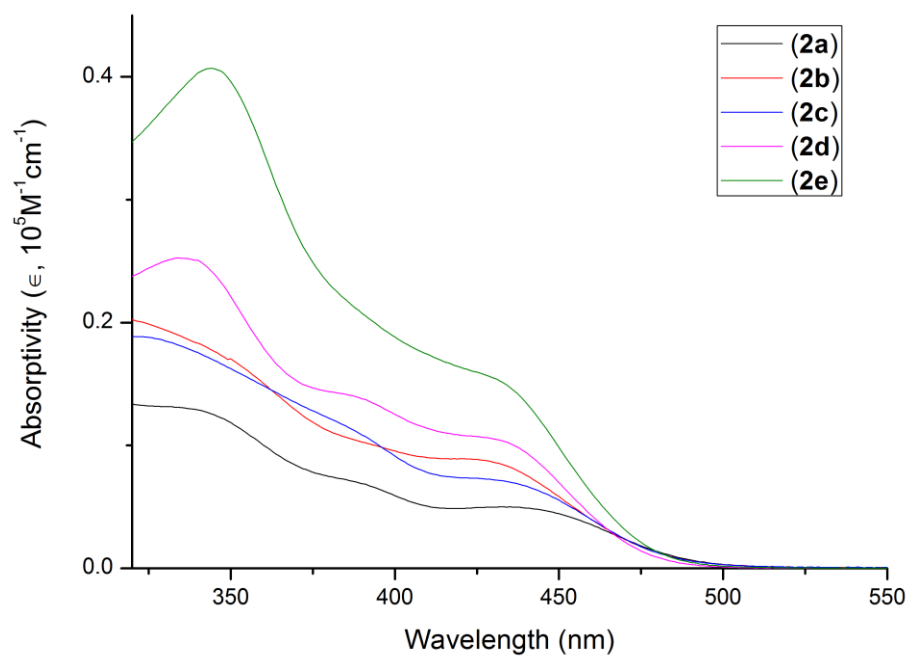


Figure 4.14b UV-Vis spectrum of complexes **2a** – **e** in dichloromethane at 298 K.

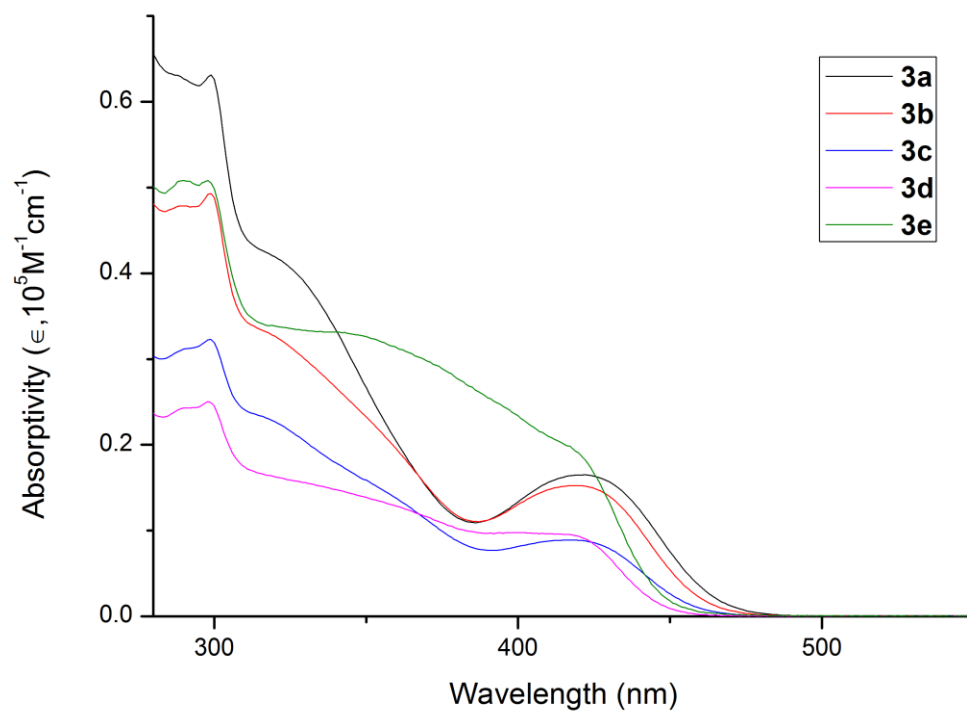


Figure 4.14c UV-Vis spectrum of complexes **3a** – **c** in dichloromethane at 298 K.

Table 4.4 Photophysical properties of complexes **1-3**.

	Absorption/nm ($\epsilon/M^{-1} \text{ cm}^{-1}$) ^a	Emission/nm ($\tau_0/\mu\text{s}$) ^b
1a	326 (31780), 445 sh (4290)	526, 562 (9.2)
1b	331 (24350), 444 sh (4202)	513, 559 (4.8)
1c	337 (24990), 449 sh (4600)	516, 552, 607 sh (30.1)
1d	323 (30220), 354 sh (22860), 420 (12390)	499, 536, 578 sh (58.3)
1e	329 (28420), 375 (22950), 430 (14424)	499,535, 579 sh (95.6)
2a	334 (13130), 387 sh (7130), 431 sh (5570)	522, 560 (33.3)
2b	335 (18800), 432 sh (8850)	518, 556 (42.0)
2c	328 (18680), 384 sh (11700), 434 sh (7030)	514, 553 (45.1)
2d	335 (25240), 389 sh (13830), 434 sh (10360)	non-emissive
2e	344 (40750), 433 (15130)	non-emissive
3a	325 sh (40480), 421 (16680)	521, 560, 610 sh (34.1)
3b	324 sh (31470), 420 (15260)	517, 554, 606 sh (42.9)
3c	321 sh (22420), 419 (9040)	516, 552, 604 sh (47.6)
3d	328 sh (15700), 418 sh (9470)	501,537,584 sh (94.4)
3e	340 sh (33150), 419 sh (19200)	500,534,581 sh (94.2)

^aIn dichloromethane at 298 K. ^bExcitation at 400 nm in EtOH/MeOH (4:1, v/v) glass at 77 K.

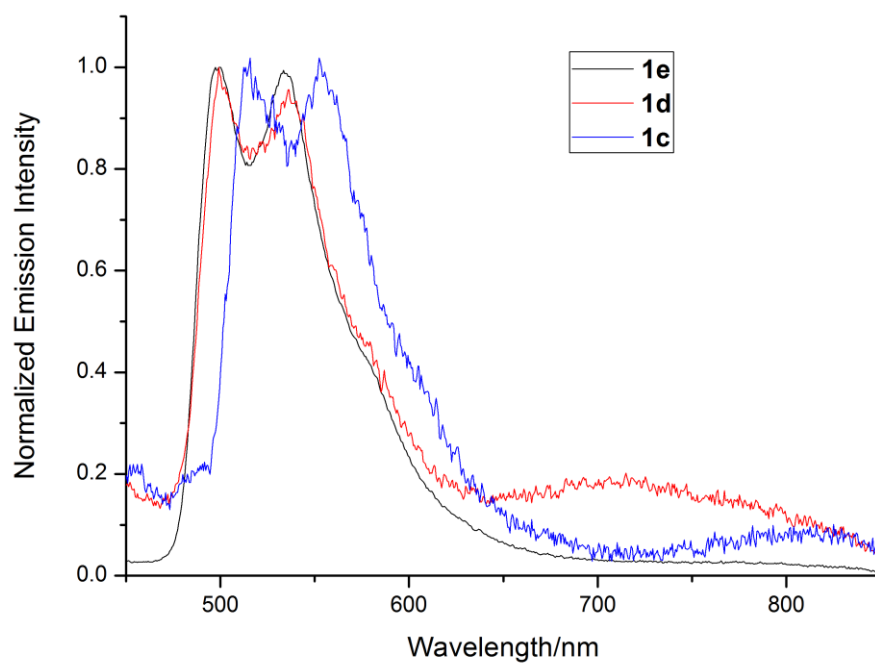


Figure 4.15a Emission spectrum of complexes **1c** – **e** in EtOH/MeOH (4:1, v/v) glass at 77K.

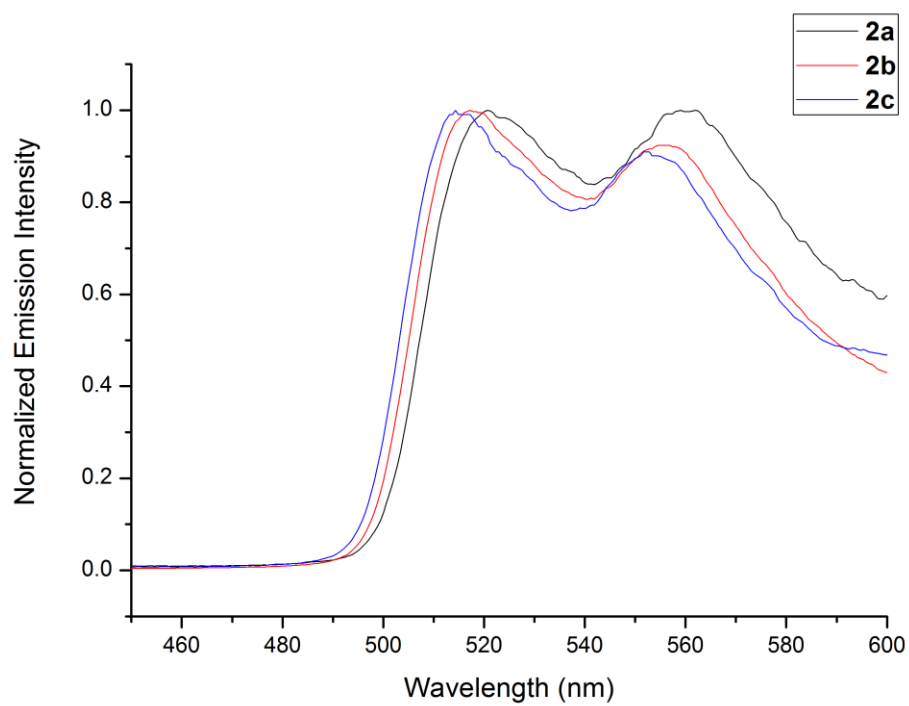


Figure 4.15b Emission spectrum of complexes **2a** – **c** in EtOH/MeOH (4:1) glass at 77K.

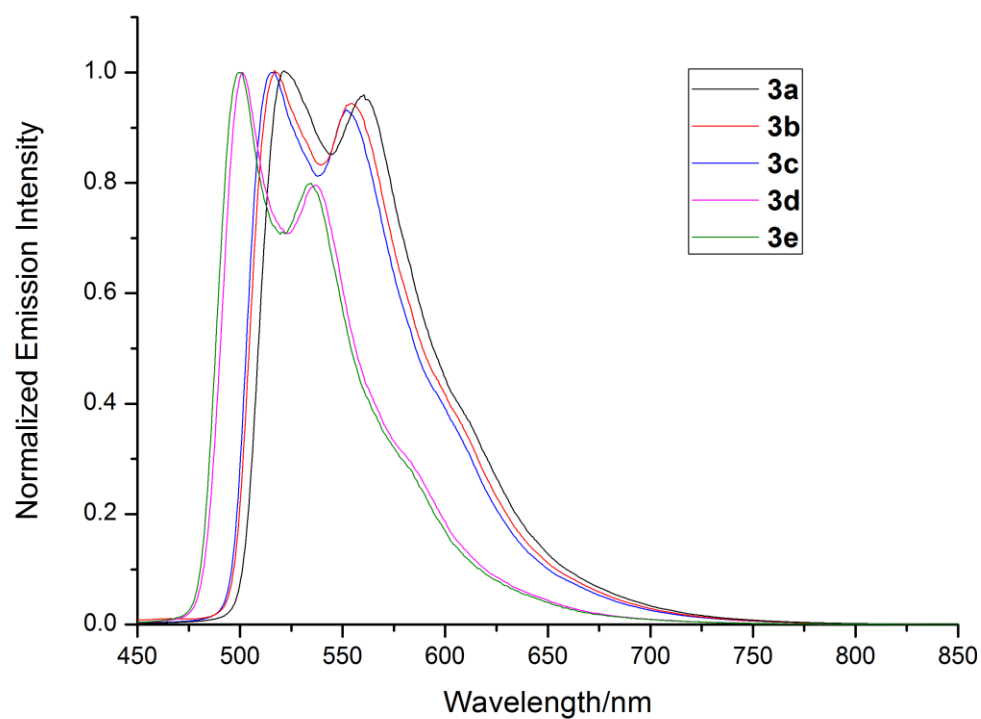


Figure 4.15c Emission spectrum of complexes **3a** – **e** in EtOH/MeOH (4:1) glass at 77K.

4.3.4 Electrochemical properties

The electrochemical properties of these ruthenium (II) complexes have been studied by cyclic voltammetry (CV) in 0.1 M [Bu_4N] PF_6 dichloromethane solution under an argon atmosphere. Typical CVs of the complexes are shown in Figure 4.16 with detailed electrochemical data summarized in Table 4.5. The *trans,trans,trans*- complexes (**1a–e**) shows a reversible and a quasi-reversible/irreversible couples centered at 0.118 – 0.335 and 1.338 – 1.423 V vs SCE, which are tentatively assigned as the metal-centered Ru(III/II) and Ru(IV/III) processes, as they are sensitive to the change in the isocyanide ligands,²²⁸ where the $E(\text{Ru}^{\text{III/II}})$ and $E(\text{Ru}^{\text{IV/III}})$ increase upon increasing π -accepting ability of the isocyanide ligands from complex **1a** to **1e**.

Similar trend was observed in complexes **2** and **3**. The first oxidation of *cis,trans*- $\text{Ru}(\text{PBO})_2(\text{CNR})(\text{PPh}_3)$ (**2a – e**) exhibit a reversible couple at 0.471 – 0.590 V vs SCE, and the *cis,trans,cis*- $[\text{Ru}(\text{PBO})_2(\text{RNC})_2]$ complexes (**3a – e**) have a reversible/quasi-reversible couple at 0.630 – 0.858 V vs SCE, they are also tentatively assigned to the $\text{Ru}^{\text{III/II}}$ process for their sensitivity to the electronegativity change of the Ru metal center cause by the change of isocyanide ligand substituent. An irreversible oxidation is observed at 1.326 – 1.344 V vs SCE and 1.241 – 1.504 V vs SCE for complexes **2a – e** and **3a – e** respectively, these are attributed to be the oxidation of the phenol site of PBO, such electrochemical properties are also reported for others Ru(II) phenolate complexes.^{235,257}

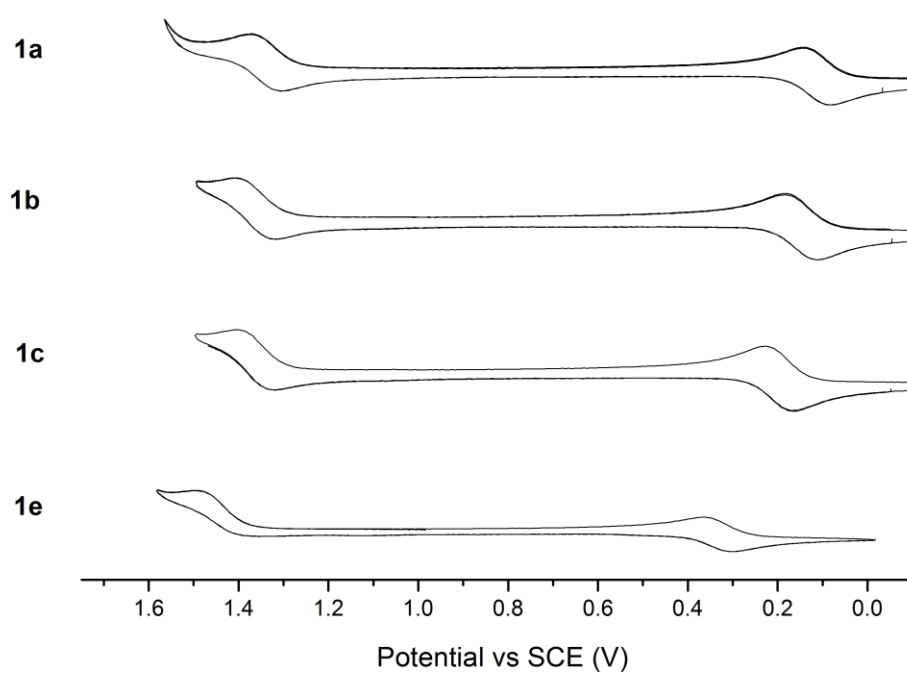


Figure 4.16a CVs of **1a** – **c** and **1e** in 0.1 M $[\text{nBu}_4\text{N}]\text{PF}_6$ solution in DCM at 298 K. Scan rate = 100 mV s^{-1} .

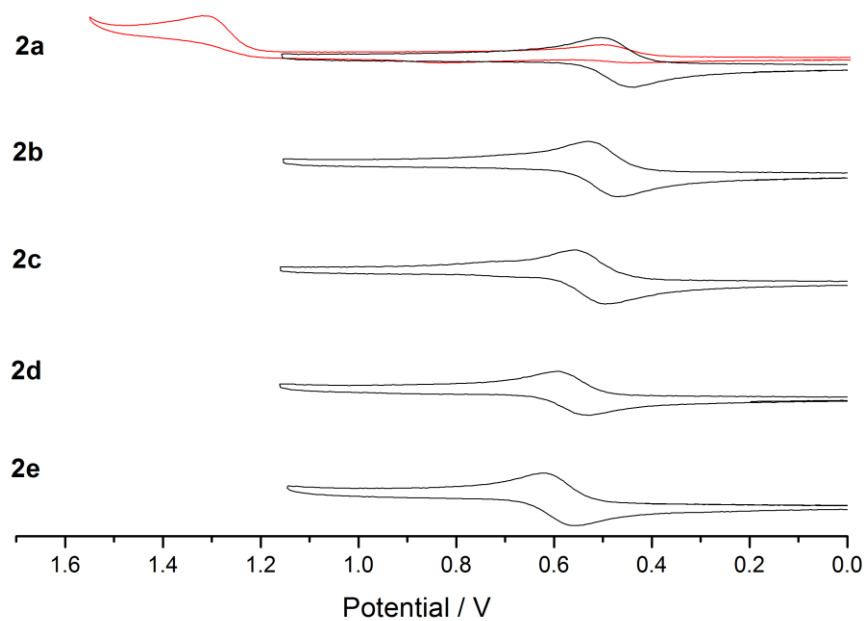


Figure 4.16b CVs of compounds **2a** – **e** in 0.1 M [^tBu₄N]PF₆ solution in DCM at 298 K. Scan rate = 100 mV s⁻¹.

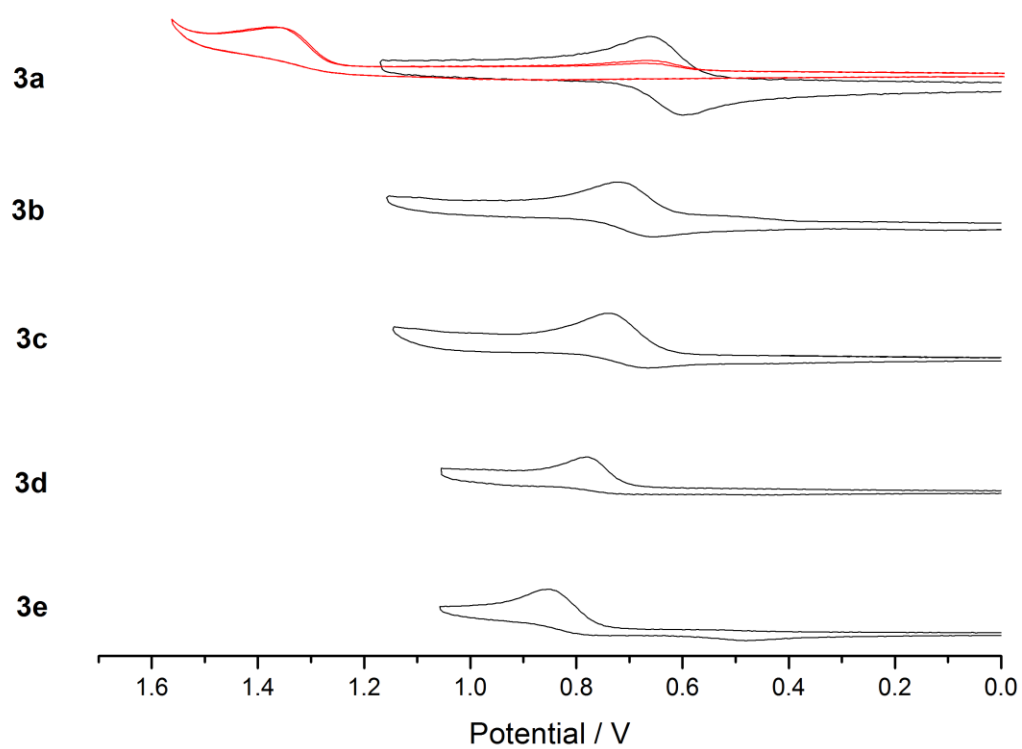


Figure 4.16c CVs of compounds **3a** – **c** in 0.1 M [ⁿBu₄N]PF₆ solution in DCM at 298 K. Scan rate = 100 mV s⁻¹.

Table 4.5 Electrochemical data of complexes **1a – e**, **2a – e** and **3a – c**.

	Oxidation E _{1/2} (ΔE) ^a or E _{pa} ^b vs SCE	
1a	0.118 (58) ^a	1.338 (62) ^a
1b	0.148 (75) ^a	1.361 (81) ^a
1c	0.200 (65) ^a	1.361 (86) ^a
1d	0.254 (69) ^a	1.395 (113) ^b
1e	0.335 (55) ^a	1.423 (138) ^b
2a	0.471 (69) ^a	1.326 ^b
2b	0.500 (61) ^a	1.330 ^b
2c	0.527 (64) ^a	1.329 ^b
2d	0.559 (58) ^a	1.344 ^b
2e	0.590 (65) ^a	1.343 ^b
3a	0.630 (61) ^a	1.373 ^b
3b	0.691 (62) ^a	1.498 ^b
3c	0.703 (76) ^a	1.504 ^b
3d	0.782 ^b	1.241 ^b
3e	0.858 ^b	1.292 ^b

^a reversible or quasi-reversible couple.

^b irreversible couple.

4.4 Conclusion

A series of Ru^{II} isocyano complexes bearing 2-(2-hydroxyphenyl)benzoxazole (HPBO) auxiliary ligands have been prepared. With different reaction time and amount of added isocyanides, *trans, trans trans*- (**1a – e**) and *trans,cis*-Ru(PBO)₂(CNR)(PPh₃) (**2a – e**) and *cis,trans,cis*-Ru(PBO)₂(CNR)(PPh₃) (**3a – e**). The complexes are found to be emissive with λ_{em} in the range of 499 – 607 nm (**1**), 514 – 560 nm (**2**) and 500 – 610 nm (**3**) respectively in 77K glass. Detailed electrochemical and photophysical studies reveal the dependence of these properties on the π -accepting ability of the isocyanide ligands and a MLCT parentage is assigned for the emission. Complementary DFT studies are now in progress and will be published in due course.

Chapter 5: Conclusion and Future Work

5.1 Summary of the Thesis

The objective of this thesis concerned with the development of new technique that detect and degrade water pollutant simultaneously. This thesis has demonstrated ICDA and CDA systems that can simultaneously detect and degrade target pollutants, and, acting as latent catalytical threshold control the degradation of the pollutants, respectively in water.

In Chapter 2, complex **RuFe 1** is the first bimetallic complex designed and synthesized for the detection and degradation of oxalic acid. The design has made use of the well-known luminescent ruthenium(II) complex and common ferric chloride salt, and its synthesis method is simple and with good yield. Throughout the investigation of **RuFe 1** complex, the results have proved that sensitivity and selectivity of this system can be designed and adjusted according to its thermodynamic properties, and that ensured the catalyst will only be activated when the target pollutant oxalic acid appear. The released catalyst will degrade oxalic acid into harmless carbon dioxide, and also enhanced the colorimetric signal when there is present of methyl orange coloring agent. These finding suggested that ICDA system can be a very versatile way of designing smart chemical device for environmental remediation.

In chapter 3, another ICDA system, **FeCu 1** was synthesized and examined. This bimetallic complex can selectively detect cyanide anion in common water bodies. The catalyst was released in the present of cyanide, degraded cyanide into less toxic cyanate anion and amplified the colorimetric signal by catalytic oxidizing phenolphthalin. A series of Fe-Cu complexes with different Fe subunit were synthesized for the study of CDA underlying relationships between their thermodynamic, kinetic and catalytic properties. The result demonstrates that apart from their thermodynamic properties, their kinetic properties were also an important factor in controlling the initiation of its catalytic properties. This demonstrates that the CDA system can be fine-tuned by using different coordination ligands, to achieve the goal of “smart” device that only function in appropriate situation.

Both **RuFe 1** and **FeCu 1** are proved capable of detection and degradation of pollutants in practical water samples with good recovery, however on-site testing are not performed in this work. A comprehensive study of the system to treat polluted water such as industrial sewage treatment plant are in interest. Furthermore, currently the systems can only detect and degrade oxalate and cyanide, by changing the receptor and catalyst subunit, different pollutants or other analyte may also applicable.

Finally, a series of ruthenium complexes **1 – 3** were synthesized and characterized. Some of their crystal structures have been studied. The spatial arrangement of PBO ligands are controlled by the reaction time, where cis-trans isomers were formed when prolonged heating. The complexes are found to be emissive with λ_{em} in the range of 499 – 607 nm (**1**), 514 – 708 nm (**2**) and 500 – 610 nm (**3**) respectively in 77K glass. The electrochemical and photophysical properties of the ruthenium complexes are found to be significantly changed with their geometric isomerism and the electronegativity of the substituents on isocyanide ligands. In other words, the complexes are optically tunable by changing the isocyanide ligand, and are suitable in the development of luminescent materials for different applications. Complementary DFT studies are now in progress and will be published in due course.

Reference

- (1) Postel, S. L.; Daily, G. C.; Ehrlich, P. R. *Science* **1996**, *271*, 785.
- (2) Jain, C.; Ali, I. *Water Research* **2000**, *34*, 4304.
- (3) Mance, G. In *Pollution threat of heavy metals in aquatic environments*; Springer: 1987, p 1.
- (4) Conway, G. R.; Pretty, J. N. *Unwelcome harvest: agriculture and pollution*; Routledge, 2013.
- (5) Mason, C. F. *Biology of freshwater pollution*; Pearson Education, 2002.
- (6) Prüss-Ustün, A.; Vickers, C.; Haefliger, P.; Bertollini, R. *Environmental health* **2011**, *10*, 9.
- (7) Fawell, J.; Nieuwenhuijsen, M. J. *British Medical Bulletin* **2003**, *68*, 199.
- (8) Mara, D. D. *Public Health* **2003**, *117*, 452.
- (9) Ritter, L.; Solomon, K.; Sibley, P.; Hall, K.; Keen, P.; Mattu, G.; Linton, B. *Journal of Toxicology and Environmental Health, Part A* **2002**, *65*, 1.
- (10) Harris, B. *Trends in Biotechnology* **1999**, *17*, 290.
- (11) Kemper, K. E. *Hydrogeology Journal* **2004**, *12*, 3.
- (12) Kumar, S.; Dhar, D. N.; Saxena, P. *Journal of Scientific and Industrial Research* **2009**, *68*, 181.
- (13) Ashraf, M. A.; Mahmood, K.; Wajid, A.; Maah, M. J.; Yusoff, I. In *International Conference on Chemistry and Chemical Process 2011*; Vol. 10, p 1.
- (14) Dhar, D. N.; Taploo, C. *Journal of Scientific & Industrial Research* **1982**, *41*, 501.
- (15) Kajal, A.; Bala, S.; Kamboj, S.; Sharma, N.; Saini, V. *Journal of Catalysts* **2013**, *2013*.
- (16) Jacobsen, E. N.; Kakiuchi, F.; Konsler, R. G.; Larrow, J. F.; Tokunaga, M. *Tetrahedron letters* **1997**, *38*, 773.
- (17) Sigman, M. S.; Jacobsen, E. N. *Journal of the American Chemical Society* **1998**, *120*, 5315.
- (18) Adamson, A. W.; Demas, J. N. *Journal of the American Chemical Society* **1971**, *93*, 1800.
- (19) Caspar, J. V.; Meyer, T. J. *Journal of the American Chemical Society* **1983**, *105*, 5583.
- (20) Dixon, I. M.; Lebon, E.; Sutra, P.; Igau, A. *Chemical Society Reviews* **2009**, *38*, 1621.
- (21) Juris, A.; Balzani, V.; Barigelletti, F.; Campagna, S.; Belser, P. I.; Von Zelewsky, A. *Coordination Chemistry Reviews* **1988**, *84*, 85.

- (22) Ganjali, M. R.; Pourjavid, M. R.; Rezapour, M.; Poursaberi, T.; Daftari, A.; Salavati-Niasari, M. *Electroanalysis* **2004**, *16*, 922.
- (23) Chowdhury, B.; Khatua, S.; Dutta, R.; Chakraborty, S.; Ghosh, P. *Inorganic chemistry* **2014**, *53*, 8061.
- (24) Gupta, V. K.; Singh, A.; Ganjali, M.; Norouzi, P.; Faridbod, F.; Mergu, N. *Sensors and Actuators B: Chemical* **2013**, *182*, 642.
- (25) Aksuner, N.; Henden, E.; Yilmaz, I.; Cukurovali, A. *Sensors and Actuators B: Chemical* **2008**, *134*, 510.
- (26) Tang, L.; Cai, M. *Sensors and Actuators B: Chemical* **2012**, *173*, 862.
- (27) Hara, D.; Komatsu, H.; Son, A.; Nishimoto, S.-i.; Tanabe, K. *Bioconjugate chemistry* **2015**, *26*, 645.
- (28) García, T.; Revenga-Parra, M.; Abruna, H.; Pariente, F.; Lorenzo, E. *Analytical chemistry* **2008**, *80*, 77.
- (29) Mugweru, A.; Wang, B.; Rusling, J. *Analytical chemistry* **2004**, *76*, 5557.
- (30) Ershad, S.; Sagathforoush, L.-A.; Karim-Nezhad, G. *Analytical Sciences* **2009**, *25*, 665.
- (31) Ferrere, S.; Gregg, B. A. *Journal of the American Chemical Society* **1998**, *120*, 843.
- (32) Ferrere, S. *Chemistry of materials* **2000**, *12*, 1083.
- (33) van den Beuken, E. K.; Feringa, B. L. *Tetrahedron* **1998**, *54*, 12985.
- (34) Garnovskii, A. D., Kharisov, B. I., Blanco, L. M., Sadimenko, A. P., Uraev, A. I., Vasilchenko, I. S., & Garnovskii, D. A. *Journal of Coordination Chemistry* **2002**, *55*, 1119.
- (35) Denti, G.; Campagna, S.; Sabatino, L.; Serroni, S.; Ciano, M.; Balzani, V. *Inorganica chimica acta* **1990**, *176*, 175.
- (36) Campagna, S.; Denti, G.; Serroni, S.; Ciano, M.; Balzani, V. *Inorganic Chemistry* **1991**, *30*, 3728.
- (37) Dammann, C. B.; Hughey, J. L.; Jicha, D. C.; Meyer, T. J.; Rakita, P. E.; Weaver, T. R. *Inorganic Chemistry* **1973**, *12*, 2206.
- (38) Bignozzi, C. A.; Scandola, F. *Inorganic Chemistry* **1984**, *23*, 1540.
- (39) Smékal, Z.; Březina, F.; Šindelář, Z.; Klička, R.; Krausová, D.; Nádvorník, M. *Synthesis and Reactivity in Inorganic and Metal-Organic Chemistry* **1996**, *26*, 1537.
- (40) LaCroce, S. J.; Cutler, A. R. *Journal of the American Chemical Society* **1982**, *104*, 2312.
- (41) Moore, K. J.; Petersen, J. D. *Polyhedron* **1983**, *2*, 279.

- (42) Atwood, J. L.; Holman, K. T.; Steed, J. W. *Chemical Communications* **1996**, 1401.
- (43) Evans, W. J.; Lee, D. S.; Ziller, J. W. *Journal of the American Chemical Society* **2004**, *126*, 454.
- (44) Mehn, M. P.; Peters, J. C. *Journal of inorganic biochemistry* **2006**, *100*, 634.
- (45) Van Wallendael, S.; Shaver, R. J.; Rillema, D. P.; Yoblinski, B.; Stathis, M.; Guarr, T. F. *Inorganic Chemistry* **1990**, *29*, 1761.
- (46) Kaim, W.; Kasack, V. *Inorganic chemistry* **1990**, *29*, 4696.
- (47) Balzani, V.; Juris, A.; Venturi, M.; Campagna, S.; Serroni, S. *Chemical reviews* **1996**, *96*, 759.
- (48) Demas, J.; Addington, J.; Peterson, S. H.; Harris, E. *The Journal of Physical Chemistry* **1977**, *81*, 1039.
- (49) Saha, D.; Das, S.; Bhaumik, C.; Dutta, S.; Baitalik, S. *Inorganic chemistry* **2010**, *49*, 2334.
- (50) Tumambac, G. E.; Rosencrance, C. M.; Wolf, C. *Tetrahedron* **2004**, *60*, 11293.
- (51) Kaur, K.; Saini, R.; Kumar, A.; Luxami, V.; Kaur, N.; Singh, P.; Kumar, S. *Coordination Chemistry Reviews* **2012**, *256*, 1992.
- (52) Choi, M. G.; Kim, Y. H.; Namgoong, J. E.; Chang, S.-K. *Chemical Communications* **2009**, 3560.
- (53) Kim, T.-H.; Swager, T. M. *Angewandte Chemie International Edition* **2003**, *42*, 4803.
- (54) Wiskur, S. L.; Ait-Haddou, H.; Lavigne, J. J.; Anslyn, E. V. *Accounts of Chemical Research* **2001**, *34*, 963.
- (55) Nguyen, B. T.; Anslyn, E. V. *Coordination Chemistry Reviews* **2006**, *250*, 3118.
- (56) Nguyen, B. T.; Wiskur, S. L.; Anslyn, E. V. *Organic Letters* **2004**, *6*, 2499.
- (57) Inouye, M.; Hashimoto, K.-i.; Isagawa, K. *Journal of the American Chemical Society* **1994**, *116*, 5517.
- (58) Metzger, A.; Anslyn, E. V. *Angewandte Chemie International Edition* **1998**, *37*, 649.
- (59) Florea, M.; Nau, W. M. *Angewandte Chemie International Edition* **2011**, *50*, 9338.
- (60) Chow, C.-F.; Chiu, B. K.; Lam, M. H.; Wong, W.-Y. *Journal of the American Chemical Society* **2003**, *125*, 7802.
- (61) Chow, C.-F.; Lam, M. H.; Wong, W.-Y. *Inorganic Chemistry* **2004**, *43*, 8387.
- (62) Koo, C.-K.; Chow, C.-F.; Chiu, B. K.-W.; Lei, N.-Y.; Lam, M. H.-W.; Wong, W.-Y. *European Journal of Inorganic Chemistry* **2008**, *2008*, 1318.

- (63) Chow, C.-F.; Kong, H.-K.; Leung, S.-W.; Chiu, B. K.; Koo, C.-K.; Lei, E. N.; Lam, M. H.; Wong, W.-T.; Wong, W.-Y. *Analytical chemistry* **2010**, *83*, 289.
- (64) Mills, A.; Davies, R. H.; Worsley, D. *Chemical Society Reviews* **1993**, *22*, 417.
- (65) Oller, I.; Malato, S.; Sánchez-Pérez, J. *Science of the total environment* **2011**, *409*, 4141.
- (66) Glaze, W. H.; Kang, J.-W.; Chapin, D. H. *Ozone: Science & Engineering* **1987**, *9*, 335.
- (67) Fenton, H. *Journal of the Chemical Society, Transactions* **1894**, *65*, 899.
- (68) Barbusiński, K. *Ecological Chemistry and Engineering. S* **2009**, *16*, 347.
- (69) Haber, F.; Weiss, J. In *Proceedings of the Royal Society of London A: Mathematical, Physical and Engineering Sciences*; The Royal Society: 1934; Vol. 147, p 332.
- (70) Pera-Titus, M.; García-Molina, V.; Baños, M. A.; Giménez, J.; Esplugas, S. *Applied Catalysis B: Environmental* **2004**, *47*, 219.
- (71) Chen, F.; Ma, W.; He, J.; Zhao, J. *The Journal of Physical Chemistry A* **2002**, *106*, 9485.
- (72) Pignatello, J. J. *Environmental Science & Technology* **1992**, *26*, 944.
- (73) Shemer, H.; Kunukcu, Y. K.; Linden, K. G. *Chemosphere* **2006**, *63*, 269.
- (74) Andreozzi, R.; Caprio, V.; Insola, A.; Marotta, R. *Catalysis today* **1999**, *53*, 51.
- (75) Shelor, C. P.; Campbell, C. A.; Kroll, M.; Dasgupta, P. K.; Smith, T. L.; Abdalla, A.; Hamilton, M.; Muhammad, T. W. *Analytical chemistry* **2011**, *83*, 8300.
- (76) Hayashi, J.; Yamada, M.; Hobo, T. *Analytica chimica acta* **1991**, *247*, 27.
- (77) Kiwi, J.; Pulgarin, C.; Peringer, P.; Grätzel, M. *Applied Catalysis B: Environmental* **1993**, *3*, 85.
- (78) Masarwa, M.; Cohen, H.; Meyerstein, D.; Hickman, D. L.; Bakac, A.; Espenson, J. *H. J. Am. Chem. Soc.;(United States)* **1988**, *110*.
- (79) Sutton, H. C.; Winterbourn, C. C. *Free Radical Biology and Medicine* **1989**, *6*, 53.
- (80) Marx, G.; Chevion, M. *Biochemical Journal* **1986**, *236*, 397.
- (81) Sandmann, G.; Böger, P. *Plant Physiology* **1980**, *66*, 797.
- (82) Strlic, M.; Kolar, J.; Selih, V.-S.; Kocar, D.; Pihlar, B. *Acta Chimica Slovenica* **2003**, *50*, 619.
- (83) Liang, X.; Zhong, Y.; He, H.; Yuan, P.; Zhu, J.; Zhu, S.; Jiang, Z. *Chemical Engineering Journal* **2012**, *191*, 177.

- (84) Bandala, E. R.; Peláez, M. A.; Dionysiou, D. D.; Gelover, S.; Garcia, J.; Macías, D. *Journal of Photochemistry and Photobiology A: Chemistry* **2007**, *186*, 357.
- (85) Baxendale, J.; Wells, C. *Transactions of the Faraday Society* **1957**, *53*, 800.
- (86) Sawyer, D. T.; Sobkowiak, A.; Matsushita, T. *Accounts of chemical research* **1996**, *29*, 409.
- (87) Torreilles, J.; Guerin, M.-C.; Slaoui-Hasnaoui, A. *Free radical research communications* **1990**, *11*, 159.
- (88) Torreilles, J.; Guérin, M.-C. *FEBS letters* **1990**, *272*, 58.
- (89) Liu, W.; Ai, Z.; Zhang, L. *Journal of hazardous materials* **2012**, *243*, 257.
- (90) O'Brien, P.; Salacinski, H. J. *Archives of toxicology* **1998**, *72*, 690.
- (91) Nieto-Juarez, J. I.; Pierzchła, K.; Sienkiewicz, A.; Kohn, T. *Environmental science & technology* **2010**, *44*, 3351.
- (92) Kitis, M.; Karakaya, E.; Yigit, N. O.; Civelekoglu, G.; Akcil, A. *Water Research* **2005**, *39*, 1652.
- (93) Abu-Saba, K. E.; Sedlak, D. L.; Flegal, A. *Marine chemistry* **2000**, *69*, 33.
- (94) Zuo, Y.; Hoigne, J. *Environmental Science & Technology* **1992**, *26*, 1014.
- (95) Tachiev, G.; Roth, J.; Bowers, A. *International Journal of Chemical Kinetics* **2000**, *32*, 24.
- (96) Pignatello, J. J.; Baehr, K. *Journal of Environmental quality* **1994**, *23*, 365.
- (97) Laipan, M.; Zhu, R.; Zhu, J.; He, H. *Journal of Molecular Catalysis A: Chemical* **2016**, *415*, 9.
- (98) Guimaraes, I. R.; Giroto, A.; Oliveira, L. C.; Guerreiro, M. C.; Lima, D. Q.; Fabris, J. D. *Applied Catalysis B: Environmental* **2009**, *91*, 581.
- (99) Yip, A. C.-K.; Lam, F. L.-Y.; Hu, X. *Chemical engineering science* **2007**, *62*, 5150.
- (100) Dong, Y.; Han, Z.; Dong, S.; Wu, J.; Ding, Z. *Catalysis today* **2011**, *175*, 299.
- (101) Butler, J. E. *Journal of immunoassay* **2000**, *21*, 165.
- (102) Bobrow, M. N.; Shaughnessy, K. J.; Litt, G. J. *Journal of immunological methods* **1991**, *137*, 103.
- (103) Meng, Y.; High, K.; Antonello, J.; Washabaugh, M. W.; Zhao, Q. *Analytical biochemistry* **2005**, *345*, 227.
- (104) Marquette, C. A.; Blum, L. c. J. *Analytica Chimica Acta* **1999**, *381*, 1.
- (105) Sanguinetti, M.; Posteraro, B.; Pagano, L.; Pagliari, G.; Fianchi, L.; Mele, L.; La Sorda, M.; Franco, A.; Fadda, G. *Journal of clinical microbiology* **2003**, *41*, 3922.

- (106) Gianneschi, N. C.; Nguyen, S. T.; Mirkin, C. A. *Journal of the American Chemical Society* **2005**, *127*, 1644.
- (107) Zhu, L.; Lynch, V. M.; Anslyn, E. V. *Tetrahedron* **2004**, *60*, 7267.
- (108) Muizebelt, W. *JCT, Journal of coatings technology* **1985**, *57*, 43.
- (109) Kamiya, K.; Suzuki, N. *International Journal of Adhesion and Adhesives* **2016**, *68*, 333.
- (110) Thomas, R. M.; Fedorov, A.; Keitz, B. K.; Grubbs, R. H. *Organometallics* **2011**, *30*, 6713.
- (111) Mauldin, T.; Kessler, M. *Journal of thermal analysis and calorimetry* **2009**, *96*, 705.
- (112) Guzmán, D.; Ramis, X.; Fernández-Francos, X.; Serra, A. *RSC Advances* **2015**, *5*, 101623.
- (113) Corcé, V.; Chamoreau, L. M.; Derat, E.; Goddard, J. P.; Ollivier, C.; Fensterbank, L. *Angewandte Chemie* **2015**, *127*, 11576.
- (114) Diesendruck, C. E.; Iliashevsky, O.; Ben-Asuly, A.; Goldberg, I.; Lemcoff, N. G. In *Macromolecular symposia*; Wiley Online Library: 2010; Vol. 293, p 33.
- (115) Groote, R.; van Haandel, L.; Sijbesma, R. P. *Journal of Polymer Science Part A: Polymer Chemistry* **2012**, *50*, 4929.
- (116) Jakobs, R. T.; Sijbesma, R. P. *Organometallics* **2012**, *31*, 2476.
- (117) Žak, P.; Rogalski, S.; Majchrzak, M.; Kubicki, M.; Pietraszuk, C. *Beilstein journal of organic chemistry* **2015**, *11*, 1910.
- (118) Samec, J. S.; Keitz, B. K.; Grubbs, R. H. *Journal of Organometallic Chemistry* **2010**, *695*, 1831.
- (119) Endo, T.; Sanda, F. In *Macromolecular Symposia*; Wiley Online Library: 1996; Vol. 107, p 237.
- (120) Wang, Y.; Kimura, M.; Sudo, A.; Endo, T. *Journal of Polymer Science Part A: Polymer Chemistry* **2016**, *54*, 2611.
- (121) Bantu, B.; Manohar Pawar, G.; Wurst, K.; Decker, U.; Schmidt, A. M.; Buchmeiser, M. R. *European Journal of Inorganic Chemistry* **2009**, *2009*, 1970.
- (122) Takata, T.; Endo, T. *Macromolecules* **1996**, *29*, 3317.
- (123) Monsaert, S.; Ledoux, N.; Drozdak, R.; Verpoort, F. *Journal of Polymer Science Part A: Polymer Chemistry* **2010**, *48*, 302.
- (124) Ung, T.; Hejl, A.; Grubbs, R. H.; Schrodi, Y. *Organometallics* **2004**, *23*, 5399.

- (125) Kishi, K.; Ishimaru, T.; Ozono, M.; Tomita, I.; Endo, T. *Journal of Polymer Science Part A: Polymer Chemistry* **2000**, *38*, 804.
- (126) Schmid, T. E.; Modicom, F.; Dumas, A.; Borré, E.; Toupet, L.; Baslé, O.; Mauduit, M. *Beilstein journal of organic chemistry* **2015**, *11*, 1541.
- (127) Hodgkinson, A.; Zarembski, P. *Calcified tissue research* **1968**, *2*, 115.
- (128) Riemenschneider, W.; Tanifuji, M. *Ullmann's Encyclopedia of Industrial Chemistry* **2000**.
- (129) Sjöde, A.; Winestrand, S.; Nilvebrant, N.-O.; Jönsson, L. J. *Enzyme and microbial technology* **2008**, *43*, 78.
- (130) *Research Report of Chinese Oxalic Acid Industry* 2009.
- (131) Norton, R.; Roberts, J.; Huebert, B. *Geophysical research letters* **1983**, *10*, 517.
- (132) Von Burg, R. *Journal of Applied Toxicology* **1994**, *14*, 233.
- (133) Kasidas, G.; Rose, G. *Clinica chimica acta* **1986**, *154*, 49.
- (134) Cao, L.-C.; Jonassen, J.; Honeyman, T. W.; Scheid, C. *American journal of nephrology* **2001**, *21*, 69.
- (135) Thamilselvan, V.; Menon, M.; Thamilselvan, S. *American Journal of Physiology-Renal Physiology* **2009**, *297*, F1399.
- (136) Zarembski, P.; Hodgkinson, A. *Biochemical Journal* **1965**, *96*, 717.
- (137) Baadenhuijsen, H.; Jansen, A. *Clinica Chimica Acta* **1975**, *62*, 315.
- (138) Sriboonlue, P.; Suwantrai, S.; Prasongwatana, V. *Clinica chimica acta* **1998**, *273*, 59.
- (139) Bergerman, J.; Elliot, J. S. *Analytical Chemistry* **1955**, *27*, 1014.
- (140) Calkins, V. *Industrial & Engineering Chemistry Analytical Edition* **1943**, *15*, 762.
- (141) Dutt, V. E.; Mottola, H. *Analytical Chemistry* **1974**, *46*, 1777.
- (142) Zhang, W.; Kjær, K. S.; Alonso-Mori, R.; Bergmann, U.; Chollet, M.; Fredin, L. A.; Hadt, R. G.; Hartsock, R. W.; Harlang, T.; Kroll, T. *Chemical Science* **2017**, *8*, 515.
- (143) Zhi-Liang, J.; Mei-Xiu, Z.; Lin-Xiu, L. *Analytica chimica acta* **1996**, *320*, 139.
- (144) Gottstein, H. D.; Zook, M. N.; Kuç, J. A. *Journal of Chromatography A* **1989**, *481*, 55.
- (145) Dutt, V. E.; Mottola, H. *Biochemical medicine* **1974**, *9*, 148.
- (146) Mayer, W. J.; McCarthy, J. P.; Greenberg, M. S. *Journal of chromatographic science* **1979**, *17*, 656.

- (147) Fabbrizzi, L.; Licchelli, M.; Mancin, F.; Pizzeghello, M.; Rabaioli, G.; Taglietti, A.; Tecilla, P.; Tonellato, U. *Chemistry-A European Journal* **2002**, *8*, 94.
- (148) Oh, D.-J.; Han, M.-S.; Kim, D. H. *Bulletin of the Korean Chemical Society* **2004**, *25*, 1495.
- (149) Espejo, E.; Agosin, E. *Applied and Environmental Microbiology* **1991**, *57*, 1980.
- (150) Kosanić, M. M. *Journal of Photochemistry and Photobiology A: Chemistry* **1998**, *119*, 119.
- (151) Avramescu, S. M.; Bradu, C.; Udrea, I.; Mihalache, N.; Ruta, F. *Catalysis Communications* **2008**, *9*, 2386.
- (152) Kato, M.; Yamauchi, S.; Hirota, N. *The Journal of Physical Chemistry* **1989**, *93*, 3422.
- (153) Crosby, G. A.; Demas, J. N. *The Journal of Physical Chemistry* **1971**, *75*, 991.
- (154) Nakamaru, K. *Bulletin of the Chemical Society of Japan* **1982**, *55*, 2697.
- (155) Connors, K. A. *Binding constants: the measurement of molecular complex stability*; Wiley-Interscience, 1987.
- (156) Hubaux, A.; Vos, G. *Analytical Chemistry* **1970**, *42*, 849.
- (157) Hardman, R. C.; Volz, D. C.; Kullman, S. W.; Hinton, D. E. *The Anatomical Record* **2007**, *290*, 770.
- (158) Krause, R. *Inorganica chimica acta* **1977**, *22*, 209.
- (159) Ülveczky, A.; Horváth, A. *Inorganica chimica acta* **1995**, *236*, 173.
- (160) Zakaria, M. B.; Chikyow, T. *Coordination Chemistry Reviews* **2017**, *352*, 328.
- (161) Itaya, K.; Uchida, I.; Neff, V. D. *Accounts of Chemical Research* **1986**, *19*, 162.
- (162) Shores, M. P.; Beauvais, L. G.; Long, J. R. *Journal of the American Chemical Society* **1999**, *121*, 775.
- (163) Karadağ, A.; Bulut, A.; Şenocak, A.; Uçar, İ.; Büyükgüngör, O. *Journal of Coordination Chemistry* **2007**, *60*, 2035.
- (164) Zhan, S.-z.; Guo, D.; Zhang, X.-y.; Du, C.-x.; Zhu, Y.; Yang, R.-n. *Inorganica Chimica Acta* **2000**, *298*, 57.
- (165) Karadağ, A.; Bulut, A.; Şenocak, A.; Uçar, İ.; Büyükgüngör, O. *Journal of Coordination Chemistry* **2007**, *60*, 2035.
- (166) Zhan, S.; Chen, X.; Meng, Q. *Transition Metal Chemistry* **1996**, *21*, 181.
- (167) Robin, M. B.; Day, P. *Advances in inorganic chemistry and radiochemistry* **1968**, *10*, 247.

- (168) Sheng, T.; Vahrenkamp, H. *European Journal of Inorganic Chemistry* **2004**, *2004*, 1198.
- (169) Bignozzi, C.; Chiorboli, C.; Indelli, M.; Rampi Scandola, M.; Varani, G.; Scandola, F. *Journal of the American Chemical Society* **1986**, *108*, 7872.
- (170) Lin, C.-T.; Sutin, N. *The Journal of Physical Chemistry* **1976**, *80*, 97.
- (171) Rodríguez, E.; Mimbbrero, M.; Masa, F. J.; Beltrán, F. J. *Water research* **2007**, *41*, 1325.
- (172) Feng, W.; Nansheng, D. *Chemosphere* **2000**, *41*, 1137.
- (173) Zuo, Y.; Hoigné, J. *Atmospheric Environment* **1994**, *28*, 1231.
- (174) Mazellier, P.; Sulzberger, B. *Environmental science & technology* **2001**, *35*, 3314.
- (175) Fiorito, P. A.; de Torresi, S. I. C. *Talanta* **2004**, *62*, 649.
- (176) Perez, E. F.; de Oliveira Neto, G.; Kubota, L. T. *Sensors and Actuators B: Chemical* **2001**, *72*, 80.
- (177) Michenfelder, J. D. *Anesthesiology* **1977**, *46*, 196.
- (178) Mudder, T.; Botz, M. In *A background paper of the UNEP/ICME Industry Codes of Practice Workshop: Cyanide Management Paris 2000*, p 26.
- (179) Korte, F.; Spitteller, M.; Coulston, F.; Elsevier: 2000.
- (180) Association, A. P. H.; Association, A. W. W.; Federation, W. P. C.; Federation, W. E. *Standard methods for the examination of water and wastewater*; American Public Health Association., 1915; Vol. 2.
- (181) Lee, C. H.; Yoon, H. J.; Shim, J. S.; Jang, W. D. *Chemistry—A European Journal* **2012**, *18*, 4513.
- (182) Lou, X.; Zhang, Y.; Qin, J.; Li, Z. *Chemistry—A European Journal* **2011**, *17*, 9691.
- (183) Chawla, H. M.; Shahid, M.; Black, D. S.; Kumar, N. *New Journal of Chemistry* **2014**, *38*, 2763.
- (184) Xu, Z.; Chen, X.; Kim, H. N.; Yoon, J. *Chemical Society Reviews* **2010**, *39*, 127.
- (185) Noroozifar, M.; Khorasani-Motlagh, M.; Hosseini, S.-N. *Analytica chimica acta* **2005**, *528*, 269.
- (186) Zhu, Z.; Fang, Z. *Analytica Chimica Acta* **1987**, *198*, 25.
- (187) Haj-Hussein, A. T.; Christian, G. D.; Ruzicka, J. *Analytical Chemistry* **1986**, *58*, 38.

- (188) Rocklin, R. D.; Johnson, E. L. *Analytical Chemistry* **1983**, *55*, 4.
- (189) Bond, A.; Heritage, I.; Wallace, G.; McCormick, M. *Analytical Chemistry* **1982**, *54*, 582.
- (190) Lindsay, A.; O'Hare, D. *Analytica chimica acta* **2006**, *558*, 158.
- (191) Shan, D.; Mousty, C.; Cosnier, S. *Analytical chemistry* **2004**, *76*, 178.
- (192) Ikebukuro, K.; Miyata, A.; Cho, S. J.; Nomura, Y.; Yamauchi, Y.; Hasebe, Y.; Uchiyama, S.; Karube, I. *Journal of biotechnology* **1996**, *48*, 73.
- (193) Smit, M. H.; Cass, A. E. *Analytical chemistry* **1990**, *62*, 2429.
- (194) Ma, J.; Dasgupta, P. K. *Analytica chimica acta* **2010**, *673*, 117.
- (195) Niamnont, N.; Khumsri, A.; Promchat, A.; Tumcharern, G.; Sukwattanasinitt, M. *Journal of hazardous materials* **2014**, *280*, 458.
- (196) Ros-Lis, J. V.; Martínez-Máñez, R.; Soto, J. *Chemical Communications* **2005**, 5260.
- (197) Lou, X.; Qiang, L.; Qin, J.; Li, Z. *ACS applied materials & interfaces* **2009**, *1*, 2529.
- (198) Kaushik, R.; Ghosh, A.; Singh, A.; Gupta, P.; Mittal, A.; Jose, D. A. *ACS Sensors* **2016**, *1*, 1265.
- (199) Chung, S.-Y.; Nam, S.-W.; Lim, J.; Park, S.; Yoon, J. *Chemical Communications* **2009**, 2866.
- (200) Young, C.; Jordan, T. In *Proceedings of the 10th Annual Conference on Hazardous Waste Research*; Kansas State University: Manhattan, KS: 1995, p 104.
- (201) Dash, R. R.; Gaur, A.; Balomajumder, C. *Journal of Hazardous Materials* **2009**, *163*, 1.
- (202) Kallel, M.; Belaid, C.; Boussahel, R.; Ksibi, M.; Montiel, A.; Elleuch, B. *Journal of Hazardous Materials* **2009**, *163*, 550.
- (203) Feng, F.; Xu, Z.; Li, X.; You, W.; Zhen, Y. *Journal of Environmental Sciences* **2010**, *22*, 1657.
- (204) Fung, P.; Sin, K.; Tsui, S. *Coloration Technology* **2000**, *116*, 170.
- (205) Choi, J.-H.; Shin, W. S.; Lee, S.-H.; Joo, D.-J.; Lee, J.-D.; Choi, S. J.; Park, L. *S. Separation Science and Technology* **2001**, *36*, 2945.
- (206) Stalter, D.; Magdeburg, A.; Weil, M.; Knacker, T.; Oehlmann, J. *water research* **2010**, *44*, 439.
- (207) Li, X.; Liu, H. *Environmental science & technology* **2005**, *39*, 4614.

- (208) Pramanik, S.; Aprahamian, I. *Journal of the American Chemical Society* **2016**, *138*, 15142.
- (209) Birch, K.; Schütz, F. *British journal of pharmacology and chemotherapy* **1946**, *1*, 186.
- (210) Schilt, A. A. *Journal of the American Chemical Society* **1960**, *82*, 3000.
- (211) Trendafilova, N.; Nikolov, G. S.; Bauer, G.; Kellner, R. *Inorganica chimica acta* **1993**, *210*, 77.
- (212) Guilloton, M.; Karst, F. *Analytical biochemistry* **1985**, *149*, 291.
- (213) Triki, S.; Sala-Pala, J.; Thétiot, F.; Gómez-García, C. J.; Daran, J. C. *European journal of inorganic chemistry* **2006**, *2006*, 185.
- (214) Beattie, J. K.; Polyblank, G. A. *Australian journal of chemistry* **1995**, *48*, 861.
- (215) Sarla, M.; Pandit, M.; Tyagi, D.; Kapoor, J. *Journal of Hazardous Materials* **2004**, *116*, 49.
- (216) Acheampong, M. A.; Meulepas, R. J.; Lens, P. N. *Journal of chemical technology and biotechnology* **2010**, *85*, 590.
- (217) García, V.; Häyrynen, P.; Landaburu-Aguirre, J.; Pirilä, M.; Keiski, R. L.; Urtiaga, A. *Journal of Chemical Technology and Biotechnology* **2014**, *89*, 803.
- (218) (EPA), T. U. S. E. P. A. *European Union, and the China Ministry of Environmental Protection (MEP) have set maximum contaminant level goals for cyanide in drinking water at 0.2, 0.05, and 0.05 ppm, respectively.*
- (219) Tsukamoto, Y.; Komai, H.; Kadotani, J.; Koi, K.; Mio, S.; Takeshiba, H.; Google Patents: 2011.
- (220) Xue, N.; Zhou, Y.; Wang, G.; Miao, W.; Qu, J. *Journal of Heterocyclic Chemistry* **2010**, *47*, 15.
- (221) Leaver, I. H.; Milligan, B. *Dyes and pigments* **1984**, *5*, 109.
- (222) Woolfe, G.; Melzig, M.; Schneider, S.; Dörr, F. *Chemical Physics* **1983**, *77*, 213.
- (223) Wang, J.; Chu, Q.; Liu, X.; Wesdemiotis, C.; Pang, Y. *The journal of physical chemistry. B* **2013**, *117*, 4127.
- (224) Chen, W.-H.; Xing, Y.; Pang, Y. *Organic letters* **2011**, *13*, 1362.
- (225) Taki, M.; Wolford, J. L.; O'Halloran, T. V. *Journal of the American Chemical Society* **2004**, *126*, 712.
- (226) Kanagaraj, K.; Pitchumani, K. *Chemistry—An Asian Journal* **2014**, *9*, 146.

- (227) Ogawa, A. K.; Abou-Zied, O. K.; Tsui, V.; Jimenez, R.; Case, D. A.; Romesberg, F. E. *Journal of the American Chemical Society* **2000**, *122*, 9917.
- (228) Novales, J.; Jonkhoff, N.; Acquaye, J. H. *Polyhedron* **2013**, *62*, 148.
- (229) Wang, H.; Zhang, H.; Abou-Zied, O.; Yu, C.; Romesberg, F.; Glasbeek, M. *Chemical physics letters* **2003**, *367*, 599.
- (230) Rai, V. K.; Srivastava, R.; Kamalasanan, M. *Journal of Luminescence* **2010**, *130*, 249.
- (231) Pal, M. K.; Kushwah, N.; Manna, D.; Wadawale, A.; Sudarsan, V.; Ghanty, T. K.; Jain, V. K. *Organometallics* **2012**, *32*, 104.
- (232) Du, X.; Zhao, J.; Yuan, S.; Zheng, C.; Lin, H.; Tao, S.; Lee, C.-S. *Journal of Materials Chemistry C* **2016**, *4*, 5907.
- (233) Das, A. K.; Sarkar, B.; Fiedler, J.; Zális, S.; Hartenbach, I.; Strobel, S.; Lahiri, G. K.; Kaim, W. *Journal of the American Chemical Society* **2009**, *131*, 8895.
- (234) Claustro, I.; Abate, G.; Sanchez, E.; Acquaye, J. H. *Inorganica chimica acta* **2003**, *342*, 29.
- (235) Keyes, T. E.; Leane, D.; Forster, R. J.; Coates, C. G.; McGarvey, J. J.; Nieuwenhuyzen, M. N.; Figgemeier, E.; Vos, J. G. *Inorganic chemistry* **2002**, *41*, 5721.
- (236) Booyesen, I. N.; Adebisi, A.; Akerman, M. P. *Inorganica Chimica Acta* **2015**, *433*, 13.
- (237) Santra, B.; Pal, C.; Lahiri, G. *Journal of the Chemical Society, Dalton Transactions* **1997**, 1387.
- (238) Griffith, W. *Transition Metal Chemistry* **1990**, *15*, 251.
- (239) Małecki, J.; Kruszynski, R.; Jaworska, M.; Lodowski, P.; Mazurak, Z. *Journal of Organometallic Chemistry* **2008**, *693*, 1096.
- (240) Małecki, J. *Polyhedron* **2012**, *31*, 159.
- (241) Horswell, S. L.; Kiely, C. J.; O'Neil, I. A.; Schiffrin, D. J. *Journal of the American Chemical Society* **1999**, *121*, 5573.
- (242) Pombeiro, A. J. *Journal of organometallic chemistry* **2005**, *690*, 6021.
- (243) Cadierno, V.; Crochet, P.; Díez, J.; García-Garrido, S. E.; Gimeno, J. *Organometallics* **2004**, *23*, 4836.
- (244) Ng, C.-O.; Lo, L. T.-L.; Ng, S.-M.; Ko, C.-C.; Zhu, N. *Inorganic chemistry* **2008**, *47*, 7447.
- (245) Leung, C.-F.; Ko, C.-C. *Journal of Organometallic Chemistry* **2016**, *804*, 101.

- (246) Rice, S. F.; Milder, S. J.; Gray, H. B.; Goldbeck, R. A.; Kliger, D. S. *Coordination Chemistry Reviews* **1982**, *43*, 349.
- (247) Wong, K. M.-C.; Yam, V. W.-W. *Accounts of chemical research* **2011**, *44*, 424.
- (248) Wong, C.-Y.; Lai, L.-M.; Leung, H.-F.; Wong, S.-H. *Organometallics* **2009**, *28*, 3537.
- (249) Chung, L.-H.; Cho, K.-S.; England, J.; Chan, S.-C.; Wieghardt, K.; Wong, C.-Y. *Inorganic chemistry* **2013**, *52*, 9885.
- (250) Wong, C.-Y.; Lai, L.-M.; Pat, P.-K. *Organometallics* **2009**, *28*, 5656.
- (251) Leung, C.-F.; Ng, S.-M.; Xiang, J.; Wong, W.-Y.; Lam, M. H.-W.; Ko, C.-C.; Lau, T.-C. *Organometallics* **2009**, *28*, 5709.
- (252) Mordziński, A.; Grabowska, A. *Chemical Physics Letters* **1982**, *90*, 122.
- (253) Hallman, P.; Stephenson, T.; Wilkinson, G. *Inorganic Syntheses, Volume 12* **2007**, 237.
- (254) Nishimura, S.; Yumoto, O.; Tsuneda, K.; Mori, H. *Bulletin of the Chemical Society of Japan* **1975**, *48*, 2603.
- (255) Ugi, I.; Fetzer, U.; Eholzer, U.; Knupfer, H.; Offermann, K. *Angewandte Chemie International Edition* **1965**, *4*, 472.
- (256) Kim, B.; Beebe, J. M.; Jun, Y.; Zhu, X.-Y.; Frisbie, C. D. *Journal of the American Chemical Society* **2006**, *128*, 4970.
- (257) Keyes, T. E.; Forster, R. J.; Jayaweera, P. M.; Coates, C. G.; McGarvey, J. J.; Vos, J. G. *Inorganic Chemistry* **1998**, *37*, 5925.

Appendix – Academic Publications

Publications:

- Chow, C. F., Ho, P. Y., Gong, C. B. (2014). An Ru(II)-Fe(III) Bimetallic Complex as a Multifunctional Device for Detecting, Signal Amplifying, and Degrading Oxalate. *Analyst*, 139, 4256-4263.
- Chow, C. F., Ho, P. Y., Wong, W. L., Gong, C. B. (2015). A Multi-functional Bimetallic Molecular Device for Ultra-sensitive Detection, Naked-eye Recognition and Elimination of Cyanide. *Chemistry-a European Journal*, 21, 12984-12990.
- Chow, C. F., Ho, P. Y., Wong, W. L., Lu, Y. J., Tang, Q., Gong, C. B. (2017). Catalyst Displacement Assay: A Supramolecular Approach for the Design of Smart Latent Catalysts for Pollutant Monitoring and Removal. *Chemical Science*, 8, 3812-3820.